Imperial College London

Department of Physics

Photonics Group

Diode-pumped Alexandrite laser development and vortex mode generation

William Richard Kerridge-Johns

Thesis submitted in partial fulfilment of the requirements for the degree of Doctor of Philosophy of Imperial College London

July 2018

I confirm that all work in this thesis is my own. Any information used or derived from the work of others has been cited at each instance with references provided at the end of the thesis.

Copywrite declaration

Acknowledgements

First thanks must go to my supervisor, Prof. Michael J. Damzen, who has supported and guided me throughout my PhD. His continued patience with data overloads (there is never too much data) and seemingly endless paper drafting has allowed me to achieve all that I have. It would also be amiss to not thank him for intoducing me to the cult of karaoke!

Thanks also go to my colleagues in the group past and present who, aside from much welcomed tea breaks and enduring my endless noughties karaoke playlists, have provided many tables full of useful optics to 'borrow'.

I am grateful that I have had the continued support of my family who have remained enthusiatic in following my PhD, even when the details have sometimes got lost in translation. I hope that I can continue to follow in my grandfather's footsteps, who I know it meant a lot to.

Finally, I must acknowledge the anonymous hand in all this work, Ella, who has dealt with my work induced insanity at times and helped keep me in touch with the world outside of lasers.

Abstract

This thesis is focussed on two aspects of solid-state laser development: optimising and understanding diode-pumped Alexandrite laser performance, and a new laser cavity design for vortex mode generation.

Due to its broad wavelength tunability (700 nm to 858 nm) and excellent physical properties, Alexandrite has a wide range of potential applications from remote sensing to quantum optics. Recent advances in red laser diode-pumping has enabled high power and efficient laser operation. In this work a continuous-wave analytical model of end-pumped Alexandrite lasers was developed and applied to experimental systems. This helped to achieve a record diode-pumped slope efficiency of 54 % with 1.2 W of output power. A record shortest wavelength (714 nm) and broadest tuning range (104 nm) was obtained through optimising the crystal temperature between 8 °C and 105 °C. Investigation and new measurements of the properties of Alexandrite gave rules applicable in general to optimising these lasers, along with assessing the fundamental limits to Alexandrite laser efficiency.

Optical vortex laser beams have attracted considerable attention from their wide range of applications that cover many areas of science, from optical communications to laser machining to microscopic laser manipulation. Directly generating them from a laser has advantages due to the pure and high power modes that can be generated. In this work an anti-resonant ring was proposed and used to couple two lasers through a shared gain medium. Using one cavity to control the output of the other, first order vortex Laguerre-Gaussian modes of power 9.0 W from 24 W of input power with high quality ($M^2 = 2.1$) were obtained, which had controllable and pure handedness. A second order vortex mode with 4.3 W of power was also created. This vortex generation geometry could be applied to any solid-state laser gain medium, which would enable vortex generation across the electromagnetic spectrum.

Publications

Journal papers

W. R. Kerridge-Johns and M. J. Damzen, "Temperature effects on tunable CW Alexandrite lasers under diode end-pumping," Opt. Express **26**, 7771-7785 (2018).

W. R. Kerridge-Johns and M. J. Damzen, "Analytical model of tunable Alexandrite lasing under diode end-pumping with experimental comparison," J. Opt. Soc. Am. B **33**, 2525-2534 (2016).

W. R. Kerridge-Johns and M. J. Damzen, "Analysis of pump excited state absorption and its impact on laser efficiency," Laser Phys. Lett. **12**, 125002 (2015).

W. R. Kerridge-Johns and M. J. Damzen, "Vortex laser modes from coupled cavities," *[Submitted to Optica]*.

M. J. Damzen and **W. R. Kerridge-Johns**, "Diode-pumped Alexandrite lasers: fundamental properties and laser performance," Prog. Quant. Electron, *[Invited review, in preparation]*.

Conference presentations

W. R. Kerridge-Johns and M. J. Damzen, "Vortex mode generation from coupled anti-resonant ring lasers," in *Laser Congress 2017 (ASSL, LAC) OSA Technical Digest (online)*, (Optical Society of America, 2017), ATu1A.2.

W. R. Kerridge-Johns and M. J. Damzen, "Anti-resonant ring laser cavities," in *2017 European Conference on Lasers and Electro-Optics and European Quantum Electronics Conference*, (Optical Society of America, 2017), CA.2.5.

G. M. Thomas, A. Minassian, **W. Kerridge-Johns**, X. Sheng, A. Coney, and M. J. Damzen, "High power and high energy diode-pumped Alexandrite lasers," in *2017 European Conference on Lasers and Electro-Optics and European Quantum Electronics Conference*, (Optical Society of America, 2017), CA.3.3.

M. Damzen, G. Thomas, A. Teppitaksak, E. Arbabzadah, **W. Kerridge-Johns**, and A. Minassian, "Diode-pumped Alexandrite laser - a new prospect for remote sensing," in

2015 Conference on Lasers and Electro-Optics Pacific Rim, (Optical Society of America, 2015), 25B3.2.

E. A. Arbabzadah, **W. Kerridge-Johns**, G. M. Thomas, A. Minassian, and M. J. Damzen, "High efficiency TEM00 diode end-pumped Alexandrite laser," in *2015 European Conference on Lasers and Electro-Optics - European Quantum Electronics Conference*, (Optical Society of America, 2015), CA.6.4.

Conference posters

W. R. Kerridge-Johns and M. J. Damzen, "Tunable CW Alexandrite lasers and fundamental limits of efficiency," in *2017 European Conference on Lasers and Electro-Optics and European Quantum Electronics Conference*, (Optical Society of America, 2017), CA.P.3.

W. R. Kerridge-Johns and M. J Damzen, "Modelling the excited state absorption effects in Alexandrite lasers", in *(2016) 7th EPS-QEOD Europhoton conference*, PO-3.32.

W. R. Kerridge-Johns, E. A. Arbabzadah, and M. J. Damzen, "Optimising Alexandrite laser performance - experiment and theory," in *(2016) 7th EPS-QEOD Europhoton conference*, PO-2.36.

Contents

List of Figures

List of Tables

List of Abbreviations

Abbreviation	Meaning
AOI	Angle of incidence
AR	Anti-reflection
ARR	Anti-resonant ring
BiFi	Birefringent filter
BM	Back mirror
BS	Beamsplitter
CCW	Counter clockwise
CM	Concave mirror
CP	Cube polariser
CW	Clockwise or continuous-wave
DPSS	Diode-pumped solid state
FP	Fabry-Perot etalon
FSR	Free spectral range
FWHM	Full width at half-maximum
ESA	Excited-state absorption
ETU	Energy transfer upconversion
GSA	Ground-state aborption
HCL	Horizontal cylinder lens
HG	Hermite-Gaussian
HWP	Half-waveplate
LED	Light emitting diode
LG	Laguerre-Gaussian
LIDAR	Light detection and ranging
NA	Numerical aperture
OAM	Orbital angular momentum
OC	Output coupler
OPO	Optical parametric oscillator
QWP	Quarter waveplate
RTM	Ray transfer matrix
SLM	Spatial light modulator
TEC	Thermoelectric cooler
TM	Turning mirror
VCL	Vertical cylinder lens
YAG	Yttrium aluminium garnet

Chapter 1

Thesis overview

Lasers are devices that convert energy into a coherent and concentrated beam of optical radiation [1]. When in this form, they provide a method for the precision control and delivery of energy, which has led to a vast array of applications that have helped to catalyse the development of modern society. They have underpinned key technological advancements, for example in optical communications, laser machining, and silicon technologies, along with supporting scientific advancements where the controlled application of electromagnetic energy is required.

A laser consists of a gain medium that amplifies light through stimulated emission. The gain medium is positioned inside a resonant optical cavity that provides feedback of the laser radiation into the amplifying gain medium, thereby creating a feedback loop. The light extracted from this feedback is the output of the laser.

Energy is supplied to the gain medium in the form of a 'pump' source. There are a wide array of energy sources, with some examples being chemical [2], electrical [3], or optical [4]. The type of pumping that can be used is dependent on the gain medium used. For efficient operation of the laser the pumping energy should be supplied to a concentrated area in the gain medium, where it can then be efficiently extracted by the resonating laser light.

Solid-state gain media are generally classified as bulk materials where a laser active ion is supported in either a crystalline or glass host. In these materials optical pumping is most commonly required. The wavelength of pump light needed determines the source that can be used and is dependent on the laser gain medium. The pump can be conventional sources of light, for example electrical gas discharge lamps have been widely used as pump sources [5]. The sun has also been used as a form of renewable pump energy [6]. A laser can itself be used as a pump source for a secondary laser [7].

In this work semiconductor diode lasers are used as pump sources for solid-state gain media, which are termed diode-pumped solid-state (DPSS) lasers. When compared to most other solid-state lasers these can have many advantages [4]. They are typically efficient, both from the high efficiency of the laser diodes and the usually precise delivery

of the optical power to the gain medium. The laser diodes are compact and have lower electrical power requirements compared to other pump sources, particularly the low efficiency gas discharge lamps. The laser diodes also have long lifetimes that allow long operation periods of the DPSS laser before replacements are needed.

Chapter 2 gives an overview of the theoretical and practical considerations of DPSS lasers. The analysis and requirements of optical cavities are shown, along with the impact of thermal effects when used as a laser cavity. The output beams of these cavities are shown in terms of the laser cavity modes, which determine the spatial and frequency structure of laser output. Methods to experimentally analyse the output of a laser cavity are demonstrated for both the spatial and frequency properties.

The remainder of this thesis is focussed on two different DPSS lasers. Chapters 3 and 4 contain work on tunable Alexandrite lasers, with Chapters 5 and 6 looking at the Nd:YVO_4 gain medium for optical vortex generation.

The first gain medium investigated in this thesis is Alexandrite, which is a broadly wavelength tunable (700 nm to 858 nm) room temperature vibronic gain medium [8]. This wide gain bandwidth gives it a range of applications. Its fundamental emission wavelengths make it suitable for vegetation light detection and ranging (LIDAR), which can be performed from aerial platforms to monitor the health of ecosystems [9]. With non-linear frequency conversion into the near and deep UV additional LIDAR methods can be used, for example water vapour [10] or metallic ion [11] measurements. The broad gain bandwidth also makes it suitable as an ultra-short pulsed source [12] with a theoretical minimum pulse duration below 10 fs [13].

Alexandrite has broad absorption bands throughout the visible spectrum, which makes it suitable for optical pumping from a range of sources [14]. Historically gas discharge lamps have been used [15]; however, recent advances in high power red laser diodes has enabled the construction of high power and efficient DPSS Alexandrite lasers [16]. Titanium doped Sapphire is another broadly tunable gain medium with a similar wavelength range, which is extensively used as both a tunable and ultra-short pulse length source; however, it is challenging to diode-pump this laser. Blue laser diodes are commonly used [17], but this brings additional heating and losses compared to the more optimal green pump wavelengths. This makes Alexandrite a potential replacement for Ti:Sapphire in some applications, bringing the advantages of DPSS laser systems.

An aim of the presented work was to develop an improved understanding of the laser mechanisms in Alexandrite lasers. The gain medium has many optical processes, with excited-state absorption (ESA) at pump [14] and laser [18] wavelengths, and ground-state absorption (GSA) at the laser wavelength [19]. These processes, along with the stimulated emission strength, are all wavelength dependent and change across the gain spectrum. Additionally, they are all temperature dependent, as is the upper state lifetime [20]. These processes makes Alexandrite a complex laser gain medium to understand and optimise.

In Chapter 3 the detailed properties of Alexandrite are investigated. To complete the set of temperature dependent parameters, the pump ESA cross sections were measured as a function of crystal temperature for the first time. The cross section was measured to decrease by 12 % from 10 °C to 90 °C. An analytical end-pumped continuous-wave (CW) laser model was derived that was applicable to Alexandrite. This allowed investigation of the effects of pump ESA on laser performance and provided a model that could be investigated across the gain bandwidth and operating temperature range of Alexandrite lasers. The model is of interest for other gain media that have similar optical processes to Alexandrite.

In Chapter 4, the second part of the work on Alexandrite was focussed on experimental demonstrations and investigations of its diode-pumped laser performance. A high efficiency 'compact' laser cavity was constructed to demonstrate the efficiencies that can be achieved in red diode-pumped Alexandrite. This resulted in the record highest slope efficiency diode-pumped Alexandrite laser to date of 54 % with 1.2 W of CW output power.

A wavelength tunable 'extended' cavity Alexandrite laser was constructed to investigate the performance and behaviour of tunable Alexandrite lasers. Using the theoretical model for comparison, the detrimental effects of pump ESA loss on the laser slope efficiency and threshold were shown, with reducing the intra-cavity losses identified as important to reducing its impact. Through optimisation of the crystal temperature a laser tuning range of 714 nm to 818 nm was achieved, which is a record lowest wavelength and total tuning range for a diode-pumped Alexandrite laser. The experimental results confirmed the accuracy of the laser model derived in Chapter 3, which was then investigated to give general rules for optimising Alexandrite lasers, where the particular importance of crystal temperature is shown.

The remainder of this thesis is focussed on the generation of optical vortex modes. An optical vortex is created when light has a spiralling phase along its propagation axis. This gives the wavefront a twisted structure and it possesses orbital angular momentum (OAM). Laser beams with an optical vortex have attracted considerable interest since their OAM was identified in 1992 [21], where the optical vortex doughnut shaped Laguerre-Gaussian (LG) modes are most commonly used. These modes have a wide range of scientific applications, with some examples being microscopy [22], laser machining [23], optical memory [24], optical communications [25], and quantum mechanics experiments [26].

The common Gaussian shaped output of lasers can be converted into optical vortices [27, 28, 29, 30]; however, these methods generally have the drawbacks of requiring specialist optics, being wavelength dependent, requiring low power input, having low conversion efficiency, and being sensitive to misalignments or variations in the input beam [31]. An alternative source of vortex beams is to have them directly generated by the laser cavity [32, 33, 34, 35], these are termed intra-cavity techniques and can

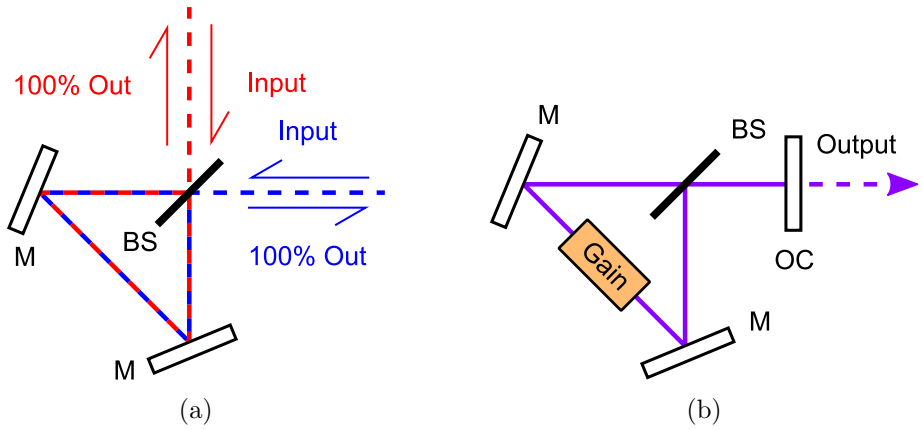

Figure 1.1: The anti-resonant ring (ARR) designs showing (a) the ARR structure with a 50 % beamsplitter (BS) and mirrors (M), which reflects input radiation, and (b) an ARR laser design with an output coupler (OC) and gain medium internal to the ring.

generate pure and high power vortex modes. An intra-cavity vortex generation method was developed in this work.

The vortex laser design investigated used an anti-resonant ring (ARR) as part of the laser cavity. This is a ring structure formed by a beamsplitter and turning mirrors that reflects any input beam, the design is shown in Figure 1.1(a). A laser cavity can be formed with the ARR with an output coupler providing feedback into the ring, as shown in Figure 1.1(b). An ARR laser with the gain medium internal to the ring has only had one published demonstration [36] since its proposal by Siegman in 1973 [37], so the first focus of this work was to understand and evaluate the performance of a laser with this design.

Chapter 5 presents work on the ARR laser geometry. This includes the theoretical basis of lasers with this configuration, with a particular focus on how the laser cavity should be designed to minimise the loss from the ARR. Experimental lasers were constructed with a side and end diode-pumped Nd:YVO_4 gain medium to investigate the experimentally achievable performance of the ARR laser geometry. The round trip loss from the ARR in the end-pumped laser was maintained below 0.02 %, which was a significant improvement on the previous demonstration of 0.4 % [36]. This low loss shows the suitability of the geometry for high power and efficient lasers. The improved performance was achieved by ensuring symmetry in the ARR. The side pumped laser had a higher loss of 1.5 %; however, this implementation had issues with ensuring symmetry of the ARR so could be improved upon with an altered design.

Chapter 6 begins with an overview of vortex generation techniques, both conversion and intra-cavity, along with the methods to correctly analyse vortex laser outputs. This is followed by the experimental work on ARR vortex lasers. The vortex outputs were generated by sharing a gain medium between two otherwise independent laser cavities. One cavity was used to alter the shape of the gain distribution, which induced the other laser to operate on vortex modes. This was achieved with the shared ARR laser

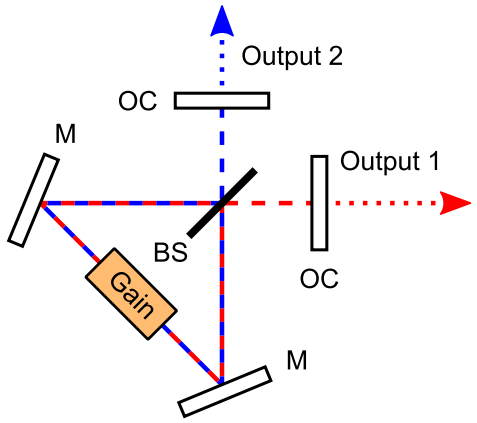

Figure 1.2: The anti-resonant ring coupled laser, where two cavities share a gain medium.

geometry shown in Figure 1.2. Each laser used a separate input into the ARR, which allowed access to a common gain medium.

The ARR coupled vortex laser used diode end-pumped Nd:YVO_4 as the gain medium. With 24 W of pump power, first order vortex beams with 9.0 W of power were generated. The handedness of the vortex could be controlled with the secondary laser cavity. Through simple adjustments to the laser cavity second order vortex beams were also produced, these had 4.3 W of power.

These results demonstrate the capability of the ARR coupled laser geometry to generate vortex laser modes. An advantage of this technique is that it could be applied to any gain medium because only a beamsplitter and mirrors are required to form the ARR. This enables the possibility of vortex beam production across the wavelength ranges accessible by existing laser gain media. Non-linear frequency conversion could then be used to further extend this range and create vortex beam sources tailored to many different applications [38].

Chapter 7 gives a summary of the main results of the thesis, along with conclusions and potential directions of future work.

In summary, the work presented in this thesis has contributed to solid-state laser science in two key ways. Firstly, the modelling capabilities and understanding of diode-pumped Alexandrite lasers has been furthered. This knowledge contributed to demonstrating record efficiencies and tuning ranges in diode-pumped Alexandrite lasers. Secondly, the ARR laser was shown to be an effective laser geometry, which could be used to construct novel coupled cavity designs. One such implementation demonstrated was vortex mode generation. This technique was effective at producing pure and high power vortex modes and could be applied to a wide range of solid-state gain media.

Chapter 2

Diode end-pumped solid state lasers

Semiconductor diodes are widely used sources for optical pumping of laser gain media. Their source of energy is from electricity, which allows for simple and efficient delivery of power to the laser system. The semiconductor emitters can either be manufactured as light emitting diodes (LED), where photons are emitted in all directions in the semiconductor, or as semiconductor laser diodes, where the semiconductor is manufactured into a resonant laser cavity.

LEDs are lower in cost per power, but they suffer as a pump source in having low brightness. This can make it challenging to reach laser threshold when used as a pump source. Luminescent concentrators can be used to increase the brightness of an array of LEDs for more efficient laser pumping [39].

Semiconductor laser diodes are more expensive per unit of power, but have orders of magnitude higher brightness than LEDs. These high brightness and high power sources make them more easily applied as pump devices.

End-pumping of a laser is where the pump beam is delivered to the gain medium along the longitudinal axis of the cavity, which gives the pumped region and the intracavity beam of the laser a high overlap. Combined with the electrical to optical efficiencies of the laser diodes that are typically above 50 % [3], diode end-pumped lasers can be high efficiency laser sources.

The following sections in this chapter present the theory of laser resonators applicable to solid-state gain media. The requirements of a suitable resonant cavity are given, with the impact of thermal lensing in the gain medium also described. The modes of the laser resonator are shown, along with experimental techniques to analyse them.

2.1 Background

The first diode-pumped solid state (DPSS) laser was demonstrated in 1964 [40]. Following this early demonstration, most early work focussed on Neodymium doped laser hosts, specifically Neodymium doped Yttrium Aluminium Garnet (YAG) in side and end-pumping configurations [4]. The relatively high gain and pump absorption of these materials made them suitable for diode-pumping.

Early DPSS lasers, although more efficient than other systems, were limited by the power available from laser diodes. As diode technology improved so did the performance of DPSS lasers. In 1988 the record electrical to optical conversion efficiency of diode lasers was approximately 25 % [4], whereas with modern technology efficiencies are commonly above 50 % with higher peak output powers [3].

Single diode emitters are limited in their output power, typically at the watt level. To increase the total power from a diode pump source multiple emitters can be coupled into a single optical fibre. This creates a high power and high brightness source that can be easily delivered to a gain medium and has a symmetrical beam profile. For end-pumping it is desirable to have a symmetrical pump source to uniformly excite the laser modes of the cavity [41]. This makes fibre-coupled diodes ideal for end-pumped systems, where a high beam overlap can be achieved by matching the fibre output to the internal cavity mode size.

The efficient and high power diodes available today commonly make them the best choice for solid-state lasers that have high overall efficiency, and are compact and cost effective; however, this performance is dependent on the diodes being available at the wavelength and brightness required for the gain medium. Advances continue to be made in diode technology that are enabling higher performance in existing DPSS lasers, along with diode-pumping in new gain media; for example, recent advances in high power red diodes have enabled efficient and high power diode-pumping of Alexandrite [16].

2.2 Cavity stability

The optical cavity of a laser is used to steer the propagating beam of electromagnetic radiation so that it can feedback into itself. The imaging properties of a paraxial cavity with no limiting apertures can be analysed in terms of a ray transfer matrix (RTM), which describes how a beam is imaged by the cavity optical elements. This concept is shown in Figure 2.1(a), where a reference plane is chosen in the cavity from which the round trip RTM is computed. Using the complex beam parameter $\widetilde{q}$ to define the beam at the reference plane, the reproducing modes are given by

$$\widetilde{q} = \frac{A\widetilde{q} + B}{C\widetilde{q} + D}\,, \tag{2.1}$$

where A, B, C and D are the components of the round trip RTM [1].

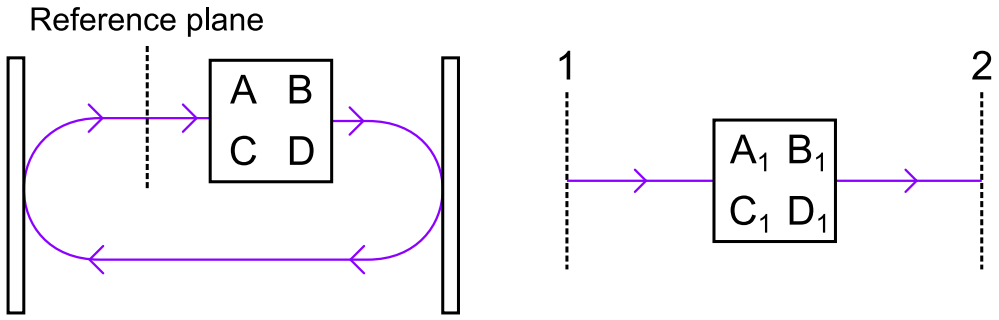

(a) (b)

Figure 2.1: The cavity round trip ray transfer matrices with respect to reference planes for (a) a general cavity round trip and (b) a one way matrix in a linear cavity between planes 1 and 2.

Although the solutions for $\widetilde{q}$ of Equation (2.1) give mathematically correct reproducing beams, they are not necessarily physically meaningful or possible. Determining the physically real solutions for $\widetilde{q}$ is the basis of laser cavity analysis. The values of A, B, C and D can be complex, which leads to additional classes of laser resonator. The most commonly used cavity class, and those in this work, are the geometrically stable cavities with real RTM elements.

The case of a linear resonator composed of two end mirrors is shown in Figure 2.1(b), where the mirrors are defined with plane reference surfaces 1 and 2. The internal optical components are given by the one way RTM of $A_1B_1C_1D_1$. In this geometry, the condition for real stable solutions to Equation (2.1) is that

$$0 < A_1 D_1 < 1\,. \tag{2.2}$$

If the cavity has a stable solution, the mode is a plane wave at each reference surface and has beam radii at surfaces 1 (w_1) and 2 (w_2) of

$$w_1 = \sqrt{\frac{\lambda}{\pi}}\left(-\frac{B_1 D_1}{A_1 C_1}\right)^{1/4}, \tag{2.3}$$

$$w_2 = \sqrt{\frac{\lambda}{\pi}}\left(-\frac{A_1 B_1}{C_1 D_1}\right)^{1/4}, \tag{2.4}$$

where λ is the radiation wavelength [42].

In this work the investigated laser cavities can be approximated to the design shown in Figure 2.2. This cavity consists of two end mirrors with curvatures R_1 and R_2, which are distances l_1 and l_2 from an internal thin lens of focal length f, respectively. The cavity can be analysed in terms of the 'g' parameters, where in this case $g_1 = A_1$ and

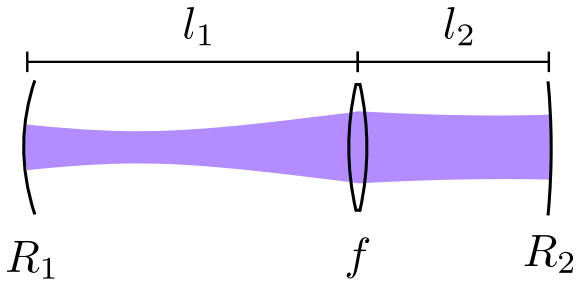

Figure 2.2: A linear cavity geometry with two mirrors ($i = 1, 2$) of curvature R_i, which are distances l_i from a lens of focal length f.

$g_2 = D_1$, which are given by

$$g_1 = 1 - \frac{l_2}{f} - \frac{l'}{R_1}\,, \tag{2.5}$$

$$g_2 = 1 - \frac{l_1}{f} - \frac{l'}{R_2}\,, \tag{2.6}$$

$$l' = l_1 + l_2 - l_1 l_2 / f\,, \tag{2.7}$$

where l' is the effective cavity length [42]. The stability condition of Equation (2.2) then becomes

$$0 < g_1 g_2 < 1\,. \tag{2.8}$$

The cavity is said to be near the edge of stability if $g_1 g_2 \approx 0$ or $g_1 g_2 \approx 1$. The beam radii (w_i) at the end mirrors (R_i) in this resonator are

$$w_1 = \sqrt{\frac{\lambda |l'|}{\pi}} \left[\frac{g_2}{g_1(1 - g_1 g_2)}\right]^{1/4}\,, \tag{2.9}$$

$$w_2 = \sqrt{\frac{\lambda |l'|}{\pi}} \left[\frac{g_1}{g_2(1 - g_1 g_2)}\right]^{1/4}\,, \tag{2.10}$$

for $i = 1, 2$. If the cavity is not near the edge of stability the mode sizes can be approximated by $w_{1,2} \approx \sqrt{\lambda |l'|}$.

In a typical laser system there will be constraints or requirements for the mode sizes, for example this could be from optical damage thresholds requiring large beam sizes or the gain region requiring small beam sizes. Adjusting the cavity length to match the required beam sizes is not usually practical because the mode sizes are not sensitive to the cavity length. For this reason, laser cavities are typically designed to operate near the edge of stability, where the g_1 and g_2 numerators or the $(1 - g_1 g_2)$ factors in the denominator of Equations (2.9) and Equation (2.10) will asymptote to zero or infinity. In this way large variations in beam sizes can be achieved with small adjustments to the cavity design.

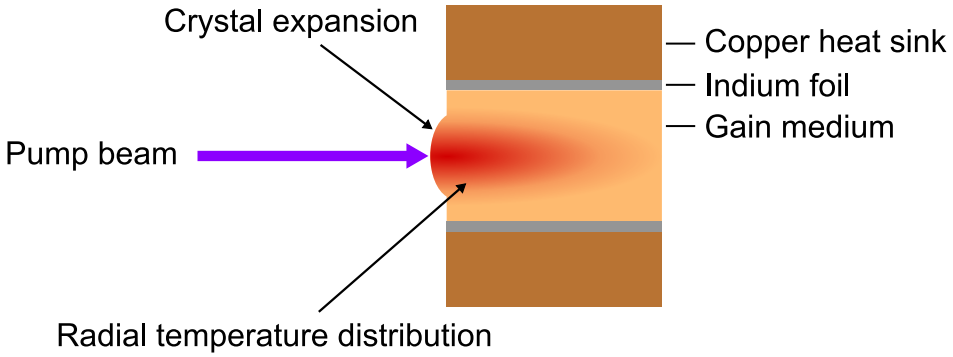

Figure 2.3: The thermal management in an end pumped gain medium. The crystal is thermally contacted to a copper heat sink with Indium foil. The absorbed pump beam creates an approximately radial temperature distribution in the crystal, with thermal expansion causing the crystal to bulge outwards at the input face.

2.2.1 Thermal lens

In most optically pumped laser gain media the pump photons have a shorter wavelength than the laser photons, which means that during the pumping process energy is lost and is usually released as heat in the gain medium. The fraction of pump energy lost in this way is called the quantum defect fraction and represents an unavoidable heating of the gain medium. Different gain media may have additional heating processes.

The gain medium is usually required to be at a certain temperature so the heat energy must be removed. A common thermal management system for end-pumped solid state gain media is shown in Figure 2.3, where the gain medium is thermally contacted to a copper heat sink through indium foil. This system allows the gain medium to be held at approximately the temperature of the heat sink.

Localised heating of the gain medium from the absorbed pump is unavoidable and an approximately radial temperature distribution will be established in the crystal. For top-hat pump beam profiles the temperature distribution is approximately quadratic [43] and gives the gain medium a lensing effect to the laser mode through three main sources.

The refractive index of a gain medium is temperature dependent through its thermo-optic coefficient. The temperature distribution results in a radially dependent optical path length for a propagating laser beam, which causes a lensing effect.

Temperature gradients cause stresses in the gain medium due to thermal expansion. The refractive index is dependent on stress, which results in additional lensing for a propagating laser beam.

In end-pumping the deposited heating power is concentrated towards the input face, where thermal expansion will cause the pumped face to deform and result in a plane surface becoming curved. This effectively turns the gain medium into a thick lens.

By making simplifying assumptions, the net thermal lens focal length for end face bulging along with thermal and stress dependent refractive indices can be analytically

calculated [44]. For more complex pumping and crystal geometries or heating processes numerical modelling can be performed. This requires precise knowledge of the gain medium properties; the thermal and mechanical mounting of the gain medium; and the pump beam distribution. It is generally challenging to accurately determine these parameters in advance, which makes prediction of the thermal lens in a given laser system a difficult task. A pragmatic approach to thermal lens management is to use simple formulae to estimate the thermal lens strength in advance and then optimise the laser of interest when operating.

2.3 Laser cavity modes

The key requirement of the propagating field in a laser cavity is that it reproduces itself exactly on one round trip of the cavity. This ensures that the field is self-reproducing and can be sustained after multiple traverses of the laser cavity. The self-reproducing fields are called the cavity modes and can be sustained in the laser cavity. The modes fit two requirements: both their transverse profile and phase must be unchanged after a cavity round trip. These properties can be thought of separately, but it will be shown that each cavity mode is uniquely defined by the combination of transverse profile and phase reproduction.

2.3.1 Transverse modes

In the following definitions the electric fields are defined through a complex field term $\widetilde{u}$, such that the electric field, E, and corresponding intensity, I, of any given field are

$$E = \mathbb{R}\left[\widetilde{u}e^{i(kz-\omega t)}\right] , \tag{2.11}$$

$$I = \frac{1}{2Z_0}\left|\widetilde{u}\right|^2 , \tag{2.12}$$

where $k = 2\pi/\lambda$ is the wavenumber, λ is the wavelength, z is the distance along the propagation axis, $\omega = 2\pi\nu$ is the angular frequency, ν is the frequency, t is time, and Z_0 is the impedance of free space.

The transverse modes of a resonator are propagation invariant, in that they do not change shape after propagation through free space. This ensures that they fulfil the self reproducing requirement of a cavity mode. They are found through solving the paraxial Helmholtz wave equation, with the solution in rectangular co-ordinates giving the Hermite-Gaussian (HG) modes and in cylindrical co-ordinates the Laguerre-Gaussian (LG) modes. The HG modes are a suitable basis set in cavities that have symmetry about the horizontal (x-z) and vertical (y-z) planes, with the LG modes appropriate for cavities with cylindrical symmetry.

The complex field parameter of the HG modes, $\widetilde{u}^{\mathrm{HG}}_{nm}$, is given in cartesian co-ordinates

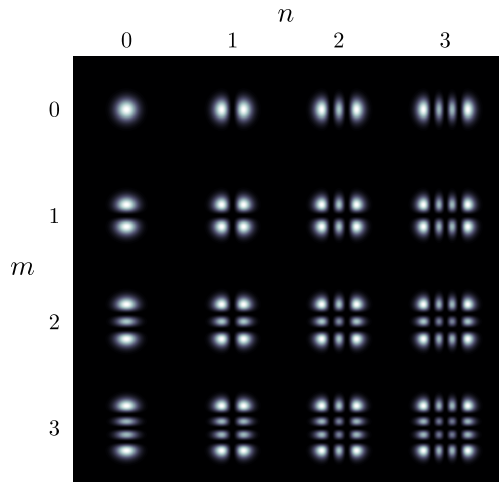

Figure 2.4: The intensity profiles of the HG_{nm} modes.

as

$$\widetilde{u}^{\mathrm{HG}}_{nm}(x,y,z) = \sqrt{\frac{2}{\pi w_{00}^2(z) 2^{n+m} n! m!}} H_n\left(\frac{x\sqrt{2}}{w_{00}(z)}\right) H_m\left(\frac{y\sqrt{2}}{w_{00}(z)}\right) \times \exp\left[-\frac{(x^2+y^2)}{w_{00}^2(z)} - ik\frac{(x^2+y^2)}{2R(z)} - i(n+m+1)\tan^{-1}\left(\frac{z}{z_{\mathrm{R}}}\right)\right], \quad (2.13)$$

where $n \geq 0$ is an integer horizontal mode order, $m \geq 0$ is an integer vertical mode order, and H_μ are the Hermite polynomials of order μ [27]. The intensity profiles of the HG_{nm} modes are shown in Figure 2.4. The number of nodes increases with the mode orders in each axes respectively, and the modes become larger with respect to the Gaussian radius w_{00}.

The complex field parameter of the LG modes, $\widetilde{u}^{\mathrm{LG}}_{pl}$, is given in cylindrical coordinates, $r = \sqrt{x^2+y^2}$ and $\phi = \tan^{-1}(y/x)$, as

$$\widetilde{u}^{\mathrm{LG}}_{pl}(r,\phi,z) = (-1)^p \sqrt{\frac{2p!}{\pi w_{00}^2(z)(p+|l|)!}} \left(\frac{r\sqrt{2}}{w_{00}(z)}\right)^{|l|} L_p^{|l|}\left(\frac{2r^2}{w_{00}^2(z)}\right) \times \exp\left[-\frac{r^2}{w_{00}^2(z)} - ik\frac{r^2}{2R(z)} - i(2p+|l|+1)\tan^{-1}\left(\frac{z}{z_{\mathrm{R}}}\right) - il\phi\right], \quad (2.14)$$

where $p \geq 0$ is an integer radial mode order, l is an integer azimuthal mode order, and $L_p^{|l|}$ are the generalised Laguerre polynomials [27]. The phase accumulated around the circumference of the mode is equal to $2\pi l$. Usually the LG modes of interest are those

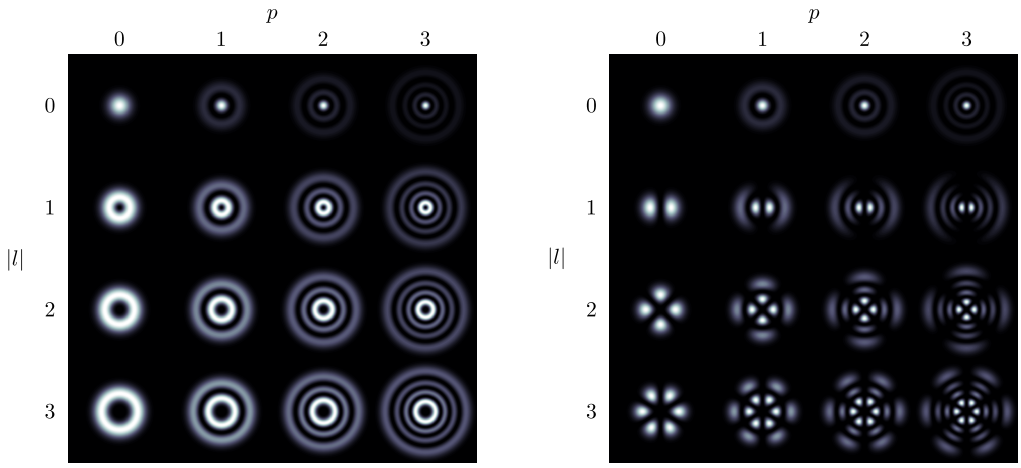

Figure 2.5: The intensity profiles of the (a) LG_{pl} modes and (b) petal $[\mathrm{LG}_{pl} + \mathrm{LG}_{p-l}]$ modes, where the nodes will be rotated for the oppositely phased superposition $[\mathrm{LG}_{pl} - \mathrm{LG}_{p-l}]$.

with zero radial mode order ($p = 0$), which have the simplified form of

$$\widetilde{u}_{0l}^{\mathrm{LG}}(r,\phi,z) = \sqrt{\frac{2}{\pi w_{00}^2(z)|l|!}} \left(\frac{r\sqrt{2}}{w_{00}(z)}\right)^{|l|} \times \exp\left[-\frac{r^2}{w_{00}^2(z)} - ik\frac{r^2}{2R(z)} - i(|l|+1)\tan^{-1}\left(\frac{z}{z_{\mathrm{R}}}\right) - il\phi\right], \quad (2.15)$$

where $L_0^{|l|} = 1$ has been used. In these definitions the fields have been normalised to $\iint \mathrm{d}x\mathrm{d}y|\widetilde{u}|^2 = 1$. The intensity profiles of the LG_{pl} modes are shown in Figure 2.5(a), where they are the same for $+l$ and $-l$ modes. An important feature of the LG modes is the result of coherently adding two modes of opposite handedness, $\mathrm{LG}_{pl} + \mathrm{LG}_{p-l}$. This addition forms the petal modes shown in Figure 2.5(b), where the azimuthal nodes are due to the $\exp(-il\phi)$ term giving constructive and destructive interference azimuthally.

The HG and LG modes propagate using the standard Gaussian beam relationships [27] of

$$R(z) = z + \frac{z_{\mathrm{R}}^2}{z}, \quad (2.16)$$

$$w_{00}(z) = w_{00}(0)\sqrt{1 + \frac{z^2}{z_{\mathrm{R}}^2}}, \quad (2.17)$$

$$z_R = \frac{\pi w_{00}^2(0)}{\lambda} = \frac{k w_{00}^2(0)}{2}, \quad (2.18)$$

where R is the radius of wavefront curvature, z_{R} is the Rayleigh length, $w_{00}(z)$ is the radius of the underlying Gaussian function, and $w_{00}(0)$ is the minimum radius that is defined to be at $z = 0$.

As both the HG and LG modes are orthogonal sets, either can be used to represent an arbitrary field distribution. For example, an arbitrary field, $U(x, y)$, can be decomposed into the HG modes as

$$U(x,y) = \sum_{n=0}^{\infty}\sum_{m=0}^{\infty} \widetilde{c}_{nm}\widetilde{u}^{\mathrm{HG}}_{nm}(x,y)\,, \tag{2.19}$$

$$\widetilde{c}_{nm} = \iint_{-\infty}^{\infty} \left[\widetilde{u}^{\mathrm{HG}}_{nm}(x,y))\right]^{*} U(x,y)\ \mathrm{d}x\mathrm{d}y\,, \tag{2.20}$$

where $\widetilde{c}_{nm}$ is a complex valued coefficient and the asterisk denotes complex conjugation [1]. The coefficients obey $\sum_{n,m}|\widetilde{c}_{nm}|^2 = 1$ when U is normalised as $\iint |U|^2\,\mathrm{d}x\mathrm{d}y = 1$. The value $|\widetilde{c}_{nm}|^2$ therefore represents the relative power of the constituent HG_{nm} modes [45].

In addition to this, each mode from one set of solutions can be decomposed into components of the other [27]. An LG mode in terms of the HG modes is given by

$$\widetilde{u}^{\mathrm{LG}}_{pl}(x,y,z) = \sum_{j=0}^{(n+m)} i^j b(n,m,j)\widetilde{u}^{\mathrm{HG}}_{(n+m-j),j}(x,y,z)\,, \tag{2.21}$$

where $p = \min(n, m)$, $l = (n - m)$, and b are real coefficients given by

$$b(n,m,j) = \left[\frac{(n+m-j)!j!}{2^{n+m}n!m!}\right]^{1/2} \frac{1}{j!}\frac{\mathrm{d}^j}{\mathrm{d}t^j}\left[(1-t)^n(1+t)^m\right]_{t=0}\,. \tag{2.22}$$

Example decompositions of the LG_{01} and LG_{02} modes are shown in Figure 2.6. The LG_{01} mode is formed from a coherent superposition of the HG_{01} and HG_{10} modes with a $\pi/2$ phase difference. To reverse the handedness of the LG modes the relative phases of the HG modes are altered; for the LG_{01} and LG_{02} decompositions given, the $-i/\sqrt{2}$ coefficient is replaced with $+i/\sqrt{2}$. In the decomposition the total mode orders of each mode are constant so $(n + m) = (2p + |l|)$. This is apparent in the LG_{02} decomposition where HG modes of order $(n + m) = 2$ are the constituent components.

2.3.2 Longitudinal modes

The phase reproduction requirement in a laser cavity determines the electromagnetic frequencies of the modes. In general, these frequencies are not independent of the transverse modes of the cavity due to different Gouy phase shifts on propagation for higher order modes. In this section the analysis will be performed for the HG_{nm} modes; however, the relations can be easily altered for the LG_{pl} modes by substituting $(n + m)$ for $(2p + |l|)$ where it appears.

For the phase of a beam to be reproduced after one cavity round trip the total phase shift must be $2\pi q$, where q is an integer and is the longitudinal mode order. This

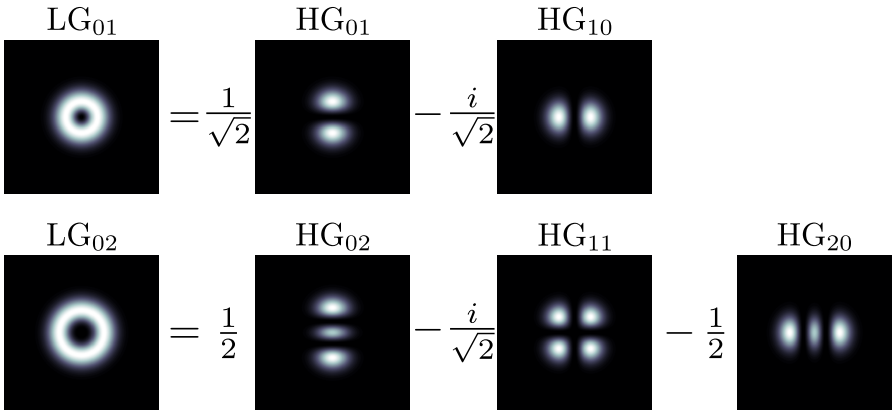

Figure 2.6: The decomposition of the LG_{01} and LG_{02} modes into their HG counterparts.

condition gives

$$\frac{2\pi p \nu_{nmq}}{c} - \Delta\psi_{nm} = 2\pi q\,, \tag{2.23}$$

where p is the round trip optical path length perimeter of the cavity, c is the speed of light, ν_{nmq} is the frequency, and $\Delta\psi_{nm}$ is the round trip phase change [42]. The quantities that are dependent on the transverse modes are explicitly labelled by their orders n and m. Rearranging the equation gives the longitudinal mode frequencies as

$$\nu_{nmq} = \frac{c}{p}\left[q + \frac{\Delta\psi_{nm}}{2\pi}\right]. \tag{2.24}$$

There may be additional phase changes on propagation in the cavity, but these will only act as a fixed frequency offset for all the cavity modes. The case of mirror inversion astigmatism will be considered in a later chapter, see Section 5.2.1.

As a Gaussian beam propagates through a focus it experiences a Gouy phase change. This is the source of the transverse mode dependent phase change, $\Delta\psi_{nm}$, as different order Gaussian modes undergo different amounts of Gouy phase changes. The amount of Gouy phase a beam will accumulate depends on how the beam is focussed on propagation, therefore, the phase changes in a laser cavity are dependent on the focussing geometry of that cavity. For a general stigmatic stable resonator this is given by

$$\Delta\psi_{nm} = \begin{cases} +(n+m+1)\cos^{-1}\left(\frac{A+D}{2}\right) & \text{for } B > 0 \\ -(n+m+1)\cos^{-1}\left(\frac{A+D}{2}\right) & \text{for } B < 0 \end{cases} \tag{2.25}$$

where A, B, and D are the components of the round trip ray transfer matrix of the cavity. This can then be used in Equation (2.24) to find the longitudinal modes of a general laser cavity.

It can be shown that for a linear cavity this gives the mode frequencies as

$$\nu_{nmq} = \frac{c}{2L}\left[q + \frac{(n+m+1)}{\pi}\cos^{-1}\left(\pm\sqrt{g_1 g_2}\right)\right], \tag{2.26}$$

where L is the cavity optical path length, $g_1 = A_1$ and $g_2 = D_1$ are the components of the one way ray transfer matrix, and the + or − signs are for $g_1, g_2 > 0$ or $g_1, g_2 < 0$ respectively [42].

In the case of an astigmatic resonator that is symmetric about the xz and yz planes (simple astigmatism), there are separate stability parameters $g_{1\mu}$, $g_{2\mu}$ for the $\mu = x, y$ planes. The mode frequencies of this cavity are then

$$\nu_{nmq} = \frac{c}{2L}\left[q + \frac{(n+\frac{1}{2})}{\pi}\cos^{-1}(\pm\sqrt{g_{1x}g_{2x}}) + \frac{(m+\frac{1}{2})}{\pi}\cos^{-1}(\pm\sqrt{g_{1y}g_{2y}})\right], \qquad (2.27)$$

where the + or − signs correspond to positive or negative $g_{1\mu}$ and $g_{2\mu}$ as before [46]. If the cavity is symmetric with $g_1 = g_{1x} = g_{1y}$ and $g_2 = g_{2x} = g_{2y}$ then the relationship simplifies to Equation (2.26). Alternatively, the cavity may have astigmatic components but satisfy $g_{1x}g_{2x} = g_{1y}g_{2y}$.

A key feature of the symmetric cavity mode frequencies, Equation (2.26), is that HG_{nm} modes are degenerate in frequency if they have the same total mode order $(n+m)$. When a cavity is astigmatic, as in Equation (2.27), this degeneracy is broken by the separate Gouy phase shifts in the different axes.

2.3.3 Mode analysis

In usual laser applications specific modes of the resonator are required, so diagnostic techniques are needed to analyse them. In this section the measurement and analysis of the transverse profile of a laser beam is presented using a beam quality parameter. The frequency analysis of the longitudinal modes of a resonator can be performed using a Fabry-Perot interferometer.

Beam quality parameter

A seemingly simple measurement of a laser beam is to measure its diameter; however, this is not a trivial task. In practice a laser will typically not oscillate on a pure transverse mode such as those given in Section 2.3.1, but potentially a mixture of them. Different applications of lasers also have varying requirements of the beam, for example the power distribution may be more important than its detailed structure.

A widely used measurement technique is the second moment width defined in ISO 11146-1/2/3. This is measured by taking an the intensity distribution $I(x, y)$ at one plane and computing the relationship

$$w_x^2 = 2\frac{\iint (x-\bar{x})^2 I(x,y)\ \mathrm{d}x\mathrm{d}y}{\iint I(x,y)\ \mathrm{d}x\mathrm{d}y}, \qquad (2.28)$$

where w_x is the second moment radius and $\bar{x}$ is the centroid location. For the Gaussian shaped HG_{00} mode this is equivalent to the distance from the peak intensity to $1/e^2$

that value. The second moment width can be calculated analytically for the transverse modes of Section 2.3.1, giving beam radii in the x, w_x, and y, w_y, directions of

$$\mathrm{HG}_{nm}: \quad \begin{cases} w_x(z) = w_{00}(z)\sqrt{2n+1}\,, \\ w_y(z) = w_{00}(z)\sqrt{2m+1}\,, \end{cases} \tag{2.29}$$

$$\mathrm{LG}_{pl}: \quad w_{x,y}(z) = w_{00}(z)\sqrt{2p+|l|+1}\,, \tag{2.30}$$

where w_{00} is the radius of the underlying Gaussian function in Equations (2.13) and (2.14).

An advantage of this measurement method is that the resulting radii obey the Gaussian beam propagation formula along the z direction of

$$w_\mu(z) = w_{\mu 0}\sqrt{1+\left(\frac{\mathrm{M}_\mu^2 \lambda z}{\pi w_{\mu 0}^2}\right)^2}\,, \tag{2.31}$$

where $\mu = x$ or y is the considered axes, w_μ is the second moment beam radius, $w_{\mu 0} = w_\mu(0)$ is the minimum beam radius located at $z = 0$, and M_μ^2 is the beam quality parameter, all with respect to the x or y direction.

To determine the M^2 parameter the beam radius is measured in many planes along z as it focusses through a beam waist. If the wavelength is known, then Equation (2.31) can be fitted to the radius measurements to find a best-fit value of M^2. If the beam is astigmatic the beam quality will be different in each axis, so this procedure is performed along orthogonal directions to give separate beam qualities of M_x^2 and M_y^2. A cylindrical beam quality M_r^2 can also be defined, which quantifies the average beam quality from each axis.

The beam quality parameter can be derived analytically for the pure Hermite-Gaussian or Laguerre-Gaussian transverse modes given in Section 2.3.1, with a beam composed of one of these pure modes having a beam quality of

$$\mathrm{HG}_{nm}: \quad \begin{cases} \mathrm{M}_x^2 = 2n+1\,, \\ \mathrm{M}_y^2 = 2m+1\,, \\ \mathrm{M}_r^2 = n+m+1\,, \end{cases} \tag{2.32}$$

$$\mathrm{LG}_{pl}: \quad \mathrm{M}_{x,y,r}^2 = 2p+|l|+1\,. \tag{2.33}$$

For a beam that is an incoherent mix of HG_{nm} modes [47], each with normalised power

fractions $|\widetilde{c}_{nm}|^2$, the beam qualities are given by

$$\mathrm{M}_x^2 = \sum_{n=0}^{\infty}\sum_{m=0}^{\infty}(2n+1)\,|\widetilde{c}_{nm}|^2 \ , \tag{2.34}$$

$$\mathrm{M}_y^2 = \sum_{n=0}^{\infty}\sum_{m=0}^{\infty}(2m+1)\,|\widetilde{c}_{nm}|^2 \ , \tag{2.35}$$

$$\mathrm{M}_r^2 = \sum_{n=0}^{\infty}\sum_{m=0}^{\infty}(n+m+1)\,|\widetilde{c}_{nm}|^2 \ . \tag{2.36}$$

Therefore, the beam qualities are the averages of the constituent HG_{nm} modes with weighting equal to $|\widetilde{c}_{nm}|^2$.

A more realistic model of a laser output allows for coherent addition of modes with equal total mode order $(n+m)$. This adds significant complexity for the M_x^2 and M_y^2 formulae [45]; however, their average value $\frac{1}{2}(\mathrm{M}_x^2+\mathrm{M}_y^2)$ gives the same result as for the cylindrical beam quality M_r^2 in the case of fully incoherent addition [48] in Equation (2.36). The LG_{pl} modes are formed of coherent additions of the HG_{nm} modes with $(n+m)=(2p+|l|)$, so for a resonator oscillating on a pure LG_{pl} mode then the expected value $\mathrm{M}_r^2=(n+m+1)\equiv(2p+|l|+1)$ of Equation (2.33) holds. For a mix of LG_{pl} and HG_{nm} components the difference between M_x^2 and M_y^2 will identify astigmatism in the beam, with M_r^2 indicating the most likely dominant LG_{pl} mode oscillating.

Beam quality measurements can be used to indicate the dominant modes in any given beam. However, this measurement alone is not sufficient to determine the precise contributions and purity of a laser mode, because for $\mathrm{M}_{x,y}^2 \neq 1$ there are infinitely many combinations of $|\widetilde{c}_{nm}|^2$ that could match any given $\mathrm{M}_{x,y,r}^2$ value.

Frequency measurement

The oscillation frequency of a laser can be measured with a spectrometer, these can measure the frequency with resolutions typically ranging from 0.5 nm to 0.07 nm for digital devices. This level of resolution is sufficient to find the average wavelength of oscillation, but is too large to analyse the finer level structure of the longitudinal modes where the mode spacing is 1 GHz for a 15 cm linear cavity, for example. This level of resolution could be measured using a large finer resolution spectrometer; however, a more efficient method can be to use a Fabry-Perot (FP) interferometer.

A FP interferometer consists of two plane partially reflecting surfaces, with reflectance R, separated by an optical distance of L [1]. The transmission, T_{FP}, of a plane wave incident at an angle β is given by

$$T_{\mathrm{FP}} = \left[1+\frac{4R}{(1-R)^2}\sin^2\left(\frac{2\pi\nu L\cos\beta}{c}\right)\right]^{-1} \ . \tag{2.37}$$

The transmission is maximised when $2\pi\nu L\cos\beta_s/c = s\pi$, where s is an integer interfe-

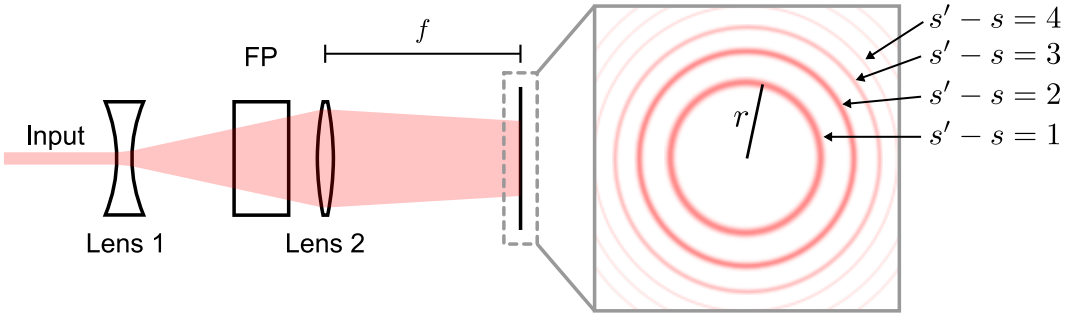

Figure 2.7: The Fabry-Perot (FP) frequency measurement technique. The input beam is diverged with lens 1 and passes through the FP. Lens 2 images the fringes at a distance equal to its focal length away, f. The observation plane has a series of concentric rings, where each corresponds to a different mode order s.

rence fringe order. The highest order fringe is at normal incidence ($\beta = 0$) and is given by $s' = 2L\nu/c$, which will typically be a large number. For example, a 1 cm long air spaced Fabry-Perot interferometer for near infrared light at 1 µm has $s' = 20\,000$. The angles of the interference peaks can then be approximated as

$$\beta_m^2 \approx \frac{2(s' - s)}{s'}\,, \tag{2.38}$$

where it has been assumed that $s' \gg 1$ and $\beta_s \ll 1$ (near normal incidence).

The free spectral range (FSR) of the interferometer is defined as the frequency difference, ν_{FSR}, between two input waves where the interference fringes overlap at fixed input angle β. It is given by

$$\nu_{\mathrm{FSR}} = \frac{c}{2L\cos\beta}\,, \tag{2.39}$$

and determines the maximum bandwidth of the input beam that can be measured before the fringes of different orders s overlap.

The finesse of a FP is $\mathfrak{F} = \pi\sqrt{R}/(1 - R)$ (for $R > 0.5$ [49]) and determines the ratio of the fringe full width half maximum (FWHM) to FSR of the interference pattern. A high finesse gives a high resolution interference pattern due to the small FWHM and allows frequency components much smaller than the FSR of the FP to be resolved. For example, $R = 0.9$ gives $\mathfrak{F} = 30$, so frequency components at least an order of magnitude smaller than ν_{FSR} could be resolved.

The FP can be used to analyse the frequency structure of a laser beam using the configuration shown in Figure 2.7. The beam to be analysed is given a large radius of curvature wavefront from a diverging lens. It is then incident on the FP, where it can be modelled as a mixture of plane waves at a range of incident angles β. The lens after the FP focusses the transmitted beam to reveal the interference fringes at the focal length away from the lens. In this way the fringe angles β_s are converted into displacements in the observation plane of $f\beta_s$.

The fringe pattern is a series of concentric circles, each corresponding to a decreasing

order s from the centre outwards, see Figure 2.7. The square of the radial distance r is proportional to $(s' - s)$, see Equation (2.38), which can be shown to be linear in frequency. The r^2 distances can be calibrated into a frequency scale using the known ν_{FSR} of the FP and the separation of the repeating fringe pattern of different mode orders s.

Using this technique the frequency separation of components of an input beam can be determined with the resolution determined by the finesse and FSR of the FP. It can give access to frequency measurement resolutions of the order of 100 MHz in a simple and compact geometry that is sufficient to analyse the longitudinal frequency structure of a laser.

Chapter 3

Alexandrite properties and model

Alexandrite was the gain medium used in the first room temperature vibronic laser in 1976 [50]. Due to its vibronic emission it possesses a broad gain bandwidth with lasing demonstrated from 701 nm to 851 nm [8, 51]. This makes it suitable for a wide range of applications from vegetation LIDAR [9] to a femtosecond pulsed source [13].

Historically flashlamp pumping has been most commonly used [15]; however, the broad absorption bands also make Alexandrite suitable for a range of pumping geometries. Recent advances in high power red laser diode technology has made this an attractive option for use with Alexandrite [16], making it a potential diode-pumped competitor to the extensively used Titanium doped Sapphire laser.

In this section the properties of Alexandrite are explored, analysing the physical and optical properties that make it suitable as a high power laser gain medium. The many optical process, such as laser and pump excited-state absorption (ESA) and laser ground state absorption (GSA), all have temperature and wavelength dependence, making it a complex material to understand. These characteristics highlight the need for a laser model to efficiently analyse its lasing properties.

A new end-pumped laser model was developed incorporating all of the Alexandrite transitions. This model and analysis was published in international peer reviewed journals, each time being recognised as significant works (Laser Physics Letters - Highlight of the year 2015 [52], Optical Society of America - Spotlight on Optics December 2016 [53]).

The temperature dependence of the pump ESA cross section was also measured for the first time, giving a complete set of parameters for Alexandrite modelling and highlighting the effect of laser performance on the temperature of crystal.

3.1 Optical and material properties

For a material to be a suitable laser gain medium it must satisfy certain physical and optical parameters. The material must be physically strong enough to withstand the

Table 3.1: Comparison of the key mechanical, thermal and optical properties of Alexandrite, Ti:Sapphire, Ruby and Nd:YAG.

	Alexandrite	**Ti:Sapphire**	**Ruby**	**Nd:YAG**	Ref.
Formula	$BeAl_2O_4:Cr^{3+}$	$Al_2O_3:Ti^{3+}$	$Al_2O_3:Cr^{3+}$	$Y_3Al_5O_{12}:Nd^{3+}$	[54, 55]
Dopant concentration (at.%)	0.05-0.2	0.1	0.03	1.0	[54, 55]
Dopant ion density (cm^{-3})	$1.75\text{-}7.0 \times 10^{-19}$	$4.56x10^{-19}$	1.58×10^{19}	1.38×10^{20}	[54, 55]
Melting point (°C)	1870	2040	2040	192	[54, 55]
Density (g cm^{-3})	3.7	3.98	3.9	4.56	[54, 55]
Thermal expansion coefficient (10^{-6} C^{-1})[a]	6.2	5	5.8	7.9	[54, 55]
Thermal conductivity (W cm^{-1} K^{-1}) at 300K[a]	0.23	0.33	0.42	0.13	[54, 55]
Heat fracture limit (W cm^{-1})	600	˜1000	1000	120	[8]
Hardness (Knoop)	2000	2000[a]	2276	1215	[56, 55]
Refractive index[a]	1.74 (750nm)	1.76 (633nm)	1.76 (693nm)	1.82 (1064nm)	[5, 55]
dn/dT (K^{-1})	8×10^{-6}	8×10^{-6}	12.6×10^{-6}	7.3×10^{-6}	[57, 55]
Scattering loss (cm^{-1})	<0.003	0.002	0.001	0.002	[5, 55]
Non-linear refractive index (10^{-20} m^2W^{-1}) at 1064nm	2.0 ± 0.2	2.8 ± 0.3	2.5 ± 0.35	7.23 ± 1.4	[58, 59]

[a]averaged over the principal axes

heat loading of pumping. It must also have a suitable energy level structure to support a population inversion for stimulated emission to provide gain. In this section, the optical and material properties of Alexandrite are explored, showing the characteristics that makes Alexandrite a suitable high power laser gain medium, along with the complexities of the material.

3.1.1 Physical properties

Alexandrite is a naturally occurring gemstone, it consists of trivalent Chromium doped in a Chrysoberyl host, with the composition $Cr^{3+}:BeAl_2O_4$. A summary of the properties of Alexandrite, compared to Titanium doped Sapphire (Ti:Sapphire), Ruby and Neodymium doped Yttrium Aluminium Garnet (YAG), is shown in Table 3.1. Ruby and Ti:Sapphire are useful for comparison as a benchmark for a laser material because their common Sapphire host material has some of the best mechanical properties for solid state lasers. Ruby is also interesting as it is another trivalent Chromium material. Nd:YAG is a highly successful solid state laser medium, so is indicative of a suitable set of material properties for a laser medium.

The thermal conductivity of a gain medium is an important property due to the many detrimental thermal effects on laser operation. These may be optical, such as thermal lensing or optical constants changing with temperature, or mechanical, such as thermal stress fracture or thermally induced birefringence. A higher conductivity will allow faster heat dissipation, aiding cooling of the crystal, reducing the severity of these effects. It can be seen from Table 3.1 that Alexandrite has a relatively high thermal conductivity, twice that of Nd:YAG, which indicates its good thermal properties and suitability as a gain medium for high power operation.

The heat fracture limit is an estimate of the heating power that can be absorbed, per

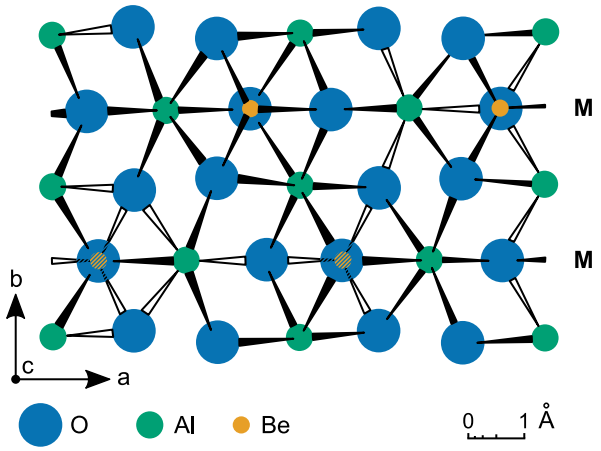

Figure 3.1: The unit cell of the Chrysoberyl host in Alexandrite projected along the c crystallographic axis, the a and b directions are indicated. The horizontal mirror planes are denoted by M. Adapted from [61]

unit length of a rod, before fracturing due to heat induced stress. Alexandrite performs well in this measure, with five times the heat loading it can withstand compared to Nd:YAG, partly due to its higher thermal conductivity and lower thermal expansion coefficient. This shows that Alexandrite can withstand the large heat loading that is necessary for high pump power operation.

High quality synthetic Alexandrite crystals can be grown via the Czochralski process [55] with typical dopant concentrations used up to 0.5 at.% Cr, where the at.% is the fractional substitution of Cr^{3+} in the crystal host Al^{3+} sites. The quality of the crystals is shown by the scattering loss being comparable to that of Nd:YAG.

Other wavelength tunable chromium doped laser gain media use colquiriite (fluoride based) hosts [60], for example Cr^{3+}:LiSAF. The key advantage of Alexandrite over these materials is its superior physical properties, being harder and having greater thermal conductivity [5].

3.1.2 Optical properties

The unit cell of the Alexandrite crystal is shown in Figure 3.1. It has orthorhombic symmetry and the Al^{3+} ions, which the Cr^{3+} replaces, are enclosed in octahedral arrangements. The octahedra can exist in two states with either mirror, when on a crystal mirror plane, or inversion symmetry [61].

It was found by Forbes [62] that for lightly doped samples (0.1-0.3 at.% Cr) grown by the Czochralski process, the mirror site occupancy fraction is $78 \pm 3\%$. It was determined that this occupancy fraction is likely to be independent of dopant concentration up to approximately 5 at.%.

The optical transition strength of Chromium in mirror sites is orders of magnitude higher than in inversion sites due their relatively strong electric dipole transitions. The inversion sites are restricted to weaker magnetic dipole transitions. This means that

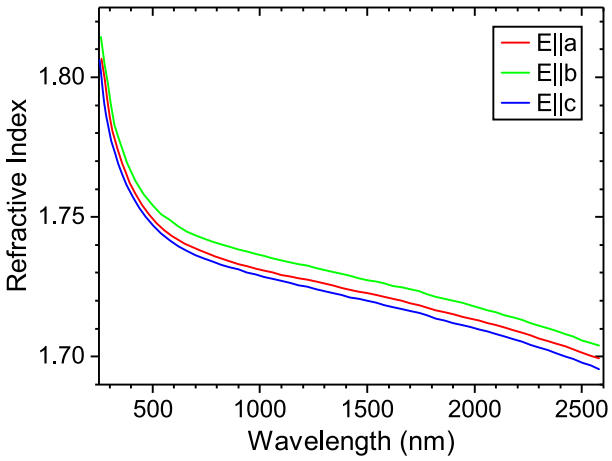

Figure 3.2: Refractive index of Alexandrite with wavelength for the three polarizations relative to the crystallographic axes. Adapted from [8]

only ions in mirror sites play a role in the spectroscopic properties of the crystal [8].

The main effect of the mirror sites is to reduce the number of optically active ions in the crystal, increasing the total Chromium doping needed for a required active ion density. The inactive ions act also as a potential energy sink via energy transfer from mirror sites [63]. They have a long fluorescence lifetime of approximately 10 ms, which raises the overall fluorescence lifetime in Alexandrite for increasing chromium doping concentrations [64]. The extra Chromium impurities in the crystal will also increase the probability of doping induced defects at higher concentrations.

The intrinsic optical damage threshold (surface and bulk) of Alexandrite has been reported to exceed power densities of 23 $GWcm^{-2}$ and fluences of 270 Jcm^{-2} [15]. These thresholds were found using a 12 ns pulse duration test beam of 16 µm diameter. The areas tested for these thresholds were pre-screened to exhibit low scattering, when this was not done, the thresholds decreased significantly. It has been found during laser experiments that optical damage from power density occurs at approximately 1.5 $GWcm^{-2}$. Repeatable damage free operation has been performed at fluences of 30 Jcm^{-2}. The decreased damage limits in operation are most likely due to surface defects.

The non-linear refractive index is lower than that of Nd:YAG, so Alexandrite is less susceptible to high intensity effects, such as self focussing.

Alexandrite is optically biaxial as a consequence of its orthorhombic symmetry. The refractive index over the wavelength range 0.25 µm to 2.5 µm is shown in Figure 3.2.

3.1.3 Laser characteristics

Alexandrite is part of a family of gain media with trivalent Chromium as the active ion. These all exhibit similar lasing characteristics, but with distinctive differences due to the different crystal hosts.

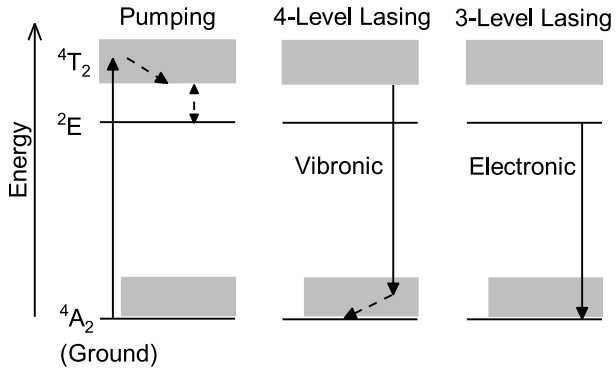

Figure 3.3: The pumping mechanism and lasing modes of the Cr^{3+} ion in Alexandrite. Solid lines are stimulated optical transitions, dashed lines are non-radiative transitions. Energy levels are labelled with their spectroscopic notation.

Lasing mechanisms of trivalent chromium

The energy levels involved in laser action for the Cr^{3+} ion are shown in Figure 3.3. Vibronic transitions can occur between the ground and $^4T_2$ excited state, resulting in a band of absorption, which is the transition used in most pumping schemes. The pump photons excite ions to a higher vibrational level of the $^4T_2$ band, which then decay non-radiatively to the base of the $^4T_2$ level. The excited ion population then becomes thermally distributed between the $^4T_2$ and ^2E states via non-radiative transitions. Two modes of lasing can then occur.

The first is a four-level scheme using the $^4T_2$ level. A vibronic transition from $^4T_2$ to a higher vibrational state of the ground level is the source of stimulated emission. The ions then decay non-radiatively down to the base of the ground level, depleting the excited vibrational population, which results in a four-level lasing scheme.

The second is a three-level scheme using the ^2E level, in which electronic transitions to the ground state occur. This has the characteristic narrow bandwidth of an electronic transition and is called R-line operation.

The type of lasing that will occur in a given system is that which has the lowest threshold inversion for laser action. It is therefore critical how the excited ion population is distributed between the excited states. Four level lasing has an intrinsically much lower threshold compared to three-level, which means that the vibronic mode will typically dominate if the $^4T_2$ level is populated.

The exact energy structure of the Cr^{3+} excited states depend on the crystal host. When the ion is present in different host media it will experience different crystal fields, which control the energies of the levels. Trivalent Chromium has a d-configuration of d^3, the simplified Tanabe-Sugano diagram [65] for a d^3 ion in an octahedral complex is shown in Figure 3.4. It can be seen that the different crystal fields result in a changing separation, $\triangle$E, of the $^4T_2$ and ^2E levels.

When the crystal field is large, as in Ruby, $\triangle$E is 2350 cm^{-1}. This means that the

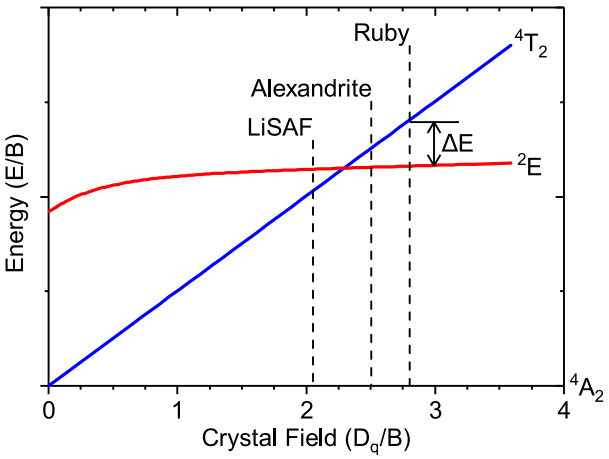

Figure 3.4: The Tanabe-Sugano diagram [65] for trivalent Chromium, the crystal fields of various crystal hosts have been marked. The crystal field splitting parameter is D_q, the energy of the state is E, B is the Racah parameter, and $\triangle$E is the energy separation of the excited states. Adapted from [66]

thermal population of the higher $^4T_2$ level is vanishingly small and almost all of the excited population resides in the ^2E level.

For a smaller crystal field, as in Cr^{3+}:LiSAF, the $^4T_2$ level is below the ^2E level, resulting in the population being distributed in the vibrational states of $^4T_2$.

In the case of Alexandrite, $^4T_2$ is above the ^2E level, but with $\triangle$E being $800\,cm^{-1}$. This means that at room temperature the $^4T_2$ level is thermally populated.

The structure of the energy levels can be used to determine the type of lasing that will occur in each crystal host. For Ruby, with its large $\triangle$E, the population in $^4T_2$ is vanishingly small, meaning only three-level lasing occurs. For LiSAF, $^4T_2$ is below ^2E so has the majority of the excited population, resulting in vibronic lasing dominating. In Alexandrite the energy separation is at a critical point where the thermal population of $^4T_2$ is approximately 4 % of the excited ions at room temperature [8], which is sufficient for four-level lasing to dominate.

The threshold inversion of four-level lasing is much lower compared to three-level. It was estimated by Sevast'Yanov [67] that the approximate fractional total population inversion required for room temperature R-line lasing is 0.508 in Alexandrite. The threshold inversion required for vibronic lasing is approximately one order of magnitude lower, which results in vibronic lasing occurring at room temperature and above in Alexandrite. If R-line lasing is required the vibronic mode must be suppressed, which can be achieved at low temperatures.

The excited ion populations in the $^4T_2$ and ^2E levels are determined by the occupation probabilities of the two levels, which are affected by both energy separation and temperature; therefore these parameters are critical to lasing characteristics. It is the variation in the populations of the excited states that gives Alexandrite its interesting thermo-optical properties.

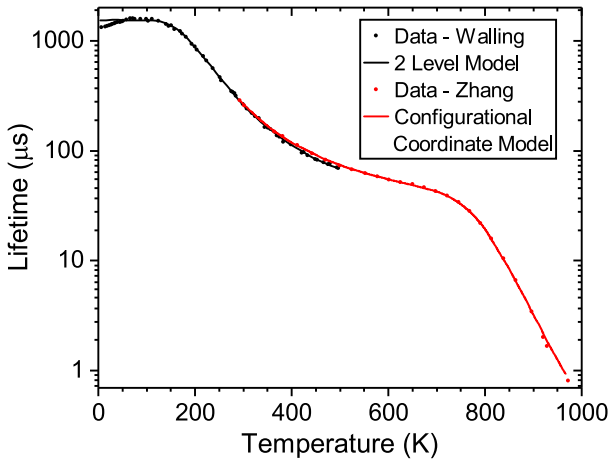

Figure 3.5: The upper state lifetime of Alexandrite as a function of temperature. The data points and models (solid lines) are shown from two groups, Walling et. al. [8] and Zhang et. al. [20]. The data from Zhang are higher than those of Walling, which is attributed to radiative trapping. Walling is assumed to be more accurate.

Spontaneous processes

An important property for a gain medium is the upper state lifetime. This is a combination of fluorescence emission and quenching processes. It is assumed that Alexandrite has 100 % quantum yield, that there are no spontaneous processes other than fluorescence for excited ions in the upper lasing level. This was supported by the accuracy of cross section calculations performed at different temperatures ranging from 77 K to 300 K [8].

The fluorescence lifetime in Alexandrite has a strong temperature dependence. This is due to lifetime of $^2\mathrm{T}_2 \rightarrow ^4\mathrm{A}_2$ being much shorter than that of $^2\mathrm{E} \rightarrow ^4\mathrm{A}_2$, because the latter is doubly forbidden by spin and parity. This gives $^4\mathrm{T}_2$ a transition strength one or two orders of magnitude stronger [66]. The fluorescence lifetime is therefore dependent on the relative populations of the two levels. A two level model was successfully used by Walling et. al. to predict the fluorescence lifetime of Alexandrite for temperatures of 70 K to 500 K, Figure 3.5, given by

$$\tau_\mathrm{f} = \tau_\mathrm{E}\left[\frac{1+\mathrm{e}^{-\triangle E/k_\mathrm{b}T}}{1+(\tau_\mathrm{E}/\tau_\mathrm{T})\mathrm{e}^{-\triangle E/k_\mathrm{b}T}}\right], \tag{3.1}$$

where k_b is the Boltzmann constant. This model assumes the total upper state lifetime is from the thermal occupation of two excited levels, each with its own intrinsic lifetime. The $^4\mathrm{T}_2$ level has a lifetime of $\tau_\mathrm{T} = 6.6\,\mu\mathrm{s}$, $^2\mathrm{E}$ of $\tau_\mathrm{E} = 1.54\,\mathrm{ms}$, and the levels have an energy separation of $\triangle E = 800\,\mathrm{cm}^{-1}$.

An investigation of the fluorescence lifetime for temperatures up to 973 K was conducted by Zhang et. al. [20], see Figure 3.5. It was found that at approximately 670 K thermal quenching occurs, where non-radiative transitions start to dominate the upper

state lifetime. This indicates that the quantum yield starts to drop below 100 % at this temperature and above. A configurational coordinate model was used to fit the lifetime data, where a thermal activation energy allowed non-radiative transition to the ground state. Their calculated lifetimes were, $\tau_{\mathrm{T}} = 7.96\,\mu\mathrm{s}$, $\tau_{\mathrm{E}} = 2.75\,\mathrm{ms}$ and 6.8 fs for thermal quenching. The energy separation of $^4\mathrm{T}_2$ and $^2\mathrm{E}$ was $\triangle E = 740\,\mathrm{cm}^{-1}$, and the activation energy for thermal quenching was $12\,400\,\mathrm{cm}^{-1}$. The excited state fluorescence lifetimes are higher than those of Walling, which was attributed to increased radiative trapping from a higher doped crystal sample; however, the Cr^{3+} concentration of 0.042-0.12 at.% is more representative of doping concentrations of laser media.

The long fluorescence lifetime of Alexandrite is a key advantage over the broadly wavelength tunable Ti:Sapphire gain medium, which has a lifetime of 3.2 µs [5]. This gives Alexandrite a greater potential for energy storage for Q-switching or as an optical amplifier, particularly when used with limited peak power laser diodes.

It is usually beneficial in laser rate equation analysis to assume non-radiative transitions are instantaneous, the approximation being that they are on a much shorter time scale than optical transitions. The intra-vibrational band non-radiative lifetimes in Alexandrite were studied by Gayen et. al. [68]. Non-radiative relaxation from higher vibrational levels of $^4\mathrm{T}_2$ to its base has a lifetime of 17 ps; the lifetime for the non-radiative transition from the base of $^4\mathrm{T}_2$ to $^2\mathrm{E}$ is 27 ps; and thermal re-population of $^4\mathrm{T}_2$ from $^2\mathrm{E}$ has a lifetime of 290 ps. These lifetimes are all many orders of magnitude shorter than the optical transitions, so the assumption that they are instantaneous holds.

3.1.4 Spectroscopic properties of Alexandrite

As in any laser material, the details of the spectroscopic properties of Alexandrite can be used to determine its lasing characteristics.

The fluorescence spectrum is shown in Figure 3.6 for the a, b and c axes. The intensity is an order of magnitude larger for E‖b (electric field parallel to the b-axis). As a consequence of the relationship between fluorescence intensity and emission cross section, this results in polarised vibronic laser emission in Alexandrite [8].

The GSA cross section is shown in Figure 3.7. The absorption and emission spectra can be understood by examining the energy level structure of the Cr^{3+} ion in Alexandrite.

The absorption spectra in the pumping region consists of two broad vibronic absorption bands at room temperature. They are centred around 420 nm and 590 nm, and are due to absorption into the vibrational bands of $^4\mathrm{T}_1$ and $^4\mathrm{T}_2$, respectively.

Absorption from the ground state into $^4\mathrm{T}_2$ is weaker and shifted to higher energies for the E‖a and E‖c polarisations compared to that of E‖b. This can partly be explained from the fine structure of $^4\mathrm{T}_2$. The crystal field and spin-orbit interactions split the $^4\mathrm{T}_2$ level into three, which are denoted as the T_1, T_2 and T_3 levels in order of low to high

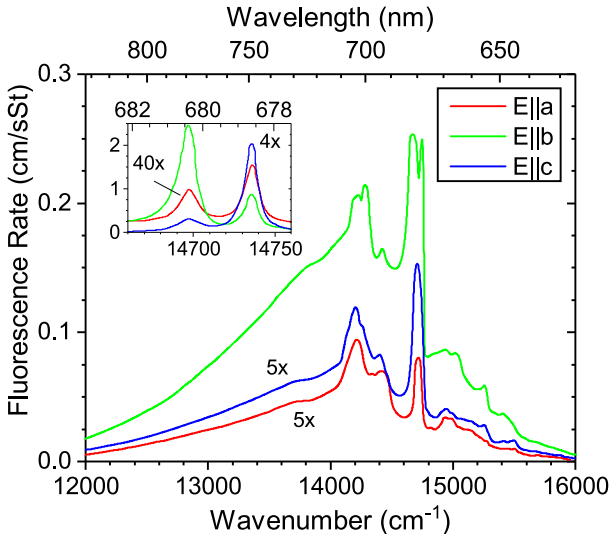

Figure 3.6: The fluorescence rate spectra of Alexandrite for the three polarizations. The E‖a and E‖c polarizations have been amplified by the amounts indicated. *Inset*: The higher resolution data around the R lines. Adapted from [8]

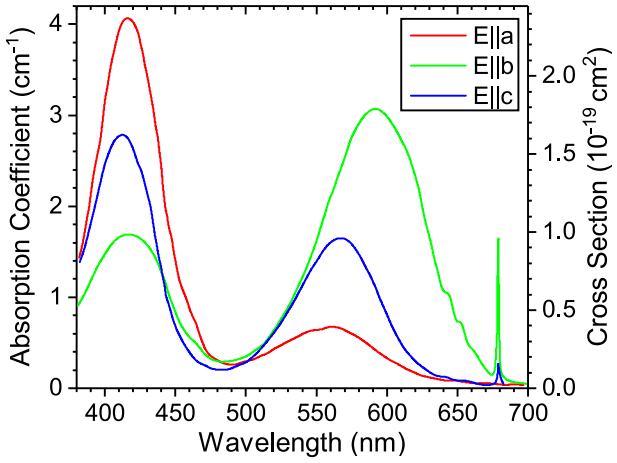

Figure 3.7: The absorption coefficient of Alexandrite in the pump region for the three polarizations. The doping concentration was $2.2 \times 10^{19}\,\mathrm{cm}^{-3}$ Cr^{3+}. Cross section calculated assumes 78 % mirror site occupancy fraction. Adapted from [8]

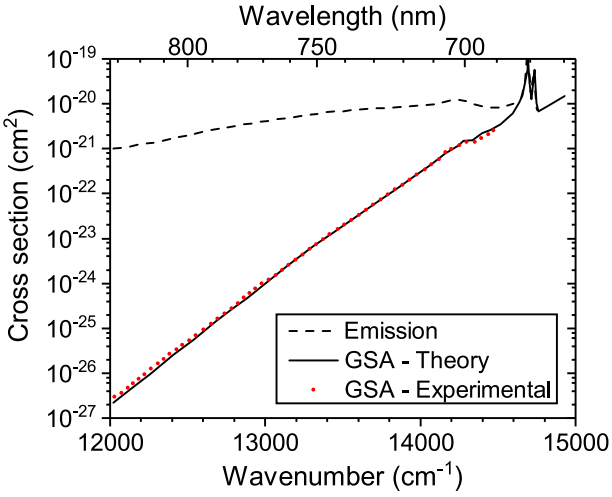

Figure 3.8: The emission and GSA cross sections of Alexandrite. The points indicate measurements, the solid line is the theoretical prediction. Adapted from [19]

energy. Vibronic transitions for E‖b are allowed between the ground state and all of the three split levels; however, transitions involving T_1 and T_2 are forbidden for the other two polarisations [63]. This means that vibronic absorption must occur with higher energy photons because T_3 is the highest energy level of the group. This causes the shift in the absorption peak to shorter wavelengths for E‖a and E‖c and a reduction in the absorption strength.

A second consequence of the selection rules is reduced vibronic fluorescence intensity for the E‖a and E‖c polarisations. This is partly due a lower occupancy of the T_3 level. The $^4T_2$ levels are thermally populated so by restricting the emission to that from T_3, the highest energy level, the available population is greatly reduced. This directly results in a lower fluorescence intensity. The less intense fluorescence is also due to weaker vibronic transition strengths for these polarizations [8].

Early Alexandrite lasers used the overlap between these bands and electrical gas discharge lamps for optical pumping of Alexandrite. Recent availability of high power red diode laser pump modules at 639 nm has enabled diode pumping of Alexandrite. This can be achieved with the shortest absorption depth for E‖b.

The GSA cross section extends into the laser wavelengths in Alexandrite and is effectively an extension of the pump absorption cross section. It was calculated and measured by Shand [19] and is shown in comparison to the emission cross section in Figure 3.8 over the typical lasing wavelength range. It is clear that GSA is insignificant at longer lasing wavelengths due to the cross section being many orders of magnitude smaller than the emission cross section. The GSA acts as a limit to the shortest lasing wavelength in Alexandrite, it is a significant loss factor due to the typically low inversions during CW operation. This has resulted in the shortest wavelength operation demonstrated of 701 nm, where the GSA cross section is one order of magnitude smaller than the emission cross section.

GSA arises from vibronic transitions from vibrational levels of the ground state into the $^4T_2$ band. The vibrational states are thermally populated, so excitation into $^4T_2$ with higher energy photons is more likely due to the higher probability of thermal occupation of the lower vibrational states. The transition probability at a specific wavelength of excitation is therefore dependent on both temperature and the transition strength, these are both embodied in the GSA cross section, which is a function of wavelength and temperature. A theoretical determination of the GSA cross section was derived by McCumber [69] and expanded upon for Alexandrite by Walling et. al. [8], the key relationship being

$$\sigma_a(E,T) = \sigma_e(E,T) \cdot \exp[(E - E^*)/k_b T]\,, \tag{3.2}$$

where E is the photon energy, E^* is the effective no-phonon transition energy, $\sigma_a(E,T)$ is the GSA cross section, $\sigma_e(E,T)$ is the effective emission cross section, k_b is Boltzmann's constant and T is the temperature of the crystal [19]. The value of E^* in wavelength units is 680.3 nm and 682.7 nm in Alexandrite at 300 K and 375 K respectively, which correspond on the graph to the point where the GSA equals the emission cross section.

The effective emission cross section, σ_e, is found from an equation relating it to the fluorescence rate and lifetime, see [19], and E^* is calculated by considering the fine energy level structure, see [8]. The key points of note are the relative exponential decrease in σ_a with decreasing E and the increasing relative strength of GSA to emission cross section for increased temperatures.

This theory is based on the assumption that the excited states of Alexandrite are in quasi-thermodynamic equilibrium, as assumed by Walling et. al. [8]. The close fit of this theory to experiment is shown in Figure 3.8, which verifies this assumption as accurate and allows the theory to be more widely applied [19].

A simplified energy level diagram of the Chromium ion is shown in Figure 3.9 up to what is thought to be the charge-transfer band [70]. The higher lying energy levels can absorb radiation via ESA, which is absorption from excited ions. In Alexandrite this is absorption from the meta-stable ^2E and $^4T_2$ levels. Once further excited through absorption, the ions then decay back to the meta-stable states non-radiatively. This constitutes a loss process, converting the optical energy into heat after absorption.

ESA occurs for photon wavelengths throughout the pumping and lasing bands, this can be clearly seen in Figure 3.9 by the broad absorption bands of the higher excited states. In Figures 3.10 and 3.11 more precise measurements of the ESA cross sections are shown. ESA will prevent lasing when the ESA and emission cross sections are equal, in the absence of GSA, because it will reduce gain to zero. This limit is reached at approximately 818 nm. Due to the relatively large ESA cross sections in both the pump and lasing regions, ESA has a substantial impact on the laser performance of Alexandrite.

It was determined by Gayen et. al. that ESA initiates from both the ^2E and $^4T_2$

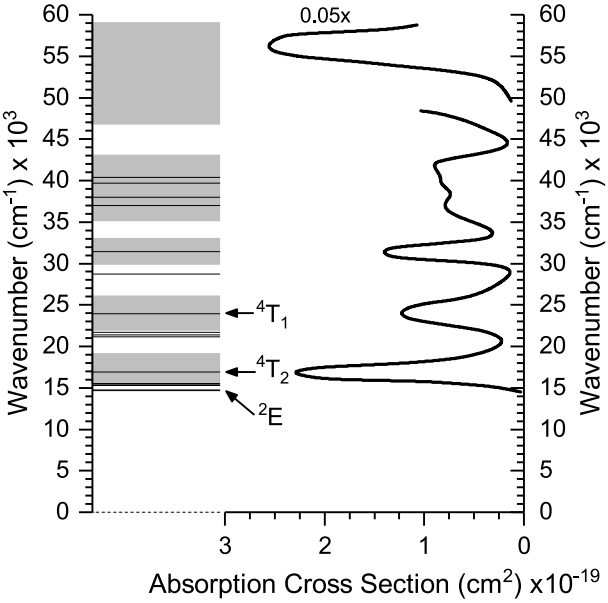

Figure 3.9: The energy levels of Alexandrite as determined by ground and excited state spectroscopy in the E‖b polarization. The key energy levels have been labelled next to their absorption peaks. The greyed areas represent broad absorption bands. Lines are the centres of absorption for different energy levels, as determined by Sevast'yanov et. al. The highest energy band absorption cross section has been multiplied by the amount indicated. Adapted from [71]

levels [68], but absorption from $^4T_2$ has a cross section seven times greater than that from ^2E. This was consistent with previous studies that assumed ESA initiated from $^4T_2$ [14, 18, 72]. Due to the much larger cross section for absorption from $^4T_2$ it can be assumed that absorption dominates from this level.

It was found that both the emission and ESA cross sections increase with temperature [72]. They increase at approximately the same rate, so that the long wavelength lasing cut-off remains at 818 nm. The increase in emission cross section can be explained by the increased $^4T_2$ population at elevated temperatures. The larger population in the lasing level will result in an increased probability of stimulated emission, which is reflected in the larger emission cross section. The same proportional increase in temperature for ESA can also be explained in this way by using the finding that ESA also initiates from $^4T_2$.

Spectral properties of lasing

By combining the absorption and emission processes the spectral and thermal characteristics of Alexandrite lasing can be explained, which can inform design considerations when making an Alexandrite laser.

The long wavelength lasing limit for Alexandrite comes from ESA. The ratio of ESA to emission cross section does not appear to change in the range of 300 K to 560 K [72], but the increase in overall gain means that the threshold for lasing can be

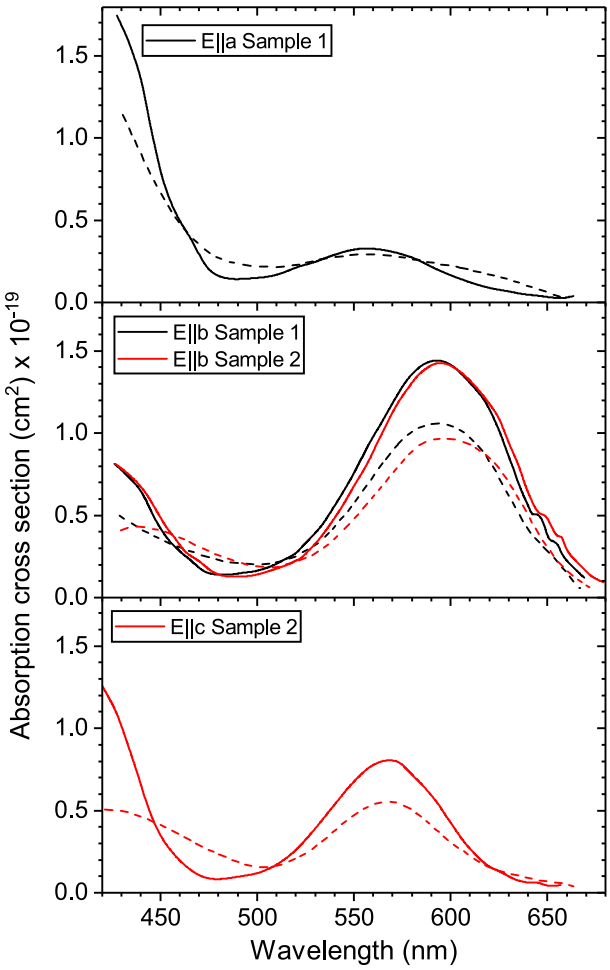

Figure 3.10: GSA (solid lines) and ESA (dashed lines) cross sections in the pump region of Alexandrite. Sample 1: $N = 1.1 \times 10^{20}\,\mathrm{cm}^{-3}$, Sample 2: $N = 9.2 \times 10^{19}\,\mathrm{cm}^{-3}$. Mirror site occupancy of 78 % assumed. Adapted from [14]

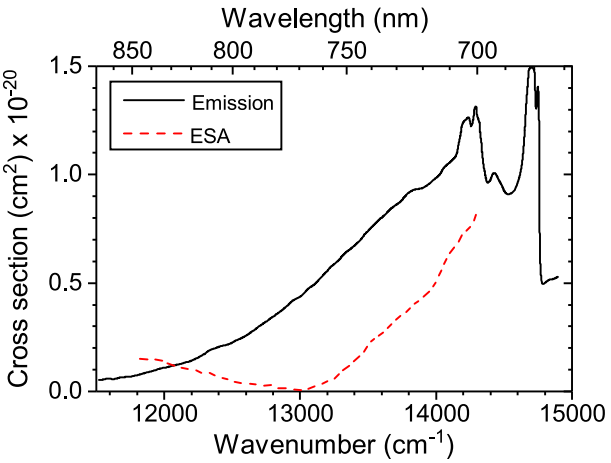

Figure 3.11: The ESA cross section in the lasing region of Alexandrite, compared to the emission cross section. Adapted from [18]

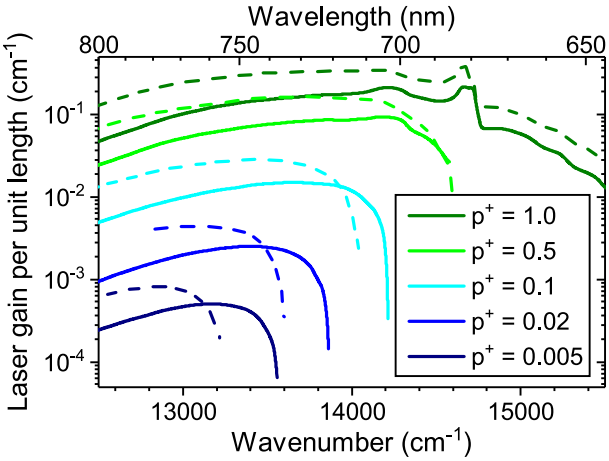

Figure 3.12: The calculated gain per unit length of Alexandrite including the effect of GSA. p^+ is the inversion fraction. Solid lines: 25 °C, dashed lines: 75 °C. Adapted from [8]

reduced at elevated temperatures [67] and increased performance found [73]. It was demonstrated by Strotkamp et. al. [74] that when an Alexandrite laser is operated at longer wavelengths the optimum operating temperature increases.

The ESA limit on lasing range was expected to be 818 nm, but it was shown by Kuper et. al. [51] that continuous tuning could be achieved up to 858 nm by operating at increasing temperatures up to a maximum of 786 K; although, this was achieved at the cost of severely reduced efficiency. This work suggests that the wavelength at which the ESA cross section equals the emission cross section increases for temperatures above 560 K. It also demonstrated that efficient lasing can be achieved in the 800 nm to 820 nm range when using these higher temperatures.

The short wavelength lasing limit for Alexandrite comes from GSA of laser radiation, which introduces a significant loss factor. The effect of GSA on laser gain, excluding the effects of ESA, is shown in Figure 3.12. A free running laser will operate at the peak of a gain curve, so these plots highlight the main impacts of GSA. Both lower inversions and higher temperatures will red shift the peak gain due to stronger GSA. The shortest demonstrated lasing wavelength for Alexandrite is 701 nm [8], limited by the pump energy available to reach laser threshold.

Analysing the general causes of the upper and lower wavelengths lasing limits in Alexandrite is useful to gain an understanding of the general characteristics of the medium; however, it does not provide information on practical limitations in terms of laser threshold or efficiency. To gain a full understanding of the lasing behaviour a laser model incorporating all these effects together is required.

3.2 Measuring Alexandrite pump ESA

Of crucial importance to quantifying the effect of pump ESA is knowing the ratio of the pump ESA, σ_1, to pump GSA, σ_0, cross sections: $\gamma = \sigma_1/\sigma_0$. This parameter has previously been measured for Alexandrite at 20 °C [14]; however, there are significant temperature dependences in Alexandrite, yet there had been no previous investigation of the effect of crystal temperature on pump ESA. In this work the temperature dependence of the pump ESA cross section in Alexandrite was measured, in order to provide a complete set of temperature dependent parameters for Alexandrite. These results have contributed to two published articles [53, 75].

The measurement can be made through pulsed pump-probe measurements by comparing the difference in transmission between the pumped and unpumped cases. Alternatively, the saturating transmission of a sample can be used to determine the pump ESA fraction [14, 76].

The simplest way of using transmission saturation would be to compare the small signal transmission to that of a highly saturated sample as in [14], but due to the limited brightness and power of the available pump source, instead the rate of crystal transmission saturation with incident intensity was used.

Theory

The transmission, T_p, of a plane wave pump beam of intensity I_0 through a saturable absorber with pump ESA is given by [76]

$$\frac{I_0}{I_\mathrm{s}} = \frac{1}{\gamma}\frac{\left[(T_\mathrm{p}/T_0)^{\frac{\gamma}{1-\gamma}} - 1\right]}{\left[1 - T_\mathrm{p}(T_\mathrm{p}/T_0)^{\frac{\gamma}{1-\gamma}}\right]}\,, \tag{3.3}$$

where $I_\mathrm{s} = h\nu_\mathrm{p}/(\sigma_0\tau_\mathrm{f})$ is the pump saturation intensity, h is the Planck constant, ν_p is the pump radiation frequency, σ_0 is the pump GSA cross section, τ_f is the fluorescence lifetime, $T_0 = \exp -(N\sigma_0 l)$ is the small signal transmission, N is the active ion population density and l is the length of the absorbing medium.

The non-linear nature of the transmission with respect to incident intensity means that non-uniform beams, such as Gaussian beams, cannot directly use this relationship to accurately give their transmissions. This relationship was adapted to apply to the Gaussian profile beams used in this work.

The intensity as a function of radius, $I_0(r)$, for an incident Gaussian beam is

$$I_0(r) = I_{0\mathrm{p}} \exp\left[-2(r/w)^2\right]\,, \tag{3.4}$$

where $I_{0\mathrm{p}}$ is the peak intensity and w is the $(1/\mathrm{e}^2)$ intensity beam radius. To find the transmission of a Gaussian beam, T_G, the ratio of output to input power is calculated

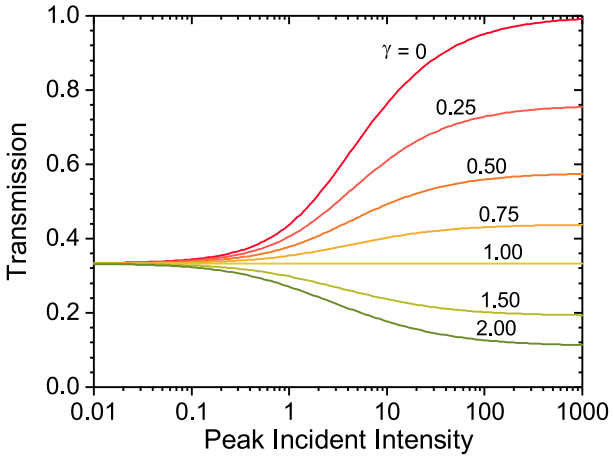

Figure 3.13: The analytical model of transmission against the normalised peak incident intensity $I_{0\mathrm{p}}/I_{\mathrm{s}}$ for different pump ESA ratios γ.

as

$$T_{\mathrm{G}} = \frac{\int_0^\infty 2\pi r I(r)\mathrm{d}r}{\int_0^\infty 2\pi r I_0(r)\mathrm{d}r}\,, \tag{3.5}$$

where $I(r)$ is the pump intensity exiting the crystal. This equation is calculated through substitution of Equation (3.4), yielding

$$T_G = 4\int_0^\infty r' \mathrm{e}^{-2r'^2} T_{\mathrm{p}}(r')\mathrm{d}r'\,, \tag{3.6}$$

where $r' = r/w$ is the normalised radius and $T_{\mathrm{p}}(r')$ is the transmission of the Gaussian beam at a normalised radius. The Gaussian beam intensity, and therefore transmission, is constant at a given radius, so Equations (3.3) and (3.4) give $T_{\mathrm{p}}(r')$.

To find the transmission of a non-divergent Gaussian beam, the integral of T_{G} is then found. This must be calculated numerically due to the transcendental nature of Equation (3.3). In the case of a diverging beam, the average beam radius over the absorbed path can be used as an approximation.

Using Equations (3.3) and (3.6), the crystal transmission versus peak incident intensity is shown in Figure 3.13 for a range of ESA ratios γ. The saturable absorber range is when $\gamma < 1$, increasing intensity causes a larger transmission because excited ions absorb less than when in the ground state. When ESA is present, the asymptotic high intensity transmission is less than one as there is residual absorption of the excited ions. When $\gamma = 1$ there is no change in transmission with intensity because the excited ion absorption is equal to that of the ground state. When $\gamma > 1$ the material is a reverse saturable absorber, so called because increasing incident intensity causes a lower transmission.

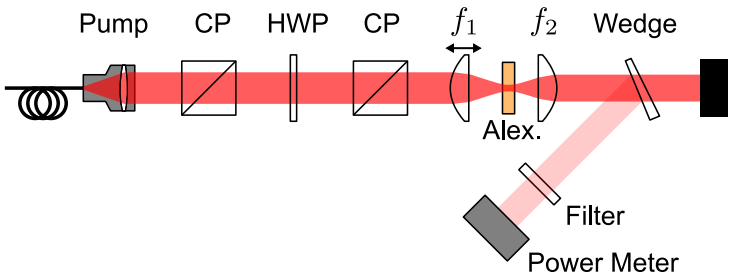

Figure 3.14: The pump ESA measurement experiment design. Pump power control was from two cube polarisers (CP) and a half-waveplate (HWP). The beam was focussed and re-collimated with two lenses (f_1, f_2) and attenuated with an anti-reflection coated wedge.

Method

The experimental apparatus that was designed to measure the pump ESA cross section is shown in Figure 3.14, which enabled the saturating transmission of the Alexandrite crystal to be measured. The pump source was a 5.7 W, 637 nm, fibre-delivered diode module that was linearly polarised with a cube polariser (CP), giving an available pump power of 3.2 W. Due to wavelength changes with diode current, its power control was achieved by rotating its linear polarisation with a $\lambda/2$ wave plate and then passing through another cube polariser, which was aligned to the b-axis of the Alexandrite sample. The pump was focussed into the crystal with an $f_1 = 26$ mm aspheric lens, resulting in a pump beam on the crystal of diameter 170 µm, Rayleigh length 0.84 mm, and $M^2 = 45$. Further details on the pump source are given in Section 4.2.

To measure the small signal transmission, the pump beam diameter at the crystal was increased by moving f_1 so that the beam waist was outside of the crystal. In this way the intensity at the crystal could be reduced, but the transmitted power was kept within the dynamic range of the power meter.

The pump transmitted through the crystal was collimated with an $f_2 = 18$ mm lens and attenuated with an anti-reflection coated wedged optic. The beam also passed through a 635 ± 10 nm band pass filter to minimise any fluorescence detection.

The crystal was a 0.16 at.% Cr Alexandrite slab with a depth of 2.08 mm mounted with indium foil on a water cooled copper heat sink. This could maintain a temperature between 10 °C to 85 °C, which was assumed to be the crystal temperature. The crystal faces were uncoated, so the Fresnel reflections were corrected for in the analysis.

The crystal transmission was measured by lowering and raising the Alexandrite crystal into the beam path and measuring the power in each case. By using this method, the attenuation of the wedge and filter did not need to be known, which enabled the high accuracy transmission measurements needed.

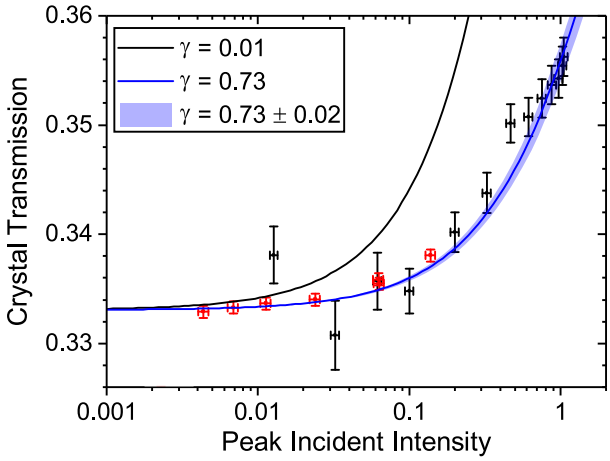

Figure 3.15: The transmission T of an Alexandrite sample at 55 °C against the ratio of peak incident intensity I_{0p} to saturation parameter I_s, compared to the model for different γ. The shaded area represents the uncertainty on γ, the black points are from pump intensity modulation with the half-wave plate, and the red points are from pump defocussing to control intensity.

Results

The saturating transmission of Alexandrite is shown in Figure 3.15 at 55 °C, with the crystal transmission, T, against normalised incident peak intensity, I_{0p}/I_s. The black points are measurements from using waveplate control and the red points from defocussing the beam to adjust the incident intensity. The defocussing control had more accurate measurements at low intensities and was used to determine the small signal transmission. The waveplate control provided higher intensity measurements to determine the slope of the saturation for γ determination.

The theoretical transmission curves were fitted to the experimental data, with a least-squares method to determine the γ measurement. The theoretical curves are shown in Figure 3.15 alongside the experimental data, with the $\gamma = 0$ curve as a reference. The modelling shows a close fit to the data, with the result $\gamma = 0.73 \pm 0.02$ for 55 °C. The relevant parameters for the fitting were taken from the literature, with $\tau_f = 197\,\mu s$ and $\sigma_0 = 8.7 \times 10^{-24}\,m^2$ at 55 °C [8, 14]. The small signal transmission at this temperature was $T_0 = 0.333$, which gave a predicted active ion density of $N = 6.08 \times 10^{25}\,m^{-3}$.

This saturation experiment was repeated at different crystal temperatures, with the resulting pump ESA ratio γ measurements shown in Figure 3.16 (red squares), with a linear fit calculated and 95% confidence bands. These results show a decrease in γ when going to higher crystal temperatures, with γ approximately 0.8 at 10 °C and 0.7 at 90 °C. These values are consistent with the previously reported measurement of $\gamma = 0.75 \pm 0.01$ at room temperature [14].

The GSA coefficient is $\alpha_0 = \sigma_0 N$. It was measured through the small signal transmission and is shown in Figure 3.16 as a function of crystal temperature, it was found to increase as has been previously reported [20, 77].

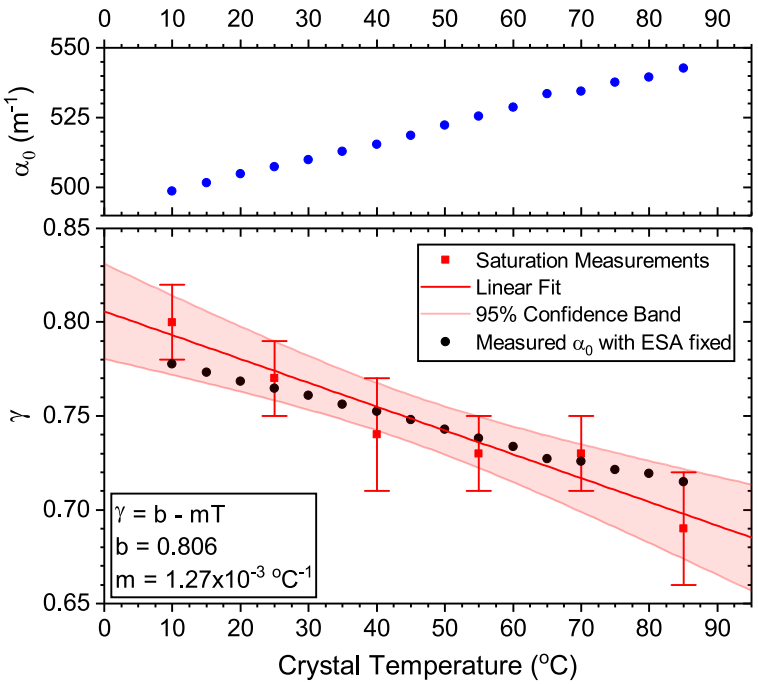

Figure 3.16: The pump ESA to GSA ratio γ values (red squares) against crystal temperature with a linear fit and 95% confidence band (red area). Also shown is how γ would change assuming the ESA coss section is constant and GSA changes from the measured small signal transmission (black points).

The ESA coefficient ($\alpha_1 = \sigma_1 N$) can be determined using $\gamma = \alpha_1/\alpha_0$, which from the measured γ values is $\alpha_1 = 388\,\mathrm{m}^{-1}$ at 45 °C. Assuming the pump ESA coefficient remains constant at that value, the expected γ from the measured α_0 is shown in Figure 3.16 (black points). The close match between the two data sets indicates that the observed γ temperature dependence could be solely due to the temperature dependence of GSA. This suggests that the trend in γ measured between 10 °C and 90 °C could be extrapolated to temperatures beyond this range with reasonable accuracy, where the temperature dependence of the pump GSA has been measured [20].

Further study would be required to determine the impact of temperature on pump ESA at other pump wavelengths, but for red diode pumping this work has highlighted a potential benefit to efficiency through moving towards higher temperatures in Alexandrite.

3.3 Alexandrite laser model

The many processes in Alexandrite make it a complicated laser medium to analyse. Even limiting the number of parameters to just the energy transitions of the ions leaves a complicated system. The laser rate equations of the system can be solved numerically, and although this approach yields solutions for the laser, the underlying behaviour and the specific effects of different laser parameters are difficult to analyse. For this reason

an analytical model is a powerful tool in assessing and optimising laser performance. It can give simple relations to quickly know the effect of the various parameters on the laser, along with identifying those that are unimportant.

For a model to be valid across the gain bandwidth of Alexandrite it must include the effects of pump and laser ESA, along with laser GSA. The diode end-pumping geometry is of particular interest in Alexandrite, so the longitudinal variation of population inversion could be important.

The effect of laser GSA has been included in many analytical laser models. Early models used the assumption of no ground state depletion [78], this would not necessarily be valid in Alexandrite where a low emission cross section could require a large population inversion to achieve threshold gain; however, a benefit to this simplification is the ability to more easily include transverse pump and laser beam profiles [79, 80]. Later works included ground state depletion [81], with the addition of pump retro-reflection and dual end-pumping [82, 83, 84]. Pump ESA could be included in some of these models [82], but this would be through a fixed pumping efficiency parameter without a way to derive what value that should be.

The effect of pump ESA has had significantly less attention in the literature. A model was developed that included laser GSA and both laser and pump ESA [85]; however, significant approximations were made in the derivation of low laser GSA and weak pump ESA. Another model that included pump and laser ESA used the approximation of low population in the analysis of their result [86].

Solutions that have transverse field distributions and require numerical analysis have been produced with laser and pump ESA [87], and with the addition of laser GSA [88]. The numerical analysis needed makes it difficult to isolate the different processes, and shows that including transverse field variation makes the problem intractable analytically.

In this section, a new model is derived that is applicable to end-pumped Alexandrite lasers, along with other gain media that have similar laser processes. The model derived in this section has contributed to three published articles [52, 53, 75], which contain the derivation of this model and its application to Alexandrite.

3.3.1 Complete model

The energy level model considered in this analysis is shown in Figure 3.17. The pump excites population from level 0 to 2 with cross section σ_0, which then decays non-radiatively to level 1 with a lifetime of τ_{21}. Gain at the laser wavelength is by stimulated emission from level 1 to 0 with cross section σ_e, and ground state absorption (GSA) occurs with cross section σ_a from level 0 to 1. There is also excited state absorption (ESA) from level 1 to 3 at both the pump and laser wavelengths with cross sections σ_1 and $\sigma_{1\mathrm{a}}$ respectively. This excited population then decays non-radiatively down to level 1 with a lifetime τ_{31}. There is also fluorescent decay from level 1 to 0 with a lifetime τ_f.

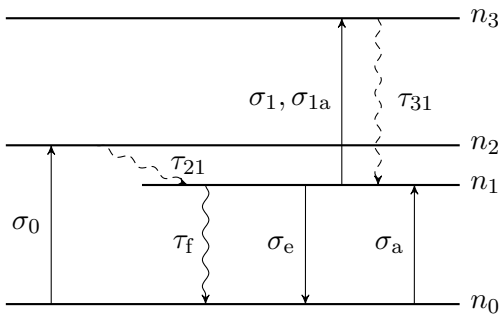

Figure 3.17: Diagram of the energy level structure of a quasi-three level laser, with a fourth level providing ESA at the pump wavelength.

Different gain media can be modelled by the energy level system in Figure 3.17, either because they directly match the system, or through appropriately combining energy levels to match those of the model. For example, in Alexandrite the population in the upper $^4T_2$ and ^2E states can be combined and treated as the single population of n_1. The thermal and spectral dynamics are implemented by using effective parameters for the fluorescence lifetime and cross sections.

Different kinds of quasi three-level systems can be modelled by altering the definition of σ_a. For example, when laser gain is from a vibronic transition and thermalisation is sufficiently fast, as in Alexandrite, the GSA cross section is given by the extended McCumber theory of Equation (3.2). Alternatively, if the terminal laser level is well defined (as in Yb:YAG) the GSA cross section can be a simple fraction of the emission cross section [82], given by the Boltzmann filling of the level.

The laser rod considered in this analysis is end pumped from the rod end position $z = 0$, resulting in a longitudinal variation in the pump radiation intensity $I(z)$, and active ion excitation density $n_1(z)$. The pump and laser radiation are taken to be collinear, monochromatic, non-divergent and have constant transverse intensity profiles. The non-radiative transition rates are assumed to be fast, such that $(\tau_{21}, \tau_{31}) \to 0$, therefore $n_2 = n_3 = 0$ and $n_0 + n_1 = N$. Under these conditions the equations governing the system are

$$\begin{aligned}\frac{\partial n_1(z,t)}{\partial t} = \tfrac{1}{h\nu_p}\eta_{p,0}\sigma_0 n_0(z,t)I(z,t) - c\sigma_e n_1(z,t)\phi(z,t) \\ +c\sigma_a n_0(z,t)\phi(z,t) - \tfrac{1}{\tau_f}n_1(z,t)\,,\end{aligned} \tag{3.7}$$

$$\frac{\mathrm{d}I_l^{\pm}}{\mathrm{d}z} = \pm[\sigma_e n_1(z,t) - \sigma_a n_0(z,t) - \sigma_{1a} n_1(z,t)]I_l^{\pm}(z,t)\,, \tag{3.8}$$

$$\frac{\mathrm{d}I}{\mathrm{d}z} = -[\sigma_0 n_0(z,t) + \sigma_1 n_1(z,t)]I(z,t)\,, \tag{3.9}$$

where $I_l^{\pm}$ is the laser radiation intensity in the forwards (+) or backwards (-) direction, I is the pump radiation intensity, $\phi = (I_l^+ + I_l^-)/h\nu_l c$ is the two way laser photon density in the medium, h is the Planck constant, ν_l is the laser radiation frequency, c is the

speed of light in the medium, and $\eta_{\mathrm{p},0}$ is the fraction of ions transferred from the upper pump level n_2 to the upper laser level n_1. The value of $\eta_{\mathrm{p},0}$ could be less than 100 % if there is decay from n_2 into a non-lasing band. The equations will be solved in the steady state so the time dependence is eliminated.

The equations are linked to a specific laser cavity through the laser round trip threshold gain condition of

$$R(1-L)G_{\mathrm{th}}^2 = 1\,, \tag{3.10}$$

where R is the output coupler reflectivity, L is the round trip cavity loss, and G_{th} is the single pass gain at threshold.

Integrating Equation (3.8) along the length of the medium, l, gives the single pass gain

$$\ln(G_{\mathrm{th}}) = \ln\left[\left(\frac{I_{\mathrm{l}}^{\pm}(l)}{I_{\mathrm{l}}^{\pm}(0)}\right)^{\pm 1}\right] = F(\alpha_{\mathrm{e}}+\alpha_{\mathrm{a}}-\alpha_{1\mathrm{a}})-\alpha_{\mathrm{a}}l\,, \tag{3.11}$$

where $F = \int_0^l f(z)\mathrm{d}z$ is an integrated population inversion function, $f(z) = n_1(z)/N$ is a normalised population inversion fraction, and $\alpha_i = \sigma_i N$ for any cross section denoted by i. Then substituting Equation (3.11) into (3.10) gives

$$F = \frac{-\ln[(1-L)R] + 2\alpha_{\mathrm{a}}l}{2(\alpha_{\mathrm{e}}+\alpha_{\mathrm{a}}-\alpha_{1\mathrm{a}})}\,, \tag{3.12}$$

which defines the integrated population inversion necessary for laser action and is fixed at and above threshold.

Solving Equation (3.7) in the steady state gives the solution

$$\frac{f}{1-f} = \frac{\eta_{\mathrm{p},0}I/I_{\mathrm{s}} + \phi/\phi_{\mathrm{a}}}{1+\phi/\phi_{\mathrm{s}}}\,, \tag{3.13}$$

where $I_{\mathrm{s}} = h\nu_{\mathrm{p}}/(\sigma_0\tau_{\mathrm{f}})$ is the pump saturation intensity, $\phi_{\mathrm{a}} = 1/(c\sigma_{\mathrm{a}}\tau_{\mathrm{f}})$ is the laser GSA saturation photon density, and $\phi_{\mathrm{s}} = 1/(c\sigma_{\mathrm{e}}\tau_{\mathrm{f}})$ is the laser emission saturation photon density.

To complete the solution Equations (3.9) and (3.13) are combined to find F under the assumption of constant laser cavity photon density, $\phi(z) = \phi$, which is accurate for all but high gain cavities [89, 90]. The derivation is given in Appendix A, which yields the relation between the input pump intensity $I(0)$ and intracavity laser photon density ϕ of

$$\frac{I(0)}{I_{\mathrm{s}}(1+\phi/\phi_{\mathrm{s}})} = \frac{(1+a\gamma)}{\gamma\eta_{\mathrm{p},0}}\left[\frac{\mathrm{e}^{\alpha_1[F-a(l-F)]}-1}{1-T\mathrm{e}^{\alpha_1[F-a(l-F)]}}\right]\,, \tag{3.14}$$

where $a = (\phi/\phi_{\mathrm{a}})/(1+\phi/\phi_{\mathrm{s}})$ is a laser saturation factor, $T = I(l)/I(0)$ is the pump transmission, and $\gamma = \sigma_1/\sigma_0$ characterises the strength of pump ESA. The output laser power, P_l, is extracted from this expression using $P_l = (1-R)I_{\mathrm{l}}^{+}(l)A \approx \frac{1}{2}\phi[-\ln(R)]h\nu_{\mathrm{l}}cA$, where A is the beam cross sectional area [5].

The laser threshold pump intensity $I_{0\mathrm{th}}$ is obtained from Equation (3.14) by setting $\phi = a = 0$, giving

$$\frac{I_{0\mathrm{th}}}{I_\mathrm{s}} = \frac{1}{\gamma\eta_{\mathrm{p},0}}\left(\frac{\mathrm{e}^{\alpha_1 F}-1}{1-T\mathrm{e}^{\alpha_1 F}}\right), \tag{3.15}$$

which is the pump intensity required for laser action from a 'cold' start with no initial intracavity flux. The gain required for a specific laser cavity is contained in the value of F.

To understand the laser efficiency the two mechanisms of pump absorption, GSA and ESA, must be evaluated. The power absorbed through GSA constitutes useful absorption as it generates inversion, whereas power absorbed as ESA is a loss because it is absorption from already excited population. The total power absorbed, P_a, is found using Equation (3.9), giving

$$P_\mathrm{a} = A[I(0) - I(l)] = P_0(1-T), \tag{3.16}$$

$$T = \mathrm{e}^{-\alpha_0 l}\mathrm{e}^{\alpha_0(1-\gamma)F}, \tag{3.17}$$

where $P_0 = AI(0)$ is the pump input power. The useful pump power absorbed, P_u, is the $\eta_{\mathrm{p},0}$ quantum efficiency fraction of the total pump GSA in the medium, given by

$$\begin{aligned} P_\mathrm{u} &= A\eta_{\mathrm{p},0}\int_0^l \sigma_0 n_0(z) I(z)\mathrm{d}z \\ &= A\alpha_0 I_\mathrm{s}\left(1+\frac{\phi}{\phi_\mathrm{s}}\right)[F - a(l-F)], \end{aligned} \tag{3.18}$$

where Equation (3.13) has been used to evaluate the integral. These two powers define two efficiency factors. The pump absorption fraction $\eta_\mathrm{a} = P_\mathrm{a}/P_0$ is the fraction of input power that is absorbed. The pump quantum efficiency $\eta_\mathrm{p} = P_\mathrm{u}/P_\mathrm{a}$ is the fraction of absorbed pump photons that generate inversion. Use of Equations (3.14), (3.16) and (3.18) give

$$\eta_\mathrm{a} = 1 - T, \tag{3.19}$$

$$\eta_\mathrm{p} = \eta_{\mathrm{p},0}\eta_{\mathrm{p,ESA}} \tag{3.20}$$

$$\eta_{\mathrm{p,ESA}} = \frac{\alpha_1}{(1+a\gamma)}\left[\frac{1-T\mathrm{e}^{\alpha_1[F-a(l-F)]}}{\mathrm{e}^{\alpha_1[F-a(l-F)]}-1}\right]\left[\frac{F-a(l-F)}{1-T}\right]. \tag{3.21}$$

The resulting pump quantum efficiency η_p can be split into two parts. The contribution from pump ESA is contained in $\eta_{\mathrm{p,ESA}}$. This reduces the quantum efficiency as ESA originates from already excited ions, which then non-radiatively decay back to the upper laser level resulting in no net generation of inversion. All other quantum efficiency factors, for example decay from the upper pump level into a state other than the upper laser transition, are contained in $\eta_{\mathrm{p},0}$.

To quantify the overall laser efficiency the slope efficiency η_s is commonly used, which

is the fraction of additional pump power that is converted to laser power above threshold. Equation (3.14) shows that the laser photon density ϕ, and hence the laser output power, is a non-linear function of input pump intensity $I(0)$, therefore the slope efficiency is not constant; however, it is asymptotically constant for $\phi \gg \phi_s$, where $a \to \sigma_a/\sigma_e$ and can be assumed to be constant. The slope efficiency is given by $\eta_s = \frac{1}{2} h\nu_l c[-\ln(R)]\frac{d\phi}{dI(0)}$, which yields

$$\eta_s = \frac{-\ln R}{2\alpha_e[F - (\sigma_a/\sigma_e)(l - F)]}\eta_q\eta_a\eta_p \,, \tag{3.22}$$

where $\eta_q = \lambda_p/\lambda_l$ is the Stokes efficiency, and λ_p and λ_l are the pump and laser wavelengths, respectively. The slope efficiency can be simplified by substituting F from Equation (3.12), giving

$$\eta_s = \eta_{oc}\eta_q\eta_a\eta_p, \tag{3.23}$$

$$\eta_{oc} = (1 - \gamma_l)\left[\frac{-\ln R}{-\ln R - \ln(1 - L) + 2\gamma_l\alpha_a l}\right] , \tag{3.24}$$

where η_{oc} is the output coupling efficiency and $\gamma_l = \sigma_{1a}/(\sigma_e + \sigma_a)$ quantifies the laser ESA fraction. The output coupling efficiency is the ratio of useful output coupling to total intracavity flux lost from the cavity, with the γ_l factors including the laser ESA loss.

The slope efficiency has now assumed a standard form involving the output coupling, Stokes, and pump absorption efficiencies (including the pump quantum efficiency). Another term in experimental systems is the mode overlap efficiency, the spatial matching of the laser and pump modes. This is not considered in the current analysis, but will be discussed in a later section when comparisons are made to experimental data.

The Stokes efficiency can normally be used as the intrinsic maximum slope efficiency, η_0, of a laser gain medium. This efficiency would occur with perfect spatial overlap and a high output coupling fraction, such that passive cavity losses are negligible; however, in the presented model there are reductions to the slope efficiency that are not affected by cavity design through both the output coupling efficiency, η_{oc}, and pump quantum efficiency, η_p, terms. These result in a modified intrinsic efficiency of

$$\eta_0 = \eta_{p,0}\frac{\lambda_p}{\lambda_l}\left[\frac{1 - \gamma_l}{1 + (\sigma_a/\sigma_e)\gamma}\right] . \tag{3.25}$$

The Stokes efficiency appears as before, laser ESA loss occurs through the γ_l term, and pump ESA loss is dependent on laser GSA in the γ term. This coupling is due to laser GSA causing inversion at threshold in the limit of $L = 0$ and $R = 1$, resulting in unavoidable pump ESA loss.

Key parameters for a laser are the threshold and slope efficiency. The full solutions for the laser threshold (Equation (3.15)) and the slope efficiency, which depends on the pump quantum efficiency (Equation (3.21)), are in forms that obscure their dependencies

on the various laser parameters. In order to elucidate the behaviour of these equations approximate forms can be derived. The first approximation that can be made is that the input pump power is totally absorbed, $T \to 0$. This is a good approximation in most lasers, as non-absorbed pump can reduce overall efficiency. The second is that $\alpha_1 F \ll 1$, which is the case of low inversion. Under these conditions the pump threshold and ESA quantum efficiency are

$$I_{0\mathrm{th}} \approx \tfrac{h\nu_\mathrm{p}}{\tau_\mathrm{f}} \alpha_0 F[1 + \tfrac{1}{2}\alpha_1 F]\,, \tag{3.26}$$

$$\eta_{\mathrm{p,ESA}} \approx \tfrac{1}{1+a\gamma}\{1 - \tfrac{1}{2}\alpha_1[F - a(l - F)]\}\,. \tag{3.27}$$

In these forms the effects of pump ESA through α_1 are more clearly seen as higher order effects in F on the underlying quasi-three level system.

3.3.2 Pump ESA effects on a four-level laser

To isolate the effect of pump ESA it is useful to first consider a simplified case where the model is reduced to a four-level laser with pump ESA. This is achieved by removing the laser ESA and GSA from the generalised model in Section 3.3.1, and removing other pump quantum efficiency factors by setting $\eta_{\mathrm{p},0} = 1$ to isolate the effect of ESA on the pump quantum efficiency. This results in the typical linear relationship between input pump power and output laser power

$$P_\mathrm{l} = \eta_\mathrm{s}(P_0 - P_{0\mathrm{th}})\,, \tag{3.28}$$

where $P_{0\mathrm{th}} = AI_{0\mathrm{th}}$ is the threshold pump power. The resulting relations are

$$\eta_\mathrm{s} = \eta_\mathrm{q}\eta_\mathrm{oc}\eta_\mathrm{a}\eta_\mathrm{p}\,, \tag{3.29}$$

$$\eta_\mathrm{q} = \frac{\lambda_\mathrm{p}}{\lambda_\mathrm{l}}\,, \tag{3.30}$$

$$\eta_\mathrm{a} = 1 - T\,, \tag{3.31}$$

$$\eta_\mathrm{oc} = \frac{-\ln(R)}{-\ln(R) - \ln(1-L)}\,, \tag{3.32}$$

$$\eta_\mathrm{p} = \frac{1 - Te^{\alpha_1 F}}{1 - T} \cdot \frac{\alpha_1 F}{e^{\alpha_1 F} - 1}\,, \tag{3.33}$$

$$\frac{I_{0\mathrm{th}}}{I_\mathrm{s}} = \frac{1}{1 - Te^{\alpha_1 F}} \cdot \frac{e^{\alpha_1 F} - 1}{\gamma}\,. \tag{3.34}$$

Approximations can be made of a suitably long gain medium ($T \ll 1$) and low inversion ($\alpha_1 F \ll 1$), giving the solutions

$$\eta_\mathrm{p} \approx 1 - \tfrac{1}{2}\alpha_1 F\,, \tag{3.35}$$

$$\frac{I_{0\mathrm{th}}}{I_\mathrm{s}} \approx \alpha_0 F(1 + \tfrac{1}{2}\alpha_1 F)\,. \tag{3.36}$$

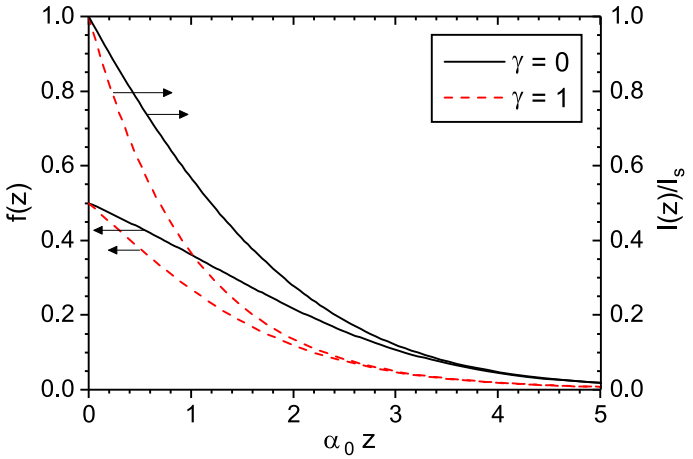

Figure 3.18: The normalised inversion, $f(z)$, and pump intensity, $I(z)/I_\mathrm{s}$, distributions with (red dashed curves) and without (black solid curves) pump ESA, for the case $I_0/I_\mathrm{s} = 1$.

To understand the impact of pump ESA its effect on the population inversion must be understood. Figure 3.18 shows the normalised inversion distribution $f(z)$ and the normalised pump intensity distribution $I(z)/I'_\mathrm{s}$ for the case with ($\gamma = 1$) and without ($\gamma = 0$) pump ESA. There is stronger absorption in the gain medium with ESA, but this extra absorption does not result in greater population inversion and concentrates it towards the input of the pump radiation. The reduction in inversion for the same input power is due to the energy lost through ESA.

Figures 3.19 and 3.20 show example solutions for the pump quantum efficiency and threshold incident pump intensity against output coupling factor ($-\ln R$) from Equations (3.33) and (3.34), respectively. These results show what is intuitively expected. A higher pump ESA fraction, γ, leads to a greater ESA loss that causes decreased efficiency and a higher lasing threshold. This is partly due to the increased ESA fraction leading to a correspondingly larger loss, but also due to the concentration of population inversion towards the pump input end, as shown in Figure 3.18, which results in the majority of pump absorption occurring over a higher population inversion. Increasing output coupling ($-\ln R$) also increases ESA loss by requiring a higher integrated population inversion for threshold gain.

To better understand the parameters affecting laser efficiency and threshold when pump ESA occurs the definition of F (Equation (3.12)) can be used with the approximate forms of η_p and $I_{0\mathrm{th}}$ (Equations (3.35) and (3.36)), giving

$$\eta_\mathrm{p} \approx 1 - \frac{\sigma_2}{\sigma_\mathrm{e}} \frac{\{-\ln[(1-L)R]\}}{4}\,, \tag{3.37}$$

$$I_\mathrm{th} \approx \frac{h\nu_\mathrm{p}}{\tau_\mathrm{f}\sigma_\mathrm{e}} \frac{\{-\ln[(1-L)R])\}}{2} \left[1 + \frac{\sigma_2}{\sigma_\mathrm{e}} \frac{\{-\ln[(1-L)R]\}}{4}\right]\,, \tag{3.38}$$

These equations show the general trend of how η_p and I_th will be affected when changing

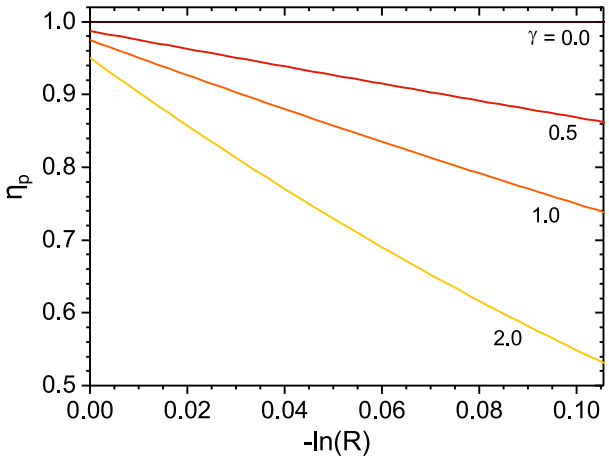

Figure 3.19: The pump quantum efficiency η_p against output coupling factor $(-\ln R)$ for different ratios of pump ESA to GSA (γ, labelled). Parameters: $\alpha_0 = 1000\,\mathrm{m}^{-1}$, $\alpha_\mathrm{e} = 100\,\mathrm{m}^{-1}$, $L = 1\,\%$ and $l = 0.01\,\mathrm{m}$.

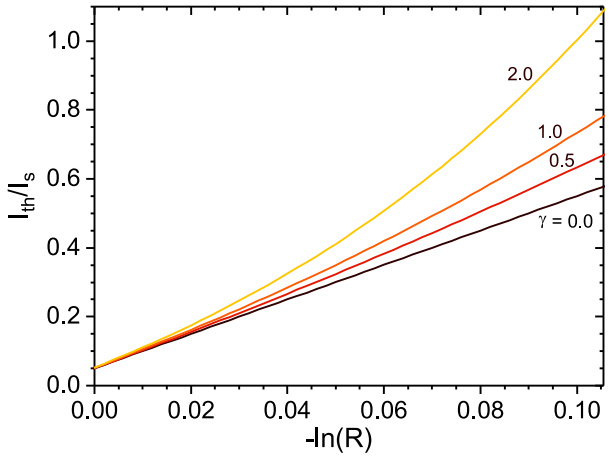

Figure 3.20: The threshold pump intensity, I_th, normalised to saturation intensity, I_s, against output coupling factor $(-\ln R)$. Parameters: see Figure 3.19.

the system parameters.

The terms involving the pump ESA cross section σ_1 in Equations (3.37) and (3.38) explicitly show the effect of pump ESA on laser threshold and efficiency. The $(-\ln[(1-L)R])$ factor quantifies the total round trip loss of laser radiation. A larger cavity loss requires a higher threshold inversion for lasing, increasing the amount of ESA.

Reducing σ_1 results in decreased pump ESA loss due to lower ESA strength. Increasing the stimulated emission cross section σ_e gives a higher gain, which leads to a lower threshold inversion and a resulting lower ESA loss. These changes both improve η_p and I_{0th}.

It should be noted that σ_0 and N are absent from the pump quantum efficiency and threshold pump intensity of Equations (3.37) and (3.38). The more exact formulations, Equations (3.33) and (3.34), are also independent of σ_0 and N, assuming a suitably long gain medium and not excessive pumping (note I'_s is inversely proportional to σ_0).

In addition to considering the material cross sections and cavity loss factors, the pumping geometry can impact the effect of pump ESA; the preceding formulation in this section was for single end pumping.

If a laser is approximated to have spatially constant population inversion fraction $\bar{f}$ the pump quantum efficiency becomes $\eta_p \approx 1 - \gamma\bar{f}$. To compare different pumping geometries the integrated inversion F, and therefore losses, of the cavities are kept constant. The different geometries result in different average population inversions needed, with the following results

$$\text{Single end-pumping:} \quad \bar{f}_s = \tfrac{\alpha_0}{2}F \qquad \eta_p \approx 1 - \gamma\bar{f}_s\,, \tag{3.39}$$

$$\text{Double end-pumping:} \quad \bar{f} = \tfrac{\alpha_0}{4}F \qquad \eta_p \approx 1 - \tfrac{1}{2}\gamma\bar{f}_s\,, \tag{3.40}$$

$$\text{Side-pumping:} \quad \bar{f} = \tfrac{1}{l}F \qquad \eta_p \approx 1 - \tfrac{2}{\alpha_0 l}\gamma\bar{f}_s\,, \tag{3.41}$$

where in the single end-pumped case the average population inversion is approximated as being distributed within two small signal absorption depths, the double end-pumped inversion is over twice that amount, and the side-pumped geometry distributes it over the pumped crystal length l. These equations show that double end-pumping requires half the average inversion of single end-pumping and has a corresponding increase in efficiency. Side pumping can also give an arbitrarily large increase in efficiency when compared to end-pumping, provided that the crystal length l is long compared to the effective single or double end-pumped length ($\approx 2/\alpha_0$ or $4/\alpha_0$).

An important descriptor of laser efficiency is the slope efficiency, η_s. To examine the effect of output coupler reflectance on η_s it is useful to define a reduced slope efficiency of $\eta'_s = \eta_p\eta_c$, which eliminates the terms not dependent on R. Figure 3.21 shows the reduced slope efficiency as a function of output coupling $(-\ln R)$ and the impact of changing the strength of pump ESA (γ). With no ESA, $\gamma = 0$ and $\eta_p = 1$, η'_s has the typical trend of a four-level laser. When ESA is present, $\gamma > 0$ and $\eta_p < 1$, there

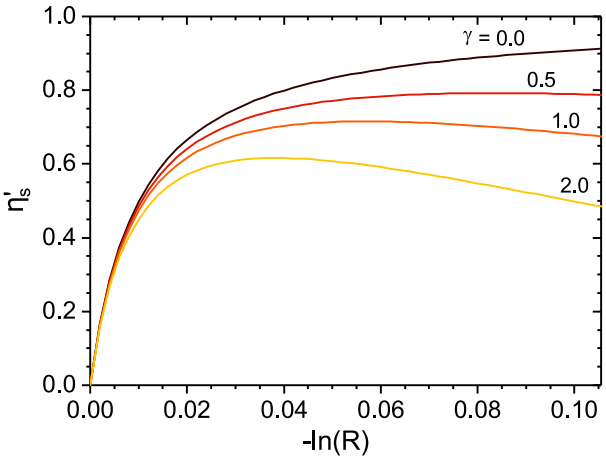

Figure 3.21: The reduced slope efficiency, $\eta'_s = \eta_p \eta_c$, versus output coupling factor $(-\ln R)$. Parameters: see Figure 3.19.

becomes an optimum R for maximum slope efficiency that increases with increasing γ. The cavity loss L becomes a doubly important design parameter for systems with pump ESA, with regards to slope efficiency, as it reduces both η_p and η_c.

The trend of slope efficiency with output coupling in Figure 3.21 has been seen in end-pumped Alexandrite lasers [16, 91], which have pump ESA [14]. In these investigations it was suggested that this could be due to energy transfer upconversion - a process that had not been identified for Alexandrite in the literature; however, the presented analysis suggests that this behaviour could be caused by the effect of pump ESA.

3.3.3 Bi-stable lasing

To analyse the full effects of pump ESA it is necessary to consider its interaction with laser ESA and GSA. To simplify the analysis and clarify the effect of pump ESA on the quantum efficiency, it will be assumed that $\eta_{p,0} = 1$ in the following section so $\eta_p = \eta_{p,ESA}$. This does not affect the results as it is a simple multiplying factor in the equations.

The key parameters that are affected by pump ESA are the laser threshold and pump quantum efficiency, which have approximate solutions that are simpler to analyse. The first approximation that can be made is that the input pump power is totally absorbed, $T \to 0$. This is a good approximation in most lasers, as non-absorbed pump can reduce overall efficiency. The second is that $\alpha_1 F \ll 1$, which is the case of low inversion. Under these conditions the pump threshold and quantum efficiency are

$$I_{0th} \approx \frac{h\nu_p}{\tau_f} \alpha_0 F \left[1 + \tfrac{1}{2}\alpha_1 F\right] , \tag{3.42}$$

$$\eta_p \approx \frac{1}{1+a\gamma} \left[1 - \tfrac{1}{2}\alpha_1 F + \tfrac{1}{2}\alpha_1 a(l - F)\right] . \tag{3.43}$$

The factors relating to pump ESA can be identified as those including α_{1a}. To first

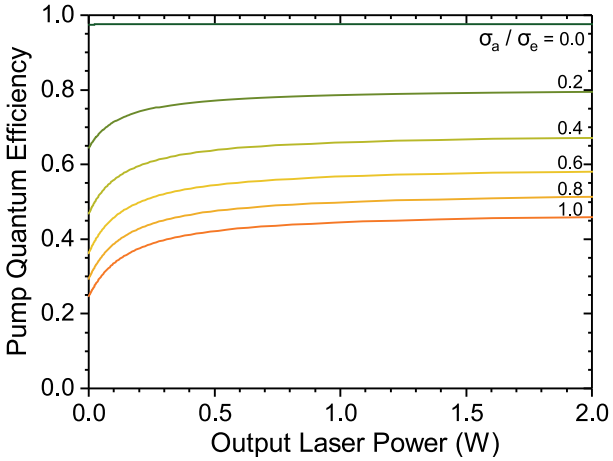

Figure 3.22: The pump quantum efficiency against laser output power for different ratios of σ_a/σ_e. $R = 99\,\%$, $L = 0.5\,\%$, $l = 10\,\text{mm}$, $\gamma = 0.8$, $A = \pi(100\,\mu\text{m})^2$, $\alpha_0 = 521\,\text{m}^{-1}$, $\alpha_e = 78\,\text{m}^{-1}$, $\alpha_{1a} = 9\,\text{m}^{-1}$, and $\tau_f = 262\,\mu\text{s}$.

order the threshold is linear in F and pump ESA is a second order effect proportional to F^2, which increases the threshold. The pump quantum efficiency is linear in F, but is also dependent on laser cavity flux through a. The effects of laser ESA and GSA enter through the integrated inversion F, see Equation (3.12), where increasing either results in a higher F value.

A plot of pump quantum efficiency against output laser power is shown in Figure 3.22 for different ratios of σ_a/σ_e, from four-level ($\sigma_a/\sigma_e = 0$) to three-level ($\sigma_a/\sigma_e = 1$) lasing with fixed laser and pump ESA. The pump quantum efficiency is at a minimum at threshold, its value approximated by Equation (3.43) when $a = 0$. It asymptotes to a maximum efficiency as laser power increases and $a \to \sigma_a/\sigma_e$.

The cause of the increasing pump quantum efficiency is clarified in Figure 3.23, which plots the population inversion distribution at different laser output powers. As laser output power increases, laser GSA causes the inversion of less pumped regions to increase; however, to satisfy the laser round trip gain condition there must be a fixed integrated inversion F, so the inversion at the pump input is correspondingly decreased. A lower population inversion over the main pump absorption region results in a smaller pump ESA loss and an increase in the pump quantum efficiency.

The increasing efficiency with laser power causes interesting effects when output laser power is compared to input pump power, as in Figure 3.24. For low GSA ratios (σ_a/σ_e) the power curves approximate to the linear form previously shown for end-pumped quasi three-level lasers. However, at higher GSA strengths the rate of change in pump quantum efficiency is large enough that multiple steady state solutions for the output laser power occur, giving bistable operation. When $T = 0$, the condition for bistability is

$$e^{\alpha_1 F}\left[1 - \frac{\alpha_1(l-F)}{(\sigma_e/\sigma_a + \gamma)}\right] < 1\,, \tag{3.44}$$

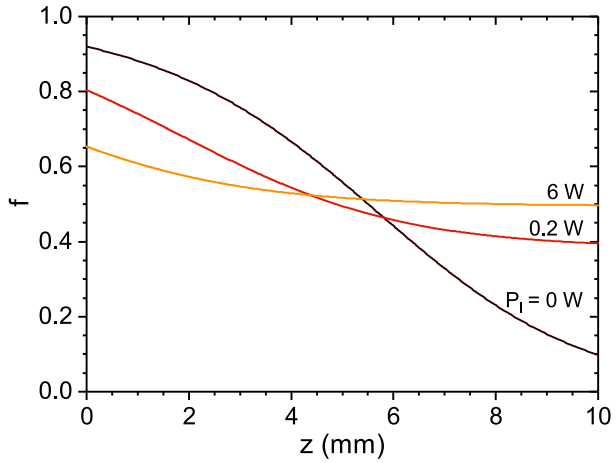

Figure 3.23: The normalised inversion (f) against distance into the gain medium for different laser output powers P_l, with $\sigma_a/\sigma_e = 1$. Other parameters as in Figure 3.22.

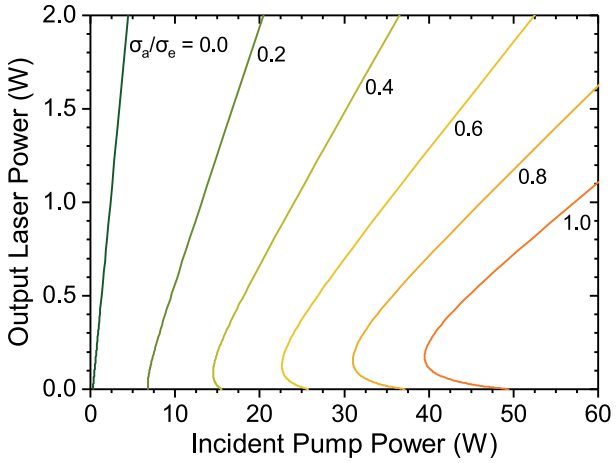

Figure 3.24: Laser output power against pump input power for changing ratios of σ_a/σ_e. Other parameters as in Figure 3.22.

which is found through differentiation of Equation (3.14) and is an equality for a cavity on the edge of bistability.

For bistable operation to occur the change in population distribution must be large enough to have a sufficiently large effect on the pump quantum efficiency. This can be achieved, for example, through making the change in population distribution larger by increasing the strength of GSA, σ_a/σ_e, or having larger areas of unpumped gain medium by increasing its length, l. Alternatively, the pump quantum efficiency change can be enhanced through a larger γ. Increasing these parameters individually gives power curves identical to those seen Figure 3.24.

Bistable power operation has been observed in CW lasers including a saturable absorber or non-linear dispersive medium [92], but has only been seen intrinsic to two classes of solid-state laser. It has been shown in the Tm, Ho [93] and Yb [94] classes of lasers, where the medium acts as its own saturable absorber; however, to the best of our

knowledge, this is the first identification of bistable behaviour in a solid state system due to a changing efficiency of pump absorption in the medium and should occur in any medium that has both pump ESA and laser GSA.

3.3.4 Heating fraction

Of particular interest in high power laser systems is the amount of heat generated in the medium. This has varying consequences, in particular thermally induced lensing. The heating fraction $\eta_{\mathrm{H}} = P_{\mathrm{H}}/P_{\mathrm{a}}$ is the fraction of absorbed pump power that is converted into heat (P_{H}).

In the laser model presented in Section 3.3.1 there are four sources of heat power: the Stokes quantum defect P_{Stokes}, the pump ESA heating $P_{\mathrm{p,ESA}}$, the laser ESA heating $P_{\mathrm{l,ESA}}$, and ions from the upper pump level that did not transfer into the upper laser level $P_{\mathrm{p,t}}$, giving

$$P_{\mathrm{H}} = P_{\mathrm{Stokes}} + P_{\mathrm{p,ESA}} + P_{\mathrm{l,ESA}} + P_{\mathrm{p,t}}\,. \tag{3.45}$$

Stokes heating is present in every laser system due to non-radiative decay from the upper pump level to the upper laser level. It is given by $P_{\mathrm{Stokes}} = P_0\eta_{\mathrm{a}}\eta_{\mathrm{p}}(1-\eta_{\mathrm{q}})$ as it is the quantum defect fraction of the pump absorbed from the ground state.

ESA generates heat because the absorbing ions non-radiatively decay back to the upper laser level, so all of the absorbed energy is converted to heat, giving $P_{\mathrm{p,ESA}} = P_0\eta_{\mathrm{a}}(1-\eta_{\mathrm{p,ESA}})$.

For ions that have transferred to a level other than the upper laser level there is a variable amount of heat that can be released, depending on how the ion decays back to the ground state - either fully non-radiatively or mixed with fluorescence. To incorporate this variability, the fraction of energy converted to heat from these ions is defined as $\eta_{\mathrm{H,t}}$, giving a heating power of $P_{\mathrm{p,t}} = P_0\eta_{\mathrm{a}}\eta_{\mathrm{p,ESA}}\eta_{\mathrm{H,t}}(1-\eta_{\mathrm{p,0}})$.

The laser ESA power is given by $P_{\mathrm{l,ESA}} = \frac{1}{2}\phi[2\alpha_{1\mathrm{a}}F]h\nu_{\mathrm{l}}cA$, which is the same as that for the laser output power expression, except that the output coupling $-\ln(R)$ has been replaced by $2\alpha_{1\mathrm{a}}F$, the effective round trip laser ESA coupling factor. This leads to an output coupling fraction of laser ESA, $\eta_{\mathrm{l,ESA}}$, of

$$\eta_{\mathrm{l,ESA}} = \frac{2\alpha_{1\mathrm{a}}F}{-\ln[R(1-L)] + 2\alpha_{1\mathrm{a}}F}\,, \tag{3.46}$$

$$= \gamma_{\mathrm{l}}\left[\frac{-\ln[R(1-L)] + 2\alpha_{\mathrm{a}}l}{-\ln[R(1-L)] + 2\gamma_{\mathrm{l}}\alpha_{\mathrm{a}}l}\right]\,, \tag{3.47}$$

which can be used to replace η_{oc} in Equation (3.23) to relate input pump power to laser ESA loss power. This means that the heating fraction scales with laser power.

By combining all the sources of heating in Equation (3.45) the heating fraction

becomes

$$\eta_{\mathrm{H}} = \begin{cases} 1-\eta_{\mathrm{p,ESA}}(1-\eta_{\mathrm{p},0})(1-\eta_{\mathrm{H,t}})-\eta_{\mathrm{p}}\eta_{\mathrm{q}}(1-\eta_{\mathrm{l,ESA}}) & \text{for} \quad P_0 \gg P_{0\mathrm{th}}\,, \\ 1-\eta_{\mathrm{p,ESA}}(1-\eta_{\mathrm{p},0})(1-\eta_{\mathrm{H,t}})-\eta_{\mathrm{p}}\eta_{\mathrm{q}} & \text{for} \quad P_0 = P_{0\mathrm{th}}\,, \end{cases} \tag{3.48}$$

where $P_{0\mathrm{th}} = AI_{0\mathrm{th}}$ is the input pump power at threshold. At an intermediate pumping level, the heating fraction is between these two limiting values and is dependent on how far above threshold the laser is operating. The largest heating fraction occurs far above laser threshold where fluorescence loss is negligible.

Useful approximations are that the laser GSA is small compared to the output coupling and cavity losses ($-\ln[R(1-L)] \gg 2\alpha_{\mathrm{a}}l$); the laser is operating far above threshold ($P_0 \gg P_{0\mathrm{th}}$); and there is negligible transfer of pumped ions into non-laser levels ($\eta_{\mathrm{p},0} = 1$), giving

$$\eta_{\mathrm{H}} \approx 1 - \tfrac{\lambda_{\mathrm{p}}}{\lambda_{\mathrm{l}}}(1-\gamma_{\mathrm{l}})\eta_{\mathrm{p,ESA}}\,, \tag{3.49}$$

where the Stokes heating factor is easily identified as $\lambda_{\mathrm{p}}/\lambda_{\mathrm{l}}$, laser ESA heating contributes through γ_{l}, and pump ESA heating is the $\eta_{\mathrm{p,ESA}}$ factor. Using this equation and the approximation for $\eta_{\mathrm{p,ESA}}$ given in Equation (3.27) will give a quick estimation of the heat load in any given laser system.

3.4 Summary

This chapter has presented an overview of the properties of the Alexandrite crystal and its suitability as a high power laser gain medium. It has excellent physical properties to withstand the heating stresses of pumping. The broad gain bandwidth gives it a diverse range of applications; however, the complications of laser and pump ESA, and laser GSA, along with other temperature related effects must be considered when designing a laser system.

The ratio of pump ESA to GSA (γ) was measured to decrease with crystal temperature from approximately 0.8 at 10 °C to 0.7 at 90 °C. With this new measurement, and values from the literature, there is a complete set of parameters for red diode-pumped Alexandrite over a range of temperatures.

An end-pumped analytical laser model was developed that is applicable to Alexandrite across its gain bandwidth, which gives insight into the effect of various parameters on laser performance. This model is also applicable to other gain media that has any set of laser and pump ESA, or laser GSA.

With the analytical model the effects of pump ESA could be isolated. This showed the negative impact on laser performance of pump ESA when intra-cavity losses are increased; however, it also provides solutions to mitigate its impact. Different pumping geometries of side and double end-pumping can reduce pump ESA loss. The combination of pump ESA and laser GSA is also predicted to have a bi-stable solution.

The heating effects of ESA through both the pump and laser radiation was formulated, with an approximate solution giving an estimation of the heat load in a laser that is an important cavity design consideration.

Chapter 4

Diode-pumped Alexandrite lasers

Lasers with tunable output wavelengths are beneficial in many applications, for example in remote sensing or scientific studies. Alexandrite, Cr^{3+}:$BeAl_2O_4$, is an attractive gain medium for these applications due to its broad tunability of 701 nm to 858 nm [8, 51], excellent thermo-mechanical properties [8], and efficiency [16, 95].

Many pumping schemes have been applied to Alexandrite. Historically, electrical gas discharge lamp pumping has been the most prolific [15]; however, solar [6], LED [39], Krypton ion [7], frequency doubled Neodymium [96], and red laser diode side [97] and end [16] pumping have been demonstrated. Of these techniques, diode end-pumping has been shown to be a route to efficient and high beam quality operation.

Alexandrite has a range of competing effects across its gain spectrum. In addition to the wavelength dependent emission cross section, these include ground state absorption (GSA) at laser wavelengths [19] and excited state absorption (ESA) at both pump [14] and laser [18] wavelengths. The complex spectral interplay of these lead to differing conditions for optimal laser performance. A key parameter and further complexity is the temperature of the gain medium, which has been shown to be important in optimising power output and crucial to accessing the full tuning range available in Alexandrite [51]. Previous works have shown by experiment the effect of temperature on Alexandrite performance [74, 98], but were limited in scope to the specific systems investigated and the conclusions drawn are not necessarily applicable to Alexandrite lasers in general.

The aim of this chapter is to elucidate, quantify, and predict the effect of temperature on laser performance in diode-pumped Alexandrite, yielding rules useful in general to optimising Alexandrite lasers. This involves understanding the temperature impact on the wavelength dependent properties, in addition to the upper-state lifetime, and provides practical advice for CW laser optimisation.

The experimental systems investigated were end-pumped with fibre-coupled red diodes. The cavities were either a 'compact' high efficiency geometry or 'extended' wavelength tunable design. In the compact geometry a record slope efficiency of 54 % was obtained, along with a route to power scaling through pump retro-reflection giving

2.05 W laser power from 5.7 W of pumping.

The wavelength tunable cavity was used to investigate, in particular, the crystal temperature related effects in Alexandrite. It achieved a record tuning range of 714 nm to 818 nm for a diode-pumped system by optimising the crystal temperature. The extended cavity was also used to verify the accuracy of the model developed in Section 3.3.1, which was then explored to find the ultimate efficiency limits of Alexandrite lasers.

Some of the results and analyses in this chapter have contributed to two published works [53, 75], which showed the high efficiency and broad tuning range that can be achieved in diode-pumped Alexandrite lasers, along with comparison to the theoretical model derived in Chapter 3 to understand and predict laser performance.

4.1 Background

When using red diode pump sources there are different schemes available. The first demonstration of diode-pumped Alexandrite used two 5 mW emitters at 680 nm in 1990 [99]. This gave an output power of 2 mW with a slope efficiency of 20 %, which demonstrated the efficiency achievable with diode-pumped Alexandrite. Recent advances in diode technology have enabled higher power applications. Single emitter diodes with high beam quality are available around 635 nm, but are limited to sub-watt level power. The high beam quality pump enables efficient laser operation, with a slope efficiency of 36 % at 48 mW output power in the HG_{00} mode demonstrated [98]. The ultimate power of these systems is limited by the pump diodes, which are not likely to have significant increases in single emitter power.

Single emitter multi-mode diodes are available with 1 W output power at 680 nm. These were used to demonstrate a tunable system from 724 nm to 816 nm with up to 200 mW laser power [91]. This had a high slope efficiency of 38 %, however this was with a multimode output of $M_x^2 = 1.25$ and $M_y^2 = 5$. To scale to multi-Watt powers in Alexandrite multiple emitters must be combined.

Seven red single emitters have been stacked to create a pulsed pump source with 14 W peak power with a symmetrical beam quality of $M^2 = 40$ [74]. With this unit a slope efficiency of 30 % in the HG_{00} mode was achieved, and a wavelength tunable cavity had a range of 745 nm to 805 nm.

To obtain a multi-ten watt pump source the single emitters can be manufactured into a row, with the rows then stacked on top of each other to closely pack together the emitters. These modules can achieve above 60 W CW power [16]. The output is highly asymmetric in both intensity profile and beam quality and requires careful reshaping optics or cavity design.

The diode stacks can be used in a side-pumping configuration, which gave the first multi-watt demonstrations of diode-pumped Alexandrite lasers [100]. This system had a high CW output power of 6.4 W from an incident 58 W pump power but with multi-

mode emission. A later higher efficiency bounce design obtained 12 W laser power from 56 W absorbed pump and a slope efficiency of 33 % [97]. The side-pumped geometry can be operated in a close to HG_{00} mode, an output power of 4.5 W was achieved at 48 W of pump power [97]; however, the efficiency was lower than that possible with end-pumping due to the difficulty in achieving good laser mode and pump beam overlap.

Using red diode stacks in the end-pumping configuration 26 W laser power from 65 W of pump has been demonstrated [16]. This power increase from red diode stacks was due to the greater overlap efficiency between the pump and laser modes, with the laser having a maximum slope efficiency of 49 %; however, in this high efficiency configuration the laser had a low beam quality of $M_x^2 = 22$ and $M_y^2 = 16$ [101]. Closer to HG_{00} operation was possible in a different design, albeit with lower efficiency. In this system, wavelength tuning of Alexandrite was achieved between 730 nm to 792 nm.

Another power scaling option for diode-pumping is coupling multiple emitters into an optical fibre. A power of 6 W can be coupled into a fibre with a core diameter of 105 µm, higher powers can be achieved using larger core diameter fibres at the cost of lower output beam quality. Mode mixing in the fibre makes the pump source both symmetric in intensity and beam quality, these properties are useful for an end-pumping source as asymmetries do not need to be corrected for in either the pump optics or the laser cavity. The mode mixing also causes the pump to lose the linear polarisation of the free-space emitters, which is potentially a disadvantage for use in Alexandrite where the pump absorption is strongly polarised along the b-axis (see Figure 3.10, p.44).

A slope efficiency in Alexandrite as high as 44 % and 1.1 W laser power in a HG_{00} mode using a 6 W fibre-coupled pump has been demonstrated [95]. In a lower power configuration the system had a tuning range of 737 nm to 796 nm with up to 600 mW laser power.

4.2 Diode pump source

For the Alexandrite lasers investigated a fibre-coupled red (636 nm) diode module was used, as this had been shown to enable watt-level laser power with a HG_{00} beam [95]. The simplicity and symmetry of this pump source also reduced the number of variables in understanding the performance of the Alexandrite lasers. The module was mounted on a water cooled copper block, had a maximum power of 5.7 W, a fibre core diameter of 105 µm with NA = 0.22, and beam qualities of $M_x^2 = 43$ and $M_y^2 = 44$ in the horizontal and vertical axes, respectively.

The pump delivery system for the Alexandrite lasers is shown in Figure 4.1. The fibre output of the module was first collimated with a 11 mm focal length collimator attachment. A cube polariser linearly polarised the beam, with the angle chosen to maximise the transmitted linearly polarised power. A half-waveplate rotated the linear polarisation to match that of the b-axis of the Alexandrite, and an f_p focal length

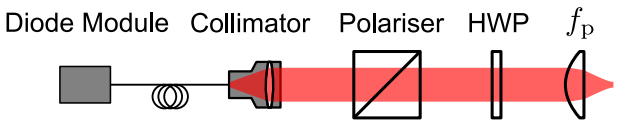

Figure 4.1: The pump delivery system for the Alexandrite lasers.

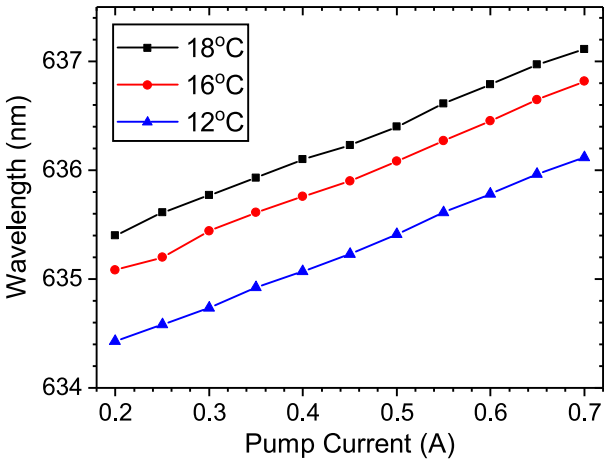

Figure 4.2: The central wavelength of the pump module for changing input current and coolant temperature.

aspheric lens then focussed the beam into the Alexandrite to the required size.

The focal length of f_p was a balance between having a small beam waist to increase the pump intensity for a low laser threshold and a large beam waist to minimise pump divergence over the absorbed path. By experiment, it was found that $f_p = 20\,\text{mm}$ was the optimum focal power, giving a $1/e^2$ beam waist diameter of $150\,\mu\text{m}$ and confocal parameter of 2.1 mm in the crystal. This matched well with the measured absorption depth of 1.9 mm for the 0.22 at.% Alexandrite crystal used.

A final consideration for the pump was the temperature of the water cooled copper mount, which had two effects. The first was the central wavelength decreased at lower temperatures, which is shown in the plot of central wavelength against pump current in Figure 4.2 at different temperatures. A shorter wavelength is beneficial in Alexandrite as this decreases the absorption depth (see Figure 3.10, p.44). The wavelength is also longer at higher pump currents due to heating of the emitters; however, this is unavoidable and the higher power output is more beneficial.

The second effect of coolant temperature was a higher power output at colder temperatures. To avoid condensation in the module, the lowest temperature used was 12 °C. The output pump power versus supplied current is shown Figure 4.3 at this temperature. The data given shows the module output directly from the collimator (unpolarised) and when linearly polarised with the cube polariser. The linearly polarised power was 57 % of the unpolarised power, which shows that the fibre did not fully mix the polarisation state of the modes.

The inset of Figure 4.3 shows the intensity profile of the pump at the beam waist,

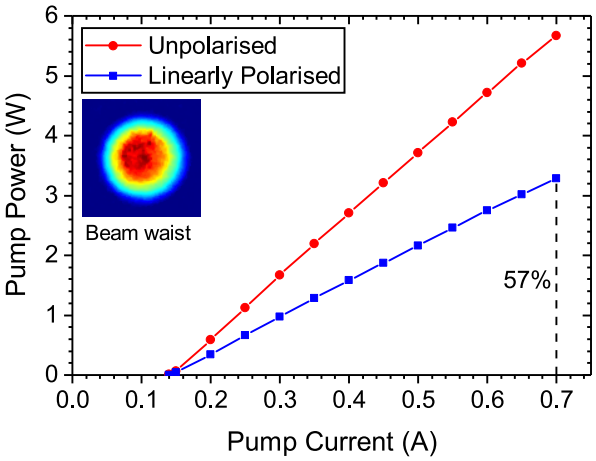

Figure 4.3: The pump power against input pump current at 12 °C when unpolarised and linearly polarised through a cube polariser. Also shown is the fraction of the linearly polarised power at 0.7 A compared to the unpolarised pump (57 %). *Inset*: The beam waist intensity profile.

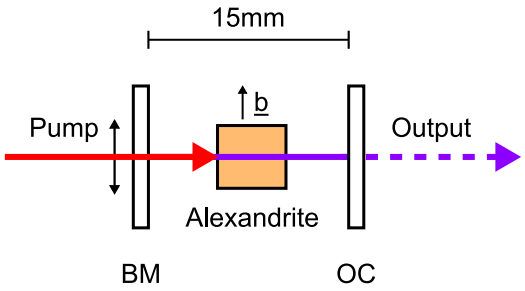

Figure 4.4: The 'compact' cavity Alexandrite laser.

which was approximately Gaussian. This suggests incomplete mode mixing in the fibre.

4.3 High efficiency compact cavity

The 'compact' laser geometry is shown in Figure 4.4. The crystal used was a 0.22 at.% Cr-doped Alexandrite rod, which was 4 mm long with a diameter of 2 mm. It had a measured pump absorption coefficient of 7.5 cm^{-1} and absorbed 95 % of incident pump radiation. It was contacted with indium foil to a water cooled copper mount, see Figure 2.3, with a thermoelectric cooler (TEC) controlled temperature range of 8 °C to 105 °C. The minimum temperature accessible was limited by the risk of condensation forming on the crystal or mount, and the maximum temperature was limited by a combination of the heating power of the TEC and the risk of the indium foil flowing under heat and pressure. The back mirror (BM) was dichroic with high transmission for the pump and high reflectance at laser wavelengths, and the partial reflectance output coupler (OC) completed the cavity.

To achieve the most efficient operation from this cavity every controllable parameter was optimised. The cavity length was changed to alter the mode size to match it to the

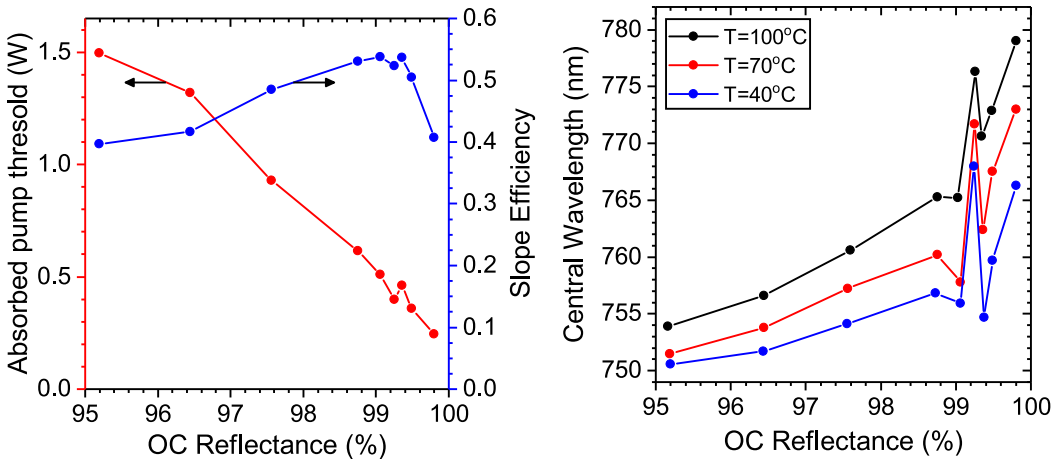

(a) (b)

Figure 4.5: The impact of the OC reflectance on the compact cavity. (a) The absorbed pump power threshold and slope efficiency against OC reflectance at 70 °C crystal temperature. (b) The central laser wavelength against output coupler reflectance at crystal temperatures of 40 °C, 70 °C, and 100 °C.

size of the pump region, with 15 mm the resulting length. The waist diameter of the pump beam was varied to find the best balance between low threshold and high slope efficiency.

The choice of OC was also important and affected the laser in two ways. The effect of the OC reflectance on the threshold and slope efficiency of the compact cavity are shown in Figure 4.5(a). A lower reflectance increased the laser threshold, on average, as would be expected from four-level laser theory. The decreasing OC reflectance had more a more complex impact on the slope efficiency. Initially, reducing from 100 % reflectance increased the slope efficiency as expected from the higher output coupling efficiency. However, there was an optimum reflectance at approximately 99.2 %, where beyond this point the slope efficiency decreased. This was due to the effect of pump ESA, as outlined in Section 3.3.2, where the higher laser threshold increased the population inversion and the pump ESA loss.

There are clear overall trends to the threshold and slope efficiency in Figure 4.5(a); however, there are deviations from this, particularly around reflectances of 99 %. This was due to the central laser wavelength changing, as shown in Figure 4.5(b) as a function of OC reflectance and crystal temperature. The wavelength of a laser is determined by the wavelength of the lowest threshold mode. As there was no specific wavelength control in the compact cavity, the lowest threshold wavelength was determined by the properties of the optical coatings of the cavity components and the properties of Alexandrite.

The laser GSA in Alexandrite is stronger at shorter wavelengths, so increases the thresholds of the modes in this region. Lower population inversions also increase laser GSA. This effect explains the trend towards longer wavelengths for higher OC reflectance, because the decreasing population inversions push the laser wavelength higher.

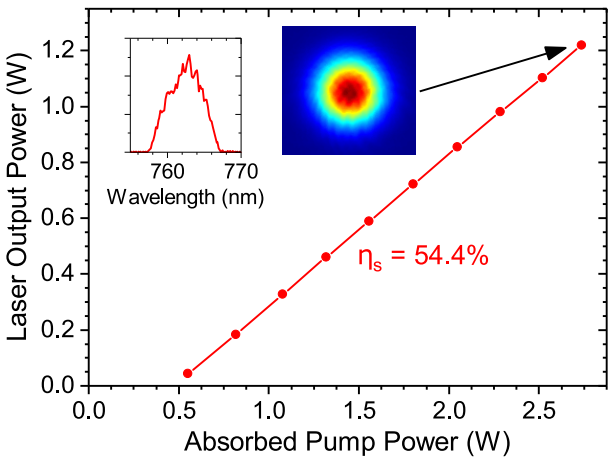

Figure 4.6: The laser output power versus absorbed pump power for the compact cavity with a record slope efficiency of 54.4 %. *Inset:* The laser intensity profile and wavelength spectrum at maximum power, FWHM = 5.7 nm.

Laser GSA is also increased at higher temperatures, which explains the increasing wavelength with crystal temperature. From these results it is clear that the crystal temperature affected the lasing wavelength, along with the Alexandrite optical properties, so requires optimisation.

The sharp changes in wavelength around 99 % reflectance were due to the wavelength dependence of the reflectance of the OCs. Depending on the spectral shape of the reflectance curve either shorter or longer wavelengths had a lower threshold. These sharp changes of wavelength also manifest themselves in the off-trend threshold and slope efficiencies in Figure 4.5(a).

The optimum OC had a reflectance of 99.5 % at 700 nm, decreasing to 99.2 % at 820 nm. With this and the other optimisations performed on the laser, the resulting laser output power versus absorbed pump power is shown in Figure 4.6. The maximum output power was 1.22 W at 762 nm from an absorbed pump power of 2.74 W. The threshold was at 0.46 W of absorbed pump power giving a slope efficiency of $\eta_s = 54.4\,\%$, which is to our knowledge the highest slope efficiency diode-pumped Alexandrite laser to date.

The output beam waist diameter was 180 µm at the OC, which matched well with the pump beam size, giving a HG_{00} spatial mode with a high beam quality of $M^2 = 1.08$. The spatial profile of the mode is shown in the inset of Figure 4.6. The compact cavity design benefited from being very low loss with an approximate round trip loss of 0.2 %, which was determined through direct loss measurements of the intra-cavity optics.

The spectral profile of the compact cavity is shown in the inset of Figure 4.6. It had a broad FWHM wavelength emission of 5.7 nm, which is typical in Alexandrite lasers without a frequency selective element [98]. The central wavelength was 762 nm with the crystal oven temperature at 70 °C.

Coarse wavelength tuning of the compact cavity was achieved by altering the cry-

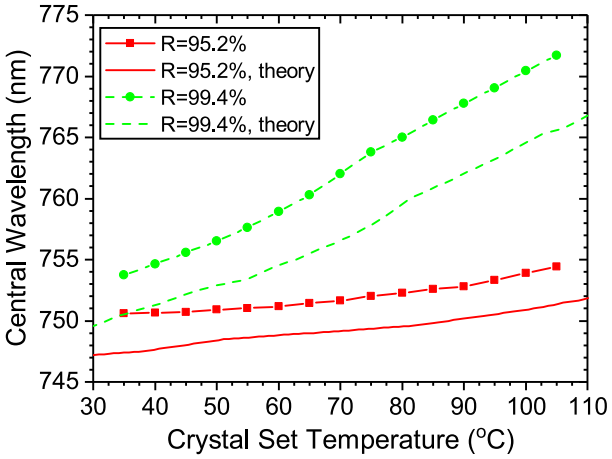

Figure 4.7: The laser wavelength versus crystal temperature in the compact cavity for output coupler reflectances R. The theoretical predictions are also shown based on the model in Section 3.3.1.

stal temperature. The effect of crystal temperature on laser wavelength is shown in Figure 4.7. The theoretical operation wavelength is also shown, which was calculated from the model presented in Section 3.3.1 [53] by finding the wavelength that minimised the threshold at a given temperature, which due to gain clamping would be the oscillating laser mode. The offset between theory and experiment was most likely due to there being a higher crystal temperature than that of the TEC set temperature from localised heating at the pumped region. Additionally, there were uncertainties in the Alexandrite properties, for example the optical cross section values, which would affect the lowest threshold wavelength. The intracavity losses were also wavelength dependent from the optical coating reflectances, which introduced additional uncertainty.

The maximum tuning range achieved solely via crystal temperature control was 18 nm, centred on 763 nm, with an output coupler reflectance of $R = 99.4\,\%$. The tuning range reduced to 4 nm when using $R = 95.2\,\%$. This shows that wavelength tuning is possible in Alexandrite via crystal temperature control when no wavelength selective elements are used, as shown in other studies [98], but has a small range compared to the gain bandwidth available and is limited to the central gain region. The tuning range possible solely from crystal temperature control is generally much smaller than the range possible with dedicated wavelength control methods.

To explore the possibility of adding intracavity components to the high efficiency compact design, the effect of cavity length was investigated by extending the output coupler away from the crystal. The laser power and threshold versus cavity length is shown in Figure 4.8. The maximum cavity length was 33 mm, at which point the laser would not operate.

Towards the maximum cavity length the alignment precision required increased rapidly, with it becoming increasingly difficult to obtain sufficient alignment for lasing. The ultimate cavity length achieved could have been due to the alignment precision

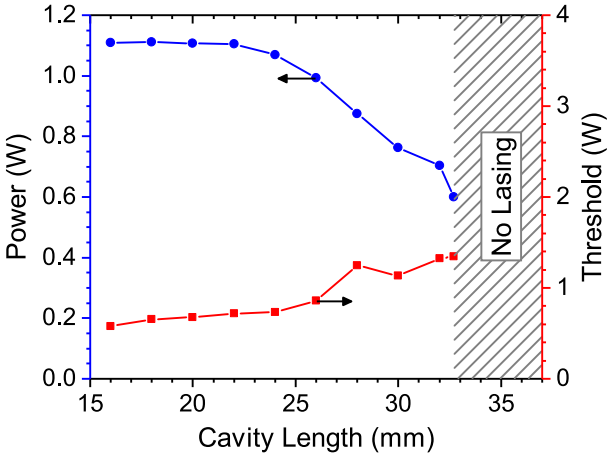

Figure 4.8: The laser output power at 3.3 W pump power and the threshold of the compact cavity versus cavity length. Beyond 33 mm lasing could not be achieved.

possible. Alternatively, it could have been due to the resonant cavity stability conditions, which would suggest a thermal lens in the crystal of length 30 mm.

It would be expected that if the cavity length was unstable at 33 mm the threshold should have increased rapidly, following the diverging mode size at the crystal [79]. However, as the threshold was only steadily increasing it is likely that the alignment precision limited the cavity length, and the thermal lens focal length was longer than 30 mm. Despite the cause, the maximum cavity length achieved in Figure 4.8 meant that up to 19 mm of intracavity space was available in the compact design.

4.3.1 Double-pass pumping

Although the compact cavity was highly efficient with respect to absorbed pump power, when end-pumped with fibre-coupled red diodes 43 % of the available pump power could not be used as it was the incorrect polarisation to be absorbed. To reduce this power loss and increase the overall power output of the laser, unabsorbed pump can be reused and absorbed by the gain medium [95].

When an unpolarised pump beam passes through a sufficiently long Alexandrite crystal the polarisation component parallel to the b-axis will be completely absorbed, and the component orthogonal to it will be almost completely transmitted. The resulting beam will therefore be linearly polarised orthogonal to the b-axis. This transmitted component can then be retro-reflected back into the crystal and its polarisation rotated to match the b-axis. The retro-reflected pump can then be efficiently absorbed in the crystal.

The laser cavity design for a retro-reflected pump is shown in Figure 4.9, which used the same 0.22 at.% 4 mm Alexandrite crystal at 70 °C and fibre-coupled diode pump as the compact cavity. The unabsorbed pump was polarised parallel to the Alexandrite c-axis. A dichroic turning mirror (TM) was included to transmit the unabsorbed pump as

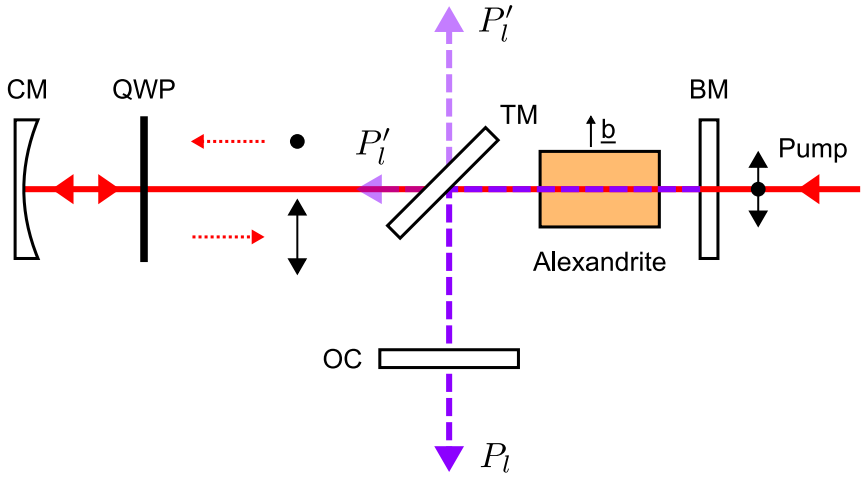

Figure 4.9: The laser geometry for retro-reflection of the unabsorbed pump. Unabsorbed pump (polarised orthogonal to Alexandrite b-axis) is refocussed and reflected back by the concave mirror (CM), with its polarisation aligned to the b-axis by the quarter-wave plate (QWP). The pump is separated by a dichroic turning mirror (TM). The laser cavity is formed between the back mirror (BM), output coupler (OC), and TM.

dichroic output couplers were unavailable. The pump beam was then reflected back by a concave mirror (CM), which was positioned a distance equal to its radius of curvature away from the crystal (25 mm). This re-imaged the pump back to an equal size beam waist at the crystal, with the position of the waist in the crystal optimised for laser output power. The double pass of the quarter-wave plate (QWP) made it act as a half-wave plate and rotated the linear polarisation. The QWP was aligned so that the polarisation of the reflected beam was parallel to the b-axis of the Alexandrite.

In the retro-reflection geometry the laser was effectively the compact cavity design with a cavity length of 24 mm, which was short enough to not significantly reduce the output power, see Figure 4.8. However, there would have been some efficiency lost from this cavity extension, along with the longer focal length ($f_p = 26$ mm) pump lens that was required to allow space for the retro-reflection optics.

The OC had a reflectance of 99.4 %, with the BM and TM both designed to be high reflectance at laser wavelengths. It was found that the TM actually had a transmission of 0.12 % at the laser wavelength and contributed to a significant output coupling of the intra-cavity laser power when compared to the 0.6 % transmission output coupler. With a better quality high reflectance coating on the TM the power lost on each pass P_l' would instead be additional power in the laser output P_l. To correct for this loss and give a more accurate measure of the laser performance, the total laser output power was calculated as $P_{l,t} = P_l + 2P_l'$.

The total laser output power against input pump power both with and without the retro-reflected pump is shown in Figure 4.10. When the pump was retro-reflected the beam quality remained high, with $M^2 = 1.08$, and the maximum laser power was higher at 2.05 W, an increase of 58 % from 1.30 W.

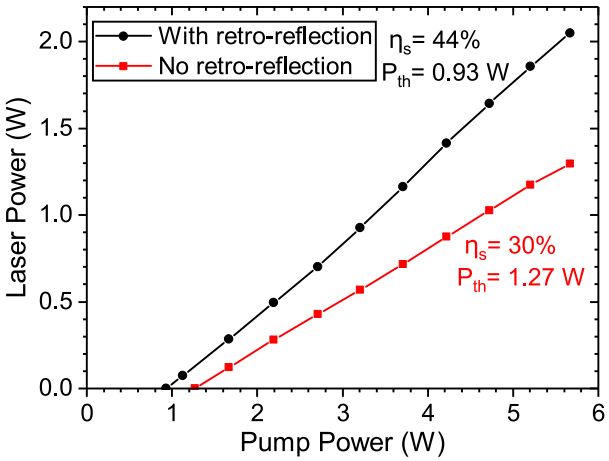

Figure 4.10: The total laser output power versus input pump power with (black circles) and without (red squares) the pump retro-reflected back into the crystal. Also shown are the slope efficiencies (η_s) and threshold pump powers (P_{th}).

For the single end-pumping laser model derived in Section 3.3.1 it can be shown that the threshold pump power $P_{0,\mathrm{th}} \propto 1/(\eta_a \eta_p)$ and the slope efficiency $\eta_s \propto \eta_a \eta_p$. Retro-reflection pumping can be approximated as increasing the absorption efficiency η_a. Assuming the pump absorption efficiency increased from $\eta_{a,0} = 0.57$ (the pump polarisation purity) to $\eta_a = 1$ with retro reflection, the slope efficiency and threshold should have changed by factors of $1/\eta_{a,0}$ and $\eta_{a,0}$, respectively.

The results in Figure 4.10 show that the slope efficiency and threshold changed by factors of 1/0.68 and 0.73, respectively, when the pump was retro-reflected. These are approximately consistent with each other, with the denominator of the slope efficiency factor being almost equal to the threshold multiplier. However, the gains in slope efficiency and threshold were lower than expected, which could have been due to several factors. The retro-reflected pump had reflection losses from a double pass of each of the rear face of the crystal, TM and QWP. Additionally, the pump will not have been ideally re-imaged back into the crystal, where a larger or more distorted re-imaged beam would have had a lower overlap efficiency with the laser mode and so contributed less to both the slope efficiency and threshold.

These results show that retro-reflection of the unabsorbed pump is an effective option to increase the overall power output and efficiency of fibre-delivered diode end-pumped Alexandrite lasers. The laser power output of a compact geometry increased by 58 % to 2.05 W for 5.7 W of pump power. If implementing this geometry with Alexandrite, care should be taken to use a high quality turning mirror to reduce losses with the low transmission OCs used.

An alternative geometry could be to use the compact cavity with no TM, where the laser output and unabsorbed pump both pass through the OC. These beams could then be separated external to the cavity with a dichroic TM, allowing the pump to be retro-reflected back. This could provide a low loss cavity and enhance the efficiency.

This would require a dichroic OC, which was not available in this investigation.

4.4 Wavelength tunable laser

To study the wavelength tuning properties of an Alexandrite laser it is important to have a laser geometry that provides full control over all aspects of the laser. These parameters include: the laser mode size at the crystal, to compensate for changing thermal lens effects in the crystal and give a consistent mode overlap efficiency; the temperature of the Alexandrite crystal, to investigate its many temperature dependent effects; and control of the laser wavelength, to be able to assess performance away from the natural gain peak.

4.4.1 Birefringent filter tuning

To construct a wavelength tunable Alexandrite laser that can access its full gain bandwidth there must be a frequency selective element for the cavity. This has been demonstrated with an external feedback grating in the Littrow configuration [16]; however, the tuning range was limited by the self-seeding strength. Alternatively, intra-cavity tuning elements can be used. A Fabry-Perot etalon is not ideal for use with Alexandrite because of the low gain available, and subsequently high reflectance output couplers used, which means that small intra-cavity losses can significantly impact performance. A birefringent filter (BiFi) tuning element at the Brewster angle can be used in Alexandrite because of its linearly polarised emission [8]. This device has a low reflective insertion loss, as it is used at the Brewster angle, and can provide sufficient losses to tune across the gain bandwidth of Alexandrite.

The implementation of a single plate BiFi is shown in Figure 4.11(a). The BiFi element is a birefringent plate of thickness d, which has ordinary and extraordinary refractive indices n_o and n_e, respectively. The input beam is p-polarised and incident at the Brewster angle θ_B, where $\tan(\theta_\mathrm{B}) = n$, and $n = (n_\mathrm{o} + n_\mathrm{e})/2$ is the average refractive index.

The angles used in the analysis of the BiFi are given in Figure 4.11(b). The optic axis of the BiFi element is parallel to the plane of its surface and is at an angle of ϕ to the plane of incidence. The angle between the optic axis and the refracted ray is η. The angle between the plane of incidence and the plane containing the optic axis and the refracted ray is α.

As the refracted ray is not propagating along the optic axis ($\eta \neq 0$) its projected polarisation components experience different refractive indices and therefore phase changes. If the relative phase difference is a multiple of 2π when incident on the exit face of the BiFi then its polarisation will be unchanged. In this case the BiFi is a full-waveplate

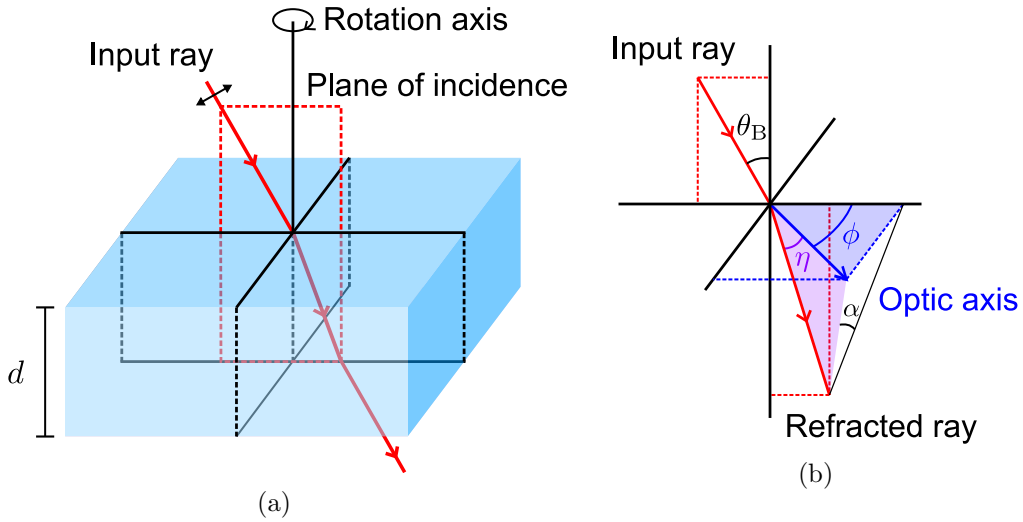

Figure 4.11: The design of a birefringent filter (BiFi) tuning element. (a) The input ray is incident on the BiFi surface with p-polarisation at the Brewster angle. The BiFi has a thickness d and is rotated about the axis normal to its surface for tuning. (b) The angle definitions used. The input ray is at the Brewster angle θ_B. The optic axis is parallel to the BiFi surface and is at an angle ϕ to the plane of incidence. The angle between the refracted ray and the optic axis is η. The angle between the plane of incidence and the plane containing the optic axis and refracted ray is α

and the ray remains p-polarised. The condition for this is given by

$$\lambda = \frac{(n_e - n_o) d \sin^2 \eta}{m' \sin \theta_B}, \tag{4.1}$$

where m' is an integer [102]. The free spectral range (FSR) is the wavelength separation ($\Delta\lambda$) of the solutions to Equation (4.1) and is given by

$$\Delta\lambda = \frac{\lambda^2 \sin \theta_B}{(n_e - n_o) d \sin^2 \eta}, \tag{4.2}$$

assuming no wavelength dispersion of the refractive index. Both of these equations hold if the optic axis is at an arbitrary angle to the BiFi surface [103].

In the case of the optic axis being parallel to the plane of the BiFi surface, the relationships between the angles are

$$\cos \eta = \cos \phi \cos \theta_B, \tag{4.3}$$

$$\tan \phi = \tan \alpha \sin \theta_B. \tag{4.4}$$

The key observation for these equations is that the angle η is a function of the BiFi rotation angle ϕ (note that θ_B is a constant).

With these relationships the wavelength tuning of a BiFi in a laser cavity can be understood. For input rays with wavelengths given in Equation (4.1) the input ray will be 100 % transmitted as it remains in p-polarisation at the exit face of the BiFi. For all

other input wavelengths there will be s-polarisation components at the exit surface of the BiFi that will undergo Fresnel reflection. This loss mechanism will give these laser modes a higher threshold, so the wavelengths of Equation (4.1) will be favoured.

Wavelength tuning of the laser is achieved through rotation of the BiFi about the axis normal to its surface. This controls ϕ, which in turn changes the angle η through Equation (4.3) and alters the fully transmitted wavelengths λ through Equation (4.1).

To effectively control the laser wavelength the FSR of the BiFi should be greater than the gain bandwidth of the laser medium. Precisely determining the FSR of a BiFi of given thickness d is not a trivial task. An approximate relation can be used of

$$\Delta\lambda \approx \frac{\lambda^2}{(n_\mathrm{e} - n_\mathrm{o})d} \frac{(1 + \sin^2\theta_\mathrm{B})}{2\sin\theta_\mathrm{B}}\,, \tag{4.5}$$

where the derivation and approximations made are given in Appendix B. For reference, it can be shown that $\sin\theta_\mathrm{B} = n/\sqrt{1+n^2}$.

The bandwidths of the transmission peaks are narrower for smaller FSR BiFis [104]. For a single element BiFi, the laser linewidth will be limited by the FSR needed. If a narrower laser linewidth is required, multiple BiFi elements of varying thicknesses can be used that each act to suppress the higher order tranmission wavelengths of the others [105]. In this way a narrower transmission bandwidth is achievable.

4.4.2 Laser design

A BiFi was chosen to provide wavelength tuning, which required an intracavity space approximately 4 cm long. The BiFi was a 0.5 mm thick quartz plate mounted at Brewster's angle. At 750 nm crystalline quartz [106] has $n_\mathrm{o} = 1.5394$, $n_\mathrm{e} = 1.5483$ and $n = 1.5439$, which gives a FSR of $\Delta\lambda \approx 130$ nm using Equation (4.5). The compact cavity design could not accommodate this device due to limitations of the cavity length (see Figure 4.8, p. 74). To use the BiFi an 'extended' cavity was designed that had sufficient intra-cavity space.

The extended end-pumped Alexandrite laser system was built with the cavity geometry shown in Figure 4.12. The Alexandrite was a nominally 0.22 at.% Cr doped rod with length 4 mm and diameter 2 mm. The crystal faces were anti-reflection (AR) coated for both the laser and pump wavelengths. It was mounted in a thermoelectric cooler (TEC) controlled copper mount with a temperature range of 10 °C to 105 °C, which allowed investigation of the temperature dependent behaviour of Alexandrite.

Stability of the cavity was achieved with an intracavity lens of focal length $f = 100$ mm, which had a super-V AR coating centred at 760 nm with a per surface loss of 0.03%, rising to 0.18% 40nm either side. Both the output coupler (OC) and back mirror (BM) were planar. By using an intracavity lens and planar mirrors there was great flexibility in the laser mode size at the crystal through simple adjustments of lens to mirror distances. An alternative would be a spherical surface OC, which would

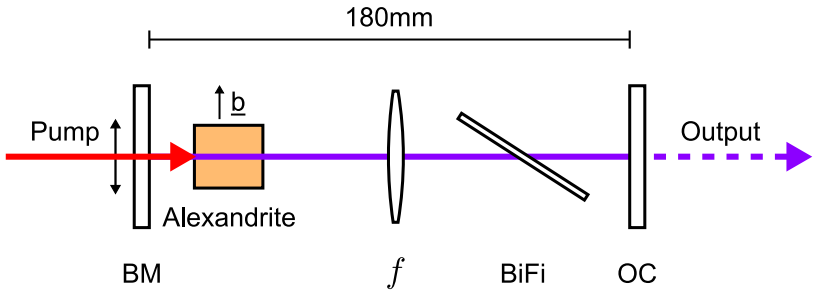

Figure 4.12: The 'extended' cavity of the wavelength tunable Alexandrite laser.

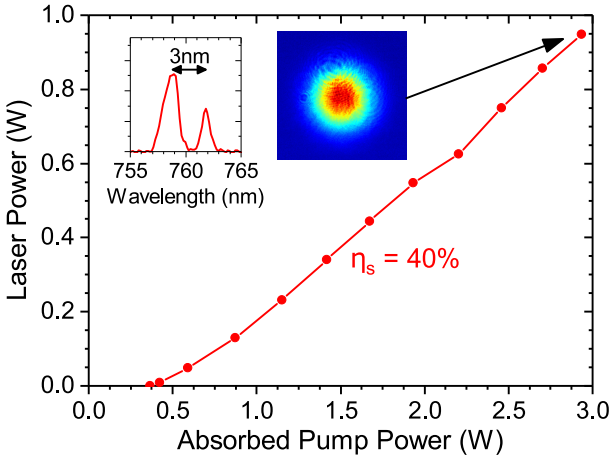

Figure 4.13: The output laser power versus input pump power for the extended cavity with no birefringent plate. *Inset:* The laser intensity profile and wavelength spectrum at maximum power.

have lower losses, but would have been more constraining in mode size control and the availability of optics.

The extended cavity laser was first operated without the birefringent element, the laser output power versus pump input power is shown in Figure 4.13 for a crystal temperature of 60°C. It operated with a wavelength of 760 nm at maximum pump power, a slope efficiency of 40 % and a HG_{00} spatial mode profile, shown in the inset of Figure 4.13. The laser operated at two wavelengths separated by 3 nm with an average wavelength of 762 nm. This is typical in Alexandrite and is attributed to birefringence of the crystal [98].

The extended cavity was then operated with the BiFi for tuning the laser wavelength. Before inserting the BiFi the polarisation direction of the cavity was measured, which accurately determined the Alexandrite b-axis orientation. The BiFi was then aligned to the Brewster angle of this polarisation by ensuring that the cavity polarisation was unchanged after insertion. The reflective round trip loss was 0.01 % from the BiFi. The laser output power against input pump power is shown in Figure 4.14(a) for three different laser wavelengths, corresponding to the three regimes of operation, at a crystal temperature of 60 °C.

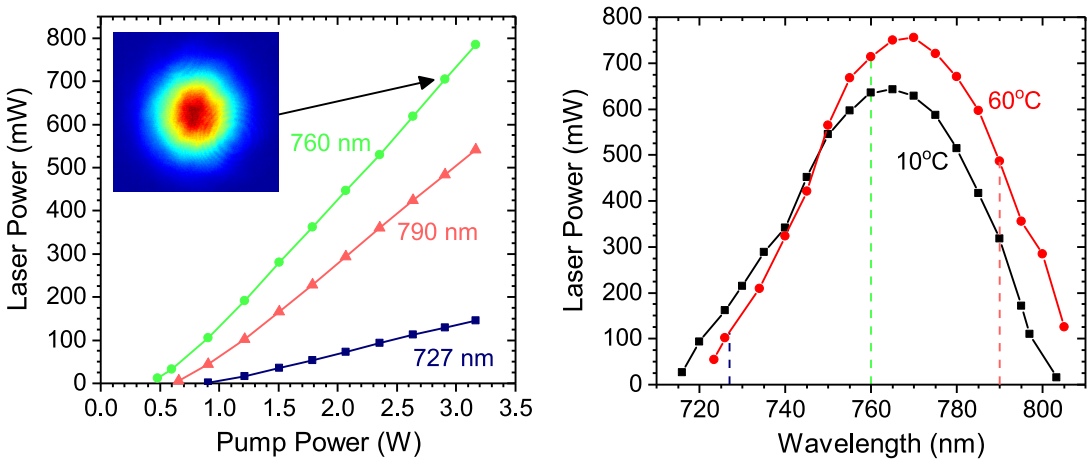

Figure 4.14: The output powers of the wavelength tunable Alexandrite laser in the typical wavelength and temperature range used. (a) The output laser power versus input pump power at three laser wavelengths, at a crystal temperature of 60 °C. The inset shows the beam profile at the indicated point. (b) The laser power against wavelength for two crystal temperatures, with an input pump power of 2.73 W. The dashed lines indicate the wavelengths shown in (a).

The laser was most efficient operating at 760 nm with a peak output power of 785 mW, lowest threshold of 0.45 W and maximum slope efficiency of 30 %. The effect of tuning to 790 nm was a slightly increased threshold of 0.63 W and reduced slope efficiency of 22 %. At 727 nm was the least efficient operation, with the highest threshold of 0.88 W and a significantly lower slope efficiency of 7 %. The laser output had excellent spatial quality in all cases and with an $M^2 = 1.02$ at 760 nm, the beam profile is shown in Figure 4.14(a). The output spectrum typically had a FWHM bandwidth of 2 GHz, which was narrower than prior work due to the presence of the BiFi [16].

The effect of laser wavelength tuning on the output power is shown in Figure 4.14(b), at crystal temperatures of 10 °C and 60 °C. The optimum wavelengths of 765 nm and 770 nm at 10 °C and 60 °C, respectively, are typical for Alexandrite [8, 91, 95]. Elevated temperatures extended the upper tuning range, as has been previously reported [51], but in turn increased the lower bound by 7 nm. The higher temperatures resulted in improved output powers above 750 nm.

It is the complex interplay of effects in Alexandrite lasers, with the changing efficiencies across the laser output spectrum seen in the experimental data, that makes it important to understand the various factors at play to aid in optimisation. With this cavity design there was full control over the parameters that could effect the lasing performance of Alexandrite. The intra-cavity lens enabled mode size control, so differing thermal lenses could be compensated for. The BiFi provided laser wavelength control to explore the gain bandwidth available. The TEC controlled oven for the Alexandrite crystal allowed a range of operation temperatures to be stably accessed. This tunable

Table 4.1: The calculation parameters used in the Alexandrite laser modelling.

		Crystal Temperature / °C						
		10			60			
		Laser wavelength / nm						
Parameter	Unit	730	760	790	730	760	790	Source
σ_e	$10^{-25}\,m^2$	6.64	4.16	2.23	11.4	8.53	5.43	[72]
σ_{1a}	$10^{-25}\,m^2$	2.03	0.03	0.53	2.13	0.12	0.60	[72]
σ_a	$10^{-25}\,m^2$	0.0376	0.0015	0.000 06	0.164	0.0118	0.0009	[19]
τ_f	µs		314			190		[8, 20]
σ_0	$10^{-25}\,m^2$	71.1						[8, 14]
$\gamma = \frac{\sigma_1}{\sigma_0}$	-	0.75						[14]
l	mm	4.00						-
N	$10^{26}\,m^{-3}$	1.01						-
A	mm^2	0.025						-

laser system could then be used to investigate the parameters that affect performance of Alexandrite lasers.

4.4.3 Pump ESA effects

The influence of pump ESA on Alexandrite laser performance has had little attention in the literature. Aside from the measurement of the pump ESA cross section [14], there has been no quantitative analysis of its effect on laser efficiency. Some models include a pump ESA loss factor but give no way to calculate it, so it must be estimated [107]. In this section, the pump ESA effects on CW Alexandrite lasers across the tuning range are investigated quantitatively for the first time, using the theoretical model developed in Section 3.3.1.

To determine the impact of pump ESA, a comparison was made between the analytical model predictions and experimental measurements from an Alexandrite laser system. Equations (3.15) and (3.23) were used to find the thresholds and slope efficiencies, respectively, using the parameters in Table 4.1. The corresponding experimental results for threshold and slope efficiency were taken from the experimental laser described in Section 4.4.

The results are shown in Figure 4.15, with experimental measurements in Figures 4.15(a) and 4.15(c), and modelling in Figures 4.15(b) and 4.15(d), at crystal temperatures of 10 °C and 60 °C respectively. The effect of output coupling was investigated at three laser wavelengths corresponding to the three regimes of lasing in Alexandrite, those distinguished in Section 4.5. The theoretical predictions were computed with (solid lines) and without (dashed lines) pump ESA, to clarify the effect of pump ESA on the laser behaviour.

The experimental thresholds were accurately computed by the model across the parameter range. For example at 727 nm and 60 °C, Figures 4.15(c) and 4.15(d), the

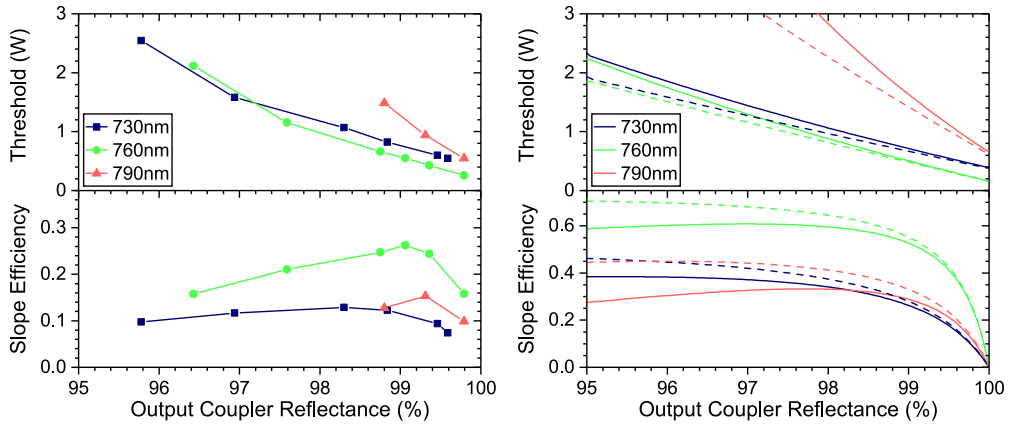

(a) 10 °C Experiment

(b) 10 °C Theory

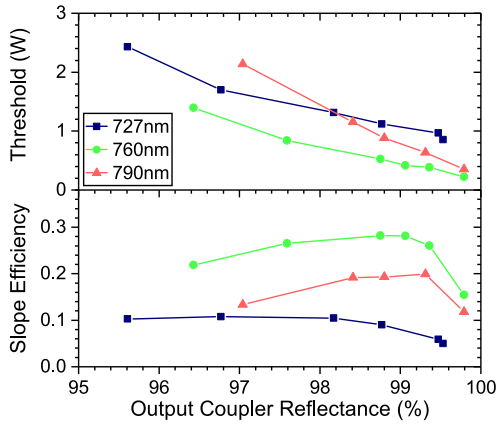

(c) 60 °C Experiment

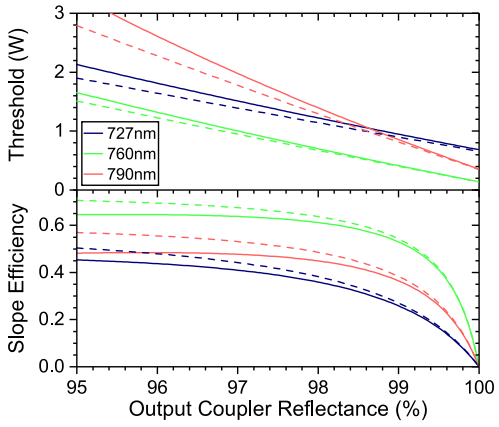

(d) 60 °C Theory

Figure 4.15: Experimental and theoretical data of the thresholds and slope efficiencies of laser operation against output coupler reflectance at different laser wavelengths, with crystal temperatures of 10 °C and 60 °C. In the theoretical plots the solid lines correspond to $\gamma = 0.75$ and the dashed lines to $\gamma = 0$.

thresholds were correctly modelled as being higher than those of the other wavelengths at high OC reflectance, but becoming lower than at 790 nm for reduced reflectances.

The theoretical slope efficiency curves exhibited the same trends as the experimental system. For example, it predicted an intersection between the 730 nm and 790 nm slope efficiency curves at 10 °C, Figure 4.15(b). This is apparent in the experimental data, Figure 4.15(a), where the efficiency is initially higher at 790 nm, but then rapidly decreases. The magnitudes of the theoretical slope efficiencies were in general higher than those of the experimental system. The most likely source of the discrepancy was the mismatch between the spatial profiles of the laser and pump beams, which was not included in the model. This effect would have caused a reduction in efficiency if included.

The modelling predicts that pump ESA causes an approximately quadratic increase in threshold with OC reflectance, Equation (3.26). This is seen throughout the modelling by comparing the thresholds with and without pump ESA in Figures 4.15(b) and 4.15(d) by the solid and dashed lines, respectively. The approximately quadratic relationship is also seen in the experimental data, being particularly clear at 760 nm at 10 °C, Figure 4.15(a). The non-linear thresholds in the experiment can therefore be confidently attributed to pump ESA effects.

The experimental slope efficiencies had an optimum output coupler reflectance for maximum slope efficiency, for example at 99 % OC reflectance with 760 nm and 10 °C in Figure 4.15(a). An optimum reflectance is apparent in the modelling, but only with the inclusion of pump ESA. This is due to a reduction in pump quantum efficiency for decreasing output coupler reflectance, Equation (3.27), with an approximate linear form. The optimum slope efficiency in Alexandrite is therefore highly likely to be from pump ESA effects and has been observed experimentally by others [16, 95].

Pump ESA gives a second order correction to the laser threshold for OC reflectance, whereas for the slope efficiency it is first order in reflectance. It is therefore clearer to determine the accuracy of the pump quantum efficiency expression through comparison of the slope efficiencies, rather than the thresholds. In the experimental measurements, the slope efficiency decreased more quickly by lowering the output coupler reflectance than in the model, being particularly clear at 760 nm and 60 °C, Figures 4.15(c) and 4.15(d). This discrepancy can be explained by a lower pump quantum efficiency in the experimental system compared to the model.

The pump quantum efficiency is reduced when inversion is concentrated in one area due to the non-linear nature of the loss. There are two factors that are most likely to have caused an overestimation of the pump quantum efficiency in the model when compared to experiment. The first is the approximation of constant transverse intensity profiles. The Gaussian profiles in the experimental system had a higher intensity in the centre than the wings and would concentrate the inversion there. The second is the assumption of a non-divergent pump beam. In the experimental laser the 4 mm crystal length was longer than the confocal parameter of the pump beam, so the intensity

varied longitudinally from divergence in addition to the absorption and would have concentrated the inversion towards the beam waist.

Although the pump quantum efficiency of the model appears to not be accurately matched in magnitude, it exhibits the same behaviours with changing laser parameters as the experimental system. The relations found from this analytical model, such as Equations (3.26) and (3.27), give insight into how the various parameters affect laser efficiency and can aid in laser cavity design, with only the sacrifice of accuracy.

If a laser model included transverse spatial variation analytical solutions would not be possible, due to the non-linear nature of the ESA loss. This would require numerical solutions, which would limit insight into the effects of different laser parameters.

4.4.4 Temperature effects on tuning range

Similarly to the pump ESA loss, there has been limited quantitative investigation into the effect of crystal temperature on the tuning range in Alexandrite lasers. It has been experimentally shown that low temperatures favour shorter wavelengths [8] and high temperatures allow longer wavelengths [51]; however, these demonstrations could not quantitatively explain the efficiencies that were achieved. This section presents an analysis of the temperature effects on laser slope efficiency and threshold in an Alexandrite laser across the tuning range, with the experimental trends explained with the use of the analytical laser model of Section 3.3.1.

The laser power versus wavelength is shown in Figure 4.16(a), where the crystal temperature was optimised from between 8 °C and 105 °C to achieve the maximum laser output power at each wavelength. The laser power with wavelength at a fixed crystal temperature of 60 °C is also shown for comparison. The flat portions of the optimum temperature curve correspond to the limits of the TEC equipment.

The laser was tunable from 714 nm to 818 nm, a record lowest wavelength and broadest range for a diode-pumped Alexandrite system. Key to achieving this tuning range was adapting the temperature of the Alexandrite crystal. A wider tuning range and higher output powers at both the upper and lower wavelength limits would have been possible without the 8 °C to 105 °C limit of the equipment used.

The wavelength tuning was continuous up to approximately 10 nm from the extremes, at this point the laser had regions of 5 nm width where it would not lase. It is likely that the crystal birefringence was interfering with the tuning effect of the birefringent element in these areas [98].

The frequency spectrum in Figure 4.16(b) shows the typical spectral structure of the laser output. Multiple longitudinal modes oscillated, separated by 680 MHz, with a resulting FWHM of 2.1 GHz. The spectrum could have been narrowed by using a BiFi with a smaller FSR, this would have given a narrower transmission peak and therefore reduced the spectral width. Alternatively, additional frequency selective elements could have been introduced, for example a Fabry-Perot etalon.

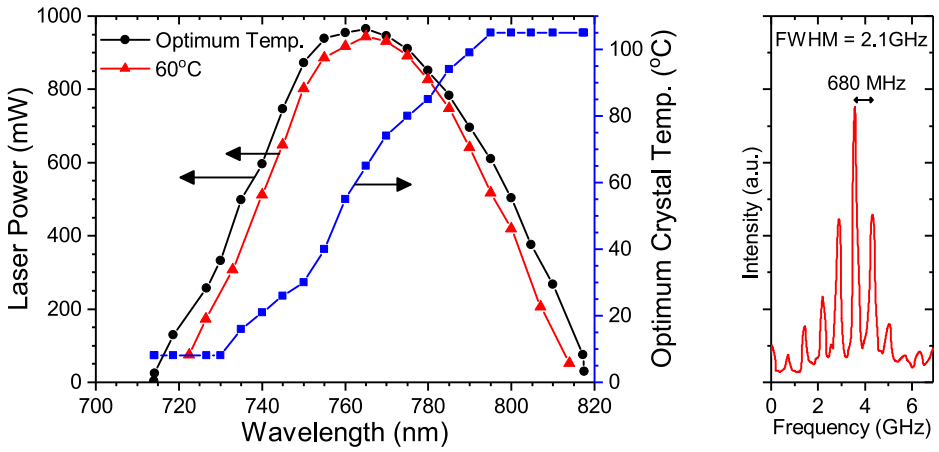

(a) (b)

Figure 4.16: (a) The laser output power versus laser wavelength at the optimum crystal temperature and at a fixed crystal temperature of 60 °C. The optimum crystal temperature is given on the right axis of the graph. (b) The typical output frequency spectrum across the tuning range, FWHM = 2.1 GHz.

The laser could be operated with $M^2 \approx 1$, similarly to without the BiFi. However, approximately 20 % higher output power could be achieved by operating at a lower beam quality with $M_x^2 = 2.3$ and $M_y^2 = 1.5$.

The output laser power is useful in giving an overview of laser performance across the lasing spectrum, but to understand its behaviour more fundamentally the slope efficiency and threshold are more useful measures. The threshold pump powers and slope efficiencies at different crystal temperatures (10 °C, 60 °C, 105 °C) across the output laser spectrum with comparison to model results are shown in Figure 4.17, with both relative to absorbed pump power.

The underlying causes of the output power changes in Figure 4.16 are apparent from Figure 4.17. Towards the edges of the tuning range the thresholds increased and slope efficiencies decreased, resulting in the reduced output power, but responded oppositely to the crystal temperature at each end. The experimental results were a close fit to the theoretical predictions for the thresholds showing the validity of the model. The slope efficiencies had similar trends in experiment and modelling, but were less accurately matched. This is likely due to mode matching efficiency not being included in the modelling.

The optimum output power for the extended cavity was at a wavelength of 765 nm, see Figure 4.16; however, when operated with no BiFi control the laser wavelength was 760 nm at 60 °C. The cause of this seeming discrepancy is that the wavelengths for the lowest threshold and highest slope efficiency were not coincident. The free running laser operated at its lowest threshold wavelength of 760 nm, and the lowest threshold of the BiFi tuned laser was also at approximately 760 nm, see Figure 4.17. However, the optimum power output was achieved at the longer wavelength of 765 nm, closer to

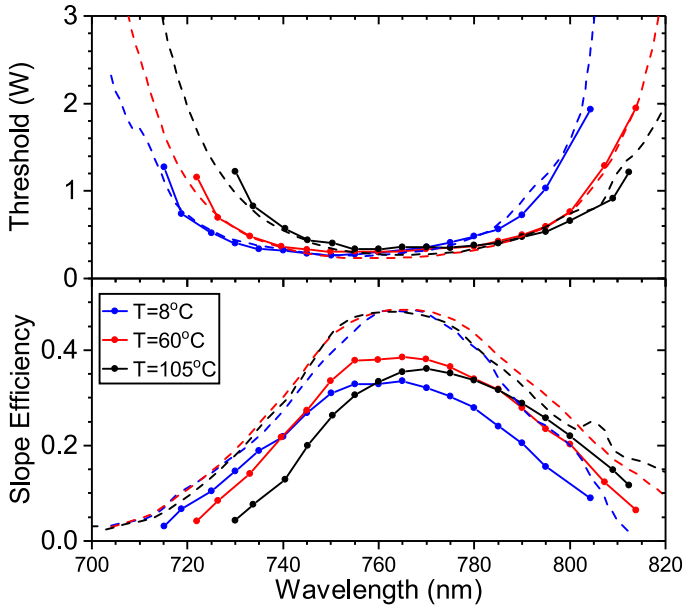

Figure 4.17: The threshold (top) and slope efficiency (bottom) of the laser at 10 °C, 60 °C and 105 °C crystal temperatures against laser output wavelength.

where the slope efficiency was highest at 770 nm.

The mismatch of lowest threshold and maximum slope efficiency is explained in Section 4.5, and is due to the different spectral forms of the laser emission and ESA cross sections. This behaviour suggests that in general Alexandrite lasers can benefit from a wavelength selective element to optimise power output by forcing it to lase at a higher threshold, but where it also has a larger slope efficiency. The significance of this effect will increase when operating at pump powers further away from threshold.

4.5 Modelling Alexandrite lasers

The experimental systems showed complicated behaviour across the wavelength tuning range, particularly with regard to the crystal temperature. This is the result of a complex interplay of factors and is best explained through interrogation of a model, where parameters not readily accessible in experiments can be isolated to explain different features in the experiment.

The dependence of the transition cross sections on laser wavelength gives Alexandrite three regimes of operation as indicated in Figure 4.18. Below 760 nm it is an increasingly quasi-three-level system with additional increasing laser ESA. Above 760 nm the laser GSA cross section becomes negligible, so from 760 nm to 780 nm it is approximately a four-level laser with the ESA cross section becoming zero at 770 nm. Above 780 nm the lasing is four-level, with an increasing influence of ESA at longer wavelengths. At 828 nm and a crystal temperature of 28 °C the laser ESA and emission cross sections are equal and no gain is possible, forming an upper wavelength limit. The boundaries between

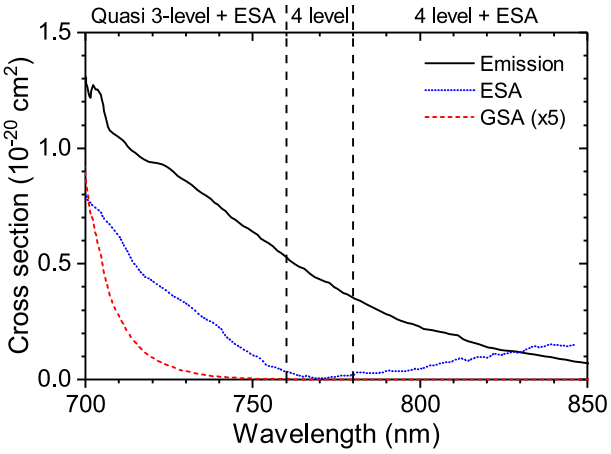

Figure 4.18: The laser GSA, ESA and emission cross sections with wavelength at 28 °C. The GSA cross section has been magnified by a factor of 5. The three regimes of operation are indicated. Source data: [18]

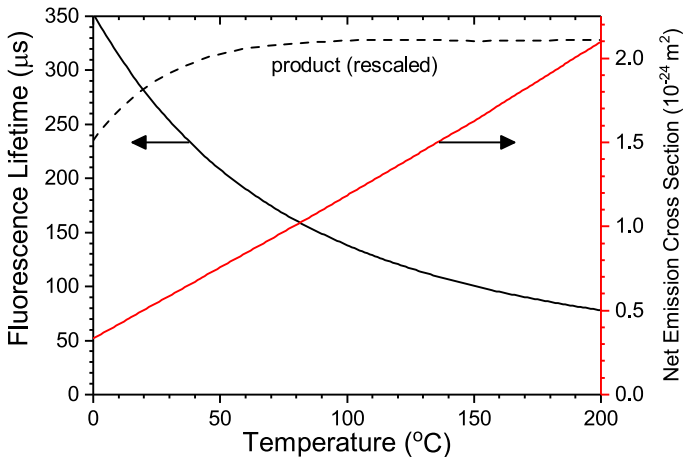

Figure 4.19: The fluorescence lifetime (black), net emission cross section ($\sigma_e - \sigma_{1a}$) at 760 nm (red), and their rescaled product in arbitrary units (dashed) against crystal temperature in Alexandrite. Source data: [8, 72]

the lasing regimes are not well defined and are presented as a guide to understanding the behaviour of Alexandrite.

Another consideration in Alexandrite is the crystal temperature, which further affects the lasing regimes. The effect of crystal temperature on the fluorescence lifetime and emission cross section is shown in Figure 4.19. The dominant cause of temperature related effects in Alexandrite is the upper laser level being split between two sub-levels. These have an effective separation of approximately 800 cm^{-1} so have a thermal Boltzmann population distribution between them [8]. The upper sub-level ($^4T_2$) has stronger vibronic transitions, with the lower sub-level (^2E) being mostly inactive and acting as a storage state. The different properties of the two levels and thermal population distribution between them results in the decreasing fluorescence lifetime and increasing emission cross section with temperature.

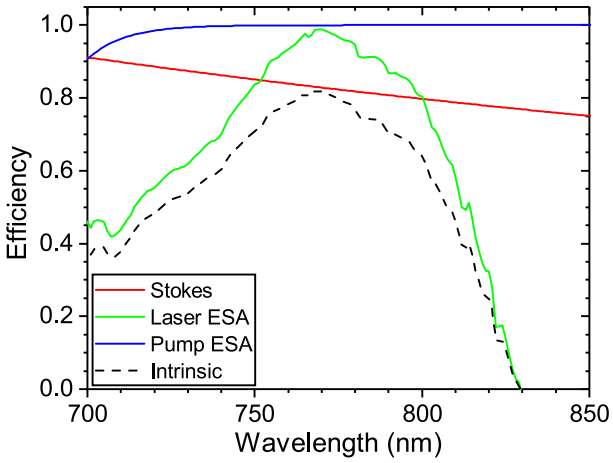

Figure 4.20: The intrinsic slope efficiency of Alexandrite at 28 °C for red diode pumping at 636 nm, with the constituent contributions from the Stokes, laser ESA and pump ESA efficiencies.

The intrinsic slope efficiency η_0 (Equation 3.25) is a useful guide to the ultimate performance of a gain medium that can be expected, and it is shown for Alexandrite as a function of wavelength in Figure 4.20 along with its constituent components for red diode pumping at 636 nm and 28 °C crystal temperature. In Alexandrite, $\eta_{p,0} = 1$ because all absorbed pump photons from GSA decay into the upper laser level [8]. The peak intrinsic efficiency of 82 % is at 770 nm, where the limiting factor is the Stokes efficiency. An efficiency of near or greater than 40 % is available from 700 nm to 815 nm, illustrating the suitability of Alexandrite as a tunable source.

The main factor reducing the intrinsic efficiency is laser ESA from $(1 - \gamma_l)$; however, its effect is minimised at 770 nm where there is negligible laser ESA [18]. At either side of this peak the efficiency decreases due to the increasing laser ESA cross section, but occurs at a higher rate towards longer wavelengths where the emission cross section is decreasing. There is an intersection point between the emission and ESA cross sections at 830 nm. At this point no gain is possible and the efficiency becomes zero.

The intrinsic slope efficiency is a function of temperature due to the temperature dependence of all cross sections in Alexandrite. The dominant effect is from laser ESA in the output coupling efficiency, which is shown against laser wavelength at different crystal temperatures in Figure 4.21. There is a shift in the intersection point of the laser emission and ESA cross sections, which increases the long wavelength lasing limit. It is difficult to minimise the effect of laser ESA as it is isolated in the efficiency terms and only a factor of material properties.

In the intrinsic slope efficiency the pump ESA component is only significant below 720 nm where laser GSA is largest; however, in a real laser non-zero cavity losses means the pump ESA needs to be more carefully considered. The pump quantum efficiency is shown in Figure 4.22 as a function of wavelength with nominal laser cavity parameters of $R = 0.98$ and $L = 0.01$ to illustrate its behaviour in a realistic laser at different

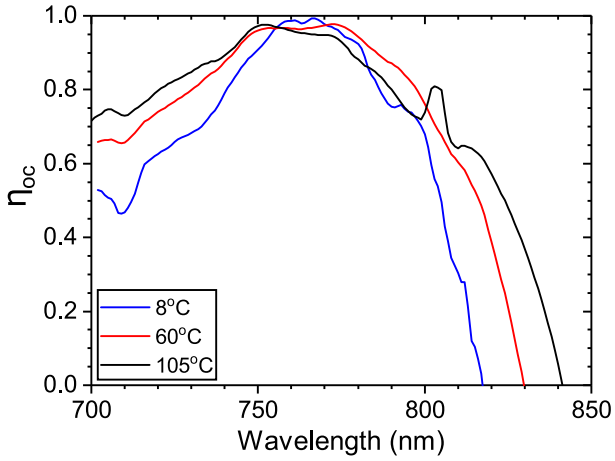

Figure 4.21: The maximum output coupling efficiency $(1 - \gamma_l)$ versus laser wavelength at different crystal temperatures.

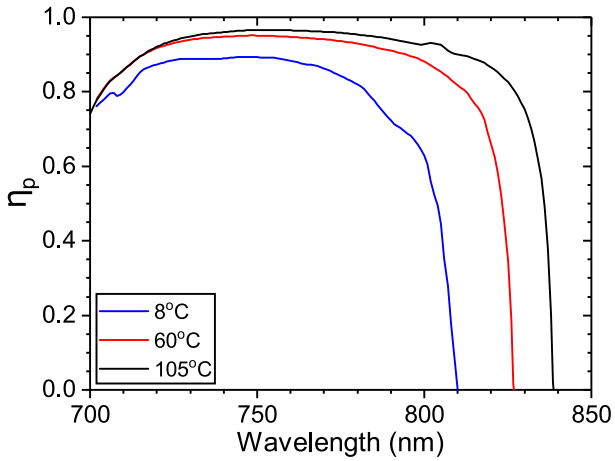

Figure 4.22: The pump ESA quantum efficiency versus laser wavelength for different crystal temperatures for $R = 0.98$ and $L = 0.01$. In Alexandrite $\eta_p = \eta_{p,ESA}$.

temperatures. As $\eta_{p,0} = 1$ in Alexandrite, only pump ESA contributes to the pump quantum efficiency and $\eta_p = \eta_{p,ESA}$.

To understand the form of the pump quantum efficiency across the tuning range, it is important to note that the pump ESA quantum efficiency decreases for increasing integrated population inversion F, see Equation (3.21). Where there is a higher net gain coefficient $(\sigma_e - \sigma_{1a})$ there will be a lower threshold inversion and a correspondingly higher pump quantum efficiency. The efficiency is maximised in the region near 750 nm, the peak net gain in Alexandrite. Towards shorter and longer wavelengths the net gain decreases giving a lower efficiency, but decreases at a much greater rate towards long wavelengths where the net gain reduces to zero. This point of zero net gain occurs at longer laser wavelengths for increasing crystal temperatures, as clearly seen in Figure 4.22.

The effect of pump ESA is less constraining than that of laser ESA because it depends

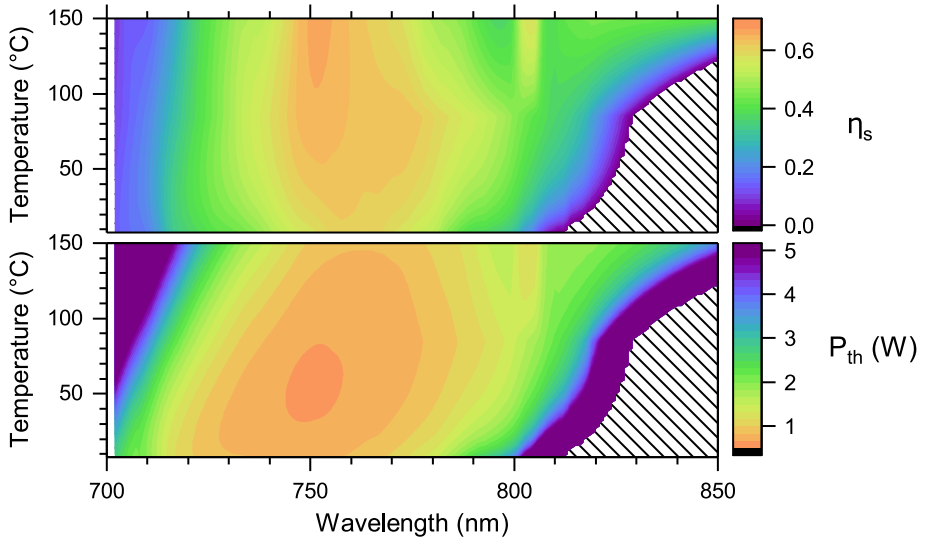

Figure 4.23: From the model in Equations (3.15-3.21), the slope efficiency (top, η_s) and threshold (bottom, P_{th}) of an Alexandrite laser with output coupler $R = 98\,\%$ and round trip loss $L = 0.5\,\%$, versus laser wavelength and crystal temperature. The hatched regions are where lasing is not possible due to zero net gain.

on the inversion level, which can be controlled to some extent by the cavity design parameters of L and R.

With an understanding of the underlying processes in Alexandrite lasing, the combination of them in a CW laser can be analysed. The medium was modelled using the pump ESA ratio measured in Figure 3.16 and all other parameters were taken from the literature. The cavity parameters were $R = 98\,\%$, $L = 0.5\,\%$, $l = 4\,\text{mm}$, and a circular pumped area diameter of $180\,\mu\text{m}$, similar to the experimental cavity in Section 4.4. The threshold and slope efficiency against laser wavelength and crystal temperature are shown in Figure 4.23 for this system.

Between 750 nm to 770 nm temperature has the least effect on both the threshold and slope efficiency, which is the region of four-level lasing where the effects of laser GSA, and pump and laser ESA are minimised. The product of the fluorescence lifetime and the emission cross section is the dominant temperature dependent factor in the laser threshold, via I_s in Equation (3.15), but as this product is approximately constant with temperature so is the threshold, see Figure 4.19.

Below 750 nm laser GSA becomes increasingly significant, with both shorter wavelengths and higher crystal temperatures increasing the laser GSA, which is the limiting factor for short wavelength lasing. A higher GSA requires more inversion for gain and increases the threshold. This means that colder crystal temperatures are optimum for short wavelength lasing. Shorter crystals are also preferential for short wavelength operation because unpumped population will increase the laser threshold, see the $2\alpha_a l$ loss term in Equation (3.12). There is a negligible impact of temperature on the slope efficiency, mainly due to the pump quantum efficiency being typically invariant with

temperature in this region, see Figure 4.22.

Above 770 nm laser GSA no longer has any effect and laser ESA is the cause of the temperature and wavelength dependent behaviour. Laser ESA creates a point of zero net gain at increasingly longer wavelengths for higher crystal temperatures. Higher temperatures are favoured in this wavelength region to maximise the available gain. This both reduces the threshold and makes certain wavelengths accessible by moving the point of zero net gain. The efficiency increases with temperature because the laser ESA efficiency $(1 - \gamma_l)$ increases (Figure 4.21) along with the pump quantum efficiency significantly improving (Figure 4.22). This is due to the higher emission cross section, hence a larger gain, that reduces the threshold population inversion. This behaviour will be common to all Alexandrite lasers due to the intrinsic nature of the laser ESA to Alexandrite.

4.6 Summary

This chapter has presented results from experimental fibre-delivered diode end-pumped Alexandrite lasers. Through optimising the crystal temperature and cavity losses, a record slope efficiency was obtained of 54 % with a power of 1.22 W in the HG_{00} mode.

Fibre-delivered pumping can achieve these high efficiencies with respect to absorbed pump power and excellent beam qualities due to the symmetry and brightness of the source. A drawback of this technique is that only a fraction of the overall pump power can be absorbed in one pass of the crystal, because absorption is polarised in Alexandrite and the fibre delivery scrambles the polarisation of the pump. It was shown that by retro-reflecting and rotating the polarisation of the transmitted pump, the power output of a laser with fibre delivered pumping could be increased by 58 %.

A tunable Alexandrite laser was developed, which achieved a record laser wavelength tuning range of 714 nm to 818 nm. Key to this achievement was shown to be through optimising the crystal temperature between 10 °C to 105 °C, with a greater wavelength range expected if the temperature range could have been increased.

The best laser performance was obtained from the compact cavity in terms of threshold pump power, slope efficiency, and output power. The highest slope efficiencies achieved in the compact and extended cavities were 54 % and 40 %, respectively. The reduced efficiency in the extended cavity was a combination of increased losses from additional intracavity optical components and a likely poorer match between the pump and laser modes.

With the tunable Alexandrite laser as an experimental reference, the analytical model was analysed to verify its accuracy. It was found to have an excellent fit with respect to laser threshold, with the slope efficiency matching the trends of the experimental system, but with an offset likely caused by the lack of a mode overlap efficiency term in the model. With the model shown to be valid in Alexandrite, it was explored to show

the effects of laser and pump ESA across its tuning range. This highlighted the importance of crystal temperature in Alexandrite laser design, with low temperatures suitable for short wavelength lasing, and high temperatures extending the range and improving performance in the longer wavelength regime.

Chapter 5

Anti-resonant ring lasers

The anti-resonant ring (ARR), also known as a Sagnac interferometer, is an interferometric device that acts like a mirror and reflects any input field, its structure is shown in Figure 5.1(a). Input fields are split by a 50 % beamsplitter (BS), propagate in opposite directions around the ring formed by turning mirrors (M), and recombine at the BS. Due to phase changes at the BS they constructively interfere towards the input direction so are reflected.

The reflection and transmission of the ARR can be altered for a wide variety of uses by modifying the alignment or reflectances of the ring structure, or by additional optical components inside the ring. In this chapter the focus is on including a gain medium inside the ARR and forming a laser cavity, as in Figure 5.1(b), by providing feedback into the ARR with a partially reflecting output coupler (OC). This geometry was first proposed by Siegman in 1973 [37], but has only been demonstrated once before in the literature in a CO_2 laser [36]. This configuration has many interesting applications through sharing a gain medium between two laser cavities.

Before applying the ARR to coupled laser geometries, the basic laser cavity of Figure 5.1(b) must first be understood. In this chapter there is an overview of the properties of the ARR, both exploring the mechanism of total reflection but also the parameters that can negatively affect it. The ARR laser geometry is then experimentally investigated using the Nd:YVO_4 gain medium in both the diode end and side-pumping configurations. This gain medium was selected due to it being a simple, high-performance four-level system that is commonly used, in contrast to Alexandrite. This allowed the focus to be maintained on the ARR laser geometry design without complications from the gain medium. Using the end-pumped solid-state gain medium the losses were reduced by a factor of twenty compared to the CO_2 laser, which for the first time demonstrates the ARR laser to be a high-performance cavity geometry.

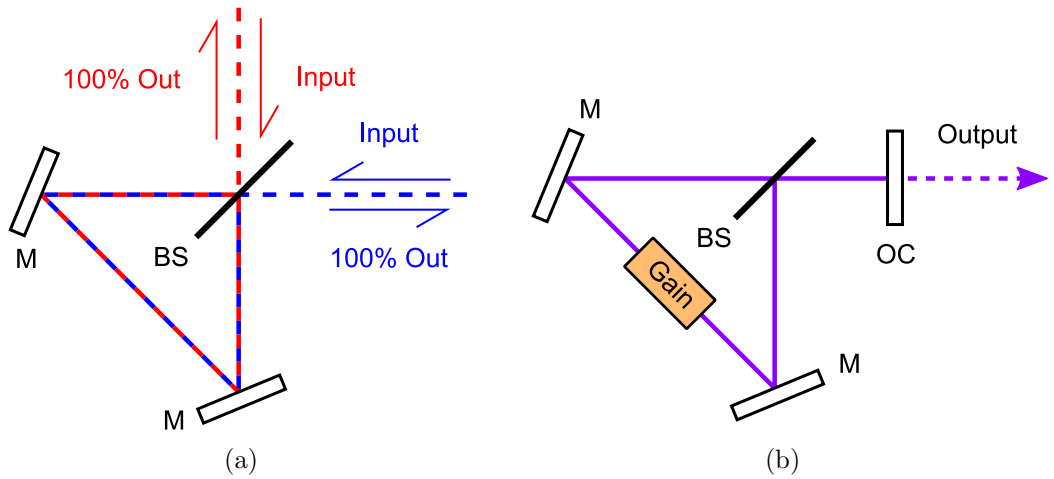

Figure 5.1: (a) The anti-resonant ring geometry, where the input beams are split by the 50 % beamsplitter (BS), which propagate around the ring formed by turning mirrors (M) and recombine at the BS. (b) The ARR laser cavity concept, with feedback provided by an output coupler (OC) and a gain medium is internal to the ring.

5.1 Background

The ARR has many uses, ranging from an optical gyroscope exploiting the Sagnac effect [108], a proposed gravitational-wave detector [109], and inverting interferometers [110]. It was first proposed for use in a laser geometry by Siegman in 1973 [37], who conducted the earliest investigations of the design.

The most common use of the ARR has been in colliding pulse mode locking, where a saturable absorber is placed inside the ARR [111]. This technique enhances the saturation effects in the absorber leading to more easily obtainable modelocking [112, 113].

Mode locking has also been implemented with an ARR by inserting a non-linear element into the ring, which made the ARR act as a non-linear mirror [114]. This implementation is similar to the non-linear amplifying loop mirror (NALM) used extensively for mode locking in fibre lasers, which uses the fibre equivalent of the free-space ARR - the Sagnac loop.

The ARR has been used as an adjustable transmission output coupler for an optical parametric oscillator (OPO), where the angle of incidence on the beamsplitter was continuously adjusted to optimise the parametric conversion process [115].

The sharing of an ARR has been demonstrated with two OPOs using it as an end mirror [116]. In this implementation, each cavity used a separate input direction to the ARR, as shown in Figure 5.1(a). This was possible due to the wavelength insensitivity of the ARR, where the reflectance is independent of the input wavelength.

The only example of the laser gain medium being internal to the ARR, as in Figure 5.1(b), was in a CO_2 cavity-dumped laser [36]. This design also incorporated an electro-optic modulator in the ARR to modulate the phase of the counter-propagating beams and generate a pulsed output from the laser. Although successful, the incorpo-

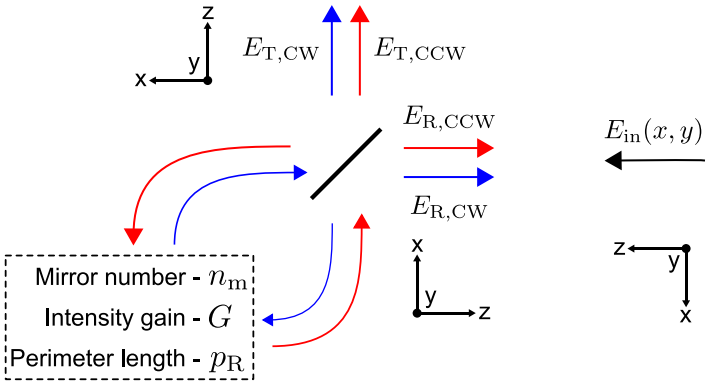

Figure 5.2: A diagram indicating the notation used for a general ARR.

ration of the electro-optic modulator, in particular, caused round trip losses of 1.5 % in the ARR.

These prior works show the suitability of an ARR in a laser cavity, along with the gain component being internal it it. These examples are also the main extent of ARR implementations in laser cavities, which highlights the opportunity to find new applications with this structure.

5.2 Anti-resonant ring properties

To understand the reflection and transmission properties of the ARR the propagation of input electric fields must be calculated. The input field, E_{in}, and the corresponding intensity, I_{in}, considered are

$$E_{\mathrm{in}} = \mathbb{R}\left[\widetilde{u}(x,y)e^{i(kz-\omega t)}\right] , \tag{5.1}$$

$$I_{\mathrm{in}} = \frac{1}{2Z_0}\left|\widetilde{u}(x,y)\right|^2 , \tag{5.2}$$

where $\widetilde{u}(x,y)$ is an arbitrary complex field distribution, k is the wavenumber of the field, ω is the frequency, t is time, and Z_0 is the impedance of free space. The input direction and axes orientation are shown in Figure 5.2. In the following derivations the electric fields will be assumed to be the real part of the complex numbers.

On entering the ring, the input field is split by a lossless beamsplitter (BS) that has intensity transmission (T) and reflection (R) coefficients such that $T + R = 1$. The clockwise (CW) and counter-clockwise (CCW) beams propagate around a ring that has n_{m} mirrors, perimeter length p_{R}, and intensity gain coefficient of G. The resultant beams are then again split by the BS with CW and CCW transmitted ($\widetilde{u}_{\mathrm{T,CW}}$, $\widetilde{u}_{\mathrm{T,CCW}}$) and reflected ($\widetilde{u}_{\mathrm{R,CW}}$, $\widetilde{u}_{\mathrm{R,CCW}}$) complex coefficients. The ring is aligned so the axes of each pair of beams are collinear. A reflection from a mirror or BS inverts the x-axis to preserve a right-handed system, with the final axes orientation shown in Figure 5.2. Considering all the above effects and defining $z = 0$ at the entrance to the ring, the

resultant fields are

$$\widetilde{u}_{\mathrm{R,CW}} = -\sqrt{GRT}\,\widetilde{u}\left[(-1)^{(n_{\mathrm{m}}+1)}x, y\right] , \tag{5.3}$$

$$\widetilde{u}_{\mathrm{R,CCW}} = -\sqrt{GRT}\,\widetilde{u}\left[(-1)^{(n_{\mathrm{m}}+1)}x, y\right] , \tag{5.4}$$

$$\widetilde{u}_{\mathrm{T,CW}} = -R\sqrt{G}\,\widetilde{u}\left[(-1)^{n_{\mathrm{m}}}x, y\right] , \tag{5.5}$$

$$\widetilde{u}_{\mathrm{T,CCW}} = T\sqrt{G}\,\widetilde{u}\left[(-1)^{n_{\mathrm{m}}}x, y\right] , \tag{5.6}$$

where the π phase shift from the BS is represented as a negative sign [117].

The total transmitted field is given by $\widetilde{u}_{\mathrm{T}} = \widetilde{u}_{\mathrm{T,CW}} + \widetilde{u}_{\mathrm{T,CCW}}$ and reflected field by $\widetilde{u}_{\mathrm{R}} = \widetilde{u}_{\mathrm{R,CW}} + \widetilde{u}_{\mathrm{R,CCW}}$. By introducing a parameter δ that defines the difference from 50 % BS reflectance, such that $R = (0.5 - \delta)$ and $T = (0.5 + \delta)$, the resulting fields are

$$\widetilde{u}_{\mathrm{R}}(x, y) = -\sqrt{1 - 4\delta^2}\sqrt{G}\,\widetilde{u}\left[(-1)^{(n_{\mathrm{m}}+1)}x, y\right] , \tag{5.7}$$

$$\widetilde{u}_{\mathrm{T}}(x, y) = 2\delta\sqrt{G}\,\widetilde{u}[(-1)^{n_{\mathrm{m}}}x, y] . \tag{5.8}$$

The corresponding reflected and transmitted field intensities (I_{R}, I_{T}) are

$$I_{\mathrm{R}}(x, y) = I_{\mathrm{in}}\left[(-1)^{(n_{\mathrm{m}}+1)}x, y\right] G\left(1 - 4\delta^2\right) , \tag{5.9}$$

$$I_{\mathrm{T}}(x, y) = I_{\mathrm{in}}\left[(-1)^{n_{\mathrm{m}}}x, y\right] G\left(4\delta^2\right) . \tag{5.10}$$

For simplicity, if plane waves are assumed the total intensity reflection ($R_{\mathrm{ARR}} = I_{\mathrm{R}}/I_{\mathrm{in}}$) and transmission ($T_{\mathrm{ARR}} = I_{\mathrm{T}}/I_{\mathrm{in}}$) coefficients of the ARR are then

$$R_{\mathrm{ARR}} = G\left(1 - 4\delta^2\right) , \tag{5.11}$$

$$T_{\mathrm{ARR}} = 4G\delta^2 . \tag{5.12}$$

With Equations (5.7-5.12) the properties of the ARR can be analysed.

The ARR reflects all incoming power when the BS has 50 % reflectance, $\delta = 0$ when $T_{\mathrm{ARR}} = 0$. A perfect 50 % BS coating is in practice impossible to achieve, so the difference from this design reflectance will always give some transmission to an ARR. A BS tolerance of $\delta = 0.01$ is not difficult to achieve in practice. In an ARR with no gain ($G = 1$) this would result in $T_{\mathrm{ARR}} = 0.04\,\%$, which would be a negligible loss in most laser systems, so this source of asymmetry loss will usually be insignificant in practice.

The dependence of T_{ARR} on the BS reflectance can be used advantageously by using the ARR as a continuously tunable transmission output coupler. This has been demonstrated by changing the BS reflectance through altering the angle of incidence [115].

The conversion to intensity reflection and transmission coefficients for the ARR also shows that an aligned ARR works at all wavelengths, with there being no wavelength term in R_{ARR} or T_{ARR}. The wavelength of the incident beam will only alter the phase of the exiting beams through k in Equation (5.1), but the intensity is unaffected. This

property is due to the common path of the interferometer, where the CW and CCW travelling beams have the same phase shift when propagating around the ring.

The wavelength invariance of the ARR is in contrast to the usual use of interferometric components in laser cavities, where it is the wavelength selectivity that is the desired property. The standard linear Fabry-Perot or ring cavities are themselves interferometers, which results in the longitudinal frequency mode selection of these geometries. Alternative interferometric cavity designs [118] or additional Fabry-Perot cavities [119] can be used for more precise frequency selection.

A more subtle feature of the ARR is the potential for horizontal reflection astigmatism. The input field can have an arbitrary field distribution $\widetilde{u}(x, y)$, see Equation (5.7). The reflected field has the distribution $\widetilde{u}\left[(-1)^{(n_\mathrm{m}+1)}x, y\right]$, Equation (5.7), where the $(-1)^{(n_\mathrm{m}+1)}$ term shows that the reflected field will be horizontally inverted for an even number of ARR mirrors.

It should be noted that in the previous analyses it was assumed that there were no time dependent phase or amplitude changes for the counter propagating fields in the ring. If there were, then the recombining fields would have asymmetries from this time dependent change that would alter the transmission and reflection properties. As the ARR has a common path design, these will only be significant when the time dependent changes are on the time-scale of the transit time of a beam around the perimeter. For a ring perimeter below one meter, this corresponds to changes with frequency components of GHz and above.

As environmental changes are typically below GHz rates, this is the reason why the ARR is insensitive to environmental perturbations. The time dependence property of the ARR can be exploited by incorporating optical elements that can effect changes on this time scale. For example, an electro-optic modular with a 3 ns rise time has been used for laser cavity dumping from an ARR [36].

If the ARR contains components that alter the wavefront of the CW and CCW propagating beams, for example lenses or diffraction from apertures [36], this can cause more transmission through the ARR due to differently phased or shaped beams incident on the BS. The case of asymmetric beam imaging was considered by Sheng [120], who theoretically analysed the cavity mode solutions in a cavity similar to the ARR laser geometry of Figure 5.1(b).

The round trip ABCD matrix of the ARR, M_R, is

$$M_\mathrm{R} = \begin{pmatrix} A_\mathrm{R} \pm \Delta & B_\mathrm{R} \\ C_\mathrm{R} & A_\mathrm{R} \mp \Delta \end{pmatrix}, \tag{5.13}$$

where the $\pm$ and $\mp$ signs refer to either CW $(+, -)$ or CCW $(-, +)$ propagation, and Δ is a measure of asymmetry in the round trip matrices. The transmission of the ARR

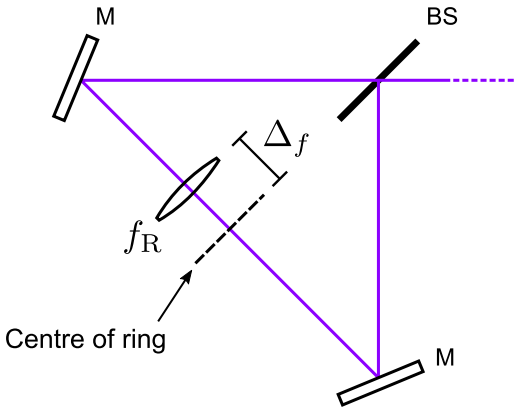

Figure 5.3: The ring section of an ARR laser with a thermal lens (f_{R}) offset from the centre of the perimeter by Δ_f.

is then given by ζ_m, where m is the mode order of the HG_{m0} mode. The solution gives

$$\zeta_0 \approx \tfrac{1}{2}\Delta^2, \quad \zeta_1 \approx 3\zeta_0, \quad \zeta_2 \approx 7\zeta_0, \quad \zeta_3 \approx 13\zeta_0\,, \tag{5.14}$$

which shows that if there is no asymmetry ($\Delta = 0$) then there will be no transmission of the ARR, as expected. It also predicts that higher order transverse modes will have a larger transmission through the ARR, which could act to suppress them. Another finding of the model was that the transmission was spatially dependent, typically with a ring shaped pattern. Despite this, the transverse modes were approximately equal to the Hermite-Gaussian set [120].

The derivation by Sheng can be applied to the ARR laser proposed in Figure 5.1(b), where a thermal lens in the crystal will be inside the ring. This geometry is shown in Figure 5.3, where a thermal lens of focal length f_{R} is offset from the centre of the ring perimeter of length p_{R} by a distance Δ_f. The ray transfer matrix of this path is

$$M_{\mathrm{R}} = \begin{bmatrix} 1 - \frac{p_{\mathrm{R}}}{2f_{\mathrm{R}}} \pm \frac{\Delta_f}{f_{\mathrm{R}}} & p_{\mathrm{R}} - \frac{(p_{\mathrm{R}} - 4\Delta_f^2)}{4f_{\mathrm{R}}} \\ \frac{-1}{f_{\mathrm{R}}} & 1 - \frac{p_{\mathrm{R}}}{2f_{\mathrm{R}}} \mp \frac{\Delta_f}{f_{\mathrm{R}}} \end{bmatrix}, \tag{5.15}$$

where the upper and lower signs are for the CW and CCW paths, respectively. This matrix fits the form of Equation (5.13) with $\Delta = \Delta_f / f_{\mathrm{R}}$, giving an ARR transmission of

$$\zeta_0 = \frac{1}{2}\left(\frac{\Delta_f}{f_{\mathrm{R}}}\right)^2. \tag{5.16}$$

This result is useful in ARR laser design, as it predicts that the transmission loss of the ARR from this form of asymmetry is independent of the perimeter of the ARR and that the position tolerance of the thermal lens in the ring will be lower for a stronger thermal lens.

Another source of transmission through the ARR is from misalignment of the intracavity components, which has two consequences. The first is a position mismatch

of the CW and CCW beams from the BS, where one field is displaced from the other, which is termed a shear. If the beams have transverse amplitude or phase modulation through $\widetilde{u}(x,y)$ then a shear will cause an amplitude and phase mismatch across the recombining fields. Any resulting field difference will result in transmission through the ARR. This effect is difficult to quantify in general as it depends on the specific form of $\widetilde{u}(x,y)$, which will change depending on quantities such as HG mode order or wavefront curvature.

The second consequence is angular misalignment of the CW and CCW beams, which introduces a linear phase difference between them. If the resulting misalignment is assumed to be in the x-z plane, with each beam misaligned by an angle α that is equal and opposite for the CW and CCW beams. The combining fields become

$$\widetilde{u}'_{\mathrm{R,CW}} = e^{i\theta x}\widetilde{u}_{\mathrm{R,CW}}\,, \tag{5.17}$$

$$\widetilde{u}'_{\mathrm{R,CCW}} = e^{-i\theta x}\widetilde{u}_{\mathrm{R,CCW}}\,, \tag{5.18}$$

$$\widetilde{u}'_{\mathrm{T,CW}} = e^{-i\theta x}\widetilde{u}_{\mathrm{T,CW}}\,, \tag{5.19}$$

$$\widetilde{u}'_{\mathrm{T,CCW}} = e^{i\theta x}\widetilde{u}_{\mathrm{T,CCW}}\,, \tag{5.20}$$

where $\theta = k\tan\alpha$ is the linear phase shift gradient and the primed fields are the tilted counterparts of those in Equations (5.3-5.6). This gives the resulting reflected and transmitted fields

$$I'_{\mathrm{R}}(x,y) = I_{\mathrm{in}}\left[(-1)^{(n_{\mathrm{m}}+1)}x, y\right] G\left(1-4\delta^2\right)\cos^2(\theta x)\,, \tag{5.21}$$

$$I'_{\mathrm{T}}(x,y) = I_{\mathrm{in}}\left[(-1)^{n_{\mathrm{m}}}x, y\right] G\left[\sin^2(\theta x) + 4\delta^2\cos^2(\theta x)\right]\,, \tag{5.22}$$

with the reflection (R'_{ARR}) and transmission (T'_{ARR}) coefficients for plane waves of

$$R'_{\mathrm{ARR}} = G\cos^2(\theta x)\left(1-4\delta^2\right)\,, \tag{5.23}$$

$$T'_{\mathrm{ARR}} = G\left[\sin^2(\theta x) + 4\delta^2\cos^2(\theta x)\right]\,. \tag{5.24}$$

These relations show the characteristic fringe pattern from tilted interfering plane waves, which can be used to aid alignment of the ARR. As is the case for shear misalignment, the sensitivity to this type of misalignment depends on the transverse profile of the incident beam so it is difficult to quantify the transmission or reflection properties in general.

The combined effects of shear and angular misalignment of the ARR, along with asymmetric beam imaging, is a complex problem. It requires numerical simulation in most cases to find the spatial form of and total transmitted intensity. However, the key difference with the ARR common path interferometer design is the insensitivity to path length or other phase changes around the ring, which makes it robust against environmental factors. This is in contrast to other interferometric designs, for example

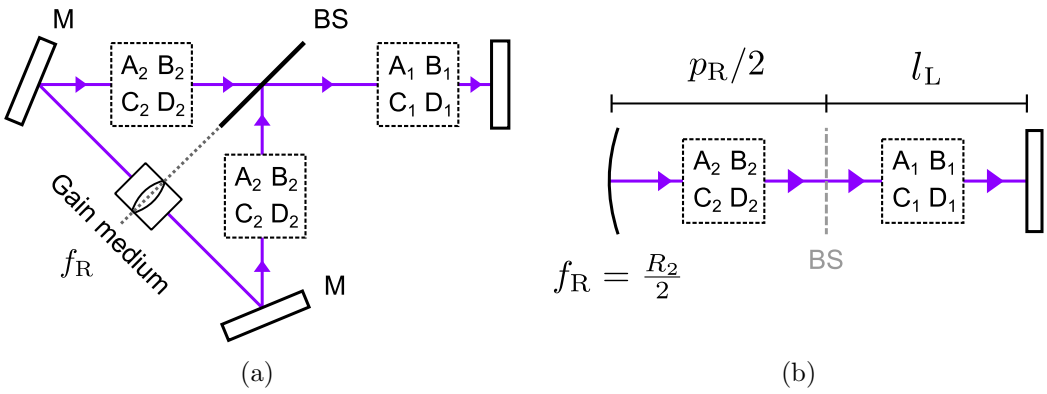

Figure 5.4: (a) The schematic of an ARR laser cavity with gain internal to the ring, which has a thermal lens of focal length f_{R}. (b) The equivalent linear cavity of the ARR laser design, where the thermal lens is a curved end mirror with a radius of curvature of R_2.

the Michelson interferometer, where careful stabilisation of the path lengths is required.

5.2.1 Laser Cavity Design

In the following section some of the design considerations for an ARR laser as in Figure 5.4 are determined. This includes spatial mode control, the mode frequencies, and a method to determine the transmission of the ARR.

A key consideration in laser cavity design is controlling the size of the intracavity modes, which is usually focussed on matching the mode diameter to that of the pumped region of the gain. In an ARR laser the same requirements must be met, so there needs to be a model of how the spatial modes of a cavity form in such a laser.

In this work the focus is on ARR lasers with the gain medium internal to the ring. A pumped gain medium will have a lensing effect on a wavefront due to heating from the absorbed pump radiation, see Section 2.2.1. Previous works have shown that asymmetric imaging of a beam will result in losses from the ARR at the BS [120], so to minimise this the gain medium should be positioned halfway around the ring perimeter p_{R}, see Figure 5.4. In a symmetrically designed ring this will be in line with the BS.

The laser cavity may need additional optical components to control the mode sizes. If these are placed inside the ring, they should be ordered and positioned symmetrically to reduce losses, as represented by the $A_2B_2C_2D_2$ matrices in Figure 5.4. Any other imaging optics, $A_1B_1C_1D_1$, can be external to the ring.

With the ARR laser designed as in Figure 5.4(a), the laser modes can be calculated using the equivalent linear cavity of Figure 5.4(b). The symmetrical ring is considered as a double pass of the equivalent linear section of length $p_{\mathrm{R}}/2$. The thermal lens in the crystal of focal length f_{R} has the same effect as a curved end mirror with a radius of curvature of $R_2 = 2f_{\mathrm{R}}$, which has equal focal power. The linear section of the ARR laser of length l_{L} remains unchanged.

The analogy to a linear cavity extends to the longitudinal modes. The longitudinal

mode frequency spacing, $\Delta\nu = (\nu_{nm(q+1)} - \nu_{nmq})$, of an ARR laser cavity is

$$\Delta\nu = \frac{c}{2(p_{\mathrm{R}}/2 + l_{\mathrm{L}})}\,, \tag{5.25}$$

where c is the speed of light in the cavity [121]. This is equivalent to that of a linear cavity of length $(p_{\mathrm{R}}/2 + l_{\mathrm{L}})$.

The model of the linear cavity equivalent of the ARR laser cavity is a conceptually useful one; however, care must be taken that the horizontal astigmatism of odd mirror ARRs will not affect the desired modes. In a typical linear cavity the end mirrors invert the horizontal axis of the incident mode, which has no significant consequences as the mode is inverted at each end of the cavity so any inversion effects are cancelled out in the round trip. However, an ARR acting as an end mirror will not invert the horizontal axis of an incident beam if it has an odd number of mirrors. This will result in the horizontally odd transverse modes to be inverted on one round trip of the cavity, which means that an additional π phase shift is required for the mode to reproduce itself. The extra phase shift is quantified as $\pi\epsilon_n$ and is an additional term on the left hand side of the round trip phase condition in Equation (2.23). The resulting longitudinal mode frequencies are

$$\nu_{nmq} = \frac{c}{2(p_{\mathrm{R}}/2 + l_{\mathrm{L}})}\left[q + \frac{(n+m+1)}{\pi}\cos^{-1}\left(\pm\sqrt{g_1 g_2}\right) + \tfrac{1}{2}\epsilon_n\right], \tag{5.26}$$

$$\epsilon_n = \begin{cases} 0 & \text{for even } n_{\mathrm{m}},\ n \text{ even} \\ 0 & \text{for even } n_{\mathrm{m}},\ n \text{ odd} \end{cases} \tag{5.27}$$

$$\epsilon_n = \begin{cases} 0 & \text{for odd } n_{\mathrm{m}},\ n \text{ even} \\ 1 & \text{for odd } n_{\mathrm{m}},\ n \text{ odd} \end{cases} \tag{5.28}$$

where the π phase shift is obtained by altering the longitudinal mode frequencies.

This horizontal inversion astigmatism is the same as that of ring lasers with an odd number of mirrors [122], which has several documented consequences in ring lasers. For example, the horizontally odd HG_{10} mode is separated from the HG_{01} mode by half a longitudinal mode frequency spacing [123]. Alternatively, there can be problems in supporting circular polarisation modes when this astigmatism is present [124]. When designing an ARR laser this astigmatism should be considered to assess whether the ARR mirror number will affect the desired cavity modes. In addition, the effects of non-reciprocal or mirror-inversion dependent elements must be carefully considered, for example Faraday rotators or other polarisation sensitive optics.

In a laser cavity, an important quantity is the intra-cavity loss. This is the fraction of internal circulating power that is lost from the cavity other than through the output coupler transmission. The ARR will have losses associated with it from the optics it uses, for example imperfect high reflectance coatings on the mirrors, which will be fixed

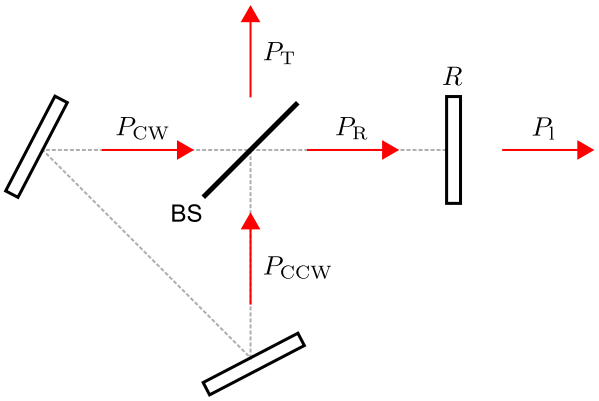

Figure 5.5: The clockwise (P_{CW}) and counter-clockwise (P_{CCW}) powers incident on the BS, and the transmitted (P_T) and reflected (P_R) powers, in an ARR laser with output coupler reflectance R and output power P_l.

quantities and independent of the alignment. An important ARR loss parameter is the fraction of power returning to the BS that is transmitted and not reflected back to the input direction, which is dependent on the ARR transmission properties discussed in the previous section. This recombination loss L_R is the round trip loss from asymmetries in the ARR, and is independent of other losses or gains in the ARR.

The notation used for the powers is shown in Figure 5.5. The powers returning to the BS are from the clockwise (P_{CW}) and counter-clockwise (P_{CCW}) paths, with the transmitted (P_T) and reflected (P_R) powers from the recombined beams. In an ARR laser, the reflected beam will return to an output coupler, with reflectance R, and result in an output laser power of $P_l = P_R(1 - R)$. Due to a lossless BS the input power equals the output power so $(P_{CW} + P_{CCW}) = (P_T + P_R)$. Using these two relations, the recombination loss becomes

$$L_R = \frac{P_T(1 - R)}{P_l + P_T(1 - R)}, \tag{5.29}$$

where it is assumed there are no losses in the propagation of P_R to the output coupler. This quantity is easily measurable for an ARR laser, needing access to only the P_T and the output laser power. It is also equal to the round trip loss of the beam recombination at the BS and can be used in standard laser equations, for example the round trip gain condition.

5.3 Experimental anti-resonant ring lasers

In this section the results of experimental ARR lasers are presented, where the gain medium is internal to the ring. The aim of these investigations was to validate the proposed ARR laser design and show that it is suitable for low loss, high performance lasers. With only one previous example in the literature of gain internal to the ring [36]

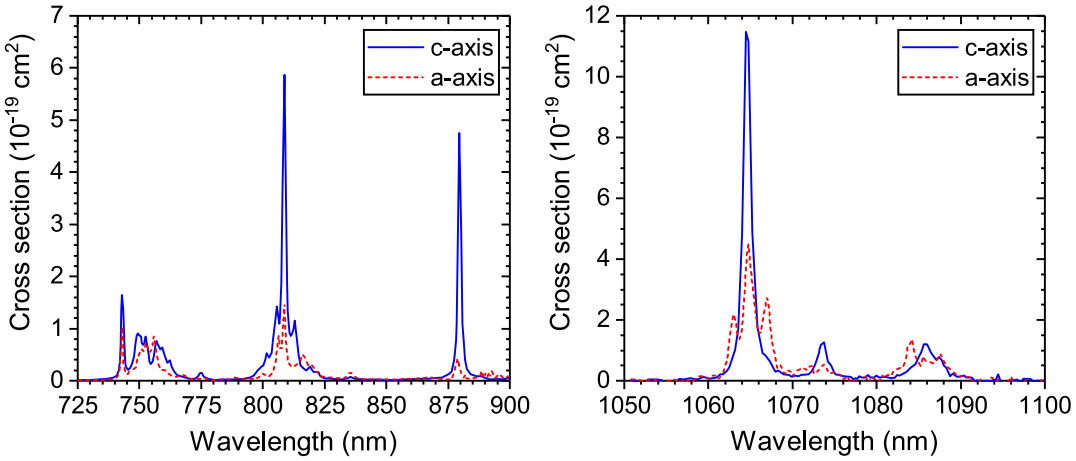

(a) Absorption (b) Emission

Figure 5.6: The main absorption (a) and emission (b) cross section lines versus wavelength in Nd:YVO_4 for polarisations parallel to the c and a-axes. Source data: [126]

that was demonstrated over 40 years ago, this work is an important demonstration of how this geometry performs with more modern technology and techniques.

Diode-pumped Nd:YVO_4 was chosen as the gain medium for this investigation. It has been widely demonstrated as an efficient and high power laser gain medium, so was suitable for this work where the focus was on the cavity design rather than the performance of the gain medium itself. It also has similarities to the widely used Nd:YAG medium, so the results presented are also an indicator of the performance that could be expected if this medium were used instead.

Two pumping geometries were investigated. A fibre-delivered 808 nm diode module was used for end-pumping of the crystal, which had the advantages of a symmetrical and well defined pumping region. An 808 nm diode bar was used in a side-pumped bounce geometry laser, which gave access to a higher gain than the fibre-delivered pump; however, this also gave rise to more challenges in controlling the intra-cavity mode.

5.3.1 Nd:YVO_4 gain medium

Neodymium is a commonly used rare-earth ion in laser gain media. A common host material is Yttrium Vanadate (Nd:YVO_4), where trivalent Neodymium replaces the similarly sized the Yttrium atom. It is an early laser material that was identified for its efficient laser characteristics [125]. It can be lamp or diode pumped, with the latter being widely adopted due to its strong absorption lines at 808 nm and 880 nm where high power laser diodes can be manufactured. The crystal absorption in this infra-red pumping region is shown in Figure 5.6(a). Nd:YVO_4 is a uniaxial crystal giving it natural birefringence, with the absorption at 808 nm being four times stronger parallel to the c-axis.

The emission cross section of Nd:YVO_4 is shown in Figure 5.6(b) around the highest

Table 5.1: Spectroscopic and physical properties of the Nd:YVO_4 and Nd:YAG gain media. Nd:YAG is isotropic so has no special crystallographic axes, and Nd:YVO_4 is uniaxial with separate properties for the c and a-axes. Source data: [5, 126, 128, 129]

	Nd:YVO_4		Nd:YAG
	c-axis	a-axis	isotropic
Emission cross section (1064 nm) / 10^{-19} cm^2	11.4	4.4	2.8
Absorption cross section (808 nm) / 10^{-19} cm^2	5.8	1.5	0.77
Absorption depth (1 % at. doping) / mm	0.14	0.54	0.94
Nd density (1 % at. doping) / 10^{20} cm^{-3}	1.24		1.38
Fluorescence lifetime / µs	98		230
Refractive index (1064 nm)	2.17	1.96	1.82
dn/dT / 10^{-6} K^{-1}	3.0	8.5	7.3
Density / gcm^3	4.22		4.56
Moh hardness	5		8.5
Thermal conductivity / Wm^{-1}K^{-1}	5.23	5.10	13
Thermal expansion / 10^{-6} K^{-1}	11.4	4.43	7.9

strength emission peak of 1064 nm that permits four-level lasing. This emission peak is polarised, being 2.5 times higher for the c-axis, which typically results in linearly polarised laser emission. There is an additional commonly used emission peak at 1342 nm that has a 3.5 times lower cross section [87].

The combination of large absorption and emission cross sections makes Nd:YVO_4 a high efficiency and low threshold gain medium. The main loss mechanism is through energy transfer upconversion (ETU). This is where an excited ion transfers its energy to a neighbouring ion exciting it to a higher energy level, which will then typically fluoresce to release its energy. This process constitutes a loss of excited population so reduces laser performance. ETU is not usually significant when operating on the 1064 nm transition, where the large emission cross section requires a low inversion for laser gain. It can however be an issue when operating on the lower cross section emission lines [127].

Another widely used host material for trivalent Neodymium is Yttrium Aluminium Garnet (Nd:YAG), where Neodymium replaces Yttrium in the crystal lattice. A summary of properties for both Nd:YAG and Nd:YVO_4 are given in Table 5.1. Unlike Nd:YVO_4, Nd:YAG has no natural birefringence and is isotropic.

Nd:YVO_4 has both higher emission and absorption cross sections, which gives it a higher gain. This makes it well suited to high pulse repetition rate lasers, where up to 160 GHz in mode-locking has been shown [130]

The fluorescence lifetime of Nd:YVO_4 is lower at 98 µs. The shorter lifetime makes it less suitable for high pulse energy Q-switched operation as it is less effective at storing energy.

The CW performance of the two media are similar, where the shorter lifetime in

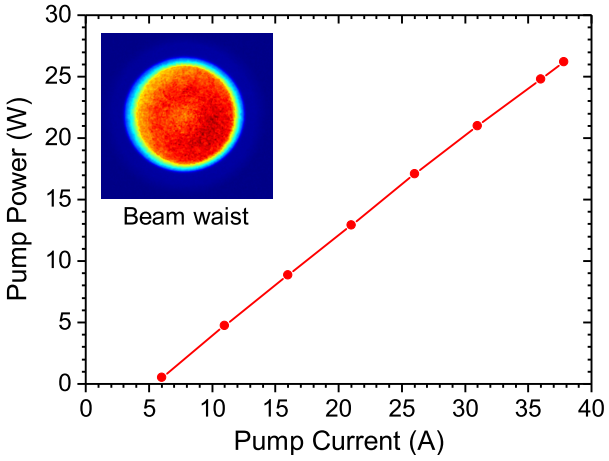

Figure 5.7: The output power of the fibre coupled diode pump versus input current, the inset shows the beam profile at the beam waist.

Nd:YVO_4 is compensated by its higher emission cross section. The thermal conductivity is lower in Nd:YVO_4, but as the temperature dependence of the refractive index also lower the thermal lensing effects are similar.

In summary, diode-pumped Nd:YVO_4 is suitable as a high power and efficient gain medium. It performs similarly to Nd:YAG in the CW regime, but is less well suited to high energy pulsed operation.

5.3.2 End-pumped laser

The pump source was a fibre-coupled 808 nm diode module (Jenoptik JOLD-30-FC-12). The output power versus input current of the module is shown in Figure 5.7. It had a maximum output power of 26.2 W that was unpolarised due to mode scrambling in the fibre.

The fibre had a 200 µm core diameter and NA = 0.22. The output was collimated with a 35 mm focal length collimator that gave a beam quality of $M_x^2 = 72$ and $M_y^2 = 73$ with a top hat profile at the beam waist, see inset of Figure 5.7. The pump was focussed into the gain medium with a 75 mm focal length lens giving a 440 µm beam waist diameter.

In an ARR laser the ARR should have the minimum losses possible to achieve the highest efficiency, therefore, a BS transmission as close as possible to 50 % is required. The BS coating was analysed to assess its performance, with its transmission for different angles of incidence (AOI) and polarisations shown in Figure 5.8. An AOI of 45° was desirable for its simplicity in aligning the ARR. With s-polarisation at 45° AOI the BS transmission best matched 50 %, so this combination was used.

The gain medium was a 0.5 % doped Nd:YVO_4 crystal, 5 mm long by 2 mm square, which was operated on the 1064 nm laser transition. It was positioned inside the ARR as shown in Figure 5.9(a). It was end-pumped through a dichroic turning mirror that

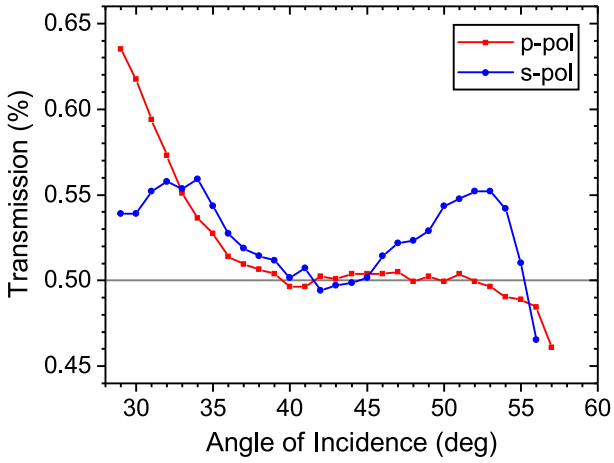

Figure 5.8: The transmission of the beamsplitter for s and p-polarised light.

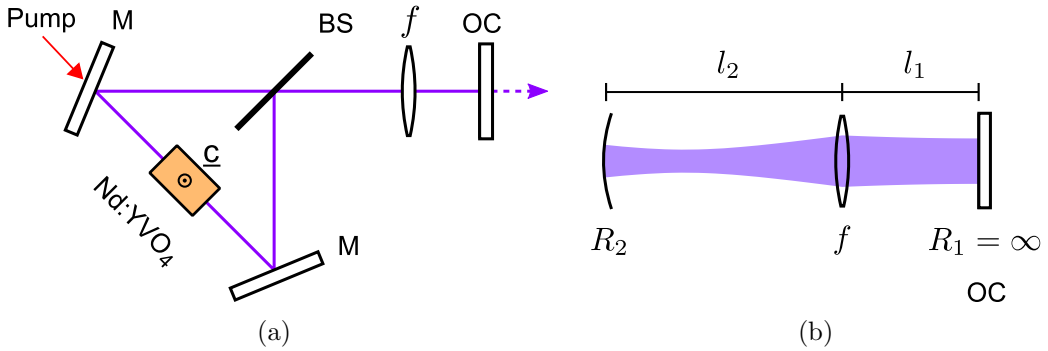

Figure 5.9: (a) The schematic of the end-pumped ARR laser cavity with gain internal to the ring. (b) The equivalent linear cavity of the ARR laser for mode analysis.

had high reflectance at 1064 nm and high transmission for the pump at 808 nm. Mode control of the cavity was through adjustment of the external arm length and intracavity lens of focal length f. The lens was positioned external to the ARR as it limited the intra-ARR focussing optics to the thermal lens in the crystal. This resulted in less probability of asymmetry in the beam focussing of the ARR and therefore lower ARR loss. The precise position of the crystal was found through minimising the loss from the ARR when moving the crystal longitudinally to the cavity mode. The equivalent linear cavity of the ARR laser is shown in Figure 5.9(b).

The ARR laser was operated in a configuration to minimise the ARR loss, with the output laser and ARR lost power versus input pump power shown in Figure 5.10(a). The maximum power was 9.7 W for 23.3 W of input, with a slope efficiency of 51.7 %, which had a ARR recombination loss power of 4 mW. The recombination loss was below 0.018 % throughout the range of pump powers, which is a significant improvement from the only other example of a similar laser system that had a loss of 0.4 % [36].

The laser was not optimised for HG_{00} operation and at higher powers the beam became increasingly multimode as the thermal lens in the crystal increased, reaching a maximum of $M_x^2 = 2.89$ and $M_y^2 = 2.43$ at the highest power. The laser mode profile at

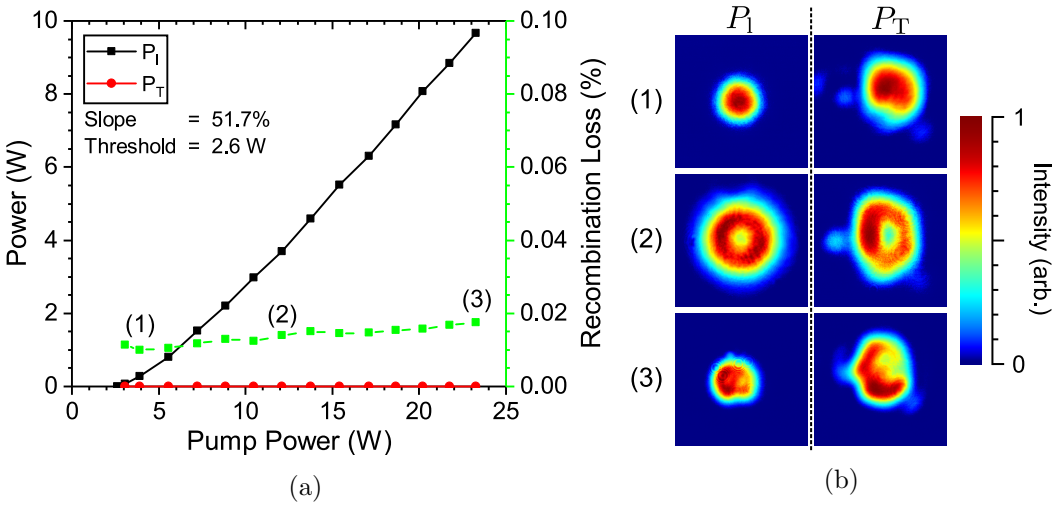

Figure 5.10: (a) The laser output power (P_I) and ARR loss power (P_T) versus input pump power for the ARR laser. Also shown is the ARR loss percentage and the slope efficiency and threshold of the output. (b) The output laser and ARR loss profiles at the indicated points.

different output powers is shown in Figure 5.10(b). The increasing proportion of higher order modes implies that the HG_{00} beam diameter was decreasing at the crystal, and was smaller than the pumped diameter. The ARR ring perimeter was 55 mm and the BS to lens distance was 72 mm, giving a crystal to lens distance of $l_2 = 100$ mm. The intracavity lens had a focal length $f = 75$ mm and $l_1 = 87$ mm. This cavity information and the knowledge that the beam diameter at the crystal was smaller than the pump diameter can be used to estimate the thermal lens in the crystal. Using the equivalent linear cavity model of Figure 5.9(b) gives an estimated thermal lens of $f_\mathrm{R} \approx 50$ mm at 24 W of pump power, from the cavity stability analysis of Section 2.2.

Higher order modes are expected to have higher recombination losses in an ARR when there is asymmetry in the intra-ARR imaging [120]. In the presented laser the recombination loss increased from 0.010 % to 0.018 % with a beam quality increase from $\mathrm{M}^2 \approx 1$ to $\mathrm{M}^2 \approx 3$. This shows that the asymmetry of the thermal lens was a small proportion of the overall recombination loss in the system. Although a multimode laser is not desired in many applications, this result is a useful demonstration that the asymmetry loss from positioning the gain medium thermal lens can be insignificant.

The profiles of the recombination loss beams are also shown in Figure 5.10(b). The loss profiles closely match those of the laser mode, which would not be expected for asymmetry in the thermal lens misalignment. The roughly uniform recombination loss of the laser mode suggests gain asymmetry in the CW and CCW beams or deviation from 50 % reflectance at the BS was the dominant asymmetry in the beam paths. The deviation from symmetrical loss profiles was most likely from residual thermal lens asymmetry. A recombination loss of 0.01 % corresponds to a BS reflectance asymmetry of $\delta = 0.5$ %, see Equation (5.12), which is within the alignment tolerance that could be

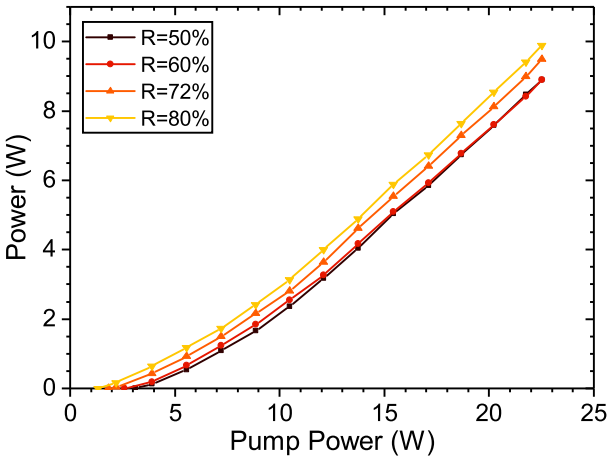

Figure 5.11: The output power versus input pump power of the ARR laser for different OC reflectances R.

expected from the BS transmission curves of Figure 5.8. This suggests that a significant part of the ARR loss was from BS reflection asymmetry and could have been further reduced with a more optimal BS AOI.

The ARR laser was operated with a range of OC reflectances from 50 % to 80 % in a slightly altered cavity geometry. The laser output versus input powers are shown in Figure 5.11. The higher reflectance OCs reduced the laser threshold, as would be expected from four level laser theory, and increased the slope efficiency from 55 % to 57 % for $R = 50\,\%$ to 80 %, respectively. The higher slope efficiency was most likely from less ETU loss from a lower population inversion at $R = 80\,\%$.

For all the OCs the ARR recombination loss was below 0.03 %, with variations due to differences in alignment between the lasers, so the ARR component had a negligible impact on performance of the laser. However, it should be noted that the ARR recombination loss power increased from 4 mW to 9 mW from $R = 50\,\%$ to 80 % due to the higher circulating intra-cavity power for the $R = 80\,\%$ OC. This had a negligible impact on the laser efficiency but could be significant in an application that requires minimal power output from the BS transmission.

To more clearly show the effect of thermal lens asymmetry on the ARR recombination loss, an ARR laser with a perimeter $p_{\mathrm{R}} = 216\,\mathrm{mm}$ was constructed to allow space for the crystal to be moved a distance $\Delta_f = 20\,\mathrm{mm}$. The output laser powers versus input pump powers for the symmetrical and asymmetrical thermal lens positions are shown in Figure 5.12. The output laser mode profiles and ARR recombination loss profiles are also shown for each case. The laser output was more multimode than the previous geometry due to the different ARR perimeter.

The symmetrical thermal lens cavity performed similarly to the previously geometry in Figure 5.10, with low dependence on the ARR recombination loss to input pump power. The ARR recombination loss remained below 0.45 % over the range of pump

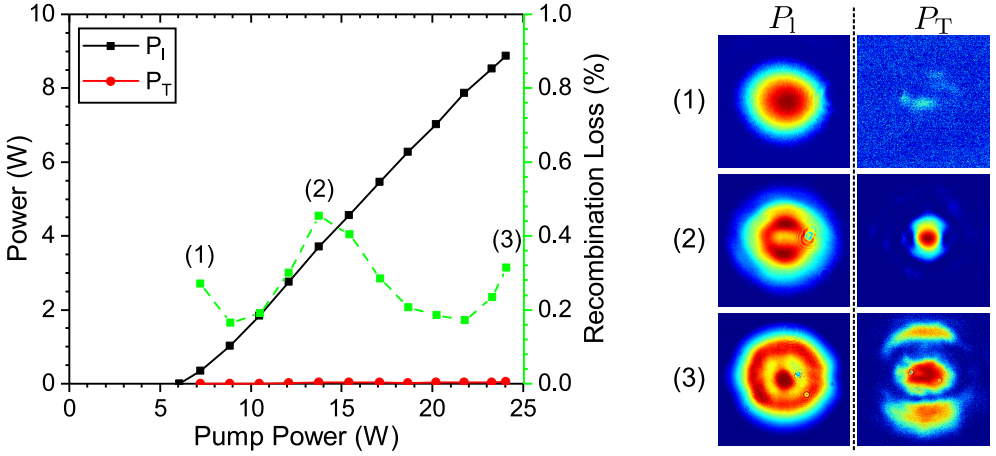

(a) Symmetrical thermal lens

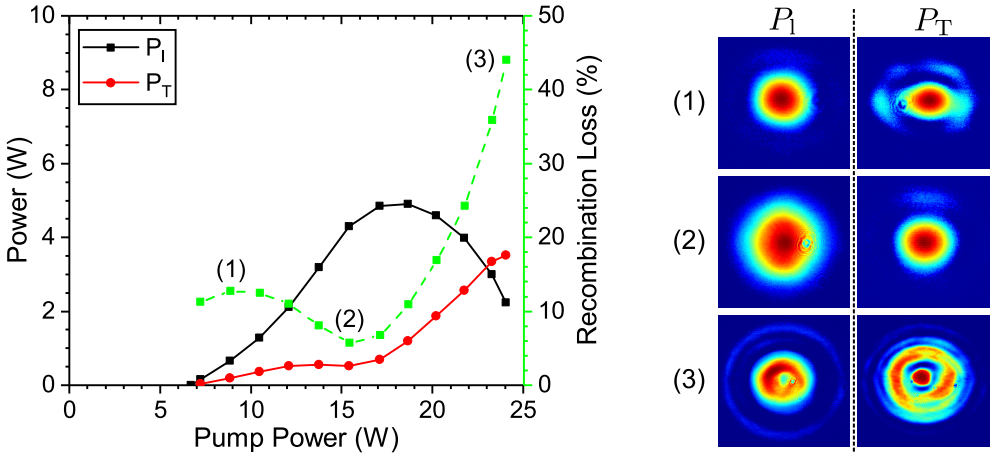

(b) Asymmetrical thermal lens

Figure 5.12: The output laser and recombination loss powers versus input pump power for (a) symmetrical thermal lens (b) asymmetrical thermal lens. Also shown is the recombination loss and the laser mode and loss profiles (right).

powers.

The asymmetrical thermal lens had higher ARR recombination losses across the range of pump powers, from a minimum of 6 % at 15 W pump power to a maximum of 44 % at 24 W pump power. This was as expected from the thermal lens asymmetry calculations of Sheng [120]. The transverse profiles of the transmitted beam are also similar to those predicted by Sheng, which consists of a central spot surrounded by concentric rings.

The initial decrease in ARR recombination loss from 11 % at laser threshold to 6 % at 15 W of pump power was most likely due to the cavity being near the edge of stability at threshold, causing a greater sensitivity to the thermal lens asymmetry. Beyond this pump power, the ARR recombination loss increases as expected. Using the thermal lens estimate at 24 W pump power of $f_{\mathrm{R}} = 50\,\mathrm{mm}$ and the thermal lens asymmetry of $\Delta_f = 20\,\mathrm{mm}$, the expected loss is 8 % for the HG_{00} mode from Equation (5.14). Considering the highly multimode laser mode profile at this pump power that would increase the losses, the experiment roughly validates the theory.

5.3.3 Side-pumped laser

Due to the low absorption depth of the pump in Nd:YVO_4, side pumping can be an effective geometry because the population inversion is highly concentrated towards the pumped face. A side-pumped Nd:YVO_4 ARR laser was constructed with the geometry shown in Figure 5.13(a). The pump source used was a diode bar that provided a line shaped pump source. This was focussed onto the crystal face with a horizontal cylinder lens (HCL) that compressed the beam vertically, which generated a line shaped population inversion next to the crystal face.

In order to efficiently extract energy from this population the laser mode must overlap with this region. It has been shown that a bounce geometry can provide the necessary overlap, where the laser mode undergoes total internal reflection (TIR) at the pump face. If a symmetrical trapezoidal Nd:YVO_4 crystal is used with a face angle of 14°, an incident beam parallel to the pump face undergoes a TIR bounce at the pumped face of 7°, which then refracts out of the opposite crystal face to give an undeflected beam. A diagram of this geometry is shown in Figure 5.13(b)

The thermal lens of a side pumped crystal is highly astigmatic, with the horizontal lens being weak due to the small temperature variation in this axis [35]. The vertical lensing is strong due to the tight vertical concentration of the pump power. To effectively match the internal laser mode to this pumped region in the cavity, HCLs were placed at their focal length of 50 mm away from the crystal to vertically focus the mode into the crystal. The horizontal mode was only focussed by the thermal lens in the crystal.

The gain medium was a 1 % doped Nd:YVO_4 slab, which had a symmetrical trapezoid shape with a 14° face angle as in Figure 5.13(b). It was contacted with Indium foil to a water cooled copper mount. Both the diode bar and copper crystal mount were cooled

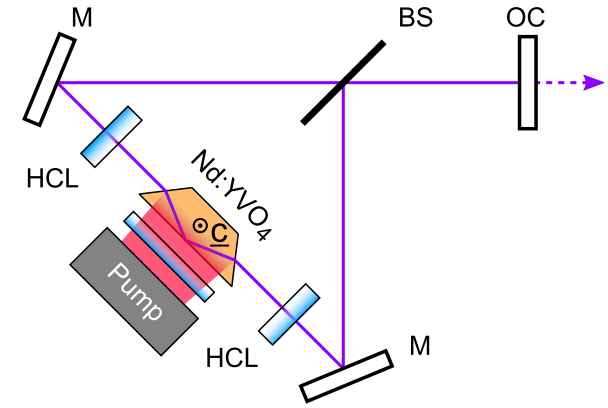

(a)

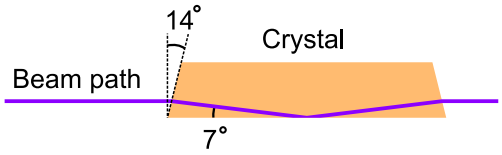

(b)

Figure 5.13: (a) The side pumped ARR laser geometry. The diode bar pump is focussed with a horizontal cylinder lens (HCL) onto the crystal face. The laser mode totally internally reflects off the pump face. HCLs control the vertical mode size in the crystal. (b) The crystal face and beam angles for Nd:YVO_4 for a 7° bounce and an undeflected input beam.

with water at a temperature of 22.5 °C. The output coupler reflectance was $R = 30\,\%$.

The output laser power and ARR recombination loss power versus input pump power are shown in Figure 5.14(a), with the output profiles in Figure 5.14(b). The laser had the typically high efficiency of this geometry, with a total output power of 19 W at 46 W pump power.

Near threshold the laser output was close to HG_{00}, but as the pump power increased the laser became increasingly multimode in the horizontal plane. This was due to a wider gain size with the increased pump power, along with a decreasing horizontal mode size at the crystal. The horizontal mode order could have been reduced by increasing the cavity length or using a shallower bounce angle in the crystal. The mode remained approximately Gaussian in the vertical axis.

Near threshold the recombination loss was 1.5 %. At this power, the horizontal fringe pattern in the loss profile in Figure 5.14(b) suggests that the dominant source was vertical asymmetry in the ring. The pair of 50 mm focal length HCLs inside the ARR were the most likely source of this, where asymmetry in their position could have caused both angular misalignment and imaging asymmetry of the recombining fields.

At maximum power the loss increased to 18.7 %, but with the horizontal axis being the dominant source due to the vertical fringe pattern. The increasingly multimode beam could have caused this, as higher order modes would have had greater losses on

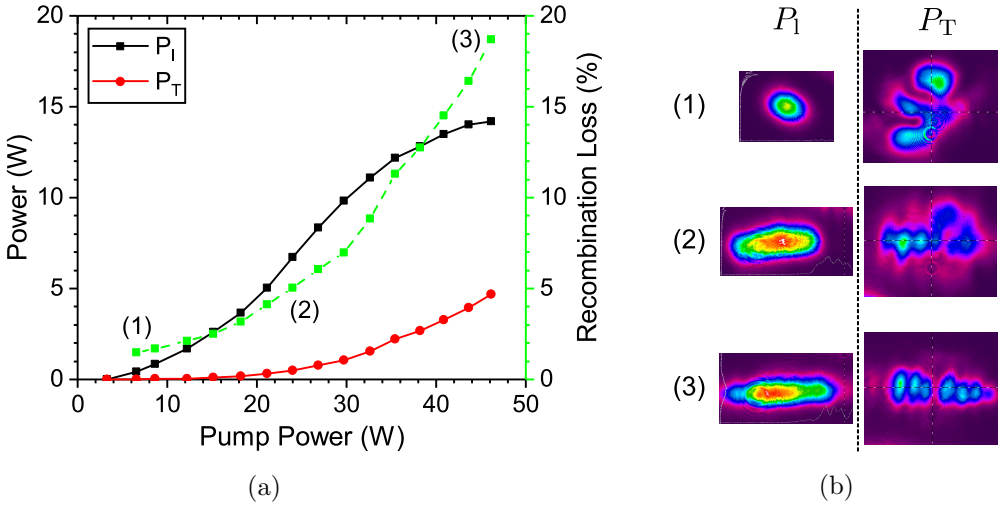

(a) (b)

Figure 5.14: The side-pumped ARR laser results, (a) The output laser and ARR loss powers versus input pump power, (b) the output profiles of the laser (P_I) and ARR transmission (P_T) at the numbered points.

recombination [120].

It has been shown that the laser mode can be maintained at HG_{00} in the bounce geometry for increasing pump powers [35]. If this was achieved in the ARR laser demonstrated, the recombination loss could have been kept near to the threshold value of 1.5 %. At this point, the main source of loss was from vertical alignment or imaging asymmetries, which were most likely from the short focal length HCL lenses used. It was not possible to place these external to the ARR in the experimental system due to physical limitations of the optical mounts; however, if these were mounted externally it is likely that the recombination loss could have been significantly reduced.

This preliminary investigation suggests that a bounce geometry gain medium internal to an ARR is a viable cavity design. It would be important to ensure that the vertically focussing optics are external to the ARR, which would significantly reduce the losses from those demonstrated in the presented system.

5.4 Summary

This chapter has investigated the application of an ARR in a laser cavity with the gain medium internal to the ring. To achieve ideal 100 % reflection from the ARR it has been shown that symmetry of the ring is required. This includes ensuring the BS has close to 50 % reflectance and that the thermal lens in the crystal is halfway around the perimeter of the ring.

It was shown that an equivalent linear cavity can be used for ARR laser design provided that the ring is symmetric, which is required for a zero transmission ARR. The mode propagation and frequencies are the same as this linear cavity, which allows the use of linear cavity design procedures.

The first demonstrations of experimental solid-state ARR lasers were constructed using the Nd:YVO_4 gain medium with diode pump sources. The end-pumped geometry achieved ARR transmissions below 0.02 %, a substantial improvement from the only other demonstration of a similar geometry of 0.4 % [36]. The ARR maintained this low loss even in multimode operation. The laser showed the typically high efficiency of Nd:YVO_4 systems, having a slope efficiency of 52 %.

The effect of asymmetry in the position of the thermal lens was demonstrated in the end-pumped laser. Where the transmission of the ARR increased as predicted from applying a theoretical analysis [120].

A side-pumped ARR laser was demonstrated. This geometry had ARR transmissions above 1.5 %, which was substantially higher than in the end-pumped lasers. This was due to insufficient HG_{00} mode control in the cavity and asymmetry of the optical components inside the ARR. These issues would be simple to overcome by using differently sized optical components, which would allow the ARR to have a smaller perimeter and decrease asymmetries. This would make the side-pumped geometry a viable cavity design for ARR laser implementations.

This work has shown how to design and implement ARR laser cavities. It has demonstrated lasers with losses below 0.02 %, making this configuration suitable for high-performance laser designs.

Chapter 6

Vortex mode generation

The generation of optical vortex beams can be broadly classified as either extra-cavity conversion, where a laser output is converted into a vortex, or intra-cavity, where the vortex is the direct output from a laser. In this work the focus is intra-cavity generation of the scalar vortex LG_{0l} laser modes. These methods can have significant advantages over extra-cavity techniques in the mode purity and power that can be obtained.

This chapter begins with the motivation for obtaining optical vortex modes. An overview of the different techniques of vortex generation is given, along with how the resulting modes can be analysed and the conditions for supporting them in a laser cavity.

The intra-cavity vortex generation method of coupling laser cavities through a common gain medium is investigated theoretically and experimentally. A new cavity geometry for vortex generation is proposed and implemented, where an anti-resonant ring (ARR) is used to couple two laser cavities. With this design, watt-level LG_{01} and LG_{02} vortex modes were obtained using a diode-pumped Nd:YVO_4 gain medium. The use of the ARR is shown to have significant advantages over other coupling methods, for example it requires no specialist optics and is wavelength insensitive.

6.1 Motivation

Since the identification of the orbital angular momentum (OAM) in vortex modes by Allen in 1992 [21] a wide variety of uses have been found for them spanning a range of scientific fields. Some of these applications exploit the doughnut intensity profile of the vortex modes. The laser machining of glasses can be enhanced using a doughnut instead of a Gaussian profile [131] and stimulated emission depletion microscopy can be performed using vortex modes as the depletion beam [132].

A key property of the vortex modes is the OAM they possess, which is from their spiral phase structure encoded in the integer l parameter of the electric field, see Section 2.3.1. The OAM can be used to transfer angular momentum to trapped particles to manipulate them for microscopy [22, 133]. Alternatively, the angular momentum can

be transferred during laser machining to manufacture nano-scale chiral structures [23]. The OAM state can also be stored to act as a form of optical memory [24].

Other applications exploit the OAM l parameter to encode information. The parameter can be used to multiplex information streams in optical communications to enhance transfer rates [25] and improve the security of free-space communications [134]. The OAM is also a rich test-bed for quantum mechanical experiments [26].

The range of wavelengths that an optical vortex can be generated in can be extended through non-linear conversion processes [38], with the conversion processes enhanced using a resonant optical parametric oscillator [135]; however, the efficiency losses and additional complexity of these techniques means that generating the vortex at the source is preferable. Additionally, these systems have been seeded by optical vortices converted from Gaussian laser outputs, so were limited by the power and vortex quality of these sources.

All of these applications require sources of optical vortex beams. Most extra-cavity methods are restricted in the wavelength range that they can be applied to, or require optics to be designed for a specific wavelength. Intra-cavity generation methods are typically limited in the range of gain media that they could be applied to. Having an intra-cavity vortex generation technique that can be applied to a variety of gain media could enable vortex generation in previously inaccessible wavelength ranges. This would exploit the benefits of intra-cavity generation and enable turn-key optical vortex lasers. The availability of these systems would help the potential of vortex beams to be fully realised.

6.2 Orbital angular momentum

The mathematical treatment of the angular momentum in LG modes was first outlined by Allen [21] and is summarised here. The angular momentum density, $\mathbf{M}$, of an electromagnetic field is given by

$$\mathbf{M} = \epsilon_0 \mathbf{r} \times (\mathbf{E} \times \mathbf{B}) \,, \tag{6.1}$$

where ϵ_0 is the permittivity of free space, $\mathbf{r}$ is the radial vector, $\mathbf{E}$ is the electric field vector, and $\mathbf{B}$ is the magnetic field vector. The total angular momentum, $\mathbf{J}$, of an electromagnetic field is then the volume integral

$$\mathbf{J} = \epsilon_0 \int \mathbf{r} \times (\mathbf{E} \times \mathbf{B}) \, \mathrm{d}\mathbf{r} \,. \tag{6.2}$$

The time averaged angular momentum density per unit power of the LG_{pl} modes

defined in Equation 2.14 is found to be

$$\mathbf{M} = \frac{l}{\omega}\frac{z}{r}\left|\widetilde{u}_{pl}\right|^2 \mathbf{r} + \frac{r}{c}\left[\frac{z^2}{(z^2+z_{\mathrm{R}}^2)} - 1\right]\left|\widetilde{u}_{pl}\right|^2 \boldsymbol{\phi} + \frac{l}{\omega}\left|\widetilde{u}_{pl}\right|^2 \mathbf{z}\,, \tag{6.3}$$

where $\boldsymbol{\phi}$ and $\mathbf{z}$ are unit vectors, and ω is the angular frequency. Upon integration over the beam profile to find the total angular momentum $\mathbf{J}$, the $\mathbf{r}$ and $\boldsymbol{\phi}$ terms disappear due to their symmetry. The per photon orbital angular momentum along the axis of propagation, L_z, is then

$$L_z = \hbar l\,. \tag{6.4}$$

This is the OAM because it is created by the Poynting vector having an azimuthal component off axis and spiralling about the propagation direction.

The OAM is not the only source of angular momentum. The previous analysis only considered linearly polarised light, but it can be generalised to include circular polarisation. The coefficient σ_z defines the polarisation state, where $\sigma_z = 0$ is linear polarisation and $\sigma_z = \pm 1$ is for right or left handed circular polarisation, respectively. The total angular momentum per photon, J_z, is then

$$J_z = L_z + S_z = \hbar(l + \sigma_z)\,, \tag{6.5}$$

where $S_z = \hbar\sigma_z$ is the spin angular momentum associated with circular polarisation states. It is worth noting that the circular polarisation is limited to giving $\pm\hbar$ angular momentum to the photons, whereas OAM is determined by l, which theoretically has the range of $\pm\infty$.

Spin angular momentum can be easily imparted onto a linearly polarised beam through a quarter-wave plate, which converts the polarisation state. The relative difficulty of making OAM states is why generating linearly polarised LG_{0l} vortex modes is the focus of this work.

The source of the OAM in the LG_{pl} modes is from the spiral phase term $\exp(-il\phi)$ of their electric field, see Section 2.3.1. This term can be visualised through the 2π equiphase surfaces of the propagating LG_{0l} modes, these are shown for $l = 0$ to 3 in Figure 6.1, where the different colour surfaces refer to increasing multiples of 2π. In the case of $l = 0$ the phase fronts are planar and there is no OAM. When $l \neq 0$ the phase fronts spiral around the propagation direction, with the total phase change around the propagation axis in any transverse plane of $2\pi l$. The increasing rate of phase rotation with l results in the increasing amounts of OAM. For opposite handedness vortices, when l is negative, the helices are in the opposite direction.

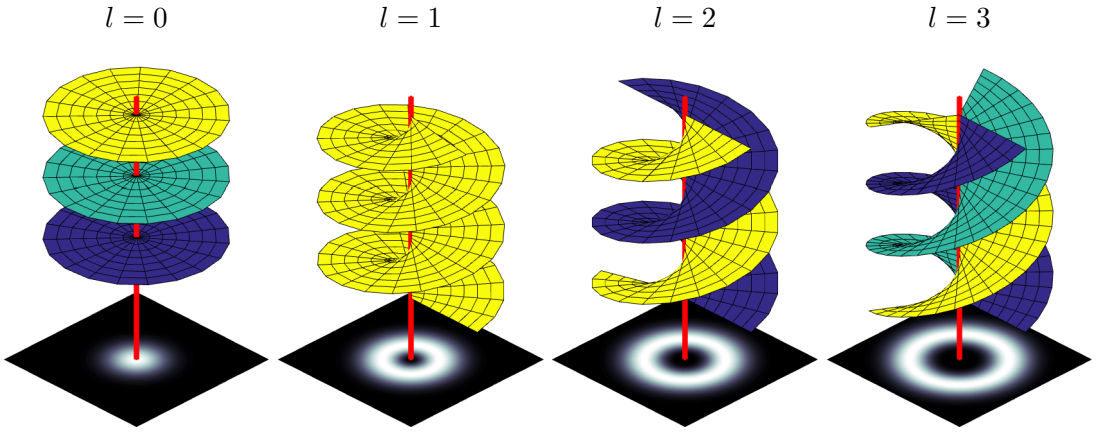

Figure 6.1: The 2π equiphase surfaces of the LG_{0l} modes. The mode profiles are shown underneath the phase fronts for upwards propagation over three wavelengths.

6.3 Vortex generation techniques

In this section a general overview of the methods to generate vortex modes is presented. These include conversion methods to convert a laser output into a vortex mode and intra-cavity techniques to directly generate a vortex from the laser itself.

An important issue for vortex generation is being able to measure the properties of a laser output to verify both the quality and if a vortex mode is being generated. The measurement techniques of the intensity and phase of the vortex output are discussed. The requirements of a laser cavity to be suitable for vortex mode generation are given, along with ways to control the handedness of the oscillation.

6.3.1 Conversion

Vortex conversion methods use laser inputs, typically in the HG modes, and convert these planar wavefront modes into beams with phase singularities that can have a LG_{0l} type profile. This can be achieved in a variety of ways, which makes these techniques attractive due to their potential flexibility of input source and well determined handedness of the output.

A Gaussian beam can be converted into an optical vortex through use of a hologram, where the Gaussian input is used as the reference beam to produce the encoded vortex. The holograms are typically computer generated and can be fixed holographic structures [28, 136] or variable with spatial light modulators [137]. An advantage of computer controlled spatial light modulators is the desired vortex can be rapidly changed through changing the hologram structure.

The spiral phase can be directly imparted on a Gaussian beam using a spiral phase plate [30], where a radially dependent phase delay is added to the beam, resulting in a spiral phase output. These can be cascaded or specifically designed to generate higher order vortices.

A vortex can be generated from self interference of a Gaussian beam [29], where the spiral phase is added through adjustment of the shear and angular alignment of the two interfering Gaussian components.

Alternatively, the spin angular momentum of a Gaussian beam from its circular polarisation can be converted into OAM through a q-plate [138]. This uses a structured birefringent medium, typically liquid crystal, to generate an optical vortex.

Using the relationships between the HG and LG modes, see Equation (2.21), HG modes can be converted into LG beams with astigmatic mode converters. This is where a Gouy phase shift is introduced along one beam axis to generate the phase differences required to convert a HG mode into a LG mode of the same total mode order, see Figure 2.6 for examples of the HG components of LG modes. This can be performed with cylindrical lenses [27, 139] or off axis spherical mirrors [140]. These conversion techniques require HG inputs, which can be produced directly from a laser cavity [141].

Vortex conversion methods have advantages, but also have significant limitations. In general, each method will suffer some of the following problems. Specialist optical components can be needed, which can be expensive and need to be tailored to the application. Additionally, they may only be manufacturable and used at a limited range of wavelengths. These optics can have limited power and intensity handling before damage will occur. The conversion can have low efficiency [31] with respect to the input power. Finally, the conversion method can be sensitive to the input beam in size, alignment, and collimation. Due to these limitations there is still a need for alternative vortex sources.

6.3.2 Intra-cavity

Vortex beams can be generated directly from a laser source, where the mode inside the optical cavity is an optical vortex, these are termed intra-cavity generation methods. An advantage of these methods is that they can exploit the natural noise filtering characteristics of lasers to produce high purity LG_{0l} modes. If the lasers are constructed with standard high power laser optics, then the vortex beams can also be produced at high power.

The earliest methods of generating a vortex mode laser used spatially dependent absorbers to suppress the usually dominant HG_{00} mode and make the LG_{0l} mode most favourable. This can simply be achieved using a spot defect mirror [33, 142], where the absorbing dot is used to suppress the HG_{00} mode but have limited impact on the doughnut LG_{0l} modes. This can be combined with circular absorbers to give additional mode control [143]. A recent implementation of this technique used modern liquid-crystal technology to have programmable phase and intensity reflective elements with a spatial light modulator (SLM), a so called digital laser [32, 144].

An alternative to increasing the loss of the HG_{00} mode is to increase the gain of the LG_{0l} modes to give them a lower threshold. This can be achieved through reshaping the

gain region to match the desired LG_{0l} mode. An annular pump beam can be used to match the doughnut shape of the vortex modes by imaging the output of a multimode capillary fibre [34, 145] or using diffractive elements to reshape a Gaussian profile [146], provided that the pump is able to be reshaped. Alternatively a more standard top-hat pump profile can be used and the gain region reshaped using a double resonator design [147, 148, 149].

Another vortex mode generation method exploited the strong negative spherical aberration in a bounce laser configuration [35, 150]. This allowed the HG_{00} to be an unstable cavity mode whilst the LG_{01} was not. In this way the lasers were forced to oscillate in the vortex mode.

The q-plate conversion method can be applied inside a laser cavity to generate a vortex output [151]. Similarly a diffractive output coupler has been used [152], where the vortex beam is the result of the interaction between the laser mode and the specially designed diffraction optic.

Using intracavity spiral phase plates has been shown to induce a vortex mode in a bulk laser [153]; however, this necessitated a more complex unstable resonator geometry. In a semiconductor laser a spiral phase perturbation has been shown to generate vortex modes [154].

The wide variety of intra-cavity vortex generation methods shows the depth of interest in this topic. Despite this, the current techniques, in general, all have limitations. The required optical components may have a limited power handling capability or be restricted in their wavelength range of operation. Alternatively, the pump may need to be able to be reshaped or the gain medium have certain properties.

6.4 Vortex mode measurement and control

Generation of the vortex LG_{0l} modes is the aim of this work, so robust measurement methods must be used to analyse them. In this section the methods and complications of measuring the LG_{0l} modes is presented. It will be shown that observing the intensity profile alone is not sufficient to identify the LG_{0l} modes and that the phase structure must be verified independently. An interferometric technique is demonstrated to directly observe the spiral phase of a beam.

There are symmetry requirements on a laser cavity to be able to support the LG_{0l} modes, which will be discussed along with techniques to break the cavity symmetry to select the handedness of the vortex phase.

6.4.1 Vortex mode analysis

For the Laguerre-Gaussian modes a key feature for their applications is the vorticity of their phase through the $\exp(il\phi)$ term in Equation (2.14), which is usually required in a pure vortex LG_{0l} mode with zero radial index p. The sign of l gives the handedness of the

phase, and therefore the direction of OAM. There may be many LG_{0l} modes at different wavelengths from a vortex source, but provided they all have the same handedness the OAM expected will be unchanged.

An unambiguous method to determine both the mode order and handedness components of a beam is to use a modal decomposition method, which can quantify the proportions of each transverse mode in a beam. This is typically performed using diffraction of the beam from a series of holograms, with the diffraction strength proportional to the fraction of the targeted mode in the beam. The holograms can be computer generated using liquid crystal phase and/or amplitude modulating devices [151, 155]. If this technique is not available then other analysis techniques may be used.

The M^2 beam quality parameter can be used as a guide to the vortex order $|l|$ by comparing the measured beam quality to that of the LG modes in Equation (2.33). However, the ambiguity of the modal components that give the resulting M^2 means that it cannot quantify the purity of an LG mode, see Equation (2.36). Another limitation is that it cannot measure the handedness of the OAM.

The beam quality measurement can be used to identify the likely dominant $LG_{0|l|}$ mode. The purity can then be assessed by comparing the transverse mode profile to that given by theory (Equation (2.15)), where a close match implies a high purity and vice versa [149].

Analysing the intensity profile of a beam is not sufficient to confirm the existence of pure handedness LG_{0l} modes. To illustrate this, two different ways of generating the correct intensity pattern for the LG_{0l} modes are shown in Figure 6.2. Firstly, in Figure 6.2(a), an incoherent combination of the HG_{10} and HG_{01} modes has the same intensity distribution of an LG_{01}; however, this beam has no OAM as the HG modes must be coherently combined with the correct phasing to possess OAM. For higher order vortex modes this is analogous to incoherent superpositions of the LG petal modes, see Figure 6.2(b) [32]. Secondly, in Figure 6.2(c), an incoherent combination of LG_{01} and $LG_{0,-1}$ modes has the intensity profile of an $LG_{0,\pm1}$ mode [156], but has no net OAM due to the opposing handedness components.

The amount of and direction of the OAM in a beam can be directly measured in a variety of ways, for example by measuring the beam twist parameter [157], astigmatic focussing with a cylindrical lens [158], or modal decomposition [159]. These techniques can measure non-integer OAM densities; alternatively, the existence of a pure OAM state can be verified by simply analysing the transverse phase profile of a beam. If the phase profile matches that expected of a pure LG mode then the pure handedness OAM is confirmed.

Interference of a beam with a plane wave reference will reveal information about its phase structure. If a collimated LG_{0l} beam is interfered with a plane wave propagating at an angle α in the x-z plane with wavenumber k, the intensity pattern in Figure 6.3(a) is formed, where the fringe boundaries match the equation $y = \mp x \tan(xk \tan\alpha)$ for

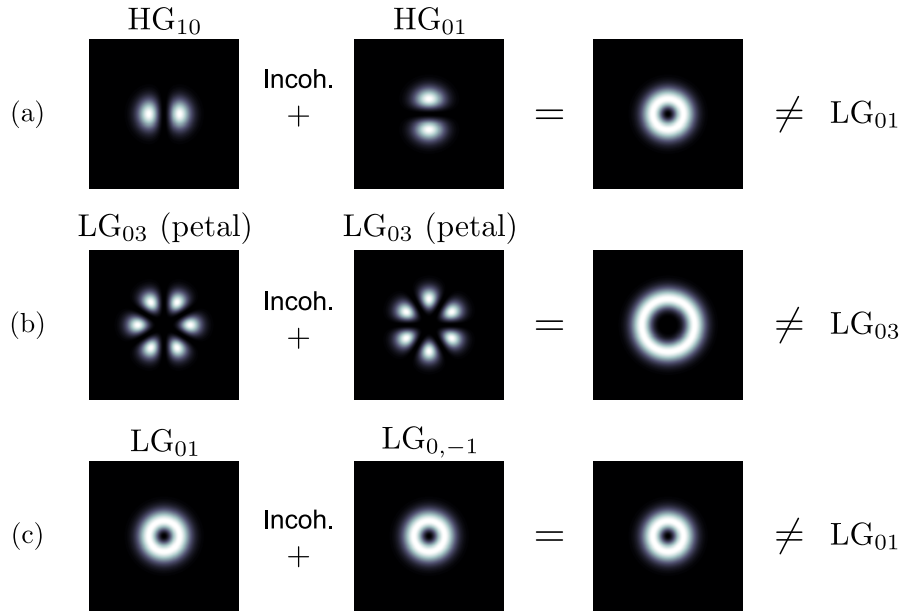

Figure 6.2: Examples of incoherent mode additions that have intensity profiles identical to a pure LG_{0l} mode but without OAM.

$l = \pm 1$ [160]. The phase singularity is revealed from the additional bright fringes above or below the origin causing a forked structure, a 'fork' interferogram. The number of additional fringes is equal to $|l|$, for example $|l| = 2$ gives a 2 additional fringes, see Figure 6.3(a). The handedness of the vortex determines whether the additional fringes are above or below the origin.

Another more suggestive visualisation of the phase singularity is to interfere a plane wave with a LG_{0l} beam that has a significant radius of curvature, R in Equation (2.14). If there is no vorticity ($l = 0$) then the interferogram forms a pattern of concentric circles. When there is a phase singularity, the multiple of 2π phase shifts on a closed path around the singularity break the azimuthal symmetry and a spiral pattern is formed, as shown in Figure 6.3(b), a 'spiral' interferogram [161]. The spiral arms follow the polar equation $r = +(2R/k)\sqrt{s2\pi - l\phi}$, where s is an integer order of interference. The charge of the vortex $|l|$ is revealed through the number of spiral arms from the centre of the pattern, with the handedness determined by the clockwise or anticlockwise fringes.

To produce the fork or spiral interferograms, the reference beam can be generated using a Mach-Zehnder interferometer, as shown in Figure 6.4. In one arm the beam is demagnified with a telescope and is termed the signal beam. In the other arm the beam propagates in free space with no modification, this is the reference beam. In this configuration, the signal beam is smaller than the reference beam when recombining at the second beamsplitter, which means that over the interference area the reference beam can be approximated to be a plane wave.

To generate a fork interferogram, the collimated signal and reference beams are adjusted so that there is a small angle between their propagation axes, as in Figure 6.4(a).

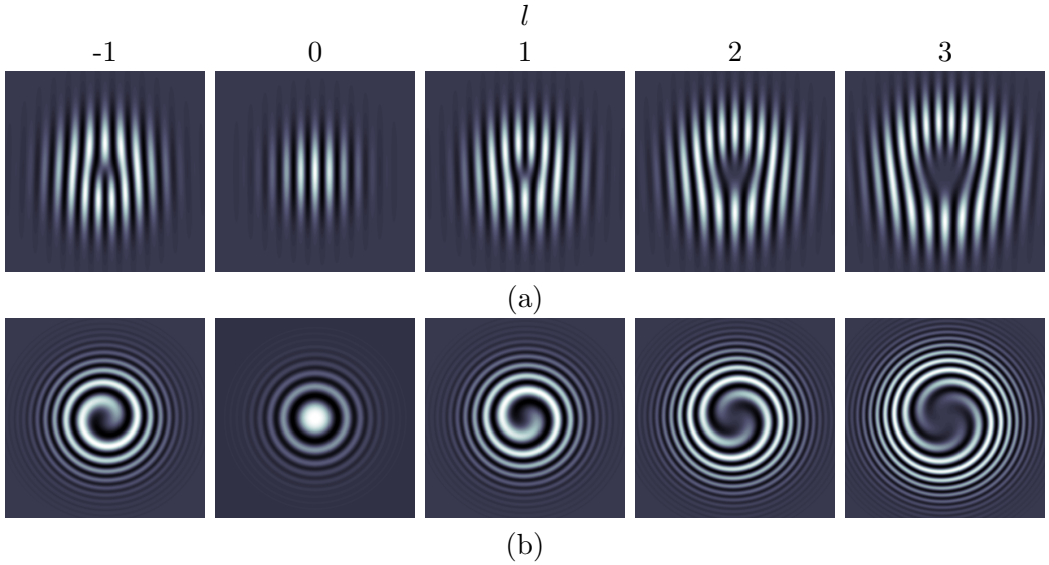

Figure 6.3: The interference patterns of the LG_{0l} modes with (a) a tilted plane wave to produce a fork pattern and (b) a plane wave with a relative radius of curvature between the wavefronts to produce a spiral pattern.

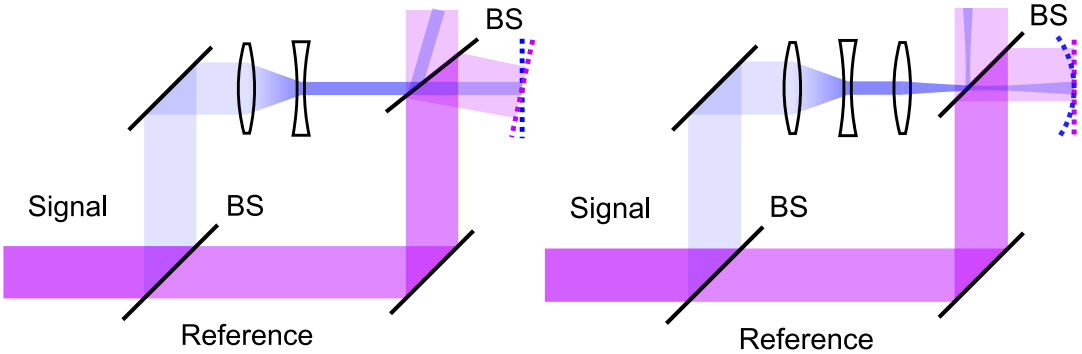

(a) Fork (b) Spiral

Figure 6.4: The Mach-Zehnder interferometer design for (a) fork and (b) spiral interferograms. The resulting wavefront alignments are shown by the dotted lines for the signal (blue) and reference (purple) beams.

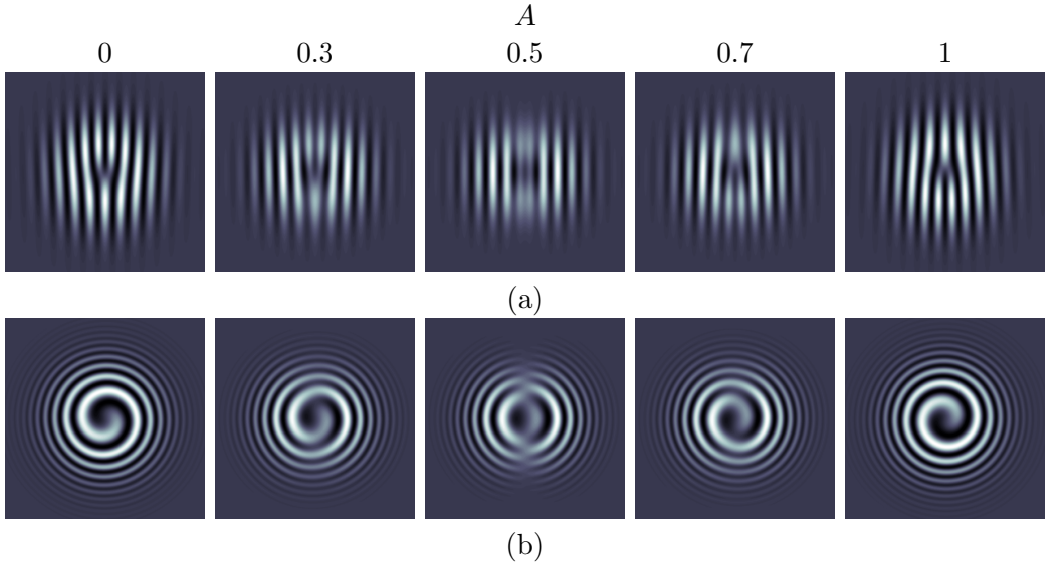

Figure 6.5: The (a) fork and (b) spiral interferograms for an incoherent superposition of $[(1-A)\mathrm{LG}_{01} + A \cdot \mathrm{LG}_{0,-1}]$ modes. The handedness purity can be assessed through the clarity of the fork or spiral pattern.

To make a spiral interferogram, the signal beam is focussed with an additional lens to give the signal wavefront curvature, and the reference beam is aligned to propagate parallel to it, Figure 6.4(b).

Typically a laser will oscillate on multiple longitudinal modes, where each mode can have different transverse mode profiles [148]. The transverse profiles will add incoherently as they are at different frequencies. Incoherent mixtures of modes can have the characteristic doughnut profile of the LG_{0l} modes yet possess no OAM. For example, incoherent mixtures of the LG petal modes can produce a doughnut intensity profile [32], see Figure 6.2. Alternatively, there could be multiple $\mathrm{LG}_{0|l|}$ modes but with a mixture of handednesses.

The fork and spiral interferograms of a vortex laser output can verify if pure handedness LG_{0l} modes are oscillating. The calculated interferograms of a superposition of two incoherent LG_{01} and $\mathrm{LG}_{0,-1}$ modes with relative intensities $(1-A)$ and A, respectively, are shown in Figure 6.5. When $A = 0$ or 1 there is only a single handedness mode, when $A = 0.5$ the opposite handedness modes are of equal intensity.

When there is no $\mathrm{LG}_{0,-1}$ component ($A = 0$) the fork and spiral interferograms appear as expected. As the $\mathrm{LG}_{0,-1}$ strength increases the interferograms become increasingly distorted until the point of equal contribution ($A = 0.5$) where the fork and spiral patterns are no longer visible. As the LG_{01} contribution decreases the interferograms return to their expected forms but for the opposite handedness ($A = 1$). For mixtures of petal beams the interferograms appear the same as for the case $A = 0.5$ [145].

6.4.2 Symmetry requirements

For a laser cavity to support LG modes it must meet a set of symmetry requirements. The LG modes are solutions to the paraxial wave equation for a cavity with cylindrical symmetry, therefore for a laser to support an LG mode it must have that symmetry. The cylindrical symmetry affects a range of laser cavity parameters.

The gain region should have circular symmetry. If the gain region is larger along one axis with respect to the mode size, then the LG modes may not have the optimal intensity distribution to exploit this. For example, if the gain region were larger in the horizontal axis then the asymetrical HG_{n0} set of modes could have a better spatial overlap with the gain region. This would make the laser preferentially oscillate in these modes rather than the circular LG modes.

In Section 2.3.1 the HG components of the LG modes were shown. The LG modes are formed of coherent combinations of HG modes, where the total mode orders of the components are the same, $(2p + |l|) = (n + m)$. The decomposition requires that the HG modes are coherently combined, which means that they must be at the same frequency. In a symmetric cavity the longitudinal modes of total mode order $(n + m)$ are degenerate in frequency, see Equation (2.26), which implies that the LG modes could be formed in such a cavity. In an astigmatic cavity with different $g_{(1,2)\,x}$ and $g_{(1,2)y}$ parameters the HG modes will not be at the same frequency so cannot coherently combine [162, 142], see Equation (2.27). For the HG modes to be degenerate the cavity must satisfy $g_{1x}g_{2x} = g_{1y}g_{2y}$.

In an ARR laser cavity the number of mirrors in the ARR can affect the mode frequencies. If there are an odd number of mirrors the odd n HG modes are different in frequency from the even n modes, see Equation (5.26). In this case the degenerate frequency set of HG modes required to form an LG mode will not exist, so LG modes could not be supported in such a cavity (unless a second ARR was used as the other end mirror).

6.4.3 Intra-cavity handedness control

If a cavity meets the symmetry requirements of the previous section it will be able to support LG modes. In general, to use these modes in applications a single handedness vortex is required. The LG modes of different handednesses are cylindrically symmetrical in intensity profile, which means that loss or gain mechanisms that are dependent on the intensity profile of the intracavity mode cannot be used to select different handedness LG modes. For example, the spot defect mirror and gain shaping techniques both use radially dependent losses to make the doughnut shaped modes have the lowest threshold and preferentially oscillate; however, as the different handedness modes have the same intensity profile each is equally likely to oscillate in these designs.

One method to generate a single handedness vortex is to force the cavity to operate

on a single longitudinal mode in combination with making the doughnut shaped modes most favourable [156]. If opposite handedness LG modes were to both oscillate they would coherently combine to form a petal structure, see Figure 2.5(b) p.24. This petal profile will have a poorer overlap with the gain region than the doughnut shaped pure handedness LG vortex, which means that a single handedness mode will have a lower threshold and preferentially oscillate. In this way a single handedness vortex can be generated; however, a further method to differentiate the handednesses is needed to select the desired handedness.

To selectively generate modes with a single handedness the symmetry of the cavity must be broken. This can sometimes be achieved through small misalignments of the cavity components [156]; however, this is not an ideal strategy due to the ambiguity of the mechanism and potential problems with repeatability. To solve this problem alternative handedness selection techniques have been developed.

The standing wave patterns of opposite handedness modes in a linear resonator have different longitudinal node positions. By using two nano-scale thickness wires, the losses of the different handedness modes can be controlled by positioning the wires at the nodes of the standing wave pattern [34]. In doing so the handedness with the lowest loss will preferentially lase, therefore generating a selected handedness mode.

Another method exploits the property of the LG modes that the Poynting vector is not parallel to the optical axis of the beam. By introducing a tilted etalon into the laser cavity the amount of loss for each handedness mode is different, therefore a selected handedness mode will preferentially oscillate [145].

The previous techniques are only necessary when the method to induce vortex modes in a laser cavity is handedness independent. When the mode selection element is inherently handedness dependent additional control methods are not necessary [151]; however, if the oscillating handedness needs to be reversed it may require replacement of intracavity optics [153].

6.5 Coupled anti-resonant ring lasers

Intra-cavity generation of vortex modes has advantages over conversion methods in terms of the mode purity and power that can be achieved. Coupling two separate laser cavities through a common gain medium can be used to induce a vortex mode output from one cavity, by using the second to control the gain distribution. In this section an overview of the techniques to couple laser cavities in this way is given, and a new ARR geometry is proposed as an alternative coupling method. The ARR has advantages over previously demonstrated coupled cavity vortex generation, for example the gain medium does not need to be isotropic [147, 148] and it can introduce negligible cavity loss.

In this section the theory and implementation of vortex generation using coupled cavities is explained. The technique is then used with ARR coupled lasers to generate

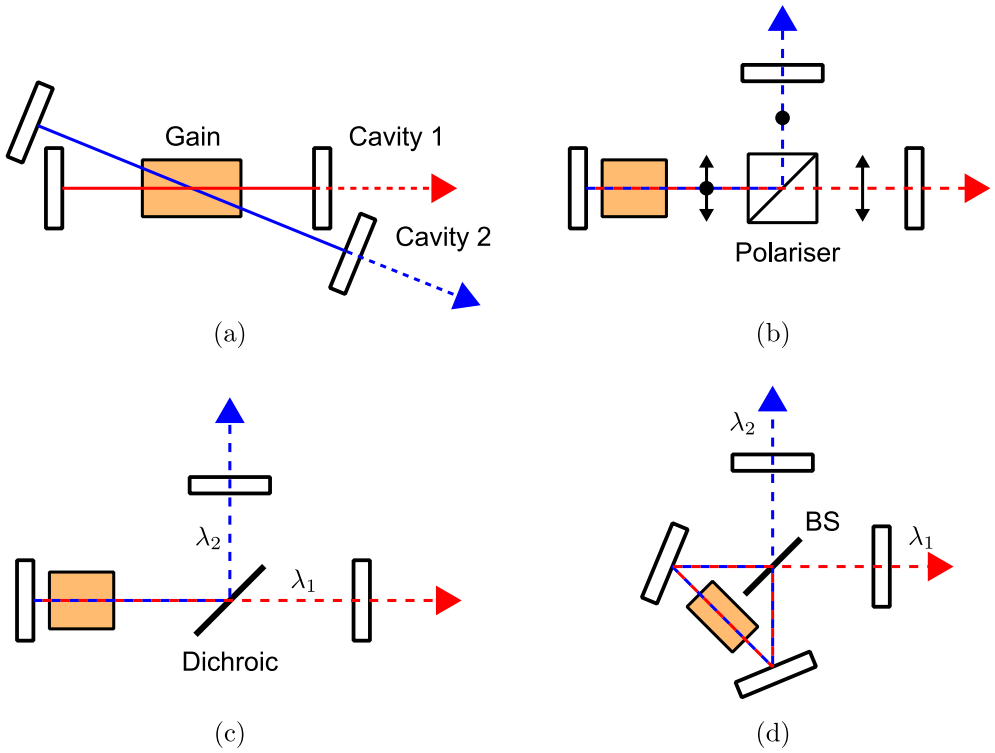

Figure 6.6: Examples of coupled cavity geometries. (a) Small relative angle. (b) Polarisation splitting. (c) Wavelength splitting with dichroic mirror. (d) Wavelength splitting with anti-resonant ring and 50 % beamsplitter (BS).

watt-level LG_{01} and LG_{02} laser modes using a diode-pumped Nd:YVO_4 gain medium.

6.5.1 Coupled laser designs

The concept of coupling two laser cavities through a gain medium provides a rich set of dynamics to explore. The competition between the two cavities for the limited gain region has the analogy of a biological system, where multiple populations (the laser modes) are competing for shared resources (the gain). As is common in biological systems, a small perturbation to one population can have a considerable influence on the other. In the context of laser cavities, this enables situations where one laser cavity controls another, which could either be active or passive, that can allow control of the laser behaviour in a way not possible through direct manipulation with optical elements. There have been some investigations on this type of system, with conceptual cavity designs shown in Figure 6.6. The challenge with these types of systems is to decouple the two laser cavities except for their shared gain. If there is additional coupling between the cavities it may prevent the rich set of dynamics forming due to the strong coupling preventing them from oscillating independently.

A simple way of decoupling is to have separate beam paths for each cavity, where a small angle between them allows the different cavity modes to be spatially separated except in the gain region, as in Figure 6.6(a). This has been shown to be effective in the

temporal control of the cavity gain to suppress unwanted breakthrough lasing in the Q-switching regime [163]. A disadvantage for this type of cavity design is that the different paths of the cavity modes means that the strength of coupling in the gain region will be weaker, or non-existent, in some regions. This can limit the strength of the coupling and therefore the performance of a system.

The cavity modes can have orthogonal polarisations, which allows a polariser to separate the modes as in Figure 6.6(b). This type of system has been used to enable spatial control of the cavity modes to generate optical vortex modes [147, 148, 149]. A limitation of this design is that it can only be used with an isotropic gain medium, where the emission cross section is independent of polarisation. Additionally, the optical components to separate the orthogonal polarisations can introduce significant intra-cavity losses [149].

The different wavelengths of the cavity modes could be used to separate them, for example, by using a dichroic mirror that reflected the wavelength of one cavity and transmitted the other, as in Figure 6.6(c). This method will be limited by the availability and quality of optics that could separate the wavelengths in this way. Dielectric mirrors will be more effective where there is a larger difference between the two wavelengths, making the transition from high reflectance to high transmittance easier to obtain. Alternatives could be prisms or diffraction gratings, but these could have limited power handling capabilities. For narrow gain bandwidth media where the wavelength difference would be of the order of 1 nm all of these methods would likely have insufficient splitting capabilities. These methods would be more suitable for gain media with a broad gain bandwidth.

An alternative to using the different diffraction or reflection and transmission properties of the beams is to separate the wavelengths with an interferometric method. This work proposes to use an ARR for wavelength separation, as in Figure 6.6(d), because the ARR can support independent inputs to the ring if they are at different wavelengths. This is due to the two inputs being incoherent when they recombine at the BS so they do not affect the interferometric recombination of each other. In this way, the ARR can separate input wavelengths when they are closely separated as the only requirement is incoherence.

The concept of gain sharing with an ARR provides significant advantages over the other methods in Figure 6.6. The alignment of the ring means that both cavities must follow collinear paths through the gain region, which ensures the maximum possible overlap of the two cavity modes. The design can be used for polarised emission gain media because each cavity can have the same polarisation, provided that the BS has equal reflectance for each polarisation. It can also be used for narrow emission bandwidth gain media as the ARR can separate incoherent wavelengths. Finally, the ARR introduces a very small intra-cavity loss. The BS will typically introduce a single anti-reflection coated face, and the recombination loss of the beams at the BS was demonstrated to

be negligibly small at 0.01 % in Section 5.3.2. These attributes gives the ARR coupled geometry the potential to be widely applied for the range of known laser gain media.

6.5.2 Mode competition vortex generation

The shape of the gain distribution in a laser will determine the modes that oscillate. Mode competition between two lasers sharing a common gain medium allows one laser cavity to alter the gain distribution, which is used to control the modes in a second cavity. In this section the theory behind this technique is explained and applied to selective generation of the LG_{0l} modes.

Generalised theory

The following analysis uses a model first developed for multiple transverse mode oscillation [164], using the notation in [79], but has been adapted in this work for the case of multiple cavities sharing a gain medium. The parameters of the separate cavities are identified through the j value and the analysis will be performed using the LG_{pl} modes, but it could equally be expanded in terms of the HG_{nm} modes. The transverse modes are assumed to be incoherent so only add in intensity.

In this model, a four-level laser medium has a total pumping rate of $R_\mathrm{p} = P_\mathrm{p}\eta_\mathrm{a}/(h\nu_\mathrm{p})$ that is distributed with the spatial form of $r_\mathrm{p}(r,\phi,z)$, which is normalised with its volume (V) integral as $\int_\mathrm{V} r_\mathrm{p}\,\mathrm{d}V = 1$. Assuming no ground state depletion, the upper laser level population, n_2, and the corresponding gain coefficient, g, are given by

$$n_2(r,\phi,z) = \frac{\tau_\mathrm{f} R_\mathrm{p} r_\mathrm{p}(r,\phi,z)}{1 + c\sigma_\mathrm{e}\tau_\mathrm{f}\sum_{j,p,l}\Phi_{jpl}\phi_{jpl}(r,\phi,z)}\,, \tag{6.6}$$

$$g(r,\phi,z) = \sigma_\mathrm{e} n_2(r,\phi,z)\,, \tag{6.7}$$

where each cavity mode is identified through its cavity label j and the LG_{pl} mode order numbers, Φ_{jpl} is the total photon number in that mode, and ϕ_{jpl} is the normalised distribution of the mode with $\int_\mathrm{V}\phi\,\mathrm{d}V = 1$. The round trip gain condition for lasing equates the power gained from stimulated emission to that lost through losses and output coupling, which in this spatially dependent case is

$$2\int_\mathrm{V} g(r,\phi,z) I_{jpl}(r,\phi,z)\,\mathrm{d}V = P_{jpl}(L_{jpl} + T_j)\,, \tag{6.8}$$

where I_{jpl} is the one way intensity of each mode, P_{jpl} is the one way power of each mode, and L_{jpl} and T_j are the round trip losses and output coupler transmissions of the jth cavity, respectively. The losses are shown as dependent on mode order (p,l) to allow for

spatially dependent loss elements. The mode intensities and powers are given by

$$I_{jpl} = \Phi_{jpl}\phi_{jpl}\frac{ch\nu_{\mathrm{l}}}{2}\,, \tag{6.9}$$

$$P_{jpl} = \Phi_{jpl}\frac{ch\nu_{\mathrm{l}}}{2L}\,, \tag{6.10}$$

where the relation for P_{jpl} is valid if the mode intensity is independent of z, and L is the cavity length. Substituting these into the round trip gain condition yields

$$J_{jpl}(\Phi_{1,0,0},\dots) = \frac{1}{\phi_{\mathrm{s}}R}\frac{c(L_{jpl}+T_j)}{2L}\,, \tag{6.11}$$

$$J_{jpl}(\Phi_{1,0,0},\dots) \equiv \int_{\mathrm{V}} \frac{r_{\mathrm{p}}\phi_{jpl}}{1+\phi_{\mathrm{s}}^{-1}\sum_{j,p,l}\Phi_{jpl}\phi_{jpl}}\,\mathrm{d}V\,, \tag{6.12}$$

where J_{jpl} is a function of all the Φ_{jpl} parameters, and $\phi_{\mathrm{s}}^{-1} = c\sigma_{\mathrm{e}}\tau_{\mathrm{f}}$ is the laser saturation factor. The solutions to this equation define how the laser modes in coupled cavities will behave.

The function J_{jpl} quantifies the quality of overlap between the (j,p,l)th mode and the pumped region. When there are no modes oscillating in the cavities, $\Phi_{jpl} = 0$, the overlap relationship is easily identified as

$$J_{jpl}(0) = \int_{\mathrm{V}} r_{\mathrm{p}}\phi_{jpl}\,\mathrm{d}V\,. \tag{6.13}$$

The additional terms in the denominator of Equation (6.12) represent the saturation of the population inversion through stimulated emission and are only present when a mode is oscillating ($\Phi_{jpl} \neq 0$).

To understand the consequences of this solution, it is easiest to consider a coupled system starting with no pumping, $R = 0$. At this point, no mode could satisfy Equation (6.11) as J_{jpl} cannot be infinite, therefore $\Phi_{jpl} = 0$ for all (j,p,l). As the pumping rate R increases the first mode to reach threshold is the first to satisfy Equation (6.11) with its $J_{jpl}(0)$ parameter.

If this were the (j,p,l)=$(1,0,0)$ mode, then as R increased beyond threshold the value of $\Phi_{1,0,0}$ would be found by ensuring that Equation (6.11) was satisfied. As both $\Phi_{1,0,0}$ and R are in the denominators, as one increases so must the other.

Further increasing the pumping rate R may mean that another mode satisfies Equation (6.11), for example the $(2,0,0)$ mode. To find the powers of each mode at this point Equation (6.11) gives a coupled system of equations in $\Phi_{1,0,0}$ and $\Phi_{2,0,0}$ that must be solved.

The complexity of using this equation should now be apparent. As multiple modes reach threshold each has its own gain condition to satisfy, giving a coupled system of equations equalling the number of modes oscillating, which will typically require a numerical solution. Despite the complexity of finding the full solution, the influences of

each parameter in Equation (6.11) can be used to qualitatively understand the behaviour of the transverse modes in a coupled cavity geometry.

Vortex generation

To induce a pure vortex mode in a laser cavity it must be made the lowest threshold mode. For the typical Gaussian or top-hat transverse pump profiles the fundamental HG_{00} will always have a lower threshold than the LG_{0l} modes. This is because the intensity of the HG_{00} is peaked at the centre of the optical axis, so matches well with the Gaussian or top-hat pump. One method to make the LG_{0l} modes lower in threshold is to reshape the transverse spatial distribution of the gain.

The transverse gain distribution in a laser will change when a laser mode is extracting energy from stimulated emission, which is shown through the Φ_{jpl} term reducing the upper level population (n_2) in Equation (6.6). This is the basis of the coupled cavity technique for vortex generation. One laser cavity is used to saturate the gain and alter its transverse profile, then a second separate cavity is induced into a pure vortex mode from the reshaped gain region.

An example geometry for vortex mode production in a coupled cavity design is shown in Figure 6.7. In this configuration the primary cavity ($j = 1$) is targeted for the vortex mode and the secondary cavity ($j = 2$) is used to control the gain distribution. Both cavities have similar HG_{00} mode sizes at the gain region, but the secondary has a lower transmission output coupler ($T_2 < T_1$) and an aperture (AP) to control the losses of higher order modes. The shared gain medium is end-pumped with a Gaussian profile, with the size of the pumped region matching that of the required LG_{0l} mode in the primary cavity.

The gain reshaping mechanism for the coupled system of Figure 6.7 is illustrated in Figure 6.8. The graphs in (a) to (d) show cross sections through the gain medium. The gain distribution (green) was calculated using Equation (6.7). The mode distributions are shown for the secondary cavity HG_{00} (blue), and the primary cavity LG_{01} (red) and LG_{02} (cyan). The mode sizes for LG_{01} generation are shown in Figure 6.8(c), with the LG_{02} configuration in Figure 6.8(d).

Below threshold the gain distribution matches the pump so is Gaussian shaped, see Figure 6.8(a). As the pumping rate increases, the secondary cavity reaches threshold first due to its lower total losses for the HG_{00} mode, $(L_{2,0,0} + T_2) < (L_{1,0,0} + T_1)$. As the pumping rate is further increased, the central gain region is clamped at the threshold value of the secondary cavity, which changes the shape of the gain distribution, see Figure 6.8(b). The higher order modes cannot reach threshold in the secondary cavity because of the AP introducing a spatially dependent loss, so $L_{2,p,l} \gg L_{2,0,0}$.

As the pumping rate is increased, gain clamping of the secondary cavity makes the gain distribution better match the targeted LG_{0l} mode in the primary cavity compared to the HG_{00}. In Figure 6.8(c) this is the LG_{01} mode, which makes it the lowest threshold

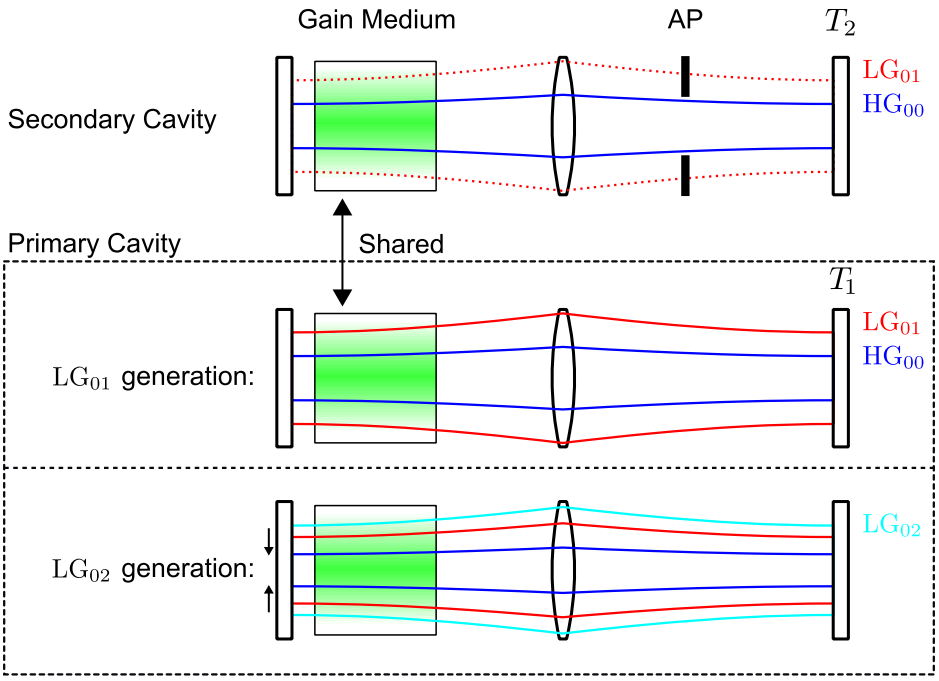

Figure 6.7: A gain coupled cavity design for vortex generation. The secondary cavity ($j = 2$) is used to control the spatial distribution of the gain using an intracavity aperture (AP), which induces a vortex mode in the primary cavity ($j = 1$) by matching the reshaped gain medium size to a LG_{0l} mode. The mode sizes are indicated for the HG_{00} (blue), LG_{01} (red) and LG_{02} (cyan) modes in each cavity, with the gain distribution in green. The output coupler transmissions are T_j.

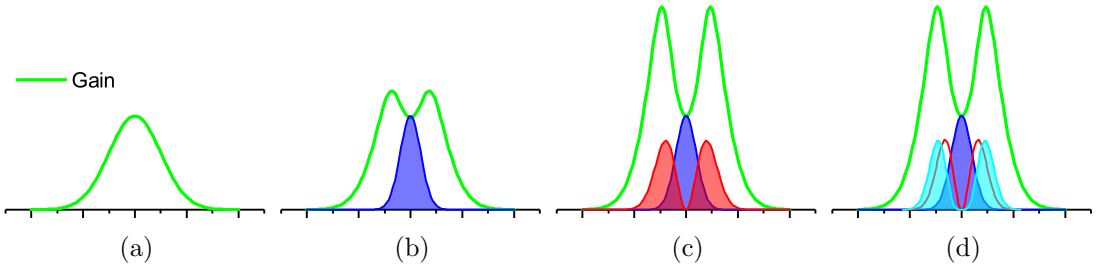

Figure 6.8: The gain reshaping for vortex generation from the cavity configuration of Figure 6.7 with Gaussian end pumping. The graphs are cross sections of the gain medium showing the: gain (green), HG_{00} size of the secondary cavity (blue), LG_{01} size in the primary cavity (red), and the LG_{02} mode size in the primary cavity (cyan). The distributions given are: (a) below laser threshold; (b) above the secondary cavity threshold; (c) at the primary cavity threshold for LG_{01} generation; and (d) at the primary cavity threshold for LG_{02} generation.

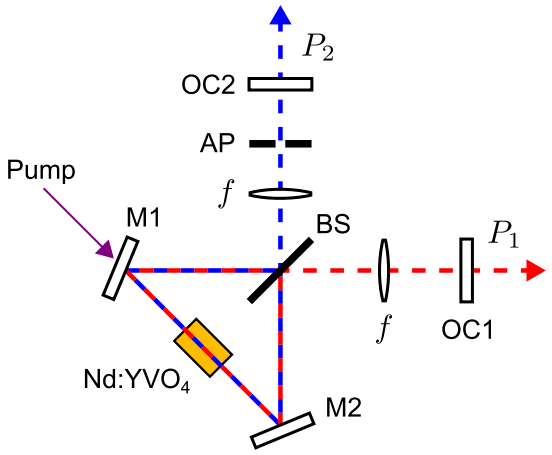

Figure 6.9: The ARR coupled laser geometry used for vortex generation. The primary and secondary cavity paths are in red and blue, respectively. The ARR is formed between a 50 % BS and two turning mirrors, M1 and M2. The primary cavity has output coupler OC1 and a lens of focal length f. The secondary cavity has output coupler OC2, a lens of focal length f, and an iris aperture (AP). The Nd:YVO_4 gain medium was end pumped through M1.

mode in the primary cavity. This is the case of $J_{1,0,1} > J_{1,0,0}$ from the generalised theory. Once the LG_{01} mode has reached threshold in the primary cavity the entire gain region is clamped by the oscillating modes and no further higher order modes can reach threshold.

This technique can be adapted to generate the higher order LG_{0l} modes by changing the relative sizes between the cavity modes and gain region. In Figure 6.7 this is achieved by reducing the mode sizes in the primary cavity so that the LG_{02} mode matches the gain region size. By doing so, the gain now overlaps the LG_{02} mode better than the LG_{01} mode giving the LG_{02} mode a lower threshold and making this the oscillating mode in the primary cavity. This situation is shown in Figure 6.8(d), where the secondary cavity now acts to suppress both the HG_{00} and LG_{01} modes in the primary cavity.

6.5.3 Experimental vortex generation

The proposed ARR coupled laser design was implemented for vortex generation using the cavity shown in Figure 6.9, which used the principles of vortex mode control in Figure 6.7. The ARR was formed between a 50 % beamsplitter (BS) and two dichroic turning mirrors M1 and M2, which both had high reflectance at laser wavelengths and high transmission for the pump at 808 nm. The ring had a perimeter of 55 mm.

The primary cavity used one input to the ARR and was formed with the output coupler OC1, which had a reflectance of 60 %, with spatial mode control from an $f =$ 75 mm lens. The secondary cavity used the other input to the ARR and was formed with the output coupler OC2, with 80 % reflectance, and had an $f = 75$ mm intra-cavity lens. The secondary cavity also had an iris aperture (AP) for higher order spatial mode control. The primary cavity was designed to support the vortex laser modes, with the

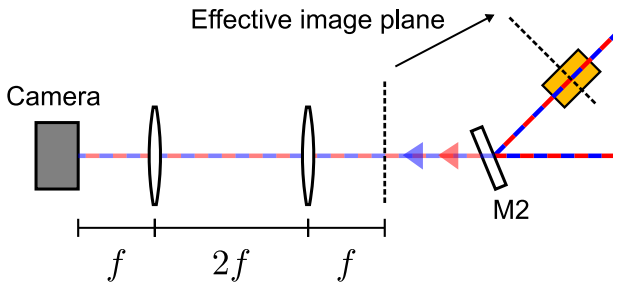

Figure 6.10: The measurement of the beam sizes at the gain region. The cavity modes were partially transmitted through M2 of the ARR, which were then relay imaged onto a camera using two lenses of focal length f. The beams were imaged at the plane at which they would have been incident on the gain region.

secondary cavity providing spatial control of the gain region.

The gain medium was a 0.5 % doped Nd:YVO_4 slab, 5 mm long by 2 mm square, which operated on the 1064 nm laser transition and was positioned centrally in the ARR. It was end-pumped through M1 with the same source as in Section 5.3.2, an 808 nm fibre coupled diode module that had a maximum power of 26.2 W. The beam waist at the crystal was 440 µm in diameter.

A key parameter for vortex generation in this design is the size of the modes at the gain region. This was adjustable in both cavities by moving the lenses or output couplers to change the intra-cavity distances and therefore the mode sizes. Accurately determining mode sizes in a laser cavity from theoretical equations, as in Section 2.2, is generally a difficult task. There are uncertainties in the dimensions and properties of the intra-cavity elements, along with accurately determining the thermal lens in the gain region. If a cavity is near a stability edge any small variation in the input parameters can have a large effect on the resulting mode sizes. If an accurate mode size measurement is required it must be measured directly.

In the ARR coupled laser geometry it was possible to directly measure the mode sizes in the gain region by imaging the fraction of the intra-cavity beams that were transmitted through M2, as shown in Figure 6.10. Two lenses of focal length f were used to reproduce the transmitted beam at the position of the gain region onto a camera, which allowed direct measurement of the mode sizes.

Directly measuring the LG_{01} diameter of the primary cavity was not possible. When the primary cavity was operating on the LG_{01} mode the transmitted beam through M2 was a mixture of both cavity modes. To find the LG_{01} mode diameter in the primary cavity, its HG_{00} mode diameter was measured by introducing an intra-cavity AP to force HG_{00} oscillation, whilst having the secondary cavity AP fully closed. This diameter corresponded to the underlying Gaussian size w_{00}, so multiplication by $\sqrt{2}$ gave the LG_{01} mode diameter, see Equation (2.30) p.28.

An angled plate has different optical paths lengths for the horizontal and vertical axes with respect to the rotation axis [162]. The BS used had a thickness of 3 mm,

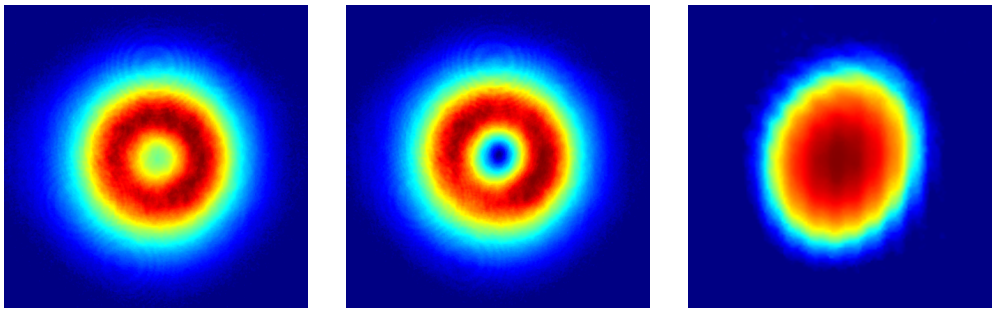

(a) Primary (b) Primary (c) Secondary

Figure 6.11: The mode profiles of the primary and secondary cavities with: (a), AP closed; (b) and (c), AP open.

which introduced an optical path length difference of 0.8 mm between the horizontal and vertical planes. The frequency difference between the $HG_{(n+1)m}$ and $HG_{n(m+1)}$ modes is $\Delta\nu = (\nu_{(n+1)mq} - \nu_{n(m+1)q})$, which is given by Equation (2.27), p.27, by introducing the path length difference when calculating the g parameters.

The dimensions of the primary cavity were, $R_1 = \infty$, $l_1 = 60\,\text{mm}$, $f = 75\,\text{mm}$, $l_2 = 100\,\text{mm}$, and $R_2 = 100\,\text{mm}$ ($f_\text{R} = 50\,\text{mm}$). From these cavity dimensions and the BS path length astigmatism, the frequency difference was calculated to be $\Delta\nu = 1.2\,\text{MHz}$. For the cavity to support LG_{01} modes the HG_{01} and HG_{10} modes must be at the same frequency ($\Delta\nu = 0$). Although from these calculations it appears that the primary cavity should not be able to support LG_{01} modes due to the frequency difference, it has been shown that for separations of the order of a few MHz the transverse modes will lock together in frequency [165].

First order vortex

The ARR coupled lasers were initially used to generate first order LG_{01} vortex modes in the primary cavity. The iris AP had no calibrated scale or adjustment mechanism, so the hole diameter had to be optimised for each measurement. The mode profiles of the primary cavity before and after opening the secondary cavity aperture are shown in Figure 6.11, along with the secondary cavity mode profile. The beam qualities of the primary cavity mode with the AP open were $M_x^2 = 2.1$ and $M_y^2 = 2.0$, which indicates an LG_{01} mode.

In vortex beam applications, an important parameter can be the azimuthal intensity fluctuation, which is how the beam intensity changes along a circular cross section. This was assessed by measuring the standard deviation of an azimuthal cross section centred on the beam centroid at the radius of maximum average intensity. With the secondary cavity blocked, the primary cavity mode in Figure 6.11(a) had an azimuthal intensity standard deviation of 4 %. When operating in the LG_{01} mode with the secondary cavity lasing, Figure 6.11(b), this increased to 7 %, which indicates that the secondary cavity introduced a small asymmetry in the primary cavity.

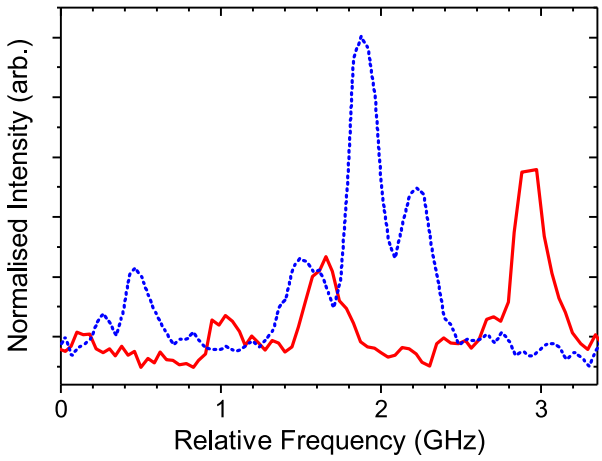

Figure 6.12: The typical frequency spectra of the primary (solid red) and secondary (dotted blue) cavities in the ARR coupled laser, measured using a FP interferometer.

With the AP fully closed so that the primary cavity had exclusive access to the gain region it oscillated on both the HG_{00} and LG_{01} modes, see Figure 6.11(a). To suppress the HG_{00} mode the AP was opened. As the AP diameter was increased it would first cause the centre of the primary cavity profile to become increasingly suppressed, until the point of zero intensity, as in Figure 6.11(b). Further increasing AP diameter would reduce the output power of the primary cavity until it was completely suppressed and only the secondary cavity oscillated.

The secondary cavity could lase without completely suppressing the HG_{00} mode in the primary cavity. At this point, the large round trip cavity losses from diffraction at the AP would make the total round trip loss in the secondary cavity comparable to that in the primary cavity. This means that both cavities had approximately equal thresholds for the HG_{00} modes so could coexist. The AP diameter could be further increased until the centre of the primary cavity profile reached zero intensity, at which point the HG_{00} mode was completely suppressed. Provided that the LG_{01} mode size in the primary cavity was properly matched to the gain region, then the primary cavity oscillated on only LG_{01} modes.

To verify that the two cavities were sufficiently decoupled by the ARR the frequency spectra of the outputs were measured with a FP etalon. The typical frequency spectra are shown in Figure 6.12 for the primary (P_1) and secondary (P_2) cavity outputs. The primary cavity oscillated on multiple longitudinal modes with 680 MHz spacing. The secondary cavity had a more complicated spectrum from the existence of higher order transverse modes. The key result from this data is that the two cavities oscillated on separate frequencies. This confirms that each laser was fully decoupled by the ARR, otherwise they would have had common frequencies due to injection locking.

The presented results have shown that vortex modes can be generated in this cavity design; however, the efficiency of pump to vortex power conversion is an important

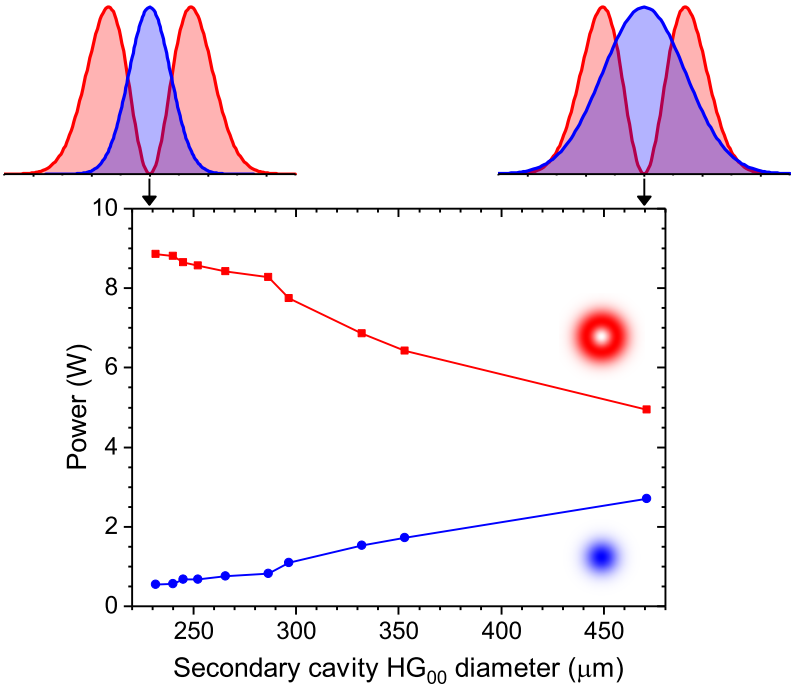

Figure 6.13: The primary (P_1, red squares) and secondary (P_2, blue circles) cavity powers for changing HG_{00} mode diameter of the secondary cavity at the gain region. The theoretical mode profiles above the graph shows the correctly scaled overlap of the modes in the gain region at the indicated points.

factor to determine the practical usefulness of this technique. The relative mode sizes of both the primary and secondary cavities compared to the gain region are important parameters, so these were investigated to find the optimum efficiency of vortex generation in the investigated system.

The mode size of the secondary cavity at the gain region was varied by altering the distance between OC2 and the intra-cavity lens, as determined by Equations (2.9) and (2.10). For a range of mode sizes the AP was optimally adjusted to maximise the power of the primary cavity whilst maintaining LG_{01} modes, with the resulting powers of the primary and secondary cavities shown in Figure 6.13. Also illustrated are the mode profiles of the secondary cavity HG_{00} and primary cavity LG_{01} modes at the crystal. For this set of measurements the LG_{01} mode diameter was 470 µm, from the underlying Gaussian diameter of 330 µm. The power in the vortex mode was optimised when the secondary cavity HG_{00} diameter was 230 µm, with $P_1 = 8.9$ W and $P_2 = 0.54$ W at a pump power of 23.2 W. As the mode size of the secondary cavity increased the power of the vortex output decreased.

The reason for the changing powers in the vortex cavity can be seen from the mode profiles shown in Figure 6.13. A large secondary cavity mode lead to a greater overlap between the LG_{01} and HG_{00} modes in the primary and secondary cavities, respectively. This meant that the secondary cavity clamped the gain region where the primary cavity could have extracted energy from. In this way, the available gain for the primary cavity

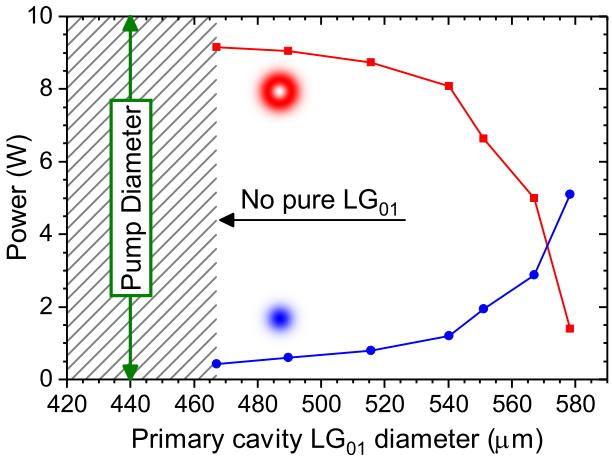

Figure 6.14: The primary (P_1, red squares) and secondary (P_2, blue circles) cavity powers for changing LG_{01} mode size of the primary cavity at the gain region. The secondary cavity AP was optimised at each point. The green line indicates the pump waist diameter.

was reduced so the power decreased. If the mode size was further increased it would have likely prevented lasing altogether in the primary cavity.

As the HG_{00} mode size became smaller in the secondary cavity the HG_{00} mode was still suppressed in the primary cavity but the LG_{01} mode had a greater overlap with the gain region, which gave a greater efficiency. If the mode size of the secondary cavity could have been decreased further there would have come a point at which its HG_{00} mode would have overlapped with too little of the gain region to suppress the HG_{00} mode in the primary cavity. At this point higher order modes would have to be allowed in the secondary cavity to fully suppress the HG_{00} mode in the primary cavity.

The vortex generation efficiency was further optimised by changing the size of the primary cavity mode in the gain region. The mode size was altered by changing the lens to OC1 distance. The output powers P_1 and P_2 are shown against the primary cavity LG_{01} mode diameter at the gain region in Figure 6.14, at each point the secondary cavity AP size was adjusted for optimum vortex power output. The power in the vortex mode increased for decreasing mode size and was optimised at a diameter of 467 µm, where $P_1 = 9.2\,\mathrm{W}$ and $P_2 = 0.43\,\mathrm{W}$ at an input pump power of 23.2 W. At this optimum power the primary cavity LG_{01} mode was 6 % larger in diameter than the pump beam waist.

If the LG_{01} mode diameter was smaller than 467 µm pure LG_{01} modes in the primary cavity could not be obtained. Other transverse modes could extract gain from areas that the LG_{01} could not, which allowed them to reach threshold and oscillate. The LG_{01} size optimisation was a balance between maximising the overlap between the LG_{01} profile and the gain region, whilst ensuring that the higher order modes did not reach threshold.

The ARR coupled lasers were tested over a range of pump powers, with the output powers of both cavities against input pump power shown in Figure 6.15(a). The changing thermal lens with pump power also affected the mode sizes in the cavities. To ensure the

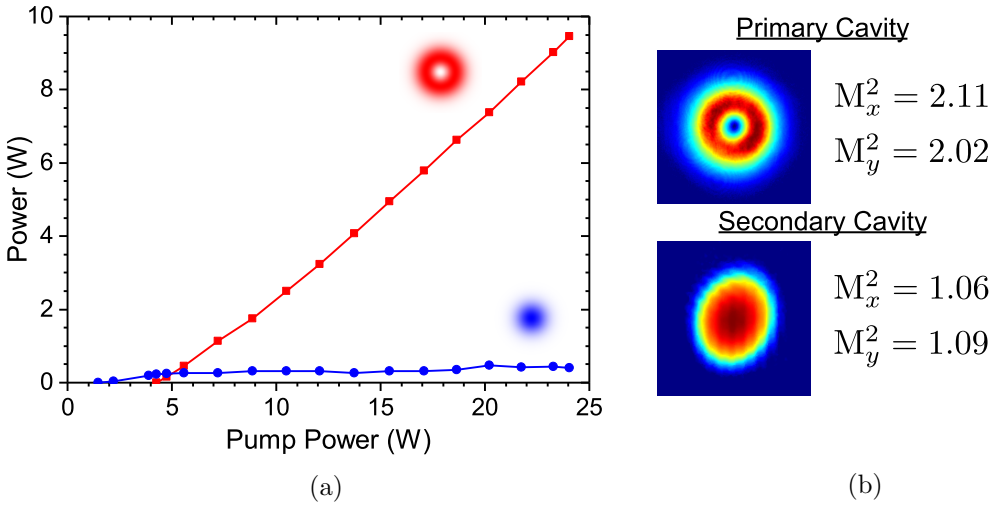

(a) (b)

Figure 6.15: (a) The output power of the primary (P_1, red squares) and secondary (P_2, blue circles) cavities for a range of input pump powers, with the output intensity profiles and beam qualities at maximum pump power in (b).

optimum mode size in the primary cavity OC1 was moved at each pump power, the AP was also adjusted for each measurement. The secondary cavity reached threshold first as expected, with the threshold of the LG_{01} mode of the primary cavity being higher. The higher power and efficiency of vortex generation was at the maximum pump power of 24.0 W, where $P_1 = 9.45\,\mathrm{W}$ and $P_2 = 0.40\,\mathrm{W}$.

The power of the LG_{01} mode was higher as it had access to a greater proportion of the gain region compared to the small HG_{00} mode of the secondary cavity. The efficiency of vortex generation will have also benefited from the HG_{00} mode size becoming smaller for increasing pump powers.

The beam profiles of the primary and secondary cavities at maximum power are shown in Figure 6.15(b). The beam qualities of the secondary cavity were $M_x^2 = 1.06$ and $M_y^2 = 1.09$, which verify that it was oscillating on the HG_{00} mode. The beam qualities of the primary cavity were $M_x^2 = 2.11$ and $M_y^2 = 2.02$, which indicates that it was composed of LG_{01} shaped modes that have $M_{x,y}^2 = 2$.

To check the phase structure of the vortex modes the fork and spiral interferograms were measured, as described in Section 6.4.1, and are shown in Figure 6.16. Both the fork and spiral pattern were not clearly defined, which shows that the modes were either not of pure handedness or were incoherent additions of other transverse modes, as discussed in Section 6.4.1. A mixture of handedness modes would be expected for a symmetrical cavity where there is no bias towards one handedness.

The handedness of the vortex could have been determined using the methods outlined in Section 6.4.3; however, an alternative method of introducing asymmetry for handedness control was found. The overlap of the two modes at the gain region is shown in Figure 6.17, which shows the experimentally measured intensity at the gain region and the corresponding primary and secondary mode positions. The initial alignment was

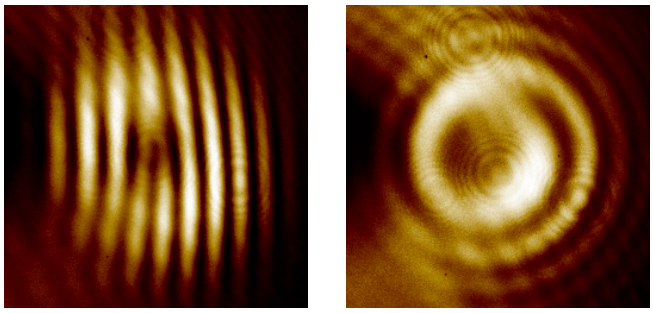

(a) (b)

Figure 6.16: The (a) fork and (b) spiral interferograms of the primary cavity output at the maximum power in Figure 6.15.

for both cavities to be collinear, as in Figure 6.17(b), which made the secondary cavity symmetrically saturate the gain. The secondary cavity mode could be diagonally offset from the central position by adjusting the horizontal and vertical tilt of OC2, as in Figures 6.17(b) and (c). In doing so, the HG_{00} mode in the primary cavity would remain suppressed without significantly effecting the output powers of the cavities; however, it would also cause the primary cavity LG_{01} modes to oscillate with a common handedness. By adjusting the position of the secondary cavity mode either handedness direction could be selectively generated.

The position of the secondary cavity mode in Figure 6.17(a) compared to (c) was a 90° rotation about the primary cavity centre. The handedness control was also effective for further 90° rotations, with opposite diagonal positions giving the same handedness modes. The precise mechanism for this method to control the vortex handedness requires further investigation; however, it is likely that the asymmetries introduced in the gain region and thermal lens by the off-centre secondary cavity mode caused conditions more favourable to one handedness than the other. Despite the precise mechanism being unknown, this method of handedness selection was robust and repeatable.

The mode profiles, and fork and spiral interferograms for the (a), (b) and (c) cases in Figure 6.17 are shown in Figure 6.18. When the secondary cavity was centered on the gain region, as in Figure 6.17(b), the fork and spiral interferogram patterns were unclear suggesting that there were multiple handededness LG_{01} modes oscillating. When the secondary cavity position was changed in (a) and (c) the inteferogram patterns became clear, showing that the LG_{01} modes were operating with common handednesses. The direction of the patterns reversed between the (a) and (c) alignments, which shows that the handedness direction of the modes reversed.

The output powers of the cavities remained approximately constant when implementing the handedness selection. For the (a), (b) and (c) alignments in Figures 6.17 and 6.18, the primary cavity outputs were 8.90 W, 9.00 W and 8.95 W, and the secondary cavity outputs were 0.86 W, 0.85 W and 0.85 W, respectively. The constant output powers were because the mode content and gain overlap of each cavity did not change

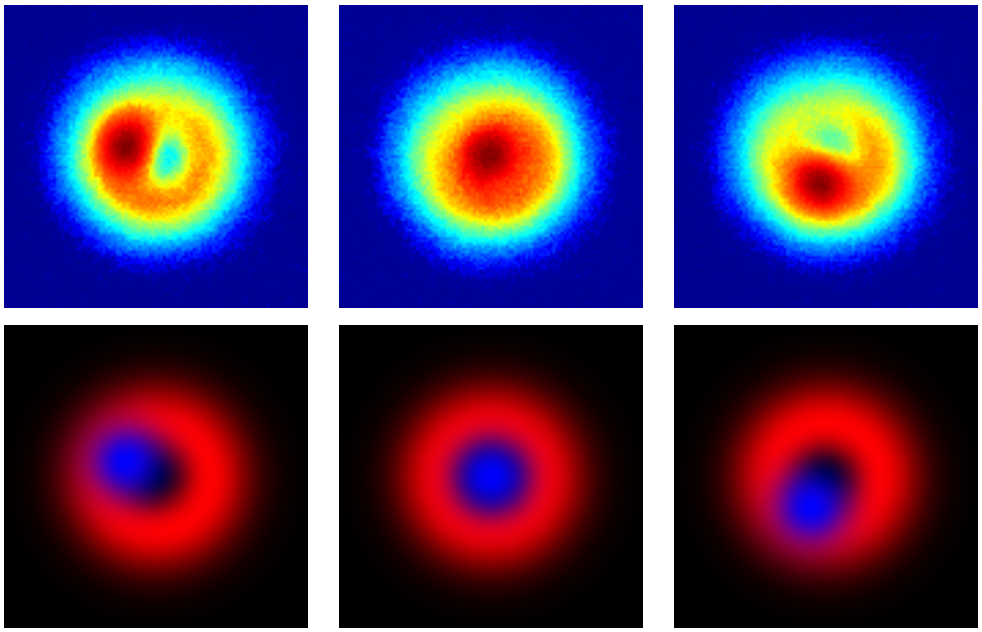

(a) (b) (c)

Figure 6.17: The handedness control method using the position of the secondary cavity mode for (b) no selection, (a) and (c) opposite handednesses. The images show the measured overlapping mode intensities at the gain region (top row) and illustrations of the components (bottom row) with the primary cavity LG_{01} mode in red and the secondary cavity HG_{00} mode in blue.

between the secondary cavity adjustments. As the secondary cavity mode was moved and saturated another part of the gain region more strongly, there was a corresponding region that was saturated less. This meant that the overall gain available to the primary cavity was approximately constant. The overall efficiency of vortex generation was lower than in Figure 6.15 because the AP diameter had to be larger for the secondary cavity to be able to saturate the HG_{00} mode in the primary cavity when not centred.

The beam qualities of the secondary cavity remained close to one when changing its mode position, so remained in the HG_{00} mode. The primary cavity had symmetrical beam qualities that were between $2.0 < M^2_{x,y} < 2.1$ for every alignment, which implies a high LG_{01} mode purity.

To further assess the mode purity of the pure handedness LG_{01} modes in Figure 6.18, intensity profile horizontal cross sections were compared to the theoretical LG_{01} mode and are shown in Figure 6.19. Both handedness modes were excellent matches to the theoretical intensity profiles of Equation (2.15); in particular, the intensity minima at the beam centres were 0.7 % and 0.3 % of the peaks in (a) and (b), respectively, with the precision limited by the dynamic range of the camera. The excellent fits to the theoretical LG_{01} profile confirm the high mode purity of the vortices generated.

Before offsetting the secondary cavity, Figure 6.18(b), the primary cavity mode azimuthal intensity standard deviation was 9 %, which was higher than in Figure 6.11(b)

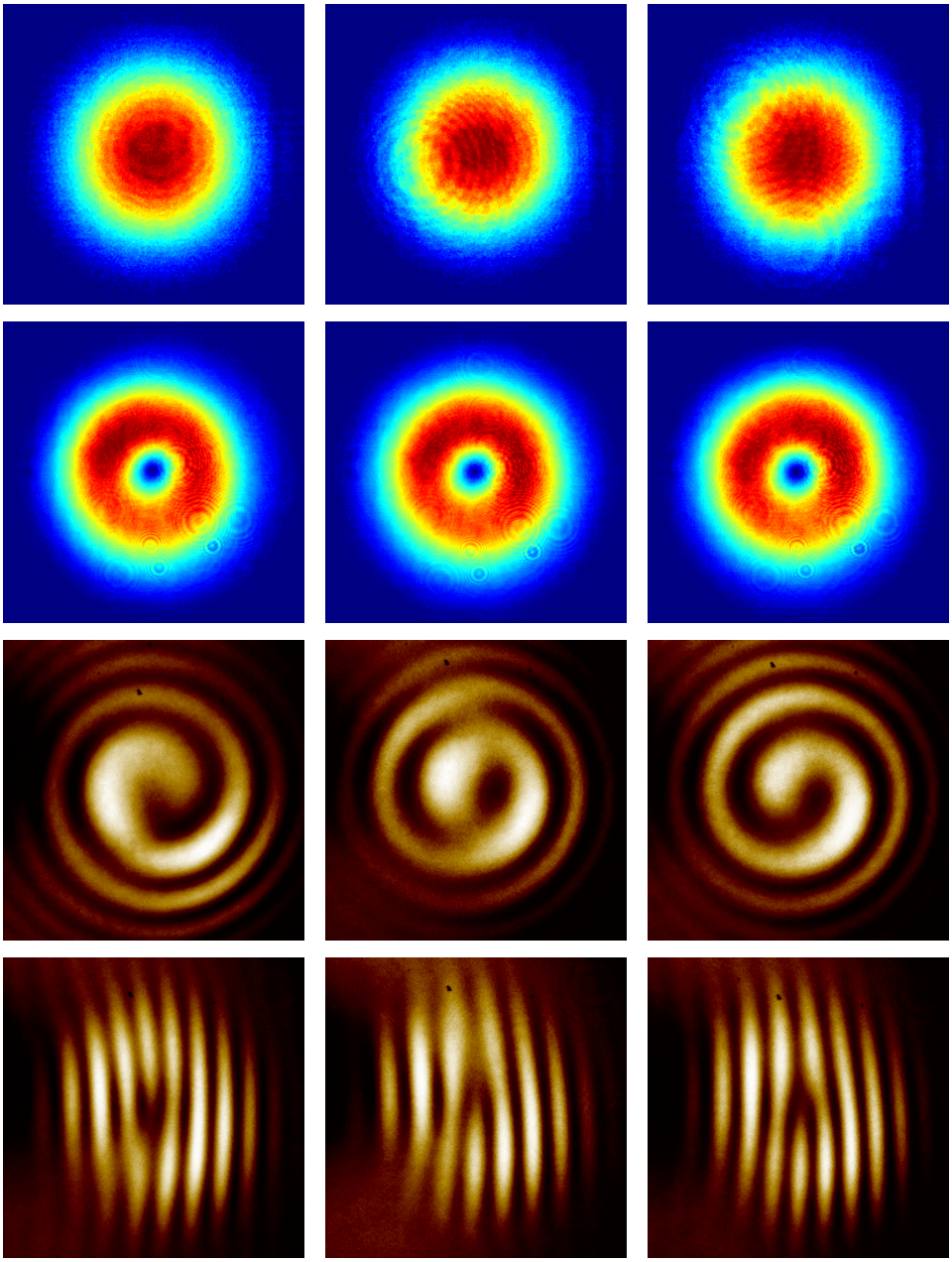

(a) (b) (c)

Figure 6.18: The laser output using the secondary cavity position handedness control for (a) one handedness, (b) no handedness selection, and (c) opposite handedness. The images show the secondary cavity (top row) and primary cavity (second row) mode profiles, with the spiral (third row) and fork (bottom row) interferograms.

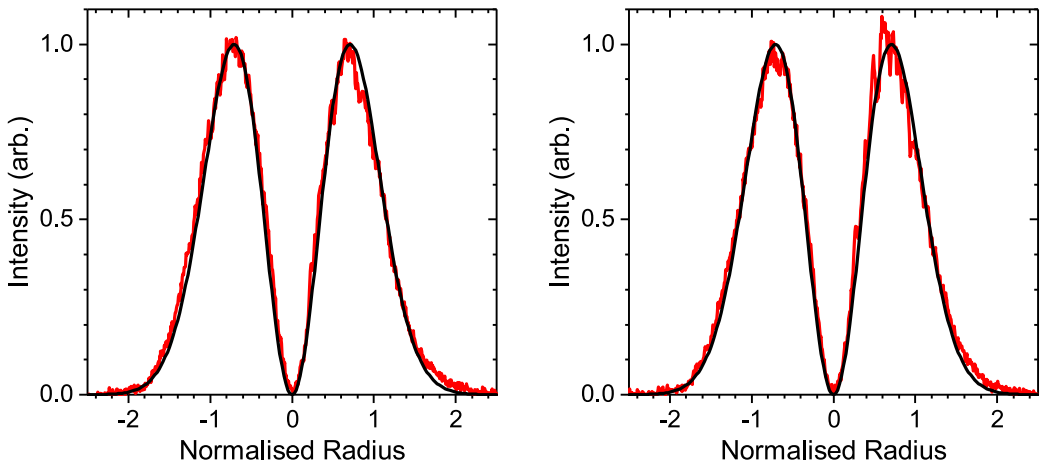

Figure 6.19: The experimental (red) and fitted theoretical (black) intensity profile horizontal cross sections of the LG_{01} pure handedness modes, where (a) is from Figure 6.18(a), and (b) is from Figure 6.18(c). The horizontal scale has been normalised to the underlying Gaussian size (w_{00}).

due to the stronger influence of the secondary cavity and therefore asymmetry effects. When offsetting the secondary cavity position to select the vortex handedness, Figures 6.18(a) and (c), the primary cavity azimuthal intensity standard deviation increased to 10 %. This suggests an almost negligible impact of the handedness selection method on the vortex beam asymmetry.

The presented results have shown that high spatial and handedness purity LG_{01} modes can be generated in the ARR coupled geometry, where the handedness could be controlled with the alignment of the secondary cavity. The vortex generation was efficient, with 9.0 W of output power from 24 W of pump power.

Second order vortex

The ARR coupled ring lasers were configured to generate a second order LG_{02} vortex mode. As described in Section 6.5.2, this required that the LG_{02} mode in the primary cavity was matched in diameter to the gain region and the secondary cavity suppressed both the HG_{00} and LG_{01} modes.

To match the gain region size to the LG_{02} mode in the primary cavity the OC1 to lens distance was increased. The secondary cavity was adjusted to suppress the LG_{01} and HG_{00} modes by increasing the AP diameter. These two parameters were optimised to give the highest power and quality LG_{02} mode in the primary cavity. The resulting mode profiles of the primary and secondary cavities are shown in Figures 6.20, along with the fork and spiral interferograms of the primary cavity output.

The power of the primary and secondary cavities were $P_1 = 4.3$ W and $P_2 = 4.4$ W, respectively, at a pump power of 24 W. The vortex power was lower than for LG_{01} generation because the secondary cavity needed to saturate the gain region that the

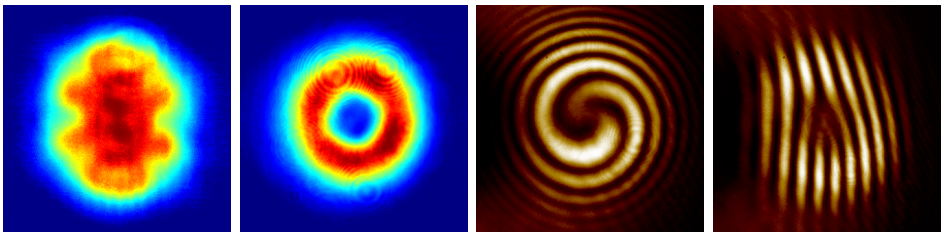

(a) (b) (c) (d)

Figure 6.20: Beam images for LG_{02} generation for: (a) secondary cavity, (b) primary cavity, (c) spiral interferogram, and (d) fork interferogram.

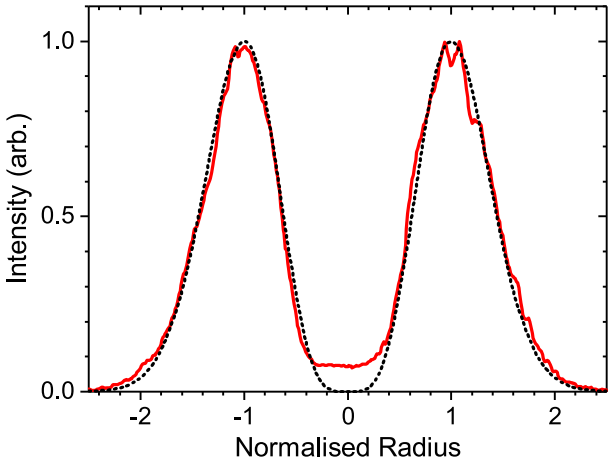

Figure 6.21: The intensity profile horizontal cross section of the primary cavity for LG_{02} generation (red), fitted to the theoretical LG_{02} profile (black). The horizontal scale has been normalised to the underlying Gaussian size (w_{00}).

LG_{02} mode could extract from to suppress the LG_{01} mode. This is in contrast to LG_{01} generation, where the HG_{01} mode that was suppressed had its highest overlap with the gain region at the centre where the LG_{01} mode had zero intensity.

The secondary cavity had a multimode beam, which was required to provide a large enough mode to suppress the LG_{01} mode in the primary cavity. The secondary cavity beam diameter at the gain region was 370 µm, which was larger than that for LG_{01} generation of 230 µm.

The LG_{02} diameter of the primary cavity at the gain region was 540 µm. The beam qualities of the primary cavity were $M_x^2 = 3.05$ and $M_y^2 = 3.13$, which matched well with the theoretical LG_{02} mode of $M_{x,y}^2 = 3$. To further assess the LG_{02} mode purity a horizontal cross section of the intensity profile was taken and compared to the theoretical LG_{02} mode and is shown in Figure 6.21. The LG_{02} mode had symmetry comparable to the LG_{01}, with an azimuthal intensity standard deviation of 9 %. The peaks of the cross section matched well with theory, which suggests that the LG_{02} mode was dominant; however, the intensity on axis was 7 % of the peak intensity and not zero as required.

The non-zero intensity on axis implies that there was some modal impurity to the primary cavity output. With reference to Figure 2.5 (p.24), the LG_{p0} modes are the only

LG modes that have intensity on axis. These modes have concentric rings of intensity surrounding the central spot. It is possible that these rings were able to overlap gain regions that were not clamped by the dominant modes of either the primary or secondary cavities, which allowed them to reach threshold.

The fork and spiral interferograms of the primary cavity output in Figure 6.20(c) and (d) show that the phase structure of the output matched that of the LG_{02} mode. The fork pattern had two extra fringes and there were two arms in the spiral interferogram. The clarity of the pattern suggests that the LG_{02} modes were oscillating with a common handedness. The handedness selection method used for LG_{01} generation was not possible for LG_{02} generation because the symmetrical position alignment of the secondary cavity was needed to induce the LG_{02} modes. If it was moved off-centre pure LG_{02} generation was not possible. The common handedness was likely due to an inbuilt asymmetry in the cavity.

Summary

The experimental ARR coupled lasers have shown that this geometry is effective in generating both first and second order LG_{0l} vortex modes. From 24 W of pump power, LG_{01} modes of 9.0 W and were generated. The mode purity was high, with symmetrical beam qualities between $2.0 < M^2_{x,y} < 2.1$ and closely matching the theoretical mode profile. The handedness could be controlled through alignment of the secondary cavity mode, enabling pure handedness oscillation in either direction.

The primary cavity was easily adjusted to support LG_{02} modes, with 4.3 W of output power for 24 W of pump power. The mode purity was good, however there remained 7 % of the peak intensity on the beam axis. The handedness of the mode was pure, but not controllable with the secondary cavity alignment. Alternative handedness control methods could be used in this configuration.

6.5.4 Intra-cavity vortex techniques comparison

An advantage of gain shaping techniques over other intracavity vortex generation methods is that they do not require specialist or lossy intracavity optics. This can improve the laser efficiency from the lower losses, but also enable higher power vortex generation in both average and peak power. Optical elements with absorbing losses will have limited power handling capability if the heating power cannot be removed sufficiently fast. By avoiding these optics, the power capability of a design is improved. For example, in the digital laser the SLM used had a total reflectance of 90 % [144].

As the coupled cavity geometry is used to match the gain region to the vortex modes it is most appropriate to compare it to other gain shaping techniques. The most common method of gain shaping is to ensure that the input pump beam matches the LG_{0l} mode required. If the pump source is coherent diffractive techniques can be used, for example

diffraction from a circular aperture [166] or a π-plate [146] can generate a doughnut shaped intensity profile. A potential limitation with these methods is that a coherent pump source is required, which could limit the pumping power available in some gain media. Additionally, the pump distribution changes as it propagates through the focus at the gain medium, meaning that the ideal doughnut intensity distribution may not be maintained over the absorption depth in the gain medium.

Another established gain shaping technique is to image of the output of a multi-mode capillary fibre [147, 167], which generates an annular pump region. The reshaped pump light necessarily has a high M^2 from the capillary fibre. This method can be effective at selectively exciting vortex modes; however, for efficient vortex generation it relies on the gain medium being able to efficiently operate with a high M^2 pump source. For this reason it has only been employed in the Nd:YVO_4 and Nd:YAG gain media that both have relatively high absorption and emission cross sections, and have access to high brightness diode pump modules.

An advantage of performing gain reshaping with the input pump radiation is that the laser cavities can have standard configurations, which can simplify the cavity design. The difficulty is instead shifted to the potentially complex reshaping optics external to the cavity, where the particular method of pump reshaping will be dependent on the gain medium being used and the pump sources available.

In coupled cavity vortex generation there are no specific requirements from the pump source as the gain reshaping is performed with the controlling cavity, which gives it great flexibility for use with different gain media. The complexity of the technique is instead focussed on the cavity designs and methods of separating the two laser cavities. Provided that a standard laser cavity can be constructed with any given gain medium and pump source, and there is a way to share the gain between two laser cavities, then a vortex output could be achieved with the coupled cavity method.

The coupling mechanism of the ARR has been demonstrated in Chapter 5 to be low loss, with a round-trip beam recombination loss as low as 0.01 %. This means that introducing the ARR should have minimal impact on laser performance.

A disadvantage of the gain reshaping technique using coupled cavities is that the saturating cavity must use some of the input pump power, so not all the input power is available for the vortex mode. This work has shown that for LG_{01} generation this impact is minimal, where the secondary cavity had 4 % of the combined primary and secondary cavity powers. For high order modes, this loss is more significant, where for LG_{02} generation the secondary cavity had 51 % of the total output power. The efficiency of both LG_{01} and LG_{02} generation could have been improved by combining pump reshaping methods with the coupled cavity technique.

The limitations of previous coupled cavity designs are not present in ARR coupling. There are no specific requirements for the gain medium of isotropy or operation wavelength. The ARR uses standard optical components and does not introduce significant

losses into the laser cavities.

6.6 Summary

The wide variety of applications for vortex beams that touch many areas of science has created a need for vortex beam sources. Intra-cavity generation is attractive due to the possibility of generating pure and high power LG_{0l} vortex modes. This work has demonstrated the use of laser cavities coupled through a common gain medium as a method of vortex mode production. An ARR was proposed and demonstrated as a device to enable the sharing of a gain medium between two laser cavities.

Gain coupled ARR lasers were constructed using a diode end-pumped Nd:YVO_4 gain medium. With 24 W of pump power, LG_{01} modes with 9.0 W power were generated, which were of high purity and quality. The handedness was controllable using the alignment of the non-vortex mode secondary laser cavity, with pure handedness modes achieved. The lasers were also configured to generate LG_{02} modes with 4.3 W of power.

This work has shown the effectiveness of vortex mode generation for gain coupling with an ARR. It could be applied to any gain medium because the ARR requires no specialist optical components. This could allow high quality vortex modes to be generated across the frequency spectrum where laser gain media are known. The presented work was in the CW regime; however, the geometry could be easily adapted to pulsed operation using standard Q-switching or mode locking methods.

Chapter 7

Thesis summary

The first part of this thesis presented work on red diode-pumped Alexandrite lasers, with the focus on understanding and optimising their performance. A new analytical model was developed of an end-pumped gain medium that included the optical processes in Alexandrite, namely excited-state absorption at pump and laser wavelengths, and ground-state absorption at the laser wavelength.

With this model, the parameters affecting laser performance in Alexandrite were identified and investigated. Pump ESA was found to be the cause of an optimum output coupler reflectance for slope efficiency, which has been seen experimentally by many authors [16, 98]. It was shown that the temperature of the Alexandrite crystal has a significant impact on laser performance; however, the temperature dependence of the ratio of pump ESA to GSA had not been measured in the literature. This was measured to decrease with crystal temperature from approximately 0.8 at 10 °C to 0.7 at 90 °C. With this new measurement and values from the literature, there is a complete set of parameters for red diode-pumped Alexandrite over a range of temperatures.

Using the understanding gained from the theoretical modelling, experimental diode-pumped Alexandrite lasers were constructed. In a high efficiency compact cavity design a record slope efficiency of 54 % with 1.2 W of output power was achieved. This result demonstrates the potential efficiency attainable in diode-pumped Alexandrite. With a wavelength tunable laser a record tuning range of 714 nm to 818 nm was obtained. Optimising the crystal temperature was key to achieving this result, with the precise effects analysed used the theoretical model.

The work and analysis presented should be useful to future development of continuous wave Alexandrite lasers, in particular narrow linewidth tunable sources are of interest. The model could also be applied to other solid-state materials that have excited-state absorption effects, so may aid laser development in other applications. A useful extension of this work would be to apply the model to pulsed Alexandrite lasers, which are of particular interest for LIDAR applications [9]. The continuous-wave model presented will help to approximate the performance of these systems; however, it

is likely that pump excited-state absorption effects will be more significant due to the higher population inversions used in these designs.

The second part of this thesis was focussed on vortex laser mode generation. This first involved assessing the suitability of the anti-resonant ring (ARR) laser geometry where the gain medium is internal to the ring, which had only one previous demonstration in the literature [36]. With a diode end-pumped Nd:YVO_4 gain medium the transmission of the ARR was 0.02 %, which was a factor of 20 lower than the previous example. This verified that the ARR could be used in end-pumped lasers with a low impact on efficiency. The side-pumped geometry had higher losses of 1.5 %; however, altering the cavity design to achieve more symmetry would improve this result.

The ARR laser design was then used to couple two laser cavities through a shared gain medium in the ARR. In this configuration one laser cavity was used to control the distribution of gain, which caused the other cavity to oscillate in a vortex mode. A diode end-pumped Nd:YVO_4 gain medium was used with 24 W of available pump power. With this system first order vortex LG_{01} modes with 9.0 W power were generated, these had a high spatial purity and were of controllable single handedness. Second order vortex LG_{02} modes were also generated with 4.3 W of power.

There were two main outcomes of the ARR vortex laser investigation. The first was demonstrating that the ARR can be a low loss component in laser cavities. This structure is interesting as it can allow sharing of optical elements between two cavities, which makes it a rich test-bed for coupled laser cavity investigations. The particular application focussed on in this work was sharing a gain medium between two laser cavities. This was used to generate vortex laser modes, but there are many other possible applications. For example, pulse control in a Q-switched laser has been shown using coupled laser cavities [163], where the performance of this system could be improved or implemented in other gain media using the ARR.

The second outcome was the demonstration of the new ARR coupled laser geometry to generate vortex modes. A particular advantage of this method is it generates vortex beams with high symmetry and power. These properties lend themselves to optical levitation, where vortex beams can trap and manipulate objects in unique ways compared to conventional methods. This has two immediate applications. The first is to use the orbital angular momentum to trap and spin a liquid droplet, this can be used to test fundamental properties of surface tension on micron sized objects, which is of particular interest in torus nuclear fusion reactors. A second application is in trapping reflective spherical metal shells in the annular intensity profile. These are a potential source of high energy protons (> 150 MeV) when vaporised with a high intensity laser pulse. This would create a revolutionary proton source for cancer treatment, being lower cost and more practical than the currently used cyclotron accelerators.

This vortex generation technique could be applied to any solid-state gain medium, which would enable vortex generation at a range of wavelengths and powers. Of particu-

lar interest would be implementing it in a wavelength tunable gain medium, for example Alexandrite, which would provide a tunable vortex source. This is usually difficult to achieve with other methods that are designed for a specific wavelength. A wavelength tunable vortex source could be useful in machining applications, where access to alternative wavelength ranges can alter the machining behaviour of different materials.

Additionally, although this method was demonstrated in CW operation the laser cavity could be adapted to pulsed operation using standard techniques, for example in Q-switching or modelocking. This would enable pure, high power, and high energy vortex modes to be generated tailored to the required application.

Bibliography

[1] A. Siegman, *Lasers* (University Science Books, 1986).

[2] W. E. McDermott, N. R. Pchelkin, D. J. Benard, and R. R. Bousek, "An electronic transition chemical laser," Appl. Phys. Lett. **32**, 469–470 (1978).

[3] P. Crump, J. Wang, S. Patterson, D. Wise, A. Basauri, M. DeFranza, S. Elim, W. Dong, S. Zhang, M. Bougher *et al.*, "Diode laser efficiency increases enable 400W peak power from 1cm bars and show a clear path to peak powers in excess of 1kW," in "High-Power Diode Laser Technology and Applications IV," , vol. 6104 (International Society for Optics and Photonics, 2006), vol. 6104, p. 610409.

[4] T. Y. Fan and R. L. Byer, "Diode laser-pumped solid-state lasers," IEEE J. Quantum Electron. **24**, 895–912 (1988).

[5] W. Koechner, *Solid-State Laser Engineering*, vol. 1 (Springer-Verlag, 2006), 6th ed.

[6] M. Lando, Y. Shimony, R. M. Benmair, D. Abramovich, V. Krupkin, and A. Yogev, "Visible solar-pumped lasers," Opt. Mater. **13**, 111–115 (1999).

[7] S. T. Lai and M. L. Shand, "High efficiency CW laser-pumped tunable Alexandrite laser," J. of Appl. Phys. **54**, 5642–5644 (1983).

[8] J. Walling, O. Peterson, H. Jenssen, R. Morris, and E. O'Dell, "Tunable Alexandrite lasers," IEEE J. Quant. Electron. **16**, 1302–1315 (1980).

[9] M. J. Damzen, G. M. Thomas, A. Teppitaksak, and A. Minassian, "Progress in diode-pumped Alexandrite lasers as a new resource for future space LIDAR missions," Proc. SPIE **10563**, 10563–10563 (2017).

[10] V. Wulfmeyer, J. Bösenberg, S. Lehmann, C. Senff, and S. Schmitz, "Injection-seeded alexandrite ring laser: performance and application in a water-vapor differential absorption lidar," Opt. Lett. **20**, 638–640 (1995).

[11] C. Granier, J. P. Jegou, and G. Megie, "Iron atoms and metallic species in the earth's upper atmosphere," Geophys. Res. Lett. **16**, 243–246 (1989).

[12] S. Ghanbari, R. Akbari, and A. Major, "Femtosecond kerr-lens mode-locked alexandrite laser," Opt. Express **24**, 14836–14840 (2016).

[13] C. Cihan, A. Muti, I. Baylam, A. Kocabas, U. Demirbas, and A. Sennaroglu, "70 femtosecond Kerr-lens mode-locked multipass-cavity Alexandrite laser," Opt. Lett. **43**, 1315–1318 (2018).

[14] M. Shand, J. Walling, and R. Morris, "Excited-state absorption in the pump region of Alexandrite," J. Appl. Phys. **52**, 953–955 (1981).

[15] J. Walling, D. Heller, H. Samelson, D. Harter, J. Pete, and R. Morris, "Tunable Alexandrite lasers: development and performance," IEEE J. Quantum Electron. **21**, 1568–1581 (1985).

[16] A. Teppitaksak, A. Minassian, G. Thomas, and M. Damzen, "High efficiency >26W diode end-pumped Alexandrite laser," Opt. Express **22**, 16386–16392 (2014).

[17] J. C. E. Coyle, A. J. Kemp, J.-M. Hopkins, and A. A. Lagatsky, "Ultrafast diode-pumped Ti:Sapphire laser with broad tunability," Opt. Express **26**, 6826–6832 (2018).

[18] M. Shand and J. Walling, "Excited-state absorption in the lasing wavelength region of Alexandrite," IEEE J. Quant. Electron. **18**, 1152–1155 (1982).

[19] M. Shand, J. Walling, and H. Jenssen, "Ground state absorption in the lasing wavelength region of Alexandrite: Theory and experiment," IEEE J. Quant. Electron. **18**, 167–169 (1982).

[20] Z. Zhang, K. Grattan, and A. Palmer, "Thermal characteristics of Alexandrite fluorescence decay at high temperatures, induced by a visible laser diode emission," J. Appl. Phys. **73**, 3493–3498 (1993).

[21] L. Allen, M. W. Beijersbergen, R. J. C. Spreeuw, and J. P. Woerdman, "Orbital angular momentum of light and the transformation of Laguerre-Gaussian laser modes," Phys. Rev. A **45**, 8185–8189 (1992).

[22] H. He, M. E. J. Friese, N. R. Heckenberg, and H. Rubinsztein-Dunlop, "Direct observation of transfer of angular momentum to absorptive particles from a laser beam with a phase singularity," Phys. Rev. Lett. **75**, 826–829 (1995).

[23] K. Toyoda, K. Miyamoto, N. Aoki, R. Morita, and T. Omatsu, "Using optical vortex to control the chirality of twisted metal nanostructures," Nano Lett. **12**, 3645–3649 (2012).

[24] L. Veissier, A. Nicolas, L. Giner, D. Maxein, A. S. Sheremet, E. Giacobino, and J. Laurat, "Reversible optical memory for twisted photons," Opt. Lett. **38**, 712–714 (2013).

[25] J. Wang, J.-Y. Yang, I. M. Fazal, N. Ahmed, Y. Yan, H. Huang, Y. Ren, Y. Yue, S. Dolinar, M. Tur *et al.*, "Terabit free-space data transmission employing orbital angular momentum multiplexing," Nat. Photonics **6**, 488 (2012).

[26] G. Molina-Terriza, J. P. Torres, and L. Torner, "Twisted photons," Nat. Phys. **3**, 305 (2007).

[27] M. Beijersbergen, L. Allen, H. van der Veen, and J. Woerdman, "Astigmatic laser mode converters and transfer of orbital angular momentum," Opt. Commun. **96**, 123 – 132 (1993).

[28] N. Heckenberg, R. McDuff, C. Smith, and A. White, "Generation of optical phase singularities by computer-generated holograms," Opt. Lett. **17**, 221–223 (1992).

[29] D. N. Naik and N. K. Viswanathan, "Generation of singular optical beams from fundamental gaussian beam using sagnac interferometer," J. Opt. **18**, 095601 (2016).

[30] W. M. Lee, X.-C. Yuan, and W. C. Cheong, "Optical vortex beam shaping by use of highly efficient irregular spiral phase plates for optical micromanipulation," Opt. Lett. **29**, 1796–1798 (2004).

[31] A. Forbes, "Controlling lights helicity at the source: orbital angular momentum states from lasers," Phil. Trans. R. Soc. A **375**, 20150436 (2017).

[32] I. A. Litvin, S. Ngcobo, D. Naidoo, K. Ait-Ameur, and A. Forbes, "Doughnut laser beam as an incoherent superposition of two petal beams," Opt. Lett. **39**, 704–707 (2014).

[33] A. Ito, Y. Kozawa, and S. Sato, "Generation of hollow scalar and vector beams using a spot-defect mirror," J. Opt. Soc. Am. A **27**, 2072–2077 (2010).

[34] D. Lin, J. M. O. Daniel, and W. A. Clarkson, "Controlling the handedness of directly excited Laguerre-Gaussian modes in a solid-state laser," Opt. Lett. **39**, 3903–3906 (2014).

[35] S. Chard, P. Shardlow, and M. Damzen, "High-power non-astigmatic TEM00 and vortex mode generation in a compact bounce laser design," Appl. Phys. B **97**, 275 (2009).

[36] R. Trutna and A. Siegman, "Laser cavity dumping using an antiresonant ring," IEEE J. Quantum Electron. **13**, 955–962 (1977).

[37] A. Siegman, "An antiresonant ring interferometer for coupled laser cavities, laser output coupling, mode locking, and cavity dumping," IEEE J. Quantum Electron. **9**, 247–250 (1973).

[38] K. Dholakia, N. B. Simpson, M. J. Padgett, and L. Allen, "Second-harmonic generation and the orbital angular momentum of light," Phys. Rev. A **54**, R3742–R3745 (1996).

[39] P. Pichon, A. Barbet, J.-P. Blanchot, F. Druon, F. Balembois, and P. Georges, "LED-pumped Alexandrite laser oscillator and amplifier," Opt. Lett. **42**, 4191–4194 (2017).

[40] R. J. Keyes and T. M. Quist, "Injection luminescent pumping of CaF2:U3+ with GaAs diode lasers," Appl. Phys. Lett. **4**, 50–52 (1964).

[41] Y. F. Chen, T. S. Liao, C. F. Kao, T. M. Huang, K. H. Lin, and S. C. Wang, "Optimization of fiber-coupled laser-diode end-pumped lasers: influence of pump-beam quality," IEEE J. Quantum Electron. **32**, 2010–2016 (1996).

[42] O. Svelto, *Principles of Lasers* (Springer US, 2010), 5th ed.

[43] W. A. Clarkson, "Thermal effects and their mitigation in end-pumped solid-state lasers," J. Phys. D **34**, 2381 (2001).

[44] W. Koechner, "Thermal lensing in a Nd:YAG laser rod," Appl. Opt. **9**, 2548–2553 (1970).

[45] O. A. Schmidt, C. Schulze, D. Flamm, R. Brüning, T. Kaiser, S. Schröter, and M. Duparré, "Real-time determination of laser beam quality by modal decomposition," Opt. Express **19**, 6741–6748 (2011).

[46] S. J. Habraken and G. Nienhuis, "Modes of a twisted optical cavity," Phys. Rev. A **75**, 033819 (2007).

[47] A. E. Siegman and S. W. Townsend, "Output beam propagation and beam quality from a multimode stable-cavity laser," IEEE J. Quantum Electron. **29**, 1212–1217 (1993).

[48] A. E. Siegman, "New developments in laser resonators," in "Optical Resonators," , vol. 1224 (International Society for Optics and Photonics, 1990), vol. 1224, pp. 2–15.

[49] N. Ismail, C. C. Kores, D. Geskus, and M. Pollnau, "Fabry-perot resonator: spectral line shapes, generic and related airy distributions, linewidths, finesses, and performance at low or frequency-dependent reflectivity," Opt. Express **24**, 16366–16389 (2016).

[50] R. Morris and C. Cline, "Chromium-doped beryllium aluminate lasers," (1976). US Patent 3,997,853.

[51] J. W. Kuper, T. Chin, and H. E. Aschoff, "Extended tuning range of Alexandrite at elevated temperatures," in "ASSL," (Optical Society of America, 1990), p. CL3.

[52] W. Kerridge-Johns and M. Damzen, "Analysis of pump excited state absorption and its impact on laser efficiency," Laser Phys. Lett. **12**, 125002 (2015).

[53] W. R. Kerridge-Johns and M. J. Damzen, "Analytical model of tunable Alexandrite lasing under diode end-pumping with experimental comparison," J. Opt. Soc. Am. B **33**, 2525–2534 (2016).

[54] "Titanium-sapphire lasers," [www.rp-photonics.com/titanium_sapphire_lasers.html]. Accessed: June 2018.

[55] P. Cheo, ed., *Handbook of Solid-State Lasers*, no. 18 in Optical Science and Engineering (CRC Press, 1988).

[56] "Main properties of sapphire," [www.mt-berlin.com/frames_cryst/descriptions/sapphire.html]. Accessed: June 2018.

[57] "Titanium doped sapphire," [www.pmoptics.com/titanium_doped_sapphire.html]. Accessed: June 2018.

[58] A. Major, F. Yoshino, I. Nikolakakos, J. S. Aitchison, and P. W. E. Smith, "Dispersion of the nonlinear refractive index in sapphire," Opt. Lett. **29**, 602–604 (2004).

[59] M. Weber, D. Milam, and W. Smith, "Nonlinear refractive index of glasses and crystals," Opt. Eng. **17**, 175463 (1978).

[60] U. Demirbas, D. Li, J. R. Birge, A. Sennaroglu, G. S. Petrich, L. A. Kolodziejski, F. X. Kärtner, and J. G. Fujimoto, "Low-cost, single-mode diode-pumped cr:colquiriite lasers," Opt. Express **17**, 14374–14388 (2009).

[61] E. F. Farrell, J. H. Fang, and R. E. Newnham, "Refinement of the chrysoberyl structure," Am. Mineral. **48**, 804–808 (1963).

[62] C. E. Forbes, "Analysis of the spin-Hamiltonian parameters for Cr^{3+} in mirror and inversion symmetry sites of Alexandrite ($Al_{2-x}Cr_xBeO_4$). Determination of the relative site occupancy by EPR," J. Chem. Phys. **79**, 2590–2599 (1983).

[63] R. C. Powell, L. Xi, X. Gang, G. J. Quarles, and J. C. Walling, "Spectroscopic properties of Alexandrite crystals," Phys. Rev. B **32**, 2788–2797 (1985).

[64] A. Suchocki, G. Gilliland, R. Powell, J. Bowen, and J. Walling, "Spectroscopic properties of Alexandrite crystals II," J. Lumin. **37**, 29 – 37 (1987).

[65] Y. Tanabe and S. Sugano, "On the absorption spectra of complex ions ii," J. Phys. Soc. Jpn. **9**, 766–779 (1954).

[66] Z. Zhang, K. Grattan, and A. Palmer, "Temperature dependences of fluorescence lifetimes in Cr^{3+}-doped insulating crystals," Phys. Rev. B **48**, 7772–7778 (1993).

[67] B. Sevast'yanov and Y. Remigaĭlo, "Optical generation of alexandrite in the temperature range 20-200°C," Sov. Phys. Dokl. **31**, 735–737 (1986).

[68] S. Gayen, W. Wang, V. Petričević, and R. Alfano, "Nonradiative transition dynamics in Alexandrite," Appl. Phys. Lett. **49**, 437–439 (1986).

[69] D. McCumber, "Theory of phonon-terminated optical masers," Phys. Rev. **134**, A299–A306 (1964).

[70] B. Sevast'yanov, "Excited-state absorption spectroscopy of crystals doped with Cr3+, Ti3+, and Nd3+ ions. review," Crystallogr. Rep. **48**, 989–1011 (2003).

[71] B. Sevast'yanov, Y. Remigailo, T. Veremeichik, and B. Orekhova, "Absorption spectra of excited Alexandrite," Sov. Phys. Dokl. **30**, 1051–1053 (1985).

[72] M. Shand and H. Jenssen, "Temperature dependence of the excited-state absorption of Alexandrite," IEEE J. Quant. Electron. **19**, 480–484 (1983).

[73] S. Guch and C. Jones, "Alexandrite-laser performance at high temperature," Opt. Lett. **7**, 608–610 (1982).

[74] M. Strotkamp, U. Witte, A. Munk, A. Hartung, S. Gausmann, S. Hengesbach, M. Traub, H.-D. Hoffmann, J. Hoeffner, and B. Jungbluth, "Broadly tunable, diode pumped Alexandrite laser," in "Advanced Solid-State Lasers Congress," (Optical Society of America, 2013), p. ATu3A.42.

[75] W. R. Kerridge-Johns and M. J. Damzen, "Temperature effects on tunable CW Alexandrite lasers under diode end-pumping," Opt. Express **26**, 7771–7785 (2018).

[76] M. Hercher, "An analysis of saturable absorbers," Appl. Opt. **6**, 947–954 (1967).

[77] M. Fibrich, J. Šulc, D. Vyhlídal, H. Jelínková, and M. Čech, "Alexandrite spectroscopic and laser characteristic investigation within a 78-400K temperature range," Laser Phys. **27**, 115801 (2017).

[78] T. Fan and R. L. Byer, "Modeling and CW operation of a quasi-three-level 946nm Nd:YAG laser," IEEE J. Quantum Electron. **23**, 605–612 (1987).

[79] W. P. Risk, "Modeling of longitudinally pumped solid-state lasers exhibiting reabsorption losses," J. Opt. Soc. Am. B **5**, 1412–1423 (1988).

[80] T. Taira, W. M. Tulloch, and R. L. Byer, "Modeling of quasi-three-level lasers and operation of CW Yb:YAG lasers," Appl. Opt. **36**, 1867–1874 (1997).

[81] P. Peterson, A. Gavrielides, and P. Sharma, "CW theory of a laser diode-pumped two-manifold solid state laser," Opt. Commun. **109**, 282–287 (1994).

[82] R. Beach, "CW theory of quasi-three level end-pumped laser oscillators," Opt. Commun. **123**, 385 – 393 (1996).

[83] P. Peterson and M. Sharma, "Back-reflection pumping versus contradirectional pumping in upconversion solid state lasers," Opt. Commun. **146**, 189–195 (1998).

[84] G. L. Bourdet, "Theoretical investigation of quasi-three-level longitudinally pumped continuous wave lasers," Appl. Opt. **39**, 966–971 (2000).

[85] O. Teschke, A. Dienes, and J. Whinnery, "Theory and operation of high-power CW and long-pulse dye lasers," IEEE J. Quantum Elect. **12**, 383–395 (1976).

[86] E. Sahar and D. Treves, "Excited singlet-state absorption in dyes and their effect on dye lasers," IEEE J. Quantum Elect. **13**, 962–967 (1977).

[87] A. Sennaroglu, A. Kurt, and S. Buhours, "Analysis and optimization of diode end-pumped solid-state lasers: application to Nd3+:YVO4 lasers at 1064 and 1342nm," Opt. Eng. **44**, 054202 (2005).

[88] J. Gao, R. Yan, X. Dai, X. Yu, L. Zhang, and X. Wu, "Quasi-three-level Neodymium Vanadate laser operation under polarized diode pumping: theoretical and experimental investigation," Laser Phys. **22**, 1279–1285 (2012).

[89] W. Rigrod, "Saturation effects in high-gain lasers," J. Appl. Phys. **36**, 2487–2490 (1965).

[90] B. Thedrez and C. Lee, "A reassessment of standard rate equations for low facet reflectivity semiconductor lasers using traveling wave rate equations," IEEE J. Quantum Elect. **28**, 2706–2713 (1992).

[91] E. Beyatli, I. Baali, B. Sumpf, G. Erbert, A. Leitenstorfer, A. Sennaroglu, and U. Demirbas, "Tapered diode-pumped continuous-wave Alexandrite laser," J. Opt. Soc. Am. B **30**, 3184–3192 (2013).

[92] E. Arimondo and B. Dinelli, "Optical bistability of a CO2 laser with intracavity saturable absorber: Experiment and model," Opt. Commun. **44**, 277 – 282 (1983).

[93] X. Zhang and Y. Wang, "Optical bistability effects in a Tm,Ho:YLF laser at room temperature," Opt. Lett. **32**, 2333–2335 (2007).

[94] J. Liu, V. Petrov, U. Griebner, F. Noack, H. Zhang, J. Wang, and M. Jiang, "Optical bistability in the operation of a continuous-wave diode-pumped Yb:LuVO4 laser," Opt. Express **14**, 12183–12187 (2006).

[95] E. Arbabzadah and M. Damzen, "Fibre-coupled red diode-pumped alexandrite TEM00 laser with single and double-pass end-pumping," Laser Phys. Lett. **13**, 065002 (2016).

[96] J. Kuper and D. Brown, "High efficiency CW green-pumped Alexandrite lasers," in "Proc.SPIE," , vol. 6100 (2006), vol. 6100, p. 61000T.

[97] M. J. Damzen, G. M. Thomas, and A. Minassian, "Diode-side-pumped Alexandrite slab lasers," Opt. Express **25**, 11622–11636 (2017).

[98] I. Yorulmaz, E. Beyatli, A. Kurt, A. Sennaroglu, and U. Demirbas, "Efficient and low-threshold Alexandrite laser pumped by a single-mode diode," Opt. Mater. Express **4**, 776–789 (2014).

[99] R. Scheps, B. M. Gately, J. F. Myers, J. S. Krasinski, and D. F. Heller, "Alexandrite laser pumped by semiconductor lasers," Appl. Phys. Lett. **56**, 2288–2290 (1990).

[100] M. Damzen, G. Thomas, and A. Minassian, "Multi-watt diode-pumped Alexandrite laser operation," in "Lasers and Electro-Optics Europe (CLEO EUROPE/IQEC), 2013 Conference on and International Quantum Electronics Conference," (2013), pp. 1–1.

[101] A. Teppitaksak, *Advanced laser sources for industrial processing and remote sensing* (PhD thesis, Imperial College London, 2015).

[102] M. Born and E. Wolf, *Principles of optics: electromagnetic theory of propagation, interference and diffraction of light* (Elsevier, 2013).

[103] S. Zhu, "Birefringent filter with tilted optic axis for tuning dye lasers: theory and design," Appl. Opt. **29**, 410–415 (1990).

[104] D. R. Preuss and J. L. Gole, "Three-stage birefringent filter tuning smoothly over the visible region: theoretical treatment and experimental design," Appl. Opt. **19**, 702–710 (1980).

[105] A. L. Bloom, "Modes of a laser resonator containing tilted birefringent plates," J. Opt. Soc. Am. **64**, 447–452 (1974).

[106] G. Ghosh, "Dispersion-equation coefficients for the refractive index and birefringence of calcite and quartz crystals," Opt. Commun. **163**, 95 – 102 (1999).

[107] H. Samelson, J. Walling, T. Wernikowski, and D. Harter, "CW arc-lamp-pumped Alexandrite lasers," IEEE J. Quant. Electron. **24**, 1141–1150 (1988).

[108] R. Bergh, H. Lefevre, and H. Shaw, "An overview of fiber-optic gyroscopes," J. Light. Technol. **2**, 91–107 (1984).

[109] K.-X. Sun, M. M. Fejer, E. Gustafson, and R. L. Byer, "Sagnac interferometer for gravitational-wave detection," Phys. Rev. Lett. **76**, 3053–3056 (1996).

[110] D. Chakrabarti, S. P. Basu, and M. De, "A triangular path inverting interferometer," J. Opt. **8**, 33 (1977).

[111] A. E. Siegman, "Passive mode locking using an antiresonant-ring laser cavity," Opt. Lett. **6**, 334–335 (1981).

[112] H. Vanherzeele, J. Van Eck, and A. Siegman, "Colliding pulse mode locking of a Nd:YAG laser with an antiresonant ring structure," Appl. Opt. **20**, 3484–3486 (1981).

[113] T. Norris, T. Sizer, and G. Mourou, "Generation of 85-fsec pulses by synchronous pumping of a colliding-pulse mode-locked dye laser," J. Opt. Soc. Am. B **2**, 613–615 (1985).

[114] T. F. Carruthers and I. N. Duling, "Passive laser mode locking with an antiresonant nonlinear mirror," Opt. Lett. **15**, 804–806 (1990).

[115] K. Devi, S. C. Kumar, A. Esteban-Martin, and M. Ebrahim-Zadeh, "Antiresonant ring output-coupled continuous-wave optical parametric oscillator," Opt. Express **20**, 19313–19321 (2012).

[116] A. Esteban-Martin, V. Ramaiah-Badarla, and M. Ebrahim-Zadeh, "Dual-wavelength optical parametric oscillator using antiresonant ring interferometer," Laser Photonics Rev. **6**, L7–L11 (2012).

[117] A. Zeilinger, "General properties of lossless beam splitters in interferometry," Am. J. Phys. **49**, 882–883 (1981).

[118] W. Rigrod, "Selectivity of open-ended interferometric resonators," IEEE J. Quantum Electron. **6**, 9–14 (1970).

[119] P. W. Smith, "Mode selection in lasers," Proc. IEEE **60**, 422–440 (1972).

[120] S.-C. Sheng and A. E. Siegman, "Perturbed gaussian modes of an unbalanced antiresonant-ring laser cavity," J. Opt. Soc. Am. **66**, 1032–1036 (1976).

[121] Y. Li, G. Eichmann, and R. Alfano, "Multistable fabry-perot resonator with an active sagnac interferometer as its retro-reflector," Opt. Commun. **61**, 75 – 80 (1987).

[122] D. Hall, *The physics and technology of laser resonators* (CRC Press, 1990).

[123] S. A. Collins, "Analysis of optical resonators involving focusing elements," Appl. Opt. **3**, 1263–1275 (1964).

[124] G. E. Stedman, H. R. Bilger, Z. Li, M. P. Poulton, C. H. Rowe, I. Vetharaniam, and P. V. Wells, "Canterbury ring laser and tests for nonreciprocal phenomena," Aust. J. Phys. **46**, 87–101 (1993).

[125] J. R. O'Connor, "Unusual crystal-field energy levels and efficient laser properties of YVO4:Nd," Appl. Phys. Lett. **9**, 407–409 (1966).

[126] R. Peterson, H. Jenssen, and A. Cassanho, "Investigation of the spectroscopic properties of Nd:YVO4," in "Advanced Solid State Lasers," (Optical Society of America, 2002), p. TuB17.

[127] S. Bjurshagen and R. Koch, "Modeling of energy-transfer upconversion and thermal effects in end-pumped quasi-three-level lasers," Appl. Opt. **43**, 4753–4767 (2004).

[128] "Properties of Nd:YVO4 crystal," [www.unitedcrystals.com/ YVO4Prop.html]. Accessed: April 2018.

[129] "Neodymium: Yttrium Aluminium Garnet," [www.northropgrumman.com/ BusinessVentures/ SYNOPTICS/ Products/ LaserCrystals/ Documents/ pageDocs/ Nd-YAG.pdf]. Accessed: April 2018.

[130] L. Krainer, R. Paschotta, S. Lecomte, M. Moser, K. J. Weingarten, and U. Keller, "Compact Nd:YVO4 lasers with pulse repetition rates up to 160Ghz," IEEE J. Quantum Electron. **38**, 1331–1338 (2002).

[131] V. P. Zhukov, A. M. Rubenchik, M. P. Fedoruk, and N. M. Bulgakova, "Interaction of doughnut-shaped laser pulses with glasses," J. Opt. Soc. Am. B **34**, 463–471 (2017).

[132] D. Wildanger, J. Bückers, V. Westphal, S. W. Hell, and L. Kastrup, "A STED microscope aligned by design," Opt. Express **17**, 16100–16110 (2009).

[133] N. Simpson, L. Allen, and M. Padgett, "Optical tweezers and optical spanners with Laguerre-Gaussian modes," J. Mod. Opt. **43**, 2485–2491 (1996).

[134] G. Gibson, J. Courtial, M. J. Padgett, M. Vasnetsov, V. Pas'ko, S. M. Barnett, and S. Franke-Arnold, "Free-space information transfer using light beams carrying orbital angular momentum," Opt. Express **12**, 5448–5456 (2004).

[135] K. Miyamoto, S. Miyagi, M. Yamada, K. Furuki, N. Aoki, M. Okida, and T. Omatsu, "Optical vortex pumped mid-infrared optical parametric oscillator," Opt. Express **19**, 12220–12226 (2011).

[136] A. V. Carpentier, H. Michinel, J. R. Salgueiro, and D. Olivieri, "Making optical vortices with computer-generated holograms," Am. J. Phys. **76**, 916–921 (2008).

[137] D. Huang, H. Timmers, A. Roberts, N. Shivaram, and A. S. Sandhu, "A low-cost spatial light modulator for use in undergraduate and graduate optics labs," Am. J. Phys. **80**, 211 (2012).

[138] L. Marrucci, C. Manzo, and D. Paparo, "Optical spin-to-orbital angular momentum conversion in inhomogeneous anisotropic media," Phys. Rev. Lett. **96**, 163905 (2006).

[139] J. Courtial and M. Padgett, "Performance of a cylindrical lens mode converter for producing Laguerre-Gaussian laser modes," Opt. Commun. **159**, 13–18 (1999).

[140] R. T. Uren and W. A. Clarkson, "Efficient astigmatic mode-converter based on spherical mirrors," in "2017 European Conference on Lasers and Electro-Optics and European Quantum Electronics Conference," (Optical Society of America, 2017), p. CA.2.2.

[141] T. Ohtomo, S.-C. Chu, and K. Otsuka, "Generation of vortex beams from lasers with controlled Hermite- and Ince-Gaussian modes," Opt. Express **16**, 5082–5094 (2008).

[142] C. Tamm, "Frequency locking of two transverse optical modes of a laser," Phys. Rev. A **38**, 5960–5963 (1988).

[143] M. Harris, C. A. Hill, P. R. Tapster, and J. M. Vaughan, "Laser modes with helical wave fronts," Phys. Rev. A **49**, 3119–3122 (1994).

[144] S. Ngcobo, I. Litvin, L. Burger, and A. Forbes, "A digital laser for on-demand laser modes," Nat. Commun. **4**, 2289 (2013).

[145] D. J. Kim and J. W. Kim, "Direct generation of an optical vortex beam in a single-frequency Nd:YVO4 laser," Opt. Lett. **40**, 399–402 (2015).

[146] D. Naidoo, T. Godin, M. Fromager, E. Cagniot, N. Passilly, A. Forbes, and K. Aït-Ameur, "Transverse mode selection in a monolithic microchip laser," Opt. Commun. **284**, 5475–5479 (2011).

[147] J. Kim and W. Clarkson, "Selective generation of Laguerre-gaussian (LG0n) mode output in a diode-laser pumped Nd:YAG laser," Opt. Commun. **296**, 109–112 (2013).

[148] D. Kim and J. Kim, "High-power TEM00 and Laguerre-Gaussian mode generation in double resonator configuration," Appl. Phys. B **121**, 401–405 (2015).

[149] D. J. Kim, J. I. Mackenzie, and J. W. Kim, "Adaptable beam profiles from a dual-cavity Nd:YAG laser," Opt. Lett. **41**, 1740–1743 (2016).

[150] T. Omatsu, M. Okida, and Y. Hayashi, "Over 10-watt vortex output from a diode-pumped solid-state laser," Topologica **2**, 010–010 (2009).

[151] D. Naidoo, F. S. Roux, A. Dudley, I. Litvin, B. Piccirillo, L. Marrucci, and A. Forbes, "Controlled generation of higher-order Poincaré sphere beams from a laser," Nat. Photonics **10**, 327–332 (2016).

[152] R. Chriki, E. Maguid, C. Tradonsky, V. Kleiner, A. A. Friesem, N. Davidson, and E. Hasman, "Spin-controlled twisted laser beams: intra-cavity multi-tasking geometric phase metasurfaces," Opt. Express **26**, 905–916 (2018).

[153] Y. Lin, C.-C. Yeh, and H.-C. Lee, "Vortex laser generation in a degenerate optical resonator with an intra-cavity spiral phase plate," in "Laser Congress 2017 (ASSL, LAC)," (Optical Society of America, 2017), p. JTu2A.52.

[154] M. S. Seghilani, M. Myara, M. Sellahi, L. Legratiet, I. Sagnes, G. Beaudoin, P. Lalanne, and A. Garnache, "Vortex laser based on III-V semiconductor metasurface: direct generation of coherent Laguerre-Gauss modes carrying controlled orbital angular momentum," Sci. Rep. **6**, 38156 (2016).

[155] D. Flamm, D. Naidoo, C. Schulze, A. Forbes, and M. Duparré, "Mode analysis with a spatial light modulator as a correlation filter," Opt. Lett. **37**, 2478–2480 (2012).

[156] D. Lin, *Doughnut-shaped beam generation in solid-state and fibre lasers* (PhD thesis, University of Southampton, 2015).

[157] R. D. Niederriter, M. E. Siemens, and J. T. Gopinath, "Continuously tunable orbital angular momentum generation using a polarization-maintaining fiber," Opt. Lett. **41**, 3213–3216 (2016).

[158] S. N. Alperin, R. D. Niederriter, J. T. Gopinath, and M. E. Siemens, "Quantitative measurement of the orbital angular momentum of light with a single, stationary lens," Opt. Lett. **41**, 5019–5022 (2016).

[159] C. Schulze, A. Dudley, D. Flamm, M. Duparré, and A. Forbes, "Measurement of the orbital angular momentum density of light by modal decomposition," New. J. Phys. **15**, 073025 (2013).

[160] A. White, C. Smith, N. Heckenberg, H. Rubinsztein-Dunlop, R. McDuff, C. Weiss, and C. Tamm, "Interferometric measurements of phase singularities in the output of a visible laser," J. Mod. Opt. **38**, 2531–2541 (1991).

[161] M. Harris, C. Hill, and J. Vaughan, "Optical helices and spiral interference fringes," Opt. Commun. **106**, 161 – 166 (1994).

[162] D. Hanna, "Astigmatic gaussian beams produced by axially asymmetric laser cavities," IEEE J. Quantum Electron. **5**, 483–488 (1969).

[163] E. A. Arbabzadah, P. C. Shardlow, A. Minassian, and M. J. Damzen, "Pulse control in a Q-switched Nd:YVO4 bounce geometry laser using a secondary cavity," Opt. Lett. **39**, 3437–3440 (2014).

[164] K. Kubodera and K. Otsuka, "Single-transverse-mode LiNdP4O12 slab waveguide laser," J. Appl. Phys. **50**, 653–659 (1979).

[165] Y. F. Chen and Y. P. Lan, "Dynamics of the laguerre gaussian $\mathrm{TEM}^{*}_{0,l}$ mode in a solid-state laser," Phys. Rev. A **63**, 063807 (2001).

[166] Y. Senatsky, J.-F. Bisson, J. Li, A. Shirakawa, M. Thirugnanasambandam, and K.-i. Ueda, "Laguerre-Gaussian modes selection in diode-pumped solid-state lasers," Opt. Rev. **19**, 201–221 (2012).

[167] D. J. Kim, J. W. Kim, and W. A. Clarkson, "Q-switched Nd:YAG optical vortex lasers," Opt. Express **21**, 29449–29454 (2013).

Appendix A

Laser model derivation

To find an equation governing the population inversion distribution, Equation (3.13) is used to eliminate I in Equation (3.9), giving

$$\frac{\mathrm{d}f}{\mathrm{d}z} = -\alpha_0(1-f)[1-(1-\gamma)f][(1+a)f-a]\,, \tag{A.1}$$

where $a = (\phi/\phi_\mathrm{a})/(1+\phi/\phi_\mathrm{s})$ is a laser saturation factor. This can be integrated, yielding

$$D(z) = D(0)\mathrm{e}^{-\alpha_0 z}\,, \tag{A.2}$$

$$D(z) = \begin{cases} (1-f)^{-\frac{1}{\gamma}}[1-(1-\gamma)f]^{\frac{1-\gamma}{\gamma(1+a\gamma)}} \\ [(1+a)f-a]^{\frac{1+a}{1+a\gamma}} \end{cases} \text{for } \gamma > 0\,, \qquad \begin{cases} (1-f)^{-(1+a)}[f(1+a)-a]^{(1+a)} \\ \exp[(1-f)^{-1}] \end{cases} \text{for } \gamma = 0\,. \tag{A.3}$$

With Equations (3.13) and (A.2) it is possible to calculate the longitudinal variation of pump intensity and population inversion in the gain medium for a given incident pump intensity and laser photon density. The input pump intensity $I(0)$ determines the population inversion $f(0)$ through Equation (3.13). This inversion is then used in Equation (A.2) to calculate $f(z)$, which through Equation (3.13) will also give $I(z)$.

To find the relationship between the incident pump and laser output intensity the integral definition $F = \int_0^l f\,\mathrm{d}z$ is calculated, through a change of variables using Equation (A.1), giving

$$\alpha_0 F = \int_{f_0}^{f(l)} \frac{-f}{(1-f)[1-(1-\gamma)f][(1+a)f-a]}\mathrm{d}f\,, \tag{A.4}$$

where $f_0 = f(0)$. Performing the integral and using Equation (3.13) for simplification yields

$$-\alpha_1(1+a\gamma)F = a\gamma\ln[T] + \ln\left[\frac{1+\gamma\frac{f(l)}{1-f(l)}}{1+\gamma\frac{f_0}{1-f_0}}\right]\,, \tag{A.5}$$

where $T = I(l)/I(0) = \mathrm{e}^{-\alpha_0 l}\mathrm{e}^{\alpha_0(1-\gamma)F}$ is the pump transmission. Further simplification can be made with Equation (3.13) through

$$\begin{aligned} \frac{f(l)}{1-f(l)} &= I(l)\left[\frac{\eta_{\mathrm{p},0}}{I_{\mathrm{s}}(1+\phi/\phi_{\mathrm{s}})}\right] + a \\ &= TI(0)\left[\frac{\eta_{\mathrm{p},0}}{I_{\mathrm{s}}(1+\phi/\phi_{\mathrm{s}})}\right] + a\,, \end{aligned} \tag{A.6}$$

where $a = (\phi/\phi_{\mathrm{a}})/(1+\phi/\phi_{\mathrm{s}})$ is a laser saturation factor. This relation is used to eliminate f in Equation (A.5) and give the final result of Equation (3.14).

Appendix B

Birefringent filter

Following the instructions of [103] the optimum thickness of a BiFi can be found for a required wavelength and FSR. However, in practise, these exact dimensions are unlikely to be available. A more realistic situation is that a BiFi of a fixed thickness is available and an estimate of its FSR is needed. To precisely determine the FSR, valid pairs of m' and η at the required wavelength should be found from

$$\lambda = \frac{(n_\mathrm{e} - n_\mathrm{o}) d \sin^2 \eta}{m' \sin \theta_\mathrm{B}} \,. \tag{B.1}$$

The corresponding values of ϕ and α for these solutions are given through Equations (4.4) and (4.3). The transmission bandwidth is at a minimum for $\alpha = 45°$ [103], so the m' and η pair that is closest to this value will be the optimal BiFi alignment. The exact FSR can then be calculated with

$$\Delta\lambda = \frac{\lambda^2 \sin \theta_\mathrm{B}}{(n_\mathrm{e} - n_\mathrm{o}) d \sin^2 \eta} \,. \tag{B.2}$$

It is not trivial to calculate the FSR in this way, so an approximate relationship can be more useful.

A approximation to calculate the FSR is to allow m' to become non-integer in Equation (B.1). When the optic axis is parallel to the plane of the BiFi surface, $\sin^2 \eta = (1 - \cos^2 \phi \cos^2 \theta_\mathrm{B})$ from Equation (4.3), and $\cos^2 \phi = 1/(1 + \sin^2 \theta_\mathrm{B})$ when $\alpha = 45°$ from Equation (4.4). Inserting the two relationships into Equation (B.2) gives

$$\Delta\lambda \approx \frac{\lambda^2}{(n_\mathrm{e} - n_\mathrm{o}) d} \frac{(1 + \sin^2 \theta_\mathrm{B})}{2 \sin \theta_\mathrm{B}} \,. \tag{B.3}$$